

**OPTIMIZATION OF DISSOLUTION PERFORMANCE FOR
AMORPHOUS SOLID DISPERSIONS**

by
Chailu Que

A Dissertation

*Submitted to the Faculty of Purdue University
In Partial Fulfillment of the Requirements for the degree of*

Doctor of Philosophy



Department of Industrial and Physical Pharmacy
West Lafayette, Indiana
December 2019

THE PURDUE UNIVERSITY GRADUATE SCHOOL
STATEMENT OF COMMITTEE APPROVAL

Dr. Lynne S. Taylor, Chair

Department of Industrial and Physical Pharmacy

Dr. Geoff G.Z. Zhang

AbbVie Inc.

Dr. Tony Zhou

Department of Industrial and Physical Pharmacy

Dr. Zoltan Nagy

School of Chemical Engineering

Dr. Michael Harris

School of Chemical Engineering

Approved by:

Dr. Rodolfo Pinal

To Mom and Dad

ACKNOWLEDGMENTS

First, I would like to thank my advisor, Prof. Lynne S. Taylor. She has been a great mentor, always guiding me when I was confused, encouraging me when I was frustrated, supporting me when I needed help, and pulling me back when I was sidetracked. I was given enough space to conduct my research, and was provided with the erudite discussions to understand complicated problems. Her mentorship helped me become a better scientist.

I want to thank my committee members, Dr. Geoff Zhang, Dr. Tony Zhou, Dr. Zoltan Nagy, and Dr. Michael Harris, for their guidance. I also want to thank my AbbVie collaborators, Geoff Zhang, Gao Yi, Shweta Raina and Anura Indulkar for their helpful discussions. Especially, I would like to thank Geoff Zhang for being a great mentor during my internship at AbbVie. I am also very grateful to all the great scientists I have worked with and learned from: Christopher Gilpin, Robert Seiler, Laurie Mueller, Xiaochun Lou, Alex Deac, Huaping Mo, Dmitry Zemlyanov, and Qingqing Qi. I am thankful to all past and present members of the Taylor lab for their suggestions, discussions, training, and support. I especially thank Jennifer Lu, Na Li, Laura Isabel Mosquera Giraldo, and Venecia R. Wilson for their companionship, help, and guidance in the lab. I also highly appreciate all the administrative help from Mary Ellen Hurt and Nancy Cramer during these years.

Exciting research cannot be done without the financial support. I would like to thank AbbVie Inc. and Migliaccio/Pfizer Graduate Fellowship in Pharmaceutical Science for their financial support.

I would like to thank all my friends, especially Alex Deac, Kelsey Lubin, Carol Maccarthy, Nathan Wilson, Yi Feng, Lia Bersin, Jenifer Lu, Na Li, Kyle Lupo, Francesco Tres, and Michinori Oikawa for making life in the cornfields much more exciting. Purdue will always remind us with those “good old days”.

Tremendous thanks to my parents for their selfless love and endless support. The wisdom in life they taught me is indispensable throughout my PhD. Although I am so far from them in physical distance most of the time, I know they are always there whenever I need them. I know things will always get better because of them.

TABLE OF CONTENTS

| | |
|--|----|
| LIST OF TABLES | 9 |
| LIST OF FIGURES | 10 |
| ABSTRACT | 14 |
| CHAPTER 1. INTRODUCTION | 15 |
| 1.1 Research Significance, Knowledge Gap, Specific Aim, and Hypotheses | 15 |
| 1.2 Solubility Advantage of Amorphous Drugs | 18 |
| 1.3 Crystallization | 20 |
| 1.3.1 Primary Nucleation | 21 |
| 1.3.2 Secondary Nucleation | 22 |
| 1.3.3 Crystal Growth | 23 |
| 1.3.3.1 Classification of Crystal Surfaces | 23 |
| 1.3.3.2 Growth Mechanisms ³⁵ | 24 |
| 1.3.3.3 Diffusion-reaction Theory | 25 |
| 1.4 Impact of Polymers on Phase Behavior of Amorphous Solid Dispersions | 26 |
| 1.5 Impact of Polymers in Supersaturated Solutions | 28 |
| 1.5.1 Impact of Polymers on Nucleation | 28 |
| 1.5.2 Impact of Polymers on Crystal Growth | 29 |
| 1.5 Dissolution of Amorphous Solid Dispersions | 33 |
| 1.5.1 Dissolution Mechanism of Amorphous Solid Dispersions | 34 |
| 1.6 Reservoir Effect | 36 |
| 1.7 Drug-polymer Interactions | 36 |
| CHAPTER 2. PACLITAXEL CRYSTAL SEEDS WITH DIFFERENT INTRINSIC PROPERTIES AND THEIR IMPACT ON DISSOLUTION OF PACLITAXEL-HPMCAS AMORPHOUS SOLID DISPERSIONS | 38 |
| 2.1 Abstract | 38 |
| 2.2 Introduction | 39 |
| 2.3 Theoretical Considerations | 40 |
| 2.4 Materials | 41 |
| 2.5 Methods | 42 |

| | | |
|--|---|----|
| 2.5.1 | Determination of Crystalline Solubility and Amorphous Solubility. | 42 |
| 2.5.2 | Nucleation Induction Time Measurements. | 43 |
| 2.5.3 | Seed Crystal Preparation. | 44 |
| 2.5.4 | Crystal Seeds Growth in the Presence and absence of HPMCAS. | 44 |
| 2.5.5 | Preparation of Amorphous Solid Dispersions (ASDs) of Paclitaxel. | 45 |
| 2.5.6 | Dissolution of Paclitaxel-HPMCAS 49/51 (wt. %) Amorphous Solid Dispersions in the Absence and Presence of Crystal Seeds. | 45 |
| 2.5.7 | Scanning Electron Microscopy. | 46 |
| 2.5.8 | Transmission Electron Microscopy. | 46 |
| 2.5.9 | Determination of Paclitaxel Growth Unit Size. | 47 |
| 2.6 | Results. | 47 |
| 2.6.1 | Crystalline and amorphous solubility. | 47 |
| 2.6.2 | Nucleation Induction Time. | 48 |
| 2.6.3 | Characterization of Crystal Seed Morphology. | 48 |
| 2.6.4 | Crystal Growth in the Absence of Polymers | 51 |
| 2.6.5 | Crystal Growth in the Presence of HPMCAS. | 54 |
| 2.6.6 | Dissolution Profiles of Paclitaxel/HPMCAS (49/51) Amorphous Solid Dispersions | 56 |
| 2.7 | Discussion. | 58 |
| 2.8 | Conclusions. | 65 |
| CHAPTER 3. INSIGHTS INTO THE DISSOLUTION BEHAVIOR OF LEDIPASVIR-COPOVIDONE AMORPHOUS SOLID DISPERSIONS: ROLE OF DRUG LOADING AND INTERMOLECULAR INTERACTIONSINTRODUCTION. | | 66 |
| 3.1 | Abstract. | 66 |
| 3.2 | Introduction. | 67 |
| 3.3 | Materials | 69 |
| 3.4 | Methods. | 70 |
| 3.4.1 | Preparation of Amorphous Solid Dispersions (ASDs) of Ledipasvir. | 70 |
| 3.4.2 | Determination of Glass Transition Temperature of Amorphous Solid Dispersions by Differential Scanning Calorimetry (DSC). | 71 |
| 3.4.3 | Dissolution of Amorphous Solid Dispersions using Rotating Disk Apparatus. | 71 |
| 3.4.4 | Concentration Analysis of Ledipasvir and PVPVA. | 71 |

| | | |
|--|---|-----|
| 3.4.5 | Tablet Morphology Study by Micro Computed Tomography (Micro CT). | 72 |
| 3.4.6 | Amorphous-Amorphous Phase Separation Study by Fluorescence Microscope. | 72 |
| 3.4.7 | X-ray Photoelectron Spectroscopy (XPS). | 73 |
| 3.4.8 | Nuclear Magnetic Resonance Spectroscopy (NMR). | 73 |
| 3.4.9 | Dynamic Light Scattering (DLS)..... | 74 |
| 3.5 | Results..... | 74 |
| 3.5.1 | Glass Transition Temperature (T_g) | 74 |
| 3.5.2 | Release profiles of Ledipasvir-PVPVA ASDs | 75 |
| 3.5.3 | Release Profiles of Ledipasvir-PVPVA ASDs containing Surfactant..... | 77 |
| 3.5.4 | Particle Size of the Drug-rich Colloids Formed during Dissolution. | 79 |
| 3.5.5 | X-ray Micro-computed Tomography Images. | 80 |
| 3.5.6 | Fluorescence Microscopy | 81 |
| 3.5.7 | X-ray photoelectron spectroscopy (XPS) | 82 |
| 3.5.8 | Nuclear Magnetic Resonance (NMR) Spectroscopy | 85 |
| 3.6 | Discussion | 93 |
| 3.7 | Conclusions..... | 99 |
| CHAPTER 4. EVIDENCE FOR HALOGEN BONDING IN SOLUBILITY-ENHANCING DRUG-POLYMER DELIVERY SYSTEMS..... | | 100 |
| 4.1 | Abstract..... | 100 |
| 4.2 | Introduction..... | 100 |
| 4.3 | Experimental Section | 104 |
| 4.4 | Results..... | 104 |
| 4.4.1 | X-ray Photoelectron Spectroscopy (XPS) | 104 |
| 4.4.2 | Nuclear Magnetic Resonance Spectroscopy (NMR) | 109 |
| 4.4.3 | Infrared (IR) Spectroscopy of ASDs | 112 |
| 4.5 | Discussion | 114 |
| 4.6 | Conclusions..... | 118 |
| CHAPTER 5. THE IMPACT OF DRUG-POLYMER INTERMOLECULAR INTERACTIONS ON DISSOLUTION PERFORMANCE OF AMORPHOUS SOLID DISPERSIONS | | 119 |
| 5.1 | Abstract..... | 119 |
| 5.2 | Introduction..... | 120 |

| | | |
|-------|---|-----|
| 5.3 | Materials | 122 |
| 5.4 | Methods..... | 123 |
| 5.4.1 | Determination of Amorphous Solubility | 123 |
| 5.4.2 | Differential Scanning Calorimetry (DSC) | 124 |
| 5.4.3 | Preparation of Amorphous Solid Dispersions (ASDs) | 124 |
| 5.4.4 | Dissolution of Amorphous Solid Dispersions | 124 |
| | Dissolution using Rotating Disk Apparatus | 124 |
| 5.4.5 | Characterization of Drug-rich Phase Generated during Release Testing | 126 |
| | Nanoparticle Tracking Analysis (NTA) | 126 |
| 5.4.6 | Infrared Spectroscopy | 127 |
| 5.4.7 | X-ray Photoelectron Spectroscopy (XPS) | 127 |
| 5.5 | Results..... | 127 |
| 5.5.1 | Physicochemical Properties of Four Model Compounds | 127 |
| 5.5.2 | Release Profiles of ASDs..... | 128 |
| | Release Profiles of TIPP, Me-TIPP, PHPH, and Me-PHPH PVPVA ASDs | 128 |
| 5.5.3 | Characterization of Drug-rich Colloidal Species Generated upon Dissolution..... | 135 |
| 5.5.4 | Solid State Characterization of ASDs..... | 136 |
| 5.6 | Discussion | 141 |
| 5.7 | Conclusions..... | 145 |
| | APPENDIX A. SUPPORTING INFORMATION FOR CHAPTER 3 | 147 |
| | APPENDIX B. SUPPORTING INFORMATION FOR CHAPTER 4 | 154 |
| | REFERENCES | 183 |
| | VITA..... | 196 |

LIST OF TABLES

| | |
|--|-----|
| Table 2-1. Crystalline (dihydrate) and amorphous solubility of paclitaxel. | 48 |
| Table 2-2. Conditions used for crystal seeds generation and corresponding abbreviation..... | 48 |
| Table 2-3. Values used to calculate p_c (eq 2). | 60 |
| Table 3-1. Midpoint glass transition temperature for all the ASDs. Mean values \pm standard deviation are shown where $n=3$ | 75 |
| Table 3-2. Summary of evidence for drug-drug hydrogen bonding and VP-drug hydrogen bonding. | 96 |
| Table 4-1. Binding energy for neat materials and for peaks shifted to the lower binding energies when it is dispersed in PVPVA..... | 108 |
| Table 4-2. KF values for halogen bonding between model compounds and 1-ethyl-2-pyrrolidone from the 1H and ^{13}C NMR titration experiments at 25 °C in cyclohexane. | 112 |
| Table 5-1. Summary of HPLC methods for model compounds and polymer. | 126 |
| Table 5-2. Physicochemical properties for model compounds. Midpoint T_g and amorphous solubility are presented as mean values \pm standard deviation, where $n = 3$ | 128 |
| Table 5-3. Particle size for drug-rich colloidal species generated during ASD dissolution. Mean values \pm standard deviation are shown where $n=3$ | 135 |

LIST OF FIGURES

| | |
|--|----|
| Figure 1-1 Schematic depiction of the variation of enthalpy (or volume) with temperature. Taken from ref. 19. | 19 |
| Figure 1-2 Concentration-Temperature Phase Diagram. Adapted from ref. 23. | 20 |
| Figure 1-3 Free energy diagram for nucleation. Taken from ref 25. | 22 |
| Figure 1-4 A schematic representation of a Kossel crystal illustrating flat, stepped and kinked surfaces. Taken from ref. 34. | 24 |
| Figure 1-5 The driving force versus growth rate relationship. Taken from ref. 38. | 25 |
| Figure 1-6 Concentration driving force for crystallization from solution. Taken from ref. 22. ... | 26 |
| Figure 1-7 Induction times for efavirenz from unseeded-desupersaturation experiments, in the absence and presence of polymers. Taken from ref. 46. | 29 |
| Figure 1-8 Crystal growth rate ratio of efavirenz at an initial drug concentration of 10 $\mu\text{g/mL}$. Taken from ref. 53. | 30 |
| Figure 1-9 (I) Schematic of polymer adsorption onto the crystal surface at pH 3 and pH 6.8 respectively; AFM images of a) HPMCAS adsorbed to felodipine in pH 3, b) HPMCAS adsorbed to felodipine in pH 6.8, c) No HPMCAS. Taken from ref. 56. | 31 |
| Figure 1-10 Model of impurity adsorption. Impurity species are assumed to be adsorbed on the step lines at kink sites and to retard the advancement of the steps. Taken from ref. 58. | 32 |
| Figure 1-11 The basic steps in drug dissolution mechanisms. (1) The solvent molecule moves towards the liquid-solid interface; (2) Adsorption-reaction takes place at the interface; (3) Diffusion of the dissolved drug molecules into the bulk solutions. Taken from ref. 59. | 33 |
| Figure 1-12 Schematic presentations of dissolution mechanisms: (A) diffusion layer model; (B) interfacial barrier model. Taken from ref. 59. | 34 |
| Figure 1-13 Schematic representation of the dissolution model for a two component system. Taken from ref. 60. | 35 |
| Figure 2-1 Chemical structures of (a) paclitaxel and (b) HPMCAS. | 42 |
| Figure 2-2. Scheme of dissolution of ASDs in the presence of crystal seeds. | 46 |
| Figure 2-3. SEM images for crystal seeds of S16, S80, S16 w/ s and S80 w/ s. | 49 |
| Figure 2-4. Size distribution in terms of length (c) and width (b) for crystal seeds. | 50 |
| Figure 2-5. Crystal end areas normalized by mass for crystal seeds. | 51 |
| Figure 2-6. Desupersaturation profiles of paclitaxel solutions at an initial concentration of 31.6 $\mu\text{g/mL}$ ($S = 88$) in 18 wt. % seed crystals produced under different crystallization conditions. ... | 52 |

| | |
|--|----|
| Figure 2-7. Size distributions before and after crystal growth of seeds in terms of length and width for crystal seeds. S16-2, S80-2, S16 w/ s-2 and S80 w/ s-2 represent crystals after growth from the original crystals, S16, S80, S16 w/ s and S80 w/ s, respectively. | 53 |
| Figure 2-8. Aspect ratios before and after growth of crystal seeds in absence of polymers. The meshed columns represent crystal seeds processed by ultra-sonication before growth. | 54 |
| Figure 2-9. TEM images for crystal seeds after growth in the presence of HPMCAS. S16-3, S80-3, S16 w/ s-3 and S80 w/ s-3 represent crystals after growth from S16, S80, S16 w/ s and S80 w/ s crystal seeds in the presence of 31.6 $\mu\text{g/mL}$ HPMCAS, S = 88 respectively. | 55 |
| Figure 2-10. Average distance between adjacent HPMCAS adsorption sites. S16-3, S80-3, S16 w/ s-3 and S80 w/ s-3 represent crystals after growth from S16, S80, S16 w/ s and S80 w/ s seeds respectively in the presence of 31.6 $\mu\text{g/mL}$ HPMCAS. | 56 |
| Figure 2-11. Dissolution profiles for paclitaxel/HPMCAS 49/51 amorphous solid dispersions in the absence and presence of 18 wt. % crystal seeds generated under different conditions. | 57 |
| Figure 2-12. Residual paclitaxel concentrations determined by HPLC after filtration to remove crystalline material, 16 h after ASD dissolution in the presence and absence of crystal seeds (18 wt. %) of differing properties. | 58 |
| Figure 2-13. Concentration-temperature phase diagram for a supersaturated solution. Adapted from ref. 32. | 59 |
| Figure 2-14. Plot of critical nucleus size as a function of supersaturation ratio, according to eq. 2, by using the values from Table 2-3. The discrete data points represent the measured average distance between HPMCAS adsorption sites at residual supersaturation ratio at the end of 16 hr dissolution experiments in the presence of different crystal seeds. | 61 |
| Figure 2-15. SEM images for S16, S80 crystal seeds after growth in the absence of polymers. . | 62 |
| Figure 2-16. SEM images and TEM images of crystal ends for S16 and S80 crystal seeds. The first four pictures are TEM images, while the last two are SEM images. | 64 |
| Figure 3-1. Chemical Structures of Ledipasvir (a) and PVPVA with VP/VA mass ratio of 60/40 (b). | 70 |
| Figure 3-2. Release profiles of (a) ledipasvir and (b) PVPVA from ledipasvir-PVPVA amorphous solid dispersions with different DLs. | 76 |
| Figure 3-3. Release profiles of (a) 7.5% DL, (b) 10% DL ASDs containing 5 wt% Poloxamer 407 and SDS, (c) ASDs containing 5 wt% SDS with DL of 20, 30, and 40%. | 78 |
| Figure 3-4. Z-average particle diameter for the drug-rich particles generated during ASD dissolution. The x-axis represents the sampling time from the dissolution vessel. | 80 |
| Figure 3-5. X-ray micro-computed tomography cross-section images for (a) tablet before dissolution (b) 5% DL tablet after dissolution for 10 min (c) 10% DL tablet after dissolution for 10 min (d) 10% DL tablet after dissolution for 30 min. The images represent the cross-sectional area at the center of the tablets and were obtained after 2D reconstruction. | 81 |

| | |
|---|-----|
| Figure 3-6. Representative fluorescence microscope images of ledipasvir-PVPVA ASDs: (a) before exposure to moisture (50% DL), (b) 5% DL after exposure to moisture, (c) 10% DL after exposure to moisture and (d) 50% DL after exposure to moisture. Samples were exposed to 100% RH, 37 °C for 3 days..... | 82 |
| Figure 3-7. Tablet surface composition before and after dissolution for tablets with initial DLs of 20% and 50%. The weight percentage of drug on the near surface increases following dissolution for 10 min..... | 84 |
| Figure 3-8. Percentage of F 1s peaks with high and low binding energies as a function of DL in the ASD. It is apparent that the low binding energy F1s peak predominates at low DLs, while the high binding energy F1s peak is dominant at high DLs. | 84 |
| Figure 3-9. Percentage of F 1s with a lower binding energy (BE) of 684.0 ± 0.2 eV for ASDs with DLs of 10%, 20% and 50%, before and after dissolution for 10 min..... | 85 |
| Figure 3-10. ^{19}F -NMR spectra of ledipasvir in deuterated-DMSO (blue line) and deuterated-toluene (red line). The peaks labeled with asterisks are results of the geminal coupling of the two ^{19}F atoms with different chemical shifts..... | 87 |
| Figure 3-11. ^{19}F -NMR spectra of ledipasvir toluene solutions with concentrations of 0.5 mg/mL (blue line), 2 mg/mL (green line) and 4 mg/mL (red line). The peaks labeled with asterisks are results of the geminal coupling of the two ^{19}F atoms with different chemical shifts..... | 88 |
| Figure 3-12. ^{19}F -NMR spectra of ledipasvir (green line), in the presence of 2 mg/mL PVPVA (blue line), and in the presence of 2 mg/mL PVA (red line). The concentration of ledipasvir is 2 mg/mL and the solvent is toluene. The peaks labeled with asterisks are results of the geminal coupling of the two ^{19}F atoms with different chemical shifts..... | 89 |
| Figure 3-13. ^{19}F -NMR spectra of ledipasvir in the presence of varying amounts of 1-vinyl-2-pyrrolidinone. From bottom to top, the concentration of 1-vinyl-2-pyrrolidinone is 0, 2, 4, 8, 16, 32, 64 and 80 mg/mL respectively. The peaks labeled with asterisks are a result of the geminal coupling of the two ^{19}F atoms with different chemical shifts..... | 90 |
| Figure 3-14. ^1H -NMR spectra of NH groups in ledipasvir in the presence of varying amounts of 1-vinyl-2-pyrrolidinone. From bottom to top, the concentration of 1-vinyl-2-pyrrolidinone is 0, 2, 4, 8, 16, 32, 64 and 80 mg/mL respectively..... | 91 |
| Figure 3-15. Schematic showing (a) intra-molecular hydrogen bonding and (b) inter-molecular hydrogen bonding. | 92 |
| Figure 3-16. The chemical shift difference between fluorine atoms (primary y axis, ^{19}F NMR data, •) and number of fluorine atoms with a lower binding energy (secondary y axis, XPS data, ▲) as a function of DL. The shaded blue area delineates congruent release..... | 97 |
| Figure 4-1. Molecular structure of (a) clotrimazole, (b) brotrimazole, (c) loratadine, (d) 3,3-bis(3,5-diiodo-4-methoxyphenyl)isobenzofuran-1(3H)-one (Me-DIBF), (e) PVPVA , (f) PVP, (g) 1-ethylpyrrolidine, and (h) 1-ethyl-2-pyrrolidone..... | 103 |
| Figure 4-2. Representative halogen X-ray photoemission spectrum for (a) clotrimazole/PVPVA ASDs, (b) clotrimazole/PVP K29-32 ASDs, (c) brotramolze/PVPVA ASDs, (d) | |

| | |
|---|-----|
| loratadine/PVPVA ASDs, and (e) Me-DIBF/PVPVA ASDs. The X-ray photoemission spectrum of neat model compound were also shown as comparison. | 106 |
| Figure 4-3. The percentage of halogen atoms with high (as found in the neat compound) and low binding energies (new peaks seen in the ASD) as a function of drug loading (DL) in the ASD for ASD system (a) clotrimazole/PVPVA, (b) clotrimazole/PVP K29-32 (c) Loratadine/PVPVA, (d) brotrimazole/PVPVA, (e) Me-DIBF/PVPVA. | 109 |
| Figure 4-4. (a) ^1H NMR chemical shift change of clotrimazole as a function of the concentration of 1-ethyl-2-pyrrolidone; (b) ^{13}C NMR chemical shift change of clotrimazole as a function of the concentration of 1-ethyl-2-pyrrolidone. | 111 |
| Figure 4-5.(Following page) Infrared spectra of the carbonyl group region of pure PVPVA and (a) clotrimazole-PVPVA ASDs, (b) brotrimazole-PVPVA ASDs, and (c) Me-DIBF-PVPVA | 113 |
| Figure 4-6. Molar ratio of free:halogen bonded vinyl-2-pyrrolidinone moieties as a function of drug loading. Dotted lines are drawn as a guide to the eye. The number of VP carbonyl groups acting as halogen bond acceptors is considered equal to the number of halogen atoms participating in halogen bonding (Fig. 3)..... | 117 |
| Figure 5-1. Chemical structures of (a) 3',3'',5',5''-Tetraiodophenolphthalein (TIPP), (b) Phenolphthalein (PHPH), (c) 3,3-bis(3,5-diiodo-4-methoxyphenyl)isobenzofuran-1(3H)-one (Me-TIPP), (d) 3,3-bis(4-methoxyphenyl)isobenzofuran-1(3H)-one (Me-PHPH), (e) PVPVA with VP/VA mass ratio of 60/40, and (f) PVP..... | 122 |
| Figure 5-2. Release profiles of (a) TIPP/PVPVA ASDs with drug loading of 10 and 15%, (b) Me-TIPP/PVPVA ASDs with drug loading of 30, 40, and 50%, (c) PHPH/PVPVA ASDs with drug loading of 5 and 10%, and (d) Me-PHPH/PVPVA ASDs with drug loading of 30, 40, and 50%. | 130 |
| Figure 5-3. Release profiles with drug loading of 40 and 50% for (a) Me-TIPP/PVP K29-32 ASDs (b) Me-PHPH/PVP K29-32 ASDs..... | 134 |
| Figure 5-4. NTA scattering images of dissolution medium obtained after dissolution of (a) TIPP, (b) Me-TIPP, (c) PHPH, and (d) Me-PHPH PVPVA ASDs at drug loading of 10, 30, 5, and 30%. The bright spots indicate the presence of drug-rich colloidal species. | 136 |
| Figure 5-5. IR spectra for (a) TIPP-PVPVA ASDs, (b) Me-TIPP/PVPVA ASDs, (c) PHPH/PVPVA ASDs, and (d) Me-PHPH/PVPVA ASDs with drug loading from 0 to 90%.... | 138 |
| Figure 5-6. Molar amount of I atoms showing lower binding energy in 100 mg PVPVA ASDs for drug loading from 10 to 40 wt.%. | 141 |
| Figure 5-7. LoC for four model compound/PVPVA ASDs, and each column are labeled with types of hydrogen bond (OH) and halogen bond donor (I) for that compound. | 145 |

ABSTRACT

Many newly discovered drugs have low aqueous solubility leading to poor dissolution behavior and inefficient drug absorption, resulting in low bioavailability. Generally, for oral dosage forms, there are two major routes of drug absorption in the gastrointestinal (GI) track: passive diffusion and carrier-mediated transportation. Regardless of the primary route, drug absorption is highly dependent on the amount of free drug present in the aqueous solution. One formulation strategy to enhance solubility is the formation of an amorphous solid dispersion (ASD), where the drug is dispersed in a hydrophilic polymer. Supersaturation can be achieved following dissolution of an ASD, which significantly increases the free drug concentration. Recent research shows that dissolution of an amorphous solid dispersion can lead to a concentration above the maximum supersaturation concentration, also known as amorphous solubility. When this occurs, the drug and solution undergo liquid-liquid phase separation resulting in the formation of a drug-rich colloidal phase. This can only be obtained when the drug and polymer undergo polymer-controlled dissolution. During polymer-controlled dissolution the dissolution rate of the drug is limited by the intrinsic dissolution rate of pure polymer and not the drug dissolution rate. This brings forth two advantages over physically stable ASD formulations that exhibit polymer-controlled dissolution. The first is that the dissolution rate of the drug is orders of magnitude higher, which allows for quick attainment of maximum supersaturation *in vivo*. The second advantage is that the drug-rich colloidal phase can serve as a reservoir with very fast replenishing rates. This extends the duration of maximum flux across biological membranes, allowing for higher bioavailability. In order to achieve the optimal dissolution performance for an ASD formulation, it is critical to understand how to achieve polymer-controlled dissolution, as well as the impact of any crystallization events, which can deplete the supersaturation advantage. Thus, my PhD research focuses on mechanistically understanding the elements that prevent apparently stable ASD formulations from attaining their optimal dissolution performance. The conclusions drawn from the research may significantly improve the bioavailability of amorphous drugs and provides fresh insight into new drug molecule candidate optimization and excipient selection when an ASD is the preferred formulation strategy.

CHAPTER 1. INTRODUCTION

1.1 Research Significance, Knowledge Gap, Specific Aim, and Hypotheses

The introduction of combinatorial chemistry and high throughput screening has led to new molecular entities with higher molecular weight, greater hydrophobicity and more hydrogen bonding groups, resulting in 90% of new molecular entities being practically insoluble.^{1, 2} In general, for oral dosage forms, the drug absorption is highly dependent on the amount of free drug present in the aqueous phase. Thus, in order to improve the bioavailability of drugs with poor aqueous solubility, formulation strategies have been used to boost solution concentrations. One promising strategy is to deliver drug as an amorphous solid dispersion (ASD), which is a molecular level mixture of drug and a polymer. Compared to the crystalline solubility, the amorphous solubility can be several times higher.³ Thus, by dissolving an ASD, supersaturation can be achieved, which significantly increases the free drug concentration in the aqueous phase. However, drug molecules in a supersaturated solution have higher chemical potential relative to crystalline drug, which can lead to crystallization. If crystallization cannot be inhibited or slowed during dissolution, the solubility advantage of the amorphous formulation will be compromised. Crystallization has two processes, nucleation and crystal growth. For ASDs containing residual crystallinity, desupersaturation can happen if crystal growth cannot be inhibited or slowed. Several commercial ASD formulations have been found to contain some residual crystals.⁴⁻⁶ However, there is little understanding regarding the impact of residual crystallinity on ASD dissolution, and only the amount of residual crystallinity is controlled in an ASD formulation. Thus, **the first aim of the research was to demonstrate that seed crystals with different intrinsic properties have a variable impact on the dissolution performance of ASDs.**

The hypothesis for this aim is: the impact of residual crystallinity on the dissolution performance of ASDs is dependent on the intrinsic properties of crystal seeds, specifically crystal shape and in turn, growth area, as well as the growth interface properties, rather than the mass of seeds present.

To achieve and maintain a supersaturated drug solution is not the only advantage of ASD formulations. Recent research has shown that dissolution of an ASD can lead to a concentration above the maximum supersaturation concentration, and drug and solution undergo liquid-liquid

phase separation (LLPS).⁷ The resulting drug-rich phase consists of colloidal species, which can serve as a reservoir to replenish the drug solution concentration which is depleted during absorption, and can extend the duration of maximum flux across biological membrane.⁸ A study has shown that these drug-rich colloidal species can further improve bioavailability *in vivo*.⁹ Hence, the optimal dissolution performance from dissolving an ASD is to exceed the amorphous solubility with the formation of drug-rich colloidal species. However, this desired outcome cannot always be achieved during ASD dissolution. It only occurs when the dissolution is controlled by the polymer.¹⁰ Some recent studies have shown that drug release switches from being polymer-controlled to drug-controlled when drug loading increased above a certain limit.^{10, 11} At low drug loadings, the dissolution is controlled by polymer, where drug and polymer release congruently. In contrast, at high drug loadings, the dissolution switches to drug-controlled dissolution. When dissolution is controlled by amorphous drug, the maximum drug concentration that can be achieved is the amorphous solubility, therefore, no drug-rich colloidal species are able to be formed. The drug loading where drug release behavior dramatically changes from polymer-controlled to drug-controlled has been termed the limit of congruency (LoC).¹⁰ The LoC seems to be highly variable and unpredictable for copovidone (PVPVA)-based dispersions, and the underlying factors influencing this threshold value are unknown. Hence, **the second aim of the research is to mechanistically understand ASD release behavior, and to reveal which drug physicochemical properties impact the LoC.**

The hypothesis for this aim is: for copovidone-based ASDs, the drug release performance is dependent on drug loading; and the strength of drug-polymer interaction plays an important role in the dissolution behavior.

One of the most frequent studied intermolecular interactions in ASDs is hydrogen bonding.¹² This interaction has been shown to slow or prevent amorphous-amorphous phase separation or crystallization in ASDs.¹³⁻¹⁵ In contrast, another noncovalent interaction, halogen bonding, has not been studied in drug formulations. Halogen bonding is the attractive interaction between the electrophilic region of halogen atoms and electron donating groups. The halogen bond is a directional interaction, similar to the hydrogen bond. In terms of bonding strength, halogen bonds can be comparable to hydrogen bonds for optimized systems.¹⁶ It has been shown in several crystal engineering studies that when both interactions can form, hydrogen bonding is favored over halogen bonding, but they can still co-exist.¹⁷ The existence of halogen bonding in ASDs has not

been demonstrated. However, the halogen atoms in drug molecules potentially can form halogen bonding with the electron-donating groups in povidone. The most common technique used to investigate halogen bonding is X-ray crystallography, which is not possible for amorphous materials. There is a knowledge gap about halogen bonding and characterization techniques for amorphous formulation. Thus, **the third aim of the research is to demonstrate the existence of halogen bonding in ASDs by using different characterization techniques.**

The hypothesis for this aim is: The halogen bearing drug molecules can form halogen bonds with the carbonyl groups of vinyl-pyrrolidinone in PVPVA- based ASDs.

Drug-polymer interactions are considered to be an important parameter when it comes to ASD performance. Intermolecular interactions such as hydrogen bonding, ionic interactions and hydrophobic interactions have been studied. Their impact on drug-miscibility, amorphous crystallization tendency, and supersaturation maintenance following ASD dissolution has been investigated. However, little research has been done to study the impact of drug-polymer interactions on drug release performance, which is a knowledge gap in the ASD formulation space. As it mentioned earlier, LoC, an indicator for drug release performance, has become an important parameter for ASD formulations. Thus, it is important to understand the impact of drug-polymer interaction on the LoC. **The fourth aim of the research is to reveal the impact of different drug-polymer intermolecular interactions on drug release performance from PVPVA based ASDs.**

The hypothesis for this aim is: for PVPVA-based ASDs, the drug loading boundary, where the dissolution of ASDs changes from polymer-controlled to drug-controlled, is dependent on drug-polymer intermolecular interactions.

In summary, this research focuses on mechanistically understanding the elements that impair ASD formulations from achieving their optimal dissolution performance. The research provides fundamental understanding about the impact of crystallization and drug-polymer interactions on ASD dissolution. The conclusions drawn from the research can help optimize the dissolution performance, provide insight into new drug candidate optimization, and streamline formulation development.

1.2 Solubility Advantage of Amorphous Drugs

The key difference between an amorphous and a crystalline solid is that the former system lacks the repetitive three-dimensional order that persists over longer length scale. The molecules do not pack as compactly as in a crystalline solid which results in greater free volume for the amorphous system. However, amorphous solids do show some short range order¹⁸ via packing of molecules to form nearest neighbor interactions through van de Waals interactions, hydrogen bonding, or electrostatic interactions.

During cooling of a melt, the specific volume (V) or enthalpy (H) of the substance decreases as the function of temperature.¹⁹ Upon rapid cooling of a melt, V and H can follow the equilibrium line from liquid to the supercooled liquid even when the temperature is lower than T_m , because crystallization is an activated process and a certain extent of undercooling is necessary. For many systems, crystallization can be avoided completely. Additional cooling of the supercooled liquid leads to an increase in viscosity, and the molecules move more slowly until the temperature reaches the glass transition temperature (T_g) where the molecules move too slowly to rearrange significantly before the temperature decreases further. The molecules are “trapped” and the rearrangements are longer than the experimental timeframe and changes of V and H become relatively slower as the function of temperature. The material in this region is a glassy amorphous solid. These processes are presented in Figure 1-1, showing that compared to the crystalline solid, amorphous materials have excess thermodynamic properties. The free energy difference between amorphous solids and crystals can be estimated by the equation derived by Hoffman²⁰:

$$\Delta G = \frac{\Delta H_{fus}(T_m - T)T}{T_m^2} \quad 1-1$$

Where ΔH_{fus} is the melting enthalpy, T_m is the melting temperature and T is the temperature at which the amorphous converts to crystalline.

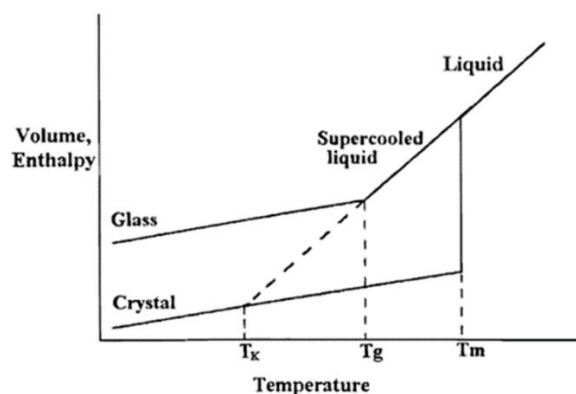


Figure 1-1 Schematic depiction of the variation of enthalpy (or volume) with temperature. Taken from ref. 19.

The higher free volume of the amorphous solid, translates to a larger molecular mobility compared to crystalline solids. When dissolving amorphous materials in aqueous solutions, no energy is needed to break down the compact crystalline structure for the amorphous form due to the lack of a crystal lattice. The solubility of amorphous form can be predicted by experimental determined crystalline solubility and free energy difference between amorphous and crystalline, expressed as the following equation²¹:

$$\Delta G = RT \ln \frac{a_{\text{amorphous}}}{a_{\text{crystalline}}} \approx RT \ln \frac{c_{\text{amorphous}}}{c_{\text{crystalline}}} \quad 1-2$$

Where a is the activity of the solute in saturated solution, c is the solubility, R is the gas constant, and T is the temperature. When in dilute solution where activity coefficients are approximately unity, the activity, a , can be assumed to be equal to the concentration, c , in an aqueous solution. From equation 2, the larger the free energy difference, the higher the potential solubility enhancement by the amorphous form. The amorphous form has been suggested to improve the aqueous solubility by a factor of 4 to 50 for different compounds.³ However, the higher free energy translates to greater thermodynamic driving force for crystallization.

1.3 Crystallization

By dissolving amorphous materials, supersaturation can be created, which means the solution concentration is higher than crystalline solubility. The supersaturation ratio is generally determined from the following relationship²²:

$$S = \frac{c}{c_{eq}} \quad 1-3$$

Where c is the drug concentration in the supersaturated solution and c_{eq} is the equilibrium crystalline solubility. A concentration-temperature phase diagram²³ is shown in Figure 1-2. When concentration is above the crystalline solubility, the chemical potential of the solute is higher than the solute in the saturated solution. This leads to thermodynamic driving force for crystallization. At low supersaturations, there is insufficient driving force to overcome the nucleation energy barrier, so that no spontaneous nucleation will occur. However, if there are crystal seeds, the crystal can grow in the metastable zone. When the concentration reaches the next region, secondary nucleation, new nuclei can be generated in the presence of crystal seeds. In the higher concentration region, the excess chemical potential can lead to spontaneous nucleation, which is termed primary nucleation. As the concentration increases further, the amorphous solubility will be reached, and liquid-liquid⁷ or glass-liquid²⁴ phase separation happens (LLPS or GLPS). Thus, when the concentration is at the amorphous solubility, several crystallization events, namely primary nucleation, secondary nucleation, and crystal growth, can occur.

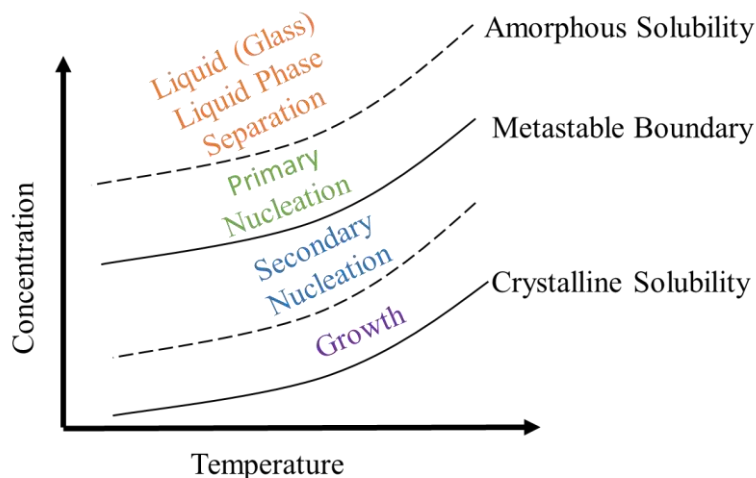


Figure 1-2 Concentration-Temperature Phase Diagram. Adapted from ref. 23.

1.3.1 Primary Nucleation

The mechanism of formation of a stable crystal nucleus from a homogenous solution is still under debate. However, the classical theory of nucleation²⁵ is widely employed. According to this theory, in order to create a new nucleus, an energy barrier needs to be surmounted. The overall free energy of nucleation, ΔG , is the summation of the positive free energy change ΔG_s , which is due to a formation of a new surface, and the negative free energy change ΔG_v , which is the excess free energy between a very large particle and the solute in the solution. Thus:

$$\Delta G = \Delta G_s + \Delta G_v = 4\pi r^2 \gamma + \frac{4}{3}\pi r^3 \Delta G_v \quad 1-4$$

Where r is the size of the nucleus, γ is the interfacial tension, and ΔG_v is the free energy change per unit volume. From equation 4, clearly ΔG_s and ΔG_v have different dependencies on the size of nucleus, so the total free energy ΔG has a maximum value, as shown in Figure 1-3. The maximum free energy, ΔG_{crit} can be calculated and is shown in eq 5, and the corresponding size of the nucleus is defined as the critical nucleus radius, r_c .

$$\Delta G_{crit} = \frac{16\pi\gamma^3 v^2}{3(kT \ln S)^2} \quad 1-5$$

Where S is supersaturation, v is molecular volume, k is the Boltzmann constant and T is the temperature. Hence, the nucleation rate can be expressed in the form of an Arrhenius equation:

$$J = A \exp \left[-\frac{16\pi\gamma^3 v^2}{3k^3 T^3 (\ln S)^2} \right] \quad 1-6$$

According to equation 6, supersaturation has a large impact on nucleation rate: the greater the supersaturation, the faster the nucleation rate is. Typically, there is a time delay between the achievement of supersaturation and the occurrence of nucleation, which is defined as the induction time. The experimental induction time (t_{ind}) is the sum of the nucleation time for critical nucleus to form (t_n) and time for nucleus to grow to a detectable size (t_g).²⁶

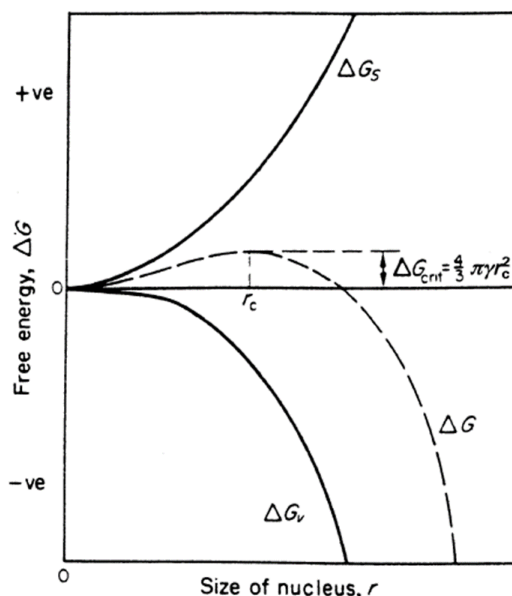


Figure 1-3 Free energy diagram for nucleation. Taken from ref 25.

1.3.2 Secondary Nucleation

When crystals of the solute are present in the supersaturated solution, nucleation at a lower supersaturation relative to that required for primary nucleation is possible. Many mechanisms have been proposed to interpret the origin of secondary nucleus. One theory is termed the embryo coagulation secondary nucleation (ECSN) theory. This theory proposes that secondary nuclei arise from displacement of the adsorbed solute layer that has not yet incorporated into crystals. Qian and Botsaris²⁷ examined the nucleation of a chiral molecule at a concentration in the secondary nucleation zone, and experimental results showed that crystals with the opposite chirality to that of the seeds were also detected. Because of the non-discriminating nature of van der Waal's forces, an embryo with different chirality will also attach to crystal seeds and undergo coagulation, which further leads to formation of nuclei.

However, only secondary nuclei with the same chirality as the parent crystals were observed by McBride and Carter²⁸, when the parent crystals were subject to multiple contacts with a magnetic stirrer. The researchers concluded that the secondary nucleus had been incorporated into the parent crystals to attain the same configuration before they were removed from the parent crystals by contact with the stirrer. Reyhani²⁹ *et al.* also found a strong connection between the morphology, movement of growth steps between embryonic and parent crystals. This mechanism

of secondary nucleation is defined as contact nucleation. Contact nucleation is highly depend on the supersaturation.³⁰ The critical nucleus size for survival decreases at higher supersaturation; the thickness of the adsorbed layer at the crystal surface increases at higher supersaturation to make more clusters available for secondary nucleation.

A mechanical shear force at the surface of crystals can also cause secondary nucleation, which is termed shear secondary nucleation. Tai *et al.*³¹ suggested that high supersaturation is necessary for shear secondary nucleation. Another common mechanism for secondary nucleation is attrition. Attrition nucleation is where fragments are removed from parent crystals by mechanical force, such as collision between crystals, or collision between crystals with other subjects, or by shear fluid. Attrition fragments often show anomalous growth behavior, namely that the crystal growth rate of fragments actually increases with fragment crystal size, and small fragments may not grow at all.³² Possible explanations are that the fragment is removed from a dislocation free area of a parent crystal or the distance of the dislocation growth site is smaller than the critical diameter.^{32, 33} Attrition secondary nucleation is a mechanical process so that it is independent on supersaturation.

1.3.3 Crystal Growth

When nuclei become larger than the critical size, they begin to grow. Similar to secondary nucleation, many different crystal growth mechanisms have been proposed in the literature. Mechanisms including as rough growth, spiral growth, and growth by two dimensional nucleation are considered here.

1.3.3.1 Classification of Crystal Surfaces

A Kossel crystal is often used as a model to illustrate crystal growth interfaces and mechanisms, and assumes that constituent units of both crystals and growth units are simple cubes (Figure 4). Kossel was the first to focus attention on the interface structure, and classified crystal surfaces into complete and incomplete surfaces.³⁴ Later, Hartman and Perdok divided crystal surfaces into three groups: flat (F), stepped (S) and kinked (K) surfaces, depending on the how many dense rows of atoms they are parallel to,^{35, 36} shown in Figure 1-4. Growth units are most

easily incorporated into a kink site, and the kinks move along the step, which eventually completes the face.³⁷

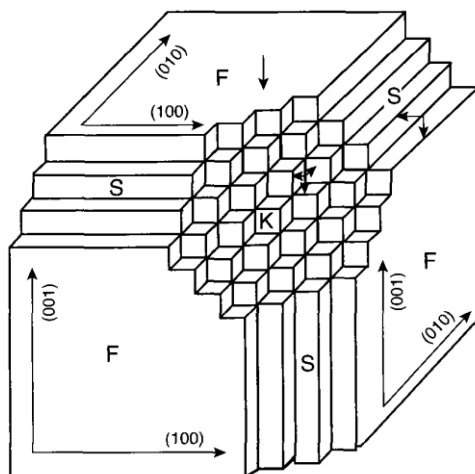


Figure 1-4 A schematic representation of a Kossel crystal illustrating flat, stepped and kinked surfaces. Taken from ref. 34.

1.3.3.2 Growth Mechanisms³⁵

The crystal surface with many kink sites available is a rough interface, and grows relatively faster. Rough faces can grow at any supersaturation higher than zero.

When the crystal surface is atomically or molecularly smooth, two dimensional nucleation is required to start a new layer. In this situation, the crystal growth is two independent processes: 1) formation of a “center of crystallization”; 2) lateral movement of the steps to complete the face. The system can undergo layer-by-layer growth, where the nucleation happens only after completion of the previous layer. In the other circumstances, nucleation takes place before completion of the previous layer, leading to multilayer growth.

As very few crystals are perfect, imperfections on crystal surface can influence the process of crystal growth. A screw dislocation formed on the surface can provide non-vanishing steps on the crystal surface. After the formation of a screw dislocation, the surface can grow forming a spiral staircase. The curvature of the spiral cannot exceed a certain value, which is determined by the two dimensional nucleus under the growth conditions.

In solution, the driving force for crystal growth is dictated by the supersaturation. For the three mechanisms, the growth rates have different dependences on supersaturations³⁸. Figure 1-5 summarizes the growth rate versus driving force for three growth mechanisms. At low driving

forces, the growth interface is smooth and growth is controlled by spiral growth. With moderate driving force, the interface is smooth, and the two dimensional growth mechanism is dominant. When the driving force increases, the interface becomes rougher.

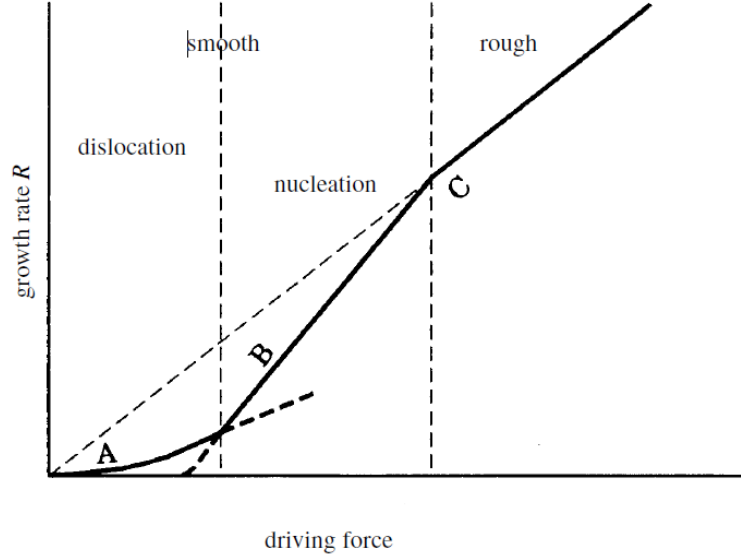


Figure 1-5 The driving force versus growth rate relationship. Taken from ref. 38.

1.3.3.3 Diffusion-reaction Theory

The diffusion theory was first introduced by Noyes and Whitney³⁹, and later was modified by Berthoud⁴⁰ and Valetton⁴¹ to diffusion-reaction theory. There are two steps in the crystal growth: 1) solute transports from bulk solution to the solid surface; 2) the solute molecule incorporates into the crystal lattice. The driving force for these two steps is concentration difference, which can be represented by the equations

$$\text{Diffusion: } \frac{dm}{dt} = k_d A (c - c_i) \quad 1-7$$

$$\text{Surface integration: } \frac{dm}{dt} = k_r A (c_i - c^*) \quad 1-8$$

$$\text{Overall growth rate: } Rg = Ak_g S^g \quad g = 1 \sim 2 \quad 1-9$$

Where k_d is a coefficient of mass transfer by diffusion, k_r is a rate constant for the surface integration process, c_i is the solute concentration in the solution at the crystal-solution interface, c is the concentration of the bulk solution, c^* is the concentration at the crystal surface, A is the

surface area of the crystal, k is an overall crystal growth coefficient, S is supersaturation, and g is the order of the overall crystal growth.

A pictorial representation of these two processes is shown in Figure 1-6. If $g = 1$, the crystallization is a diffusion controlled process, and while $g = 2$ indicates surface integration controlled crystallization. In many cases, the crystal growth is integration controlled, such as screw dislocation and 2-dimensional nucleation mechanisms.

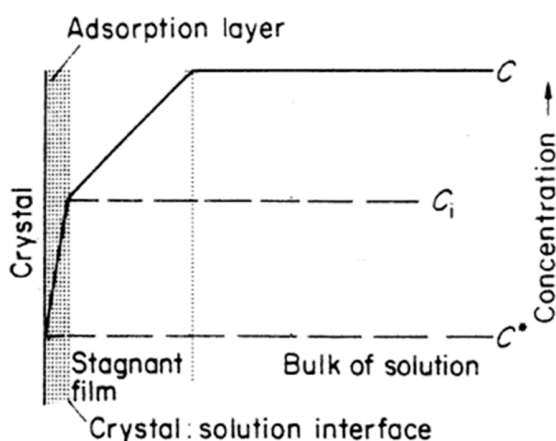


Figure 1-6 Concentration driving force for crystallization from solution. Taken from ref. 22.

1.4 Impact of Polymers on Phase Behavior of Amorphous Solid Dispersions

In ASDs, amorphous drugs and polymers are mixed at the molecular level, resulting in a miscible, single phase system. ASDs can be prepared by either melting the two components followed by quench cooling of the mixture, or dissolving both components, and then evaporating the solvent.⁴² In the pharmaceutical industry, the scaled processes are hot melt extrusion and spray drying, respectively. Hancock et al. studied several glasses in terms of their molecular mobility by monitoring enthalpy relaxation with time due to the molecular motion below the glass transition temperature (T_g), and the results show that amorphous materials are more stable at temperatures much lower than the T_g .⁴³ Thus, mixing a high T_g polymer with an amorphous drug can increase T_g , resulting in better stability of the drug to crystallization at room temperature. The polymer not only modulates T_g , but also reduces the local molecular mobility to prevent the rearrangement of the drug molecules to form crystals.

In order to prevent the amorphous drug from crystallization, the drug and polymer need to be miscible. The free energy of mixing (ΔG_{mix}) for drug-polymer binary system can be determined by Flory-Huggins theory.⁴⁴ The entropy of mixing (ΔS_{mix}) is determined by the number of configurational states of drug and polymer, which is always favorable to mixing. The enthalpy of mixing (ΔH_{mix}) is dependent on the drug-drug, drug-polymer, and polymer-polymer interactions. If the drug-polymer interactions are favorable, ΔH_{mix} is negative. When the drug-polymer interactions are unfavorable, ΔH_{mix} is positive. ΔG_{mix} , ΔS_{mix} , and ΔH_{mix} are given by the following equation,

$$\frac{\Delta G_{mix}}{RT} = n_d \ln \phi_d + n_p \ln \phi_p + \chi_{dp} n_d \phi_p \quad 1-10$$

$$\frac{\Delta S_{mix}}{RT} = -n_d \ln \phi_d - n_p \ln \phi_p \quad 1-11$$

$$\frac{\Delta H_{mix}}{RT} = \chi_{dp} n_d \phi_p \quad 1-12$$

Where the d and p represent drug and polymer respectively, n and ϕ are mole fraction and volume fraction respectively, and χ is the Flory-Huggins interaction parameter between drug and polymer.

However, drug-polymer phase separation can occur in the presence of moisture, resulting in drug-rich and polymer-rich phases. A drug-rich phase has higher tendency for crystallization. In the presence of water, a ternary system composed of water, drug, and polymer is formed. In this case, the free energy of mixing can be given by equation 1-13.⁴⁵ ΔS_{mix} is typically favorable to mixing. Hence, the interactions between water-drug, water-polymer, and drug-polymer, which are reflected in the ΔH_{mix} term, decide if the mixing is favorable. When the interaction energies between the components are quite different, amorphous-amorphous phase separation can happen in the presence of moisture. However, when the formation of drug-rich and polymer-rich is preferred thermodynamically, sufficient molecular mobility is still required to kinetically enable phase separation to occur.⁴⁵

$$\frac{\Delta G_{mix}}{RT} = n_w \ln \phi_w + n_d \ln \phi_d + n_p \ln \phi_p + \chi_{wd} n_w \phi_d + \chi_{wp} n_w \phi_p + \chi_{dp} n_d \phi_p \quad 1-13$$

Where w stands for water.

A suitable polymer can inhibit crystallization of the drug in the matrix, prevent nucleation of the drug in supersaturated solutions, and inhibit crystal growth when there are crystal seeds in solution.

1.5 Impact of Polymers in Supersaturated Solutions

1.5.1 Impact of Polymers on Nucleation

By dissolving an amorphous drug, supersaturation can be achieved in aqueous solutions. However, nucleation is likely to happen due to the higher chemical potential of the solute in the supersaturated solution. The higher the concentration, the greater the driving force for primary nucleation. Polymers have been demonstrated to inhibit nucleation of poorly water soluble drugs to some extent, and can thus lead to a longer duration of supersaturation.⁴⁶⁻⁴⁸ As shown in Figure 1-7, efavirenz is a good crystallizer, thus in the absence of polymers, primary nucleation occurs within 5 min. In the presence of various polymers, the induction time is increased to around 30 min.⁴⁶ However, how these polymers exert their effect is still unclear, partly due to difficulties associated with performing molecular-level experiments. Based on experimental observations and molecular simulations, solute-polymer interactions are key for nucleation prevention. When there are strong interactions between polymer and solute, the polymers are able to influence the packing of solute molecules into nuclei.⁴⁹

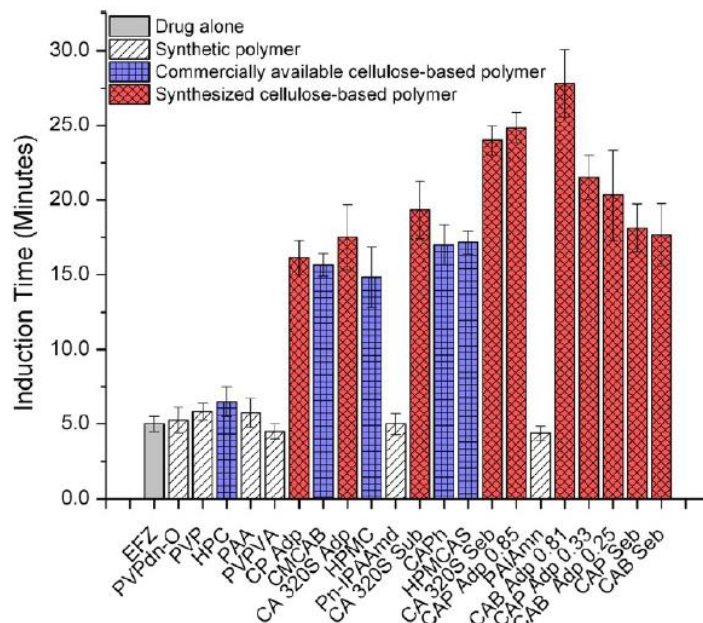


Figure 1-7 Induction times for efavirenz from unseeded-desupersaturation experiments, in the absence and presence of polymers. Taken from ref. 46.

For secondary nucleation, very few studies have been conducted to shed any fundamental light on impurities effects, including polymers, on secondary nucleation. Secondary nucleation is assumed to be related to interfacial supersaturation, so that any addition of impurities leading to a change of interfacial supersaturation will impact secondary nucleation.⁵⁰ In another study of impact of polymers on secondary nucleation, it was shown that secondary nucleation was suppressed by polymers in a manner dependent on the solution viscosity.⁵¹

1.5.2 Impact of Polymers on Crystal Growth

Maintaining solution supersaturation, thereby maximizing the drug absorption is very important after ASD dissolution. Hence, incorporating a good crystal growth inhibitor into the formulation is desirable since crystalline-free ASDs are not always possible in practice. Several studies^{48, 52, 53} have shown that polymers are able to inhibit or retard crystal growth of water-insoluble drugs in supersaturated solutions. In Figure 1-8, the y axis represents the ratio of the crystal growth rate in the absence of polymers to that in the presence of polymers, and it can be noted that several polymers are able to inhibit efavirenz crystal growth, at least to some extent.

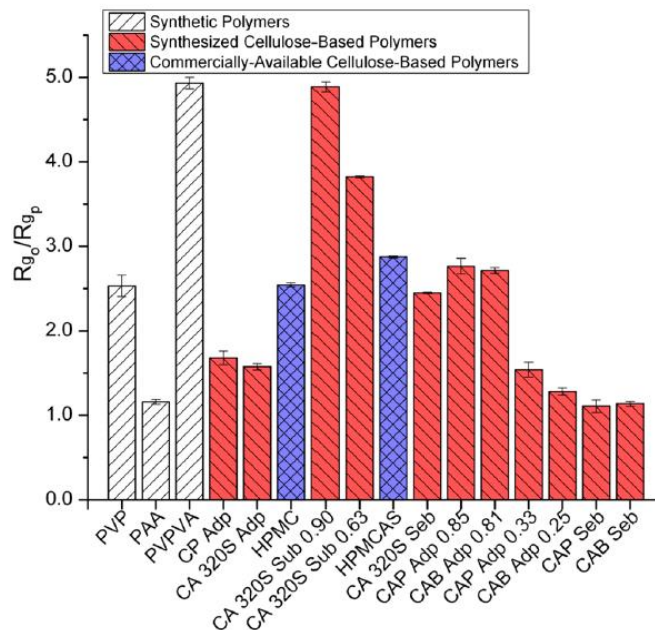
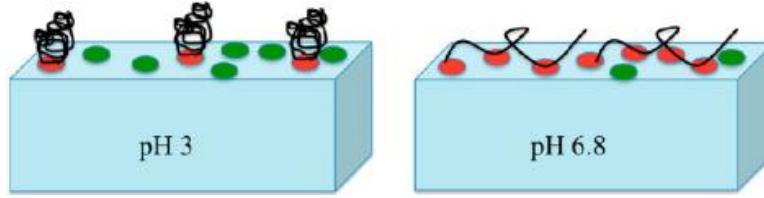


Figure 1-8 Crystal growth rate ratio of efavirenz at an initial drug concentration of 10 µg/mL.
Taken from ref. 53.

For inhibition of crystal growth by polymers, there is a general consensus that adsorption of polymers onto the crystal surface is a required step. Studies show that the hydrophobicity, polymer conformation, and amphiphilic nature of the polymer, play an important role in dictating the extent of crystal growth inhibition. If polymers are too hydrophilic, they tend to interact with solvent molecules. When polymers are too hydrophobic, it is likely they interact more favorably with other monomer units, resulting in less interaction with drug molecules.⁵² For polymer conformations including trains, loops and tails, the balance among these three sub-chains gives the absorbed layer its unique properties, which further impact the polymer adsorption on the crystal surfaces.⁵⁴ The amphiphilic nature of polymers is shown to further enhance their ability to inhibit crystal growth.⁵² Polymers with a higher degree of carboxylic acid (COOH) substitution tend to be more effective at inhibiting crystal growth, and the degree of ionization of the COOH group varies with pH, which in turn influences the conformation of the polymers on the crystal surface.⁵⁵ Atomic force microscopy has been used to study the conformational changes of HPMCAS on crystal surface at different pHs.⁵⁶ The results, shown in Figure 1-9, show that at pH 3, below the pKa of HPMCAS, globules of polymer are observed because of self-aggregation of the unionized polymer, and the effectiveness of HPMCAS as a crystal growth inhibitor reduces. In contrast, at

pH 6.8, above pKa, the ionized COOH groups are more “water-loving”, so that the polymers more uniformly cover the surface, rendering HPMCAS a better crystal growth inhibitor at this pH.

I)



II)

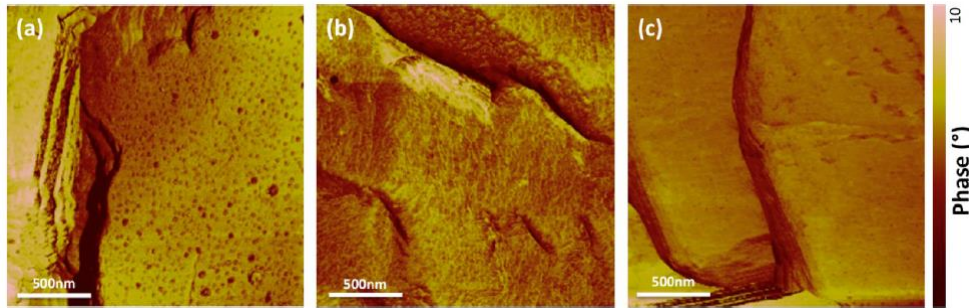


Figure 1-9 (I) Schematic of polymer adsorption onto the crystal surface at pH 3 and pH 6.8 respectively; AFM images of a) HPMCAS adsorbed to felodipine in pH 3, b) HPMCAS adsorbed to felodipine in pH 6.8, c) No HPMCAS. Taken from ref. 56.

For the mechanism of how adsorbed impurities (polymers) impact the crystal growth rate, Kubota and Mullin⁵⁷ have proposed a mathematical model. This model (Figure 1-10) is based on the adsorption layer theory, which assumes the atoms continuously adsorb onto the crystal surface and then build into active sites until the whole crystal face is completed, and to initialize a new growth face, a two-dimensional nucleus needs to be created. The critical radius of a two dimensional nucleus ρ_c is given by Burton et al³³,

$$\rho_c = \frac{\gamma a}{kT(\ln S)} \quad 1-10$$

Where γ is the edge free energy, a is the size of a growth unit, k is the Boltzmann constant, T is the solution temperature and S is the supersaturation ratio.

According to this theory, crystal growth is a step-wise build-up leading to a linear advancement on the crystal face. The velocity of a linear step, v_0 , can be hindered if polymers

adsorb at kink sites along the step lines by a pinning mechanism.⁵⁸ Based on this model, the linear step is forced to curve and the advancement velocity of a curved step is related to the average distance between adjacent adsorbed polymers, l . Then the time-average advancement velocity, v , of the step with adsorbed polymers can be given by the equation^{57, 58}

$$\frac{\vartheta}{\vartheta_0} = 1 - \rho_c/l \text{ (for } l > \rho_c \text{)} \quad 1-11$$

Where $v = 0$ for $l < \rho_c$.

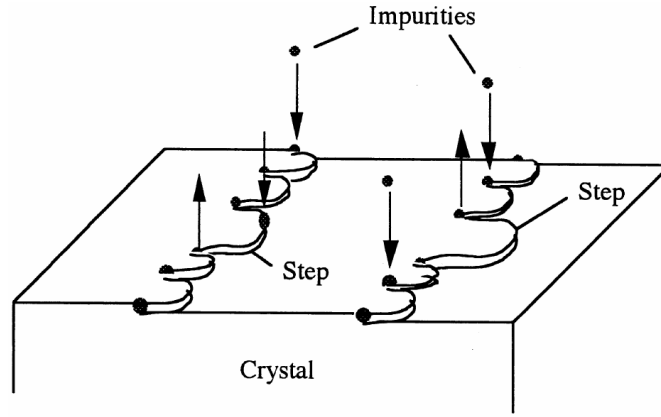


Figure 1-10 Model of impurity adsorption. Impurity species are assumed to be adsorbed on the step lines at kink sites and to retard the advancement of the steps. Taken from ref. 58.

The coverage of active sites by polymers, θ , is related to the average distance between the active sites, L , and the average distance between adjacent polymers, l .

$$\theta = \frac{L}{l} \quad 1-12$$

Insertion of eqs. (10) and (12) into eq. 11 gives the following equation,

$$\frac{\vartheta}{\vartheta_0} = 1 - \frac{\gamma a}{kT(\ln S)L} \theta \quad 1-13$$

The impurity effectiveness factor, α , is defined as

$$\alpha = \frac{\gamma a}{kT(\ln S)L} \quad 1-14$$

1.6 Dissolution of Amorphous Solid Dispersions

Since the 1960s, dissolution of drugs became a very important research subject in pharmaceuticals. The basic step of drug dissolution is the reaction between solid drug and the dissolution medium. Therefore, the dissolution kinetics are dependent on the flow rate of the medium towards the solid-liquid interface, the reaction rate at the interface, and diffusion rate of dissolved drug molecules from interface to bulk solutions, shown in Figure 1-11.⁵⁹ Steps 2 and 3 in Figure 1-11 are highly dependent on the hydrodynamic conditions, especially the microenvironment of the solids.

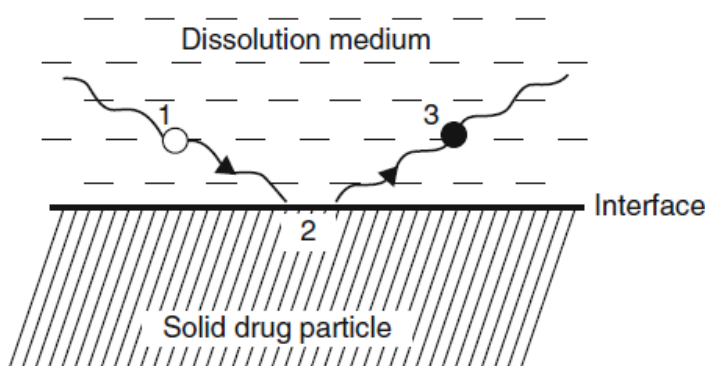


Figure 1-11 The basic steps in drug dissolution mechanisms. (1) The solvent molecule moves towards the liquid-solid interface; (2) Adsorption-reaction takes place at the interface; (3) Diffusion of the dissolved drug molecules into the bulk solutions. Taken from ref. 59.

Based on either diffusion of the dissolved drug molecules from interface to bulk solution or reaction of the interface of liquid-solid, the dissolution mechanisms can be interpreted by two models: the diffusion layer model and the interfacial barrier model, respectively. These two models are illustrated in Figure 1-12. Both of these models are based on the assumption that there is a stagnant liquid layer in contact with the solid interface. In general, the diffusion layer model is more commonly used.

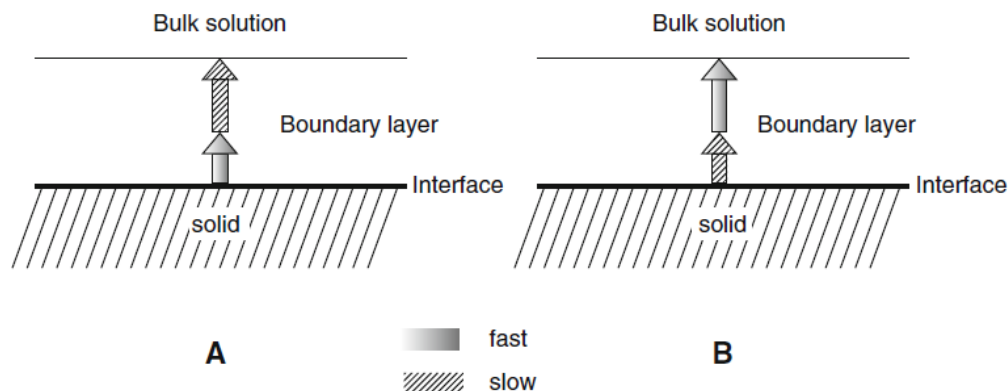


Figure 1-12 Schematic presentations of dissolution mechanisms: (A) diffusion layer model; (B) interfacial barrier model. Taken from ref. 59.

Noyes and Whitney³⁹ were the first to conduct quantitative studies of dissolution processes. They proposed an equation stating that the rate of the mass, M , of solids dissolved in solution is proportional to the surface area of the solid, A , the solubility of the solid, S , and the concentration, C , at time t , which gives the equation,

$$\frac{dM}{dt} = -kA(S - C) \quad 1-15$$

Where k is the mass transfer dissolution rate constant, and has the dimension of length/time (cm/sec). According to the equation, when dissolving pure amorphous drug, the maximum concentration can be achieved is amorphous solubility.

1.6.1 Dissolution Mechanism of Amorphous Solid Dispersions

The general dissolution mechanisms of a single component have been discussed earlier, but in terms of ASD dissolution, the situation is more complicated due to the presence of an intimate mixture of two components: the polymer and the drug. Higuchi *et al.* published a mathematical model to describe dissolution mechanism of polyphase mixtures.⁶⁰ Upon exposure of two components to solvent, they dissolve with the rates proportional to their solubility, C_s , and diffusion coefficients, D , as described in a dissolution model for a single component. In this model, the component which diffuses faster, forms an interfacial layer at the dissolution front, and the

other component has to diffuse through this layer prior to release into in the bulk solution (Figure 1-13).

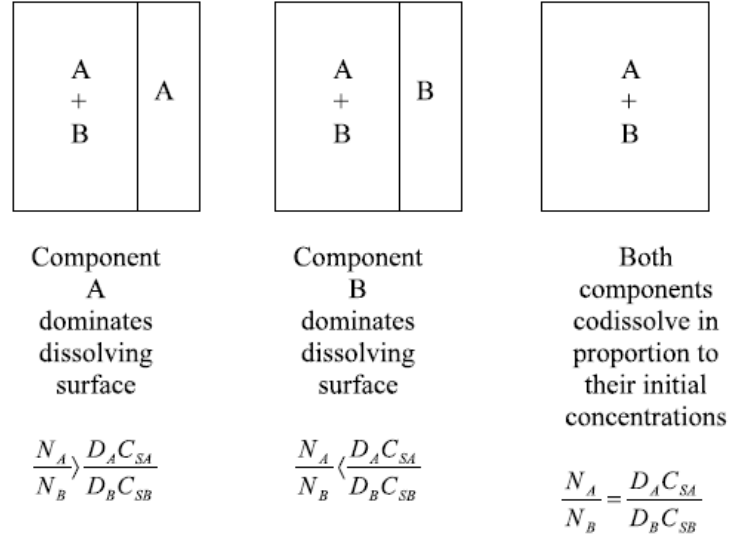


Figure 1-13 Schematic representation of the dissolution model for a two component system.
Taken from ref. 60.

If component A diffuses faster, the component A rich phase forms at the interface of solid-liquid,

$$\frac{N_A}{N_B} > \frac{D_A C_{SA}}{D_B C_{SB}} \quad 1-16$$

Where N_A and N_B denote the proportion of component A and B, respectively. In this situation the dissolution rates of each component are given by,

$$G_A = \frac{C_{SA} D_A}{h} \quad 1-17$$

$$G_B = \frac{N_B}{N_A} G_A \quad 1-18$$

Where G is the diffusion rate per unit area, and h is the thickness of the diffusion layer. This model predicts that the dissolution rate of the minor component is controlled by the dissolution rate of the excess component. This model has been confirmed by experimental studies of the dissolution

rates of polyvinylpyrrolidone (PVP) sulfathiazole coprecipitates.⁶¹ This study showed that the dissolution rate of sulfathiazole is independent of the dissolution rate of PVP at low PVP weight fractions, while the dissolution rate of sulfathiazole increases with an increasing dissolution rate of PVP at high PVP weight fractions.

Recent studies have shown that for miscible PVPVA-based ASDs, the dissolution behavior falls into two different dissolution regimens depending on drug loading.¹⁰ At low drug loadings, drug and polymer dissolve congruently (i.e. at the same rate), and the dissolution rate is comparable to pure PVPVA dissolution rate. In this regimen, the formulation can achieved 100% release resulting in the formation of drug-rich colloidal species. However, at higher drug loadings, the tablet surface becomes drug-enriched, and the dissolution is dominated by amorphous drug. In this case, insufficient drug and polymer release were observed. This pattern of behavior was proposed as the consequence of competition between ASD dissolution and amorphous-amorphous phase separation (AAPS) at the dissolution front. A faster AAPS kinetics leads to lower extent of release. Similar dissolution behavior has been reported for other ASDs.¹¹

1.7 Reservoir Effect

Raina *et al.* has demonstrated that the flux across membrane increases with increasing supersaturation until the free drug concentration reaches the amorphous solubility.⁶² Amorphous solubility is the maximum free drug concentration can be attained. LLPS occurs when the concentration exceeds amorphous solubility LLPS occurs, which leads to formation of drug-rich colloidal species. Indulkar *et. al* proved that these drug-rich colloidal species can quickly replenish the solution concentration, which can extend the duration of the maximum flux. The advantage of this drug-rich phase is defined as the “reservoir effect”. Because of the reservoir effect, the bioavailability of amorphous formulations can be further improved *in vivo*.^{9, 63} Thus, drug-rich colloidal species are beneficial for drug absorption, and it is desirable to surpass amorphous solubility when dissolving an ASD.

1.8 Drug-polymer Interactions

Drug-polymer intermolecular interactions are considered to play an important role in ASD formulation performance. There are several interactions that have been studied, such as hydrogen

bonding, ionic interactions, and hydrophobic interactions. Among these three interactions, hydrogen bonding is the most frequently studied interaction. For povidone (PVP) or PVPVA ASDs, the hydroxyl groups in the drug molecules are able to form hydrogen bonds with the carbonyl group of vinyl pyrrolidinone.^{12, 14, 64} With drug-polymer hydrogen bonding, the physical stability of ASDs was improved by reducing drug crystallization kinetics in the ASD matrix.⁶⁵ The enhanced drug-polymer miscibility by hydrogen bonding also leads to better hot melt extrusion processability for PVP-based ASDs.⁶⁶ Infrared (IR) spectroscopy, solution nuclear magnetic resonance (NMR) and solid state NMR have been used to characterize the hydrogen bonding in ASDs.^{12, 67, 68} Ionic interactions also have proven to delay drug crystallization in the ASD matrix.⁶⁹ Hydrophobic interactions between HPMCAS and drug molecules in solution can help maintain the supersaturation following ASD dissolution.⁷⁰

CHAPTER 2. PACLITAXEL CRYSTAL SEEDS WITH DIFFERENT INTRINSIC PROPERTIES AND THEIR IMPACT ON DISSOLUTION OF PACLITAXEL-HPMCAS AMORPHOUS SOLID DISPERSIONS

A version of this chapter has been previously published in *Crystal Growth & Design*
DOI: 10.1021/acs.cgd.7b01521

2.1 Abstract

Dissolving a formulation containing the drug in amorphous form can lead to supersaturation and increase the free drug concentration relative to that achieved by dissolving the crystalline form. However, the amorphous form is thermodynamically metastable and hence crystallization can occur both in the formulation and from the supersaturated drug solution generated upon dissolution. From a practical perspective, it may not be possible to always produce amorphous solid dispersions (ASDs) that are completely free of residual crystallinity. Crystals formed in different environments can have dissimilar intrinsic properties, which in turn can influence crystal growth kinetics and hence the dissolution profile of the ASD. Herein, paclitaxel, a compound that crystallizes as needles, was used as a model compound to explore the impact of crystal seeds on the (de)supersaturation profile obtained following dissolution of an amorphous solid dispersion. Crystal seeds generated under four different conditions had different available growth areas, size distributions, and interface structure. These differences translated to variations in crystal growth rates from supersaturated solutions, which in turn impacted the supersaturation profiles observed following dissolution of the amorphous solid dispersions. Furthermore, in the presence of a polymeric growth inhibitor, the crystal growth rate was reduced. This was attributed to polymer adsorption onto the crystal surface whereby the average distance between polymer adsorption sites was of the same order of magnitude as the critical nucleus size for 2D growth (at a given supersaturation). Our study clearly demonstrates that for ASD performance, the mass of crystal seeds is not the relevant parameter, rather it is the available growth area and interface structure of the seeds. Thus, in considering the likely impact of residual crystals on ASD performance, crystal morphology and growth area, interface structure, as well as the effectiveness of additives in poisoning growth need to be taken into account.

Keywords: crystal seeds; amorphous solid dispersions; supersaturation; solubility

2.2 Introduction

Many newly discovered drugs have low aqueous solubility leading to poor dissolution behavior and inefficient drug absorption, resulting in low bioavailability.⁷¹ Generally, for oral dosage forms there are two major routes of drug absorption in the gastrointestinal (GI) track: passive diffusion and carrier-mediated transportation.⁷² Regardless of the primary route, drug absorption is highly dependent on the amount of free drug present in the aqueous solution. One formulation strategy to enhance solubility is the formation of an amorphous solid dispersion (ASD), where the drug is dispersed in a hydrophilic polymer.^{71, 73} Under non-sink conditions, supersaturation can be achieved following dissolution of an ASD, which significantly increases the available molecularly dissolved drug.^{3, 21} Although the amorphous drug provides a solubility advantage, the higher chemical potential of the solute in a supersaturated solution relative to the crystalline form provides a driving force for crystallization.^{20, 74} If crystallization cannot be slowed down or inhibited completely during dissolution, the generated supersaturation will be depleted, and the solubility enhancement of the amorphous formulation will be reduced.

Crystallization involves two processes, nucleation and crystal growth. Certain polymers have been found to slow down or inhibit the nucleation of amorphous drugs either in the solid state^{75, 76} or from the supersaturated solutions generated upon dissolution^{46, 47}. For some systems, exposure to atmospheric water and/or elevated temperatures can lead to crystallization of the amorphous drug in the matrix⁷⁷; this can happen during manufacturing, storage or dissolution. Thus for some systems, the drug is not completely amorphous in the formulation; e.g. the formulation patent for KalydecoTM which contains ivacaftor, a drug used to treat cystic fibrosis, indicates that the amorphous solid dispersion contains up to 15% crystalline drug.⁴ Trasi et al. have suggested that a commercial formulation of tacrolimus contains predominantly amorphous drug with a low level of crystalline seeds, which are produced during the manufacturing process.⁵ In another study, a commercial lyophilized formulation of paclitaxel was found to contain trace amounts of paclitaxel crystals.⁶ Several techniques such as x-ray diffraction, thermal analysis, microscopy and Raman spectroscopy are used to detect the formation of crystals in ASD matrices^{74, 78, 79}, but crystallinity levels below 1% are challenging to detect with these common analytical approaches⁸⁰. Therefore, from a practical perspective, it may not be possible to always produce

amorphous solid dispersions or other amorphous formulations that are completely free of residual crystallinity. The presence of crystal seeds will potentially reduce the solubility enhancement of the amorphous form if crystal growth cannot be inhibited during the dissolution process.⁸¹

It is clearly important to understand the impact of residual crystallinity on the dissolution performance of ASDs. However, to date, little research has been conducted in this area. Furthermore, crystals produced from conventional solvent crystallization processes have been employed to evaluate the impact of seeds on supersaturation profiles.^{46, 81} However, the crystal seeds present in an ASD may have different properties from the bulk crystalline active pharmaceutical ingredient (API) typically used to evaluate the impact of crystallinity as well as to set specifications for crystallinity limits. Indeed, previous studies have shown that crystals evolved in different environments can result in different crystal growth rate kinetics.^{82, 83}

The hypothesis under evaluation in the current study is that seed crystals with different morphologies will have a variable impact on the dissolution profiles of amorphous solid dispersions when compared at equivalent initial weight percent crystallinity levels. To test this hypothesis, paclitaxel seed crystals generated under different conditions were added to the dissolution medium. Paclitaxel ASDs were then dissolved and the impact of the different seeds on the dissolution performance was evaluated in terms of the level of supersaturation achieved and the rate of desupersaturation. Bulk API crystals were also used for comparison. Scanning and transmission electron microscopy were used to better understand seed properties.

2.3 Theoretical Considerations

Supersaturation. The supersaturation ratio is generally determined from the following relationship²²:

$$S = \frac{a}{a^*} = \frac{c\gamma'}{c^*(\gamma')^*} \quad 2-1$$

Where a is the activity of solute in a solution, c is the drug concentration in the supersaturated solution, γ' is the activity coefficient, and the superscript “*” represents the properties of the system at saturation. When studies conducted in simple media, $\gamma' / (\gamma')^*$ is assumed to be 1, and supersaturation ratio can be determined by the ratio of solute concentration to equilibrium crystalline solubility in solutions.

Impact of Polymers on Crystal Growth. The adsorption layer theory is a well-recognized approach to describe crystal growth. Atoms/molecules continuously adsorb onto the crystal surface and then incorporate into kink sites along the growth steps, followed by the advancement of the growth steps across the entire crystal face. To initialize a new growth face, a two-dimensional nucleus needs to be created. The critical radius of a two dimensional nucleus ρ_c is given by³³,

$$\rho_c = \frac{\gamma a}{kT(\ln S)} \quad 2-2$$

Where γ is the edge free energy, a is the size of a growth unit, k is the Boltzmann constant, T is the solution temperature and S is the supersaturation ratio.

According to this theory, crystal growth is a step-wise build-up leading to a linear advancement of steps on the crystal face. The velocity of a linear step, v_0 , can be hindered if polymer molecules adsorb at kink sites along the step lines by a pinning mechanism.⁵⁸ According to this model, the linear step is forced to curve and the advancement velocity of a curved step is then related to the average distance between adjacent adsorbed polymer molecules, l . In this case, the time-average advancement velocity, v , of the step with adsorbed polymers can be given by equation 3^{57, 58, 84}

$$\frac{v}{v_0} = 1 - \rho_c/l \text{ (for } l > \rho_c \text{)} \quad 2-3$$

Where $v = 0$ for $l < \rho_c$.

2.4 Materials

Paclitaxel (Figure 2-1a) was purchased from Attix Pharmaceuticals (Toronto, ON, Canada), as the dihydrate form, as confirmed from the x-ray diffraction pattern (data not shown) and thermogravimetric analysis (data not shown). Hydroxypropyl methyl cellulose acetate succinate grade AS-MF (HPMCAS-MF) was from Shin Etsu Chemical Co., Ltd. (Tokyo, Japan). Methanol, and tetrahydrofuran (THF) were obtained from Macron Chemicals (Philipsburg, NJ, USA). 50 mM pH 6.8 phosphate buffer with ionic strength of 0.16 was prepared by dissolving sodium phosphate dibasic and sodium phosphate monobasic monohydrate in water. Both sodium

phosphate dibasic and sodium phosphate monobasic monohydrate were purchased from Macron Chemicals (Philipsburg, NJ, USA).

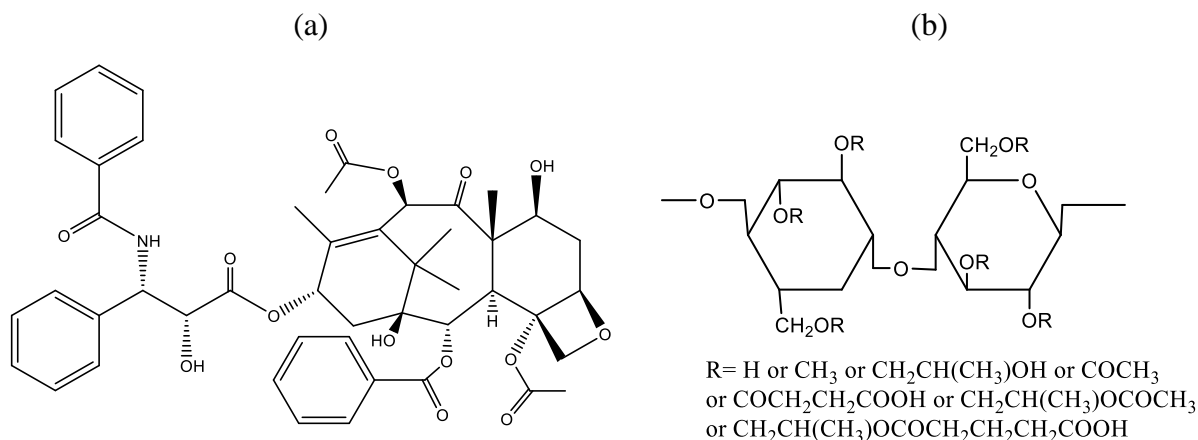


Figure 2-1 Chemical structures of (a) paclitaxel and (b) HPMCAS.

2.5 Methods

2.5.1 Determination of Crystalline Solubility and Amorphous Solubility.

The equilibrium crystalline solubility of paclitaxel dihydrate in 50 mM pH 6.8 phosphate buffer was determined by stirring an excess amount of paclitaxel in buffer at 37 °C at 300 rpm for 48 hrs. The undissolved solid was separated from the saturated solution by ultracentrifugation at 35000 rpm using an Optima L-100 XP ultracentrifuge (Beckman Coulter, Inc., Brea, CA) equipped with a swinging-bucket rotor SW 41Ti and the concentration in supernatant was analyzed by high performance liquid chromatography (HPLC) system (Agilent Technologies, Santa Clara, CA). For the HPLC method, a mobile phase of 55% acetonitrile and 45% water (v/v) at flow rate of 0.2 mL/min with injection volume of 60 µL and an ultraviolet (UV) detection wavelength of 205 nm was used. The separation column used was an Ascentis Express C18 column (10 cm x 3.0 mm, 2.7 µm particle size).

The amorphous solubility was determined in the presence of 20 µg/mL HPMCAS-MF using three independent methods. The first method was to measure the UV-visible extinction increase caused by the formation of a drug-rich phase in solution at a wavelength of 400 nm, which is a non-absorbing wavelength for paclitaxel. A stock solution of paclitaxel in methanol (10 mg/mL)

was added at a rate of 25 $\mu\text{L}/\text{min}$ using a syringe pump (Harvard Apparatus, Holliston, MA) to 15 mL buffer while stirring at 300 rpm, 37 $^{\circ}\text{C}$. The signal change at 400 nm was monitored using a UV/visible spectrophotometer (SI Photonics, Tuscon, AZ) with an *in situ* probe. The amorphous solubility was estimated from the paclitaxel concentration where the scattering started to increase beyond the baseline noise. The second method was to utilize pyrene as an environment sensitive fluorescence probe to determine when the paclitaxel drug-rich phase formed. The intensity ratios of the pyrene emission fluorescence peaks at 373 nm and 383 nm change with the polarity of local environment, indicating when a drug-rich phase is formed.⁸⁵ The experiments were carried out by gradually adding a stock solution of 10 mg/mL paclitaxel in methanol to 15 mL buffer with 1 μM pyrene to achieve paclitaxel concentrations between 3 $\mu\text{g}/\text{mL}$ and 70 $\mu\text{g}/\text{mL}$. The emission fluorescence spectra were obtained using a RF-5301 PC Spectrofluorophotometer (Shimadzu, Tokyo, Japan) with an excitation wavelength of 332 nm. The intensity ratios for pyrene were determined as a function of paclitaxel concentration and plotted. The amorphous solubility is indicated by the paclitaxel concentration where the ratio changes substantially. The third method to obtain amorphous solubility was to measure paclitaxel concentration in the aqueous phase following equilibration with the drug-rich phase. The drug-rich phase was created by adding 10 mg/mL stock solution of paclitaxel in methanol to 15 mL buffer, stirred at 300 rpm at 37 $^{\circ}\text{C}$, to yield a final added concentration of 40 $\mu\text{g}/\text{mL}$. The drug-rich phase was separated from the drug-lean aqueous solution by ultracentrifugation at 35000 rpm for 35 min. The supernatant was analyzed by HPLC (Agilent Technologies, Santa Clara, CA) with a mobile phase of 50% acetonitrile and 50% water (v/v) at a flow rate of 0.35 mL/min with injection volume of 2 μL . The UV detection wavelength was 205 nm. All the experiments were performed in triplicate.

2.5.2 Nucleation Induction Time Measurements.

The primary nucleation induction time in pH 6.8 buffer at 37 $^{\circ}\text{C}$ was determined in the absence and presence of 20 $\mu\text{g}/\text{mL}$ HPMCAS. The experimental induction time (t_{ind}) is the sum of the nucleation time for a critical nucleus to form (t_{n}) and time for nucleus to grow to a detectable size (t_{g}).²⁶ The induction time experiments were performed at an initial paclitaxel concentration of 30.7 $\mu\text{g}/\text{mL}$, achieved by adding stock solution of 10 mg/mL paclitaxel in methanol to 50 mL of medium, stirred at 300 rpm, 37 $^{\circ}\text{C}$. The induction time was determined by monitoring the light scattering (extinction) changes at a non-absorbing wavelength of 400 nm using a UV/visible

spectrophotometer (SI Photonics, Tuscon, AZ) with an *in situ* probe. The extinction increased upon the formation of crystals.

2.5.3 Seed Crystal Preparation.

Crystal seeds were created by crystallization from supersaturated solutions produced by anti-solvent addition. A methanolic stock solution of paclitaxel (10 mg/mL) was used to create solutions of concentration 5.8 $\mu\text{g/mL}$ ($S = 16$) or 28.8 $\mu\text{g/mL}$ ($S = 80$) in 15 mL buffer stirred at 300 rpm. The crystal seeds were grown for 5.5 h, to produce crystal seeds with a common history.⁸⁶ The resultant crystals were needles with a high aspect ratio. To obtain shorter crystals seeds, a sonication probe (Sonics, Newtown, CT, USA) at 40% amplitude with a 4s on and 2s-off duty cycle was introduced to the seeding solution for 10 min post crystallization. An ice bath was used during sonication to prevent the solution from overheating. Paclitaxel crystals, as received from the supplier, were also used for seeding. To ensure wetting, this material was slurried with buffer for 5.5 h before use.

2.5.4 Crystal Seeds Growth in the Presence and absence of HPMCAS.

The suspension containing the crystal seeds was diluted to yield the desired mass-based concentration of crystal seeds, 18 wt. % relative to initial paclitaxel concentration used to induce growth, with 15 mL as the final volume. HPMCAS was added to the seed solution prior to generation of supersaturation to achieve a final polymer concentration of 33 $\mu\text{g/mL}$. After 2 min stirring at 300 rpm, 37 °C, a small aliquot of paclitaxel methanolic stock solution (10 mg/mL) was added to produce an initial concentration at 31.6 $\mu\text{g/mL}$ ($S = 88$). For crystal seeds growth without polymers the procedure was the same, but no polymer was present in the buffer. The apparent concentration of paclitaxel as a function of time was monitored using a UV/visible spectrophotometer (SI Photonics, Tuscon, AZ) with an *in situ* probe at 230 nm. Extinction at 400 nm was subtracted from absorption at 230 nm to reduce the impact of any scattering caused by crystal seeds.

2.5.5 Preparation of Amorphous Solid Dispersions (ASDs) of Paclitaxel.

Amorphous solid dispersions of paclitaxel and HPMCAS-MF at a ratio of 49:51 (wt. %) were prepared by solvent evaporation from THF using a rotary evaporator. The ASD was produced in a 20 mL glass scintillation vial. The mass of ASD formed was sufficient to create a solution saturated at the amorphous solubility upon addition of 15mL of buffer if complete dissolution was achieved. THF was removed by a rotary evaporator (Brinkman Instruments, Westbury, NY) using a water bath temperature of 45 °C. A thin, clear paclitaxel ASD film was formed on the vial wall.

2.5.6 Dissolution of Paclitaxel-HPMCAS 49/51 (wt. %) Amorphous Solid Dispersions in the Absence and Presence of Crystal Seeds.

Dissolution of ASDs in the absence of crystal seeds was conducted by adding 15 mL of buffer saturated with respect to crystalline paclitaxel to the vial containing the ASD. Dissolution experiments in the presence of crystals seeds were carried out by adding 15mL of the seed suspension to the vial containing the ASD. To maintain the same mass of seeds added, seed suspensions generated at different supersaturations were diluted with buffer saturated with paclitaxel (Figure 2-2). The final volume of added dissolution media (either saturated solution or seed suspension) was 15 mL and the UV spectra were monitored by a UV/visible spectrophotometer (SI Photonics, Tuscon, AZ) with an *in situ* probe. The apparent concentrations were attained by subtracting the baseline at 400 nm from the absorption peak at 230 nm. The residual paclitaxel concentrations at the end of the dissolution experiments were measured by HPLC after filtration using glass fiber syringe filters with a pore diameter of 0.45 µm to separate solution from solid material.

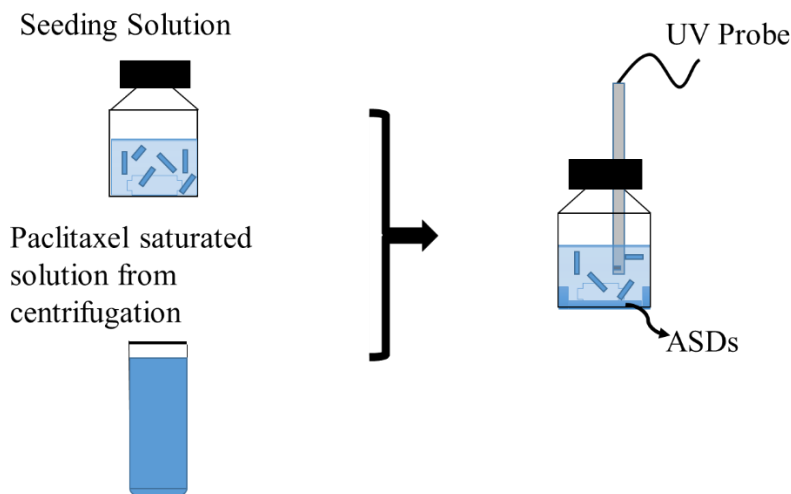


Figure 2-2. Scheme of dissolution of ASDs in the presence of crystal seeds.

2.5.7 Scanning Electron Microscopy.

Scanning electron microscopy (SEM) was used to characterize the morphology of crystal seeds. Approximately 4 μL of the suspension containing crystal seeds was deposited on a glass slide. The sample was dried for one week under vacuum at room temperature. The sample was then mounted on a pin stub using copper tape and sputter-coated with platinum for 120 s and conductive liquid silver paint was applied to the corners of the slide. An FEI NOVA nanoSEM Field Emission SEM (Fei, Hillsboro, OR), equipped with Everhart-Thornley (ET) detector and through-the-lens detector (TLD) was used to take images. The SEM was operated with 5kV accelerating voltage, 4-5 mm working distance and a beam spot size of 3. The image processing and analysis software Image J (National Institute of Health, Bethesda, MD) was used to analyze the SEM images. For each sample, 100 crystals were measured and the size distributions were generated by the statistics software, Minitab (State College, PA).

2.5.8 Transmission Electron Microscopy.

Transmission electron microscopy (TEM) was utilized to study the morphology of the crystal seeds before and after growth in the presence and absence of polymers. Approximately 1 μL solution containing the crystal seeds was added to a carbon film with a 300 mesh copper grid (Electron Microscopy Science, Hatfield, PA). The film was dried for one week at room temperature under vacuum. Before taking images, 1% phosphotungstic acid (PTA) was applied to

the grid for 30 s. The images were acquired using a FEI Tecnai G2 20 Transmission Electron Microscope (Fei, Hillsboro, OR), with a 200 KV LaB6 filament. The detector was a Fischione high angle annular dark field (HAADF).

2.5.9 Determination of Paclitaxel Growth Unit Size.

The paclitaxel crystal structure used to measure the molecular length and width was the crystal form with the ref code RIGKUP in the Cambridge Structural Database. The distances between atoms were determined using the crystal structure visualization software, Mercury (Cambridge Crystallographic Data Centre, Cambridge, UK).⁸⁷ The molecular length was taken as the distance between the H atom on the benzene ring of benzoyl amide and the H atom on the methyl group on cyclohexane. The width was taken as the distance between the H atom on the benzene ring of benzoate and H atom on the other acetate. By measuring the width and length, the area of a growth unit was calculated.

2.6 Results

2.6.1 Crystalline and amorphous solubility.

The crystalline solubility of paclitaxel dihydrate in pH 6.8 buffer was found to be 0.36 $\mu\text{g/mL}$. The amorphous solubility was determined by three methods. For UV extinction measurements, scattering at 400 nm increased when drug concentration reached 31.5 $\mu\text{g/mL}$, indicating the formation of a new phase. In fluorescence experiments, the ratio of pyrene emission peaks at 383 nm and 373 nm increased upon the formation of drug-rich phase, observed at a paclitaxel concentration of 30.9 $\mu\text{g/mL}$. The concentration of the aqueous phase after pelleting the drug-rich phase was determined as 32.3 $\mu\text{g/mL}$. Thus good agreement was observed between the three methods used to determine the amorphous solubility and results are summarized in Table 2-1. The average amorphous solubility from three methods is about 31.6 $\mu\text{g/mL}$. The amorphous form is thus around 88 times more soluble than the dihydrate crystalline form.

Table 2-1. Crystalline (dihydrate) and amorphous solubility of paclitaxel.

| | Solubility ($\mu\text{g/mL}$) |
|---------------------|---------------------------------|
| Crystalline | 0.36 ± 0.01 |
| Amorphous | |
| UV extinction | 31.5 ± 0.8 |
| Fluorescence | 30.9 ± 1.8 |
| Ultracentrifugation | 32.3 ± 0.4 |

2.6.2 Nucleation Induction Time.

The primary nucleation induction time was conducted at the amorphous solubility, i.e. the supersaturation ratio was 88, in the absence and presence of HPMCAS. Without polymers, paclitaxel crystallized within 6 min. HPMCAS was a highly effective nucleation inhibitor and in the presence of this polymer the supersaturation was maintained for more than 16 h.

2.6.3 Characterization of Crystal Seed Morphology.

Crystal seeds were generated at paclitaxel concentrations of $5.8 \mu\text{g/mL}$ and $28.8 \mu\text{g/mL}$, corresponding to supersaturation ratios of 16 and 80, respectively, with and without sonication. The seeds generation conditions and the abbreviations used to identify seeds produced at each condition are summarized in Table 2-2.

Table 2-2. Conditions used for crystal seeds generation and corresponding abbreviation.

| Generation Conditions | Abbreviations |
|---|---------------|
| at low supersaturation of 16 | S16 |
| at high supersaturation of 80 | S80 |
| at low supersaturation of 16 with ultra-sonication | S16 w/ s |
| at high supersaturation of 80 with ultra-sonication | S80 w/ s |

SEM images of the seeds are shown in Figure 2-3. Paclitaxel crystallizes as needles with high aspect ratio, indicating fast growth at the ends of the crystals. Ultra-sonication is able to break the crystals yielding shorter crystals that presumably have a higher surface area for growth (i.e. more “ends”). Crystal morphology was analyzed further by measuring the length, c , and width, b , of 100 crystals for each crystallization condition, and the size frequency distributions in terms of length and width are shown in Figure 2-4. From the size frequency distribution based on crystal length, c , S80 crystals have relatively more fine crystals compared to S16 crystals, an observation which can be readily explained by classical nucleation theory.²² The critical free energy of nucleus formation is much lower at a higher supersaturation ratio, hence an increased nucleation rate is anticipated at the higher supersaturation, resulting in relatively smaller crystals. After sonication, the crystals seeds were broken into much shorter crystals. According to the distribution of the widths, b , there is no significant difference among S80, S16 and S80 w/ s crystal seeds, but the width of S16 w/ s crystals shifted to lower values.

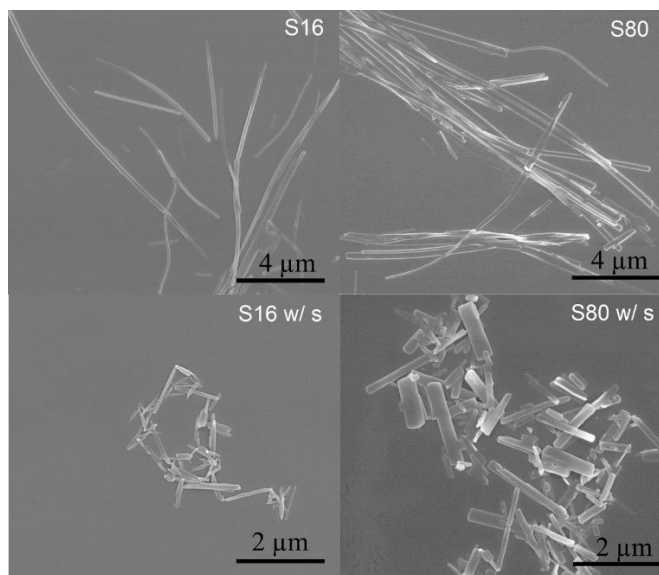


Figure 2-3. SEM images for crystal seeds of S16, S80, S16 w/ s and S80 w/ s.

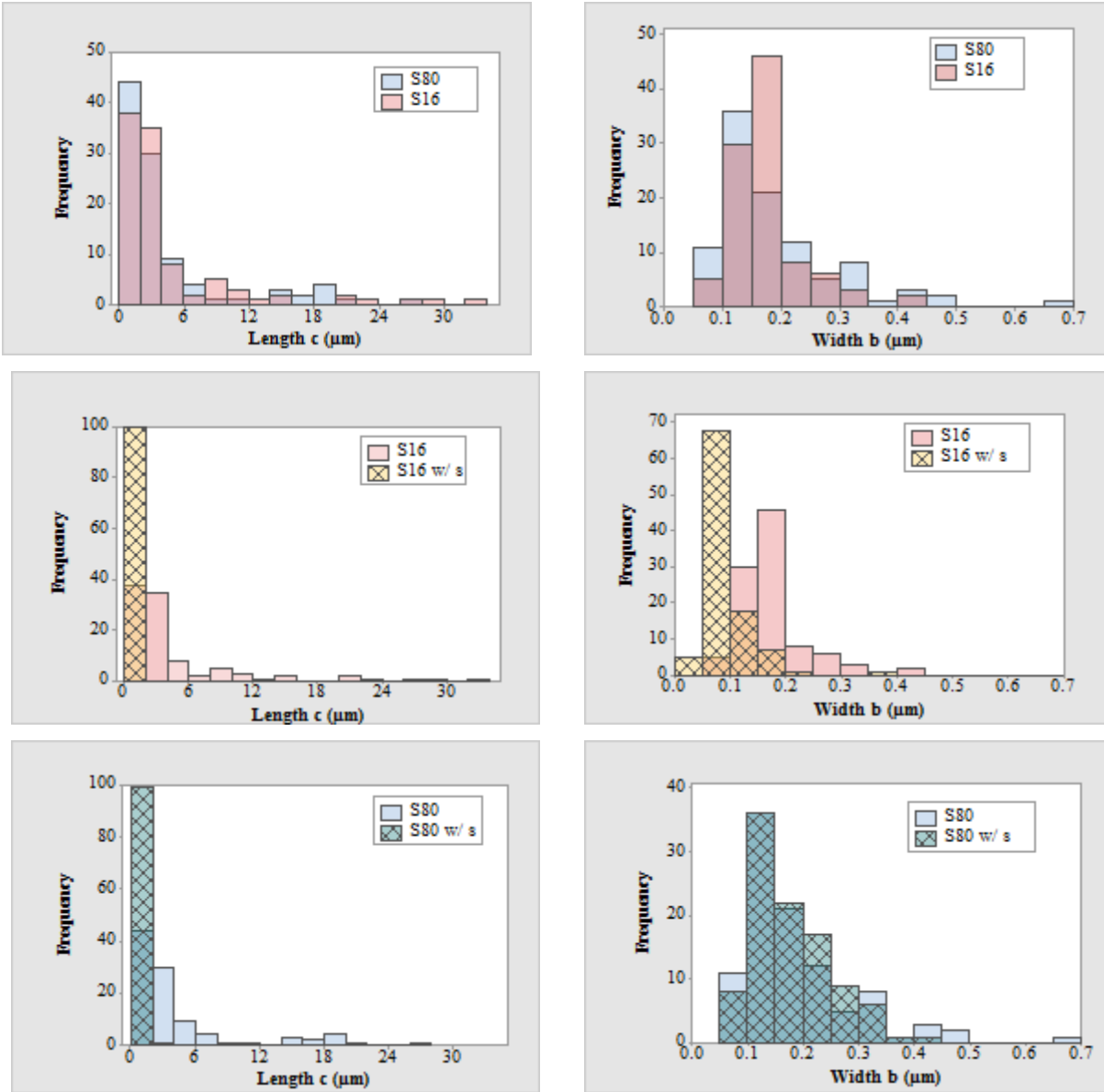


Figure 2-4. Size distribution in terms of length (c) and width (b) for crystal seeds.

Assuming each crystal is cuboidal (i.e. each of the faces is a rectangle), the crystal end areas normalized by mass can be estimated based on measurements of 100 crystals for each condition. The results are shown in Figure 2-5. For an equal mass, crystal seeds of S16 and S80 have similar end areas, which are correspondingly about 7-8 fold smaller than for S16 w/ s and S80 w/ s crystals.

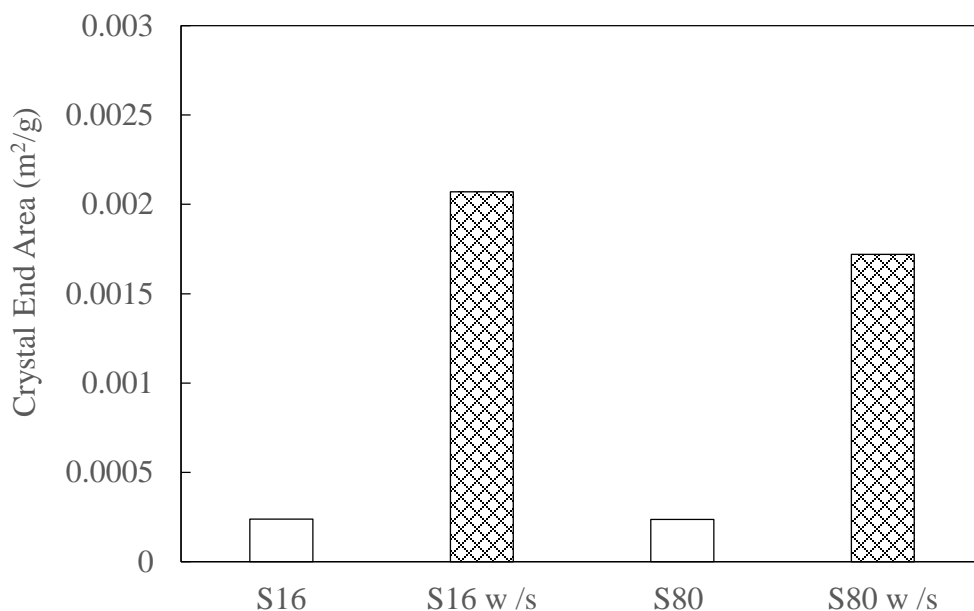


Figure 2-5. Crystal end areas normalized by mass for crystal seeds.

2.6.4 Crystal Growth in the Absence of Polymers

Crystal growth was evaluated at a supersaturation corresponding to the amorphous solubility (31.6 $\mu\text{g/mL}$, $S = 88$). This is the maximum supersaturation that can be achieved by dissolution of a solubility enhancing formulation.⁸⁸ In the presence of 18 wt.% crystal seeds, desupersaturation happened immediately, as shown in Figure 2-6. S16 w/s and S80 w/s seeds lead to similar slopes indicating a similar rate of desupersaturation. The rate of desupersaturation is faster for these seeds compared to an equivalent mass of the S16 and S80 seeds, presumably because of the greater area of growth sites available due to a larger end area. S80 showed different growth kinetics from S16 seeds, despite a similar estimated area of crystal ends, perhaps suggesting that additional events are occurring in addition to only crystal growth at the needle ends. SEM was used to analyze the crystal morphology after growth, again measuring the characteristic lengths (c) and widths (b) for 100 crystals. The resultant size distributions with a comparison to the crystals prior to growth are shown in Figure 2-7.

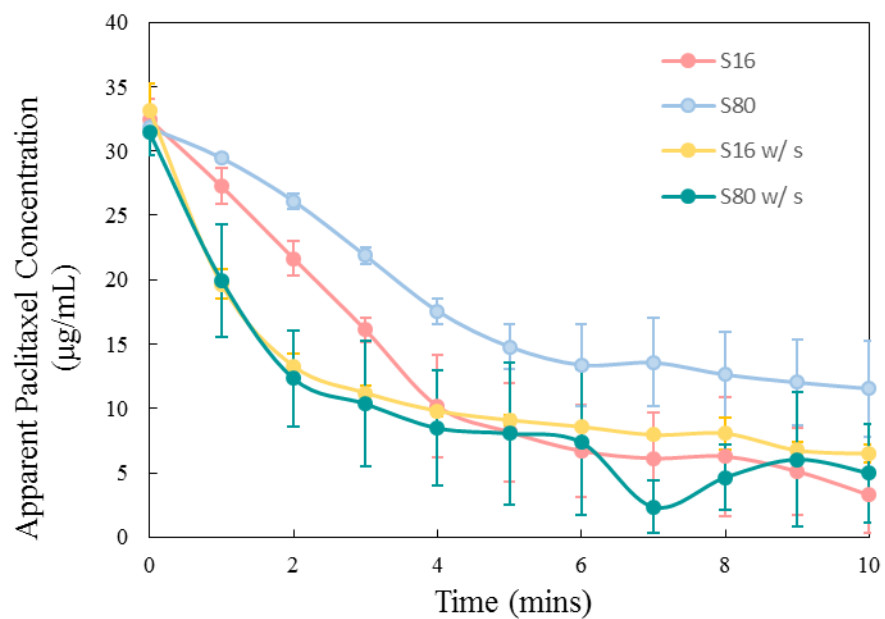


Figure 2-6. Desupersaturation profiles of paclitaxel solutions at an initial concentration of 31.6 µg/mL ($S = 88$) in 18 wt. % seed crystals produced under different crystallization conditions.

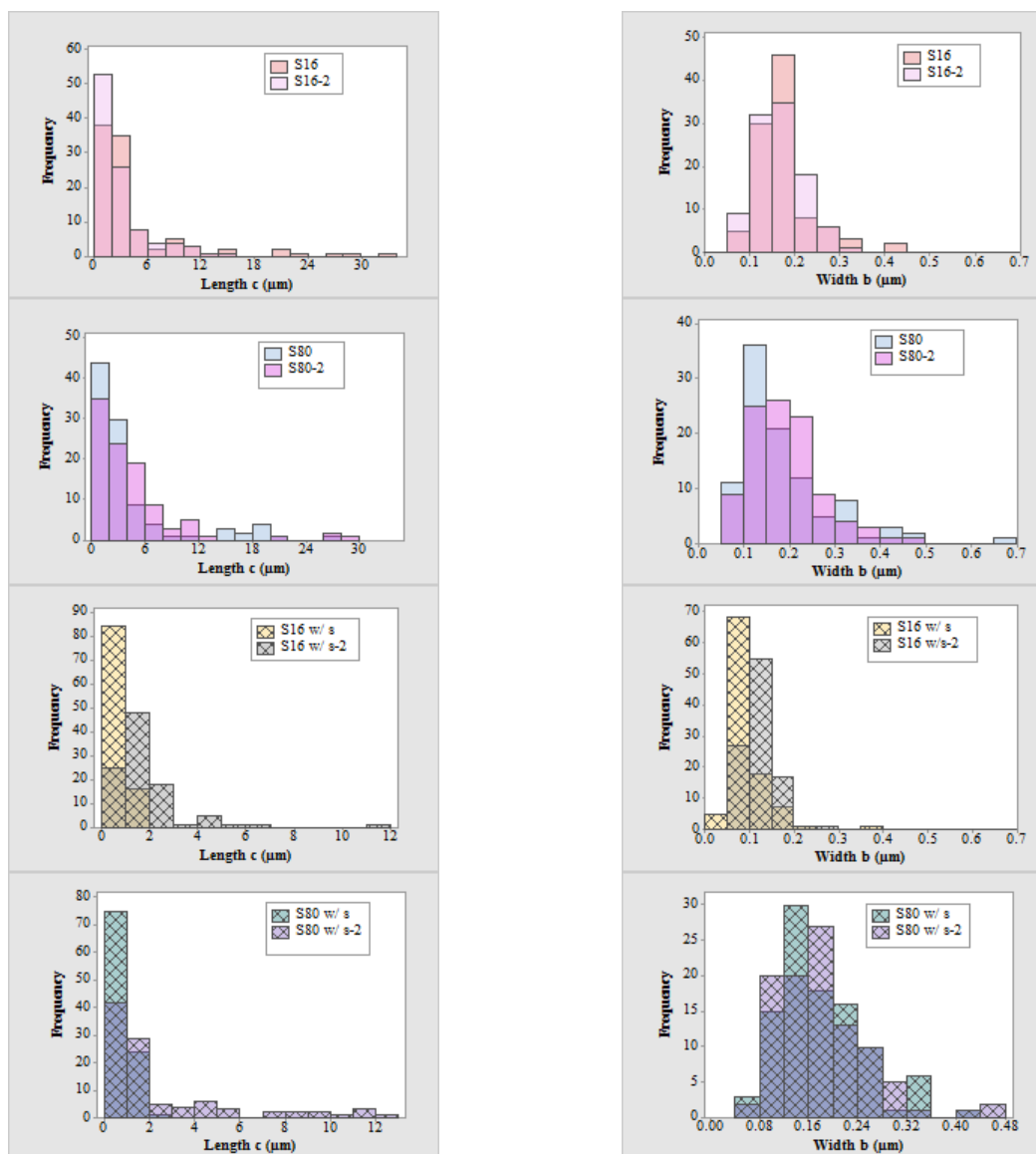


Figure 2-7. Size distributions before and after crystal growth of seeds in terms of length and width for crystal seeds. S16-2, S80-2, S16 w/ s-2 and S80 w/ s-2 represent crystals after growth from the original crystals, S16, S80, S16 w/ s and S80 w/ s, respectively.

For S80 crystal seeds, the distribution of the shorter crystal lengths decreased somewhat and the number of slightly longer crystals increased after growth. For S16 crystal seeds, the length distribution did not move towards longer crystals; instead and somewhat unexpectedly, more fine crystals were observed. S16 w/ s and S80 w/ s crystal seeds demonstrated obvious growth in terms of length. S16, S80 and S80 w/ s were found to have comparable width distributions before and after the growth, while a clear width increase was seen for S16 w/ s.

One of the terms to describe an acicular crystal is the aspect ratio, which is defined as the quotient of the length to width of a crystal. The average aspect ratio of 100 crystals for each condition was calculated for each sample before and after growth, and the results are summarized in Figure 2-8. The aspect ratio increased for S80, S16 w/ s and S80 w/ s seeds, but to different extents. The opposite phenomenon was unexpectedly observed for S16.

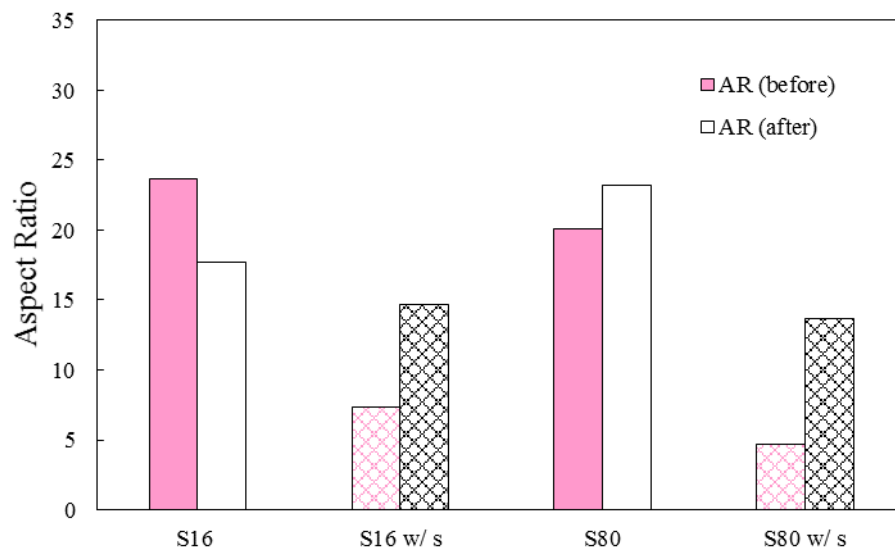


Figure 2-8. Aspect ratios before and after growth of crystal seeds in absence of polymers. The meshed columns represent crystal seeds processed by ultra-sonication before growth.

2.6.5 Crystal Growth in the Presence of HPMCAS

The morphology of the seed crystals following growth at a supersaturation of 80 in the presence of 31.6 $\mu\text{g/mL}$ HPMCAS was studied by TEM to enable higher space resolution than achievable with SEM. The seed loading was again 18 wt. %. The TEM images for the various types of seeds after growth are presented in Figure 2-9.

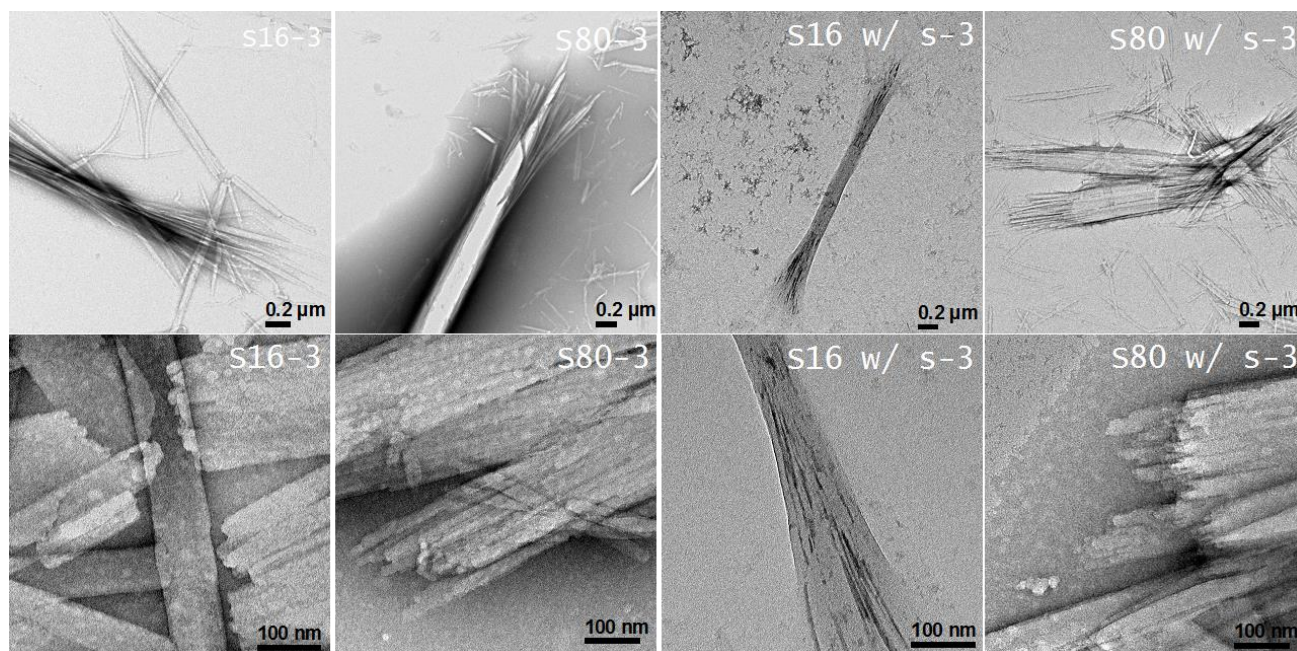


Figure 2-9. TEM images for crystal seeds after growth in the presence of HPMCAS. S16-3, S80-3, S16 w/ s-3 and S80 w/ s-3 represent crystals after growth from S16, S80, S16 w/ s and S80 w/ s crystal seeds in the presence of 31.6 $\mu\text{g/mL}$ HPMCAS, $S = 88$ respectively.

The morphology of the seed crystals is altered by growth in the presence of the polymer. The ends of the needles show dendritic growth. It was not possible to calculate crystal size distributions since many fine crystals were produced due to breakage of the dendritic crystals formed from growth of the polymer-poisoned seed crystals. The origin of the dendritic crystals can be explained by adsorption of HPMCAS onto the seed crystals, with subsequent step pinning whereby crystals are forced to grow in between the HPMCAS adsorption sites, as described in the model proposed by Kubota and Mullin⁵⁷. Thus the width of each crystal “finger” can be taken as an indication of the distance between two adjacent HPMCAS adsorption sites on the crystal surface. For each sample, 20 measurements of dendrite crystal width were taken to evaluate the distance between two adsorption sites where mean values are presented in Figure 2-10. The mean distances vary somewhat among the crystals grown from different seeds, but fall within values of 10 to 16 nm.

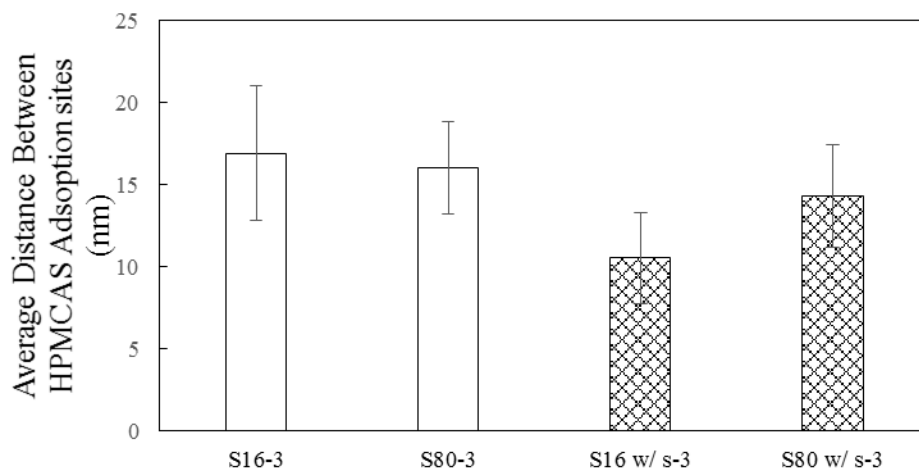


Figure 2-10. Average distance between adjacent HPMCAS adsorption sites. S16-3, S80-3, S16 w/ s-3 and S80 w/ s-3 represent crystals after growth from S16, S80, S16 w/ s and S80 w/ s seeds respectively in the presence of 31.6 $\mu\text{g/mL}$ HPMCAS.

2.6.6 Dissolution Profiles of Paclitaxel/HPMCAS (49/51) Amorphous Solid Dispersions

The dissolution profiles of paclitaxel/HPMCAS ASDs in the presence and absence of seed crystals are summarized in Figure 2-11. In the absence of seeds, the ASD dissolves to achieve the amorphous solubility of paclitaxel. Even though this concentration represents a very high supersaturation ($S = 88$), no desupersaturation is observed over 16 hours, in agreement with our earlier observation that HPMCAS is a very effective nucleation inhibitor for this compound. When the dissolution media contained 18 wt.% crystal seeds, desupersaturation was observed, due to crystal growth. Thus, HPMCAS is unable to completely block crystal growth, although the rate of desupersaturation is considerably lower than that observed in the absence of polymer (Figure 2-6). However, the kinetics of desupersaturation varied depending on the types of seeds added. For all cases, and within experimental error, the amorphous solubility was reached. The addition of S16 w/ s and S80 w/ s crystal seeds resulted in similar desupersaturation profiles that were initially fast and became progressively slower as the supersaturation decreased. In contrast, for S16, S80 and bulk API crystal seeds, the slope of the desupersaturation profile was more constant over the time frame of experiments whereby the S80 seeds resulted in a faster rate of desupersaturation than the S16 and bulk API seeds.

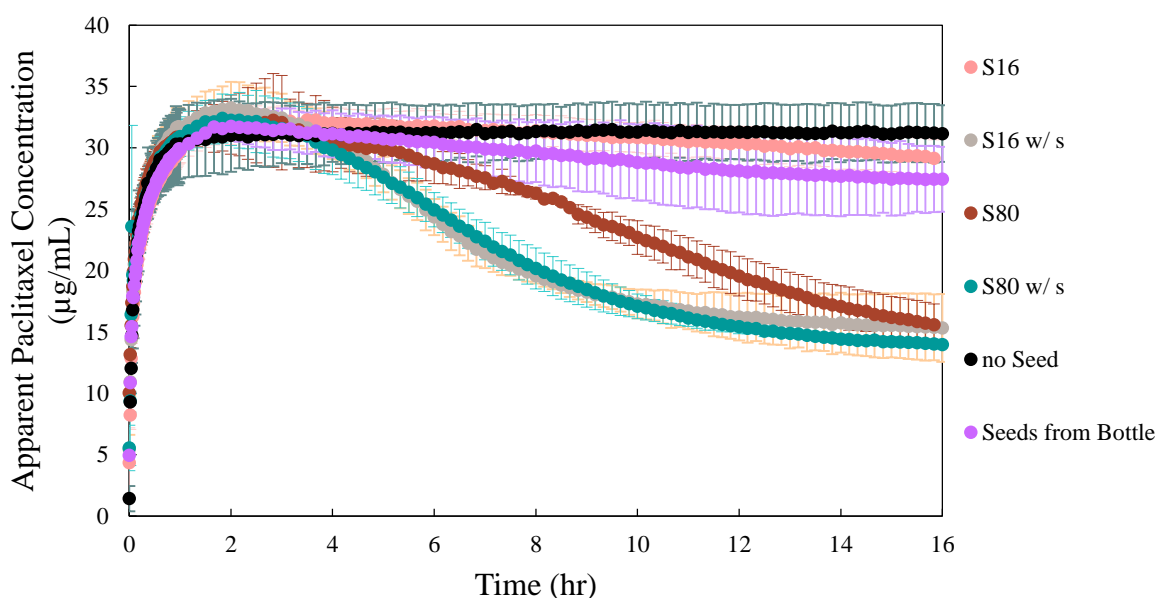


Figure 2-11. Dissolution profiles for paclitaxel/HPMCAS 49/51 amorphous solid dispersions in the absence and presence of 18 wt. % crystal seeds generated under different conditions.

Final concentrations at the end of the experiment were confirmed using HPLC analysis with results summarized in Figure 2-12. Bulk API and S16 seeds led to moderate decreases in solution concentrations over the 16 h experiment where the final solution concentrations were ~25 and 19 $\mu\text{g/mL}$ respectively. Thus considerable residual supersaturation remains even when 18 wt. % seeds have been added. In contrast, the residual concentrations for dissolution experiments performed with S80, S16 w/ s and S80 w/ s were much lower, ~ 10, 8 and 9 $\mu\text{g/mL}$ respectively. These values are still considerably above the crystalline solubility of paclitaxel dihydrate (~0.4 $\mu\text{g/mL}$), indicating that HPMCAS is a very effective crystal growth inhibitor at somewhat lower supersaturations.

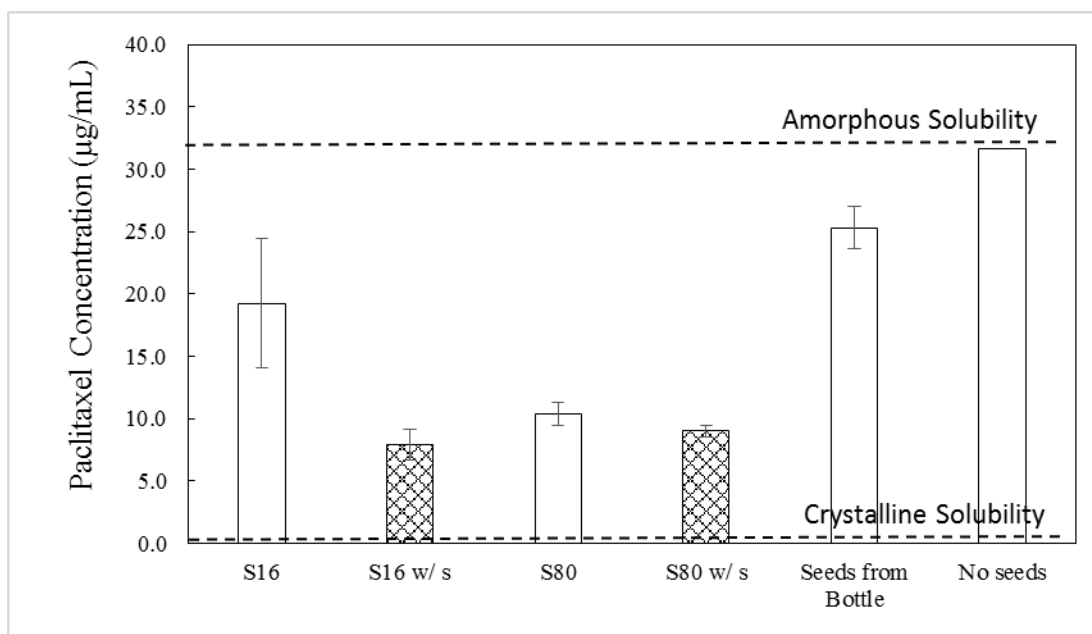


Figure 2-12. Residual paclitaxel concentrations determined by HPLC after filtration to remove crystalline material, 16 h after ASD dissolution in the presence and absence of crystal seeds (18 wt. %) of differing properties.

2.7 Discussion

Interestingly Dissolution of amorphous drug formulations can generate a supersaturated solution, which in turn is thought to improve the bioavailability of compounds where the intestinal absorption is solubility limited.⁸⁹ However, it is important to consider the stability of the supersaturated solution in the context of various crystallization events that can occur, depending on the degree of supersaturation generated and the presence or absence of crystal seeds. The phase behavior of supersaturated solutions is usefully depicted by a concentration-temperature phase diagram²³, as shown in Figure 2-13. When the drug concentration reaches and exceeds the amorphous solubility, phase separation to an amorphous form of the drug will occur if nucleation and subsequent crystal growth can be avoided.^{7, 24} For paclitaxel, the amorphous solubility is about 88 times higher than crystalline solubility. Hence, dissolution of amorphous formulations in non-sink conditions can lead to a very highly supersaturated solution. Consequently, crystallization, initiated via primary nucleation can occur. If residual crystalline material is present, crystallinity can evolve via crystal growth and secondary nucleation may also occur. These crystallization

events will lead to a depletion of supersaturation. Therefore, the overall dissolution profile of an ASD depends on the interplay of the dissolution rate and the crystallization kinetics.

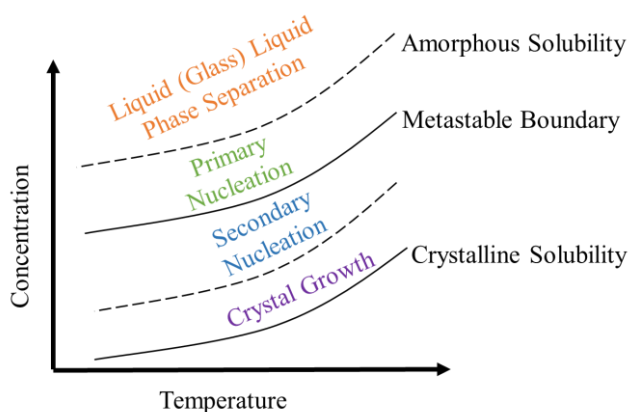


Figure 2-13. Concentration-temperature phase diagram for a supersaturated solution. Adapted from ref. 32.

We note that the nucleation induction time for paclitaxel at a supersaturation equivalent to the amorphous solubility is very short in the absence of a polymer, and that HPMCAS is a very effective inhibitor of primary nucleation. Therefore, an ASD of HPMCAS and paclitaxel is able to dissolve to create a supersaturation equivalent to the amorphous solubility and maintain this very high degree of supersaturation for several hours. However, the presence of crystal seeds results in desupersaturation. Thus, although HPMCAS is a good primary nucleation inhibitor, crystal growth cannot be completely blocked by this polymer. The inability of HPMCAS to completely inhibit crystal growth can be explained by considering the size of the critical nucleus for 2D growth, described in Section 2.2, and the average distance between adsorbed polymer molecules. To estimate the critical nucleus, a value for the interfacial tension between the crystal and water is needed. Due to problems with experimental determination of this parameter, different values of this quantity was used based on literature values for representative compounds. The compounds chosen have a range of hydrophobicities based on consideration of log P. The critical nucleus radius was estimated using eq. 2, and the quantities used for calculations as well as results are listed in Table 2-3. From these estimations, ρ_c is 5~7 nm at a supersaturation ratio of 88. This value is smaller than the measured average distance between HPMCAS adsorption sites, assessed from the width of the crystals grown on the seed ends in the presence of the polymer which are ~10-20 nm (Figure 2-10). Thus, HPMCAS cannot prevent paclitaxel crystal seeds from growing,

based on a consideration of eq. 3, due to the very small size of the critical nucleus, which in turn presumably results from the very high supersaturation achieved at the amorphous solubility. However, the polymer does poison the growth interface, leading to much slower growth rates and the formation of very thin crystals that evolve from the poisoned growth surface.

Table 2-3. Values used to calculate ρ_c (eq 2).

| Value used to calculate ρ_c | Methylene Iodide (log P =1.6) | Octane (log P =5.15) | Felodipine (log P =3.4) |
|---|----------------------------------|-------------------------|----------------------------|
| γ (J/nm ²) $\times 10^{-20}$ | 4.16 ⁹⁰ | 5.08 ⁹¹ | 3.90 ⁸² |
| a (nm ²) | | 2.64 | |
| k (J/K) | | 1.38 $\times 10^{-23}$ | |
| T (K) | | 310 | |
| lnS | | 4.47 | |
| ρ_c (nm) | 5.7 | 7.0 | 5.4 |

It is also of interest to consider how the critical nucleus size varies as a function of supersaturation, given the observation that considerable supersaturation persists after 16 h of seed growth (Figure 2-11). In Figure 2-14, the relationship between critical nucleus size and supersaturation is plotted, using the values from Table 2-3; also included in the plot are the residual supersaturation levels measured for the different seeds after 16 h, as well as the mean distances between HPMCAS adsorption sites for the different seeds. According to eq. 3, the closer the distance between adsorbed polymer molecules, relative to the critical nucleus size, the slower the crystal growth rate will be. Further, we can predict that when the supersaturation decreases to such an extent that the critical nucleus size is equal to the average distance between polymer adsorption sites, crystal growth will stop, and the residual supersaturation will persist. Figure 2-14 illustrates that the distance between polymer adsorption sites for S16 w/ s and S80 w/ s seeds are similar to the estimated critical nucleus size for the supersaturation level observed after 16 h, explaining the almost zero growth rate observed at this time point for these samples (Figure 2-11). Figure 2-14 provides the theoretical underpinning for previous observations of residual supersaturation in the presence of crystal seeds.⁹² This is clearly important when considering supersaturation-time profiles *in vivo* as a function of time in the presence of growth inhibitors; current physiologically based pharmacokinetic absorption models assume that the concentration returns to the equilibrium crystalline solubility following crystallization. This is clearly not supported either by experimental observations or theoretical considerations, and improved models clearly need to be developed.

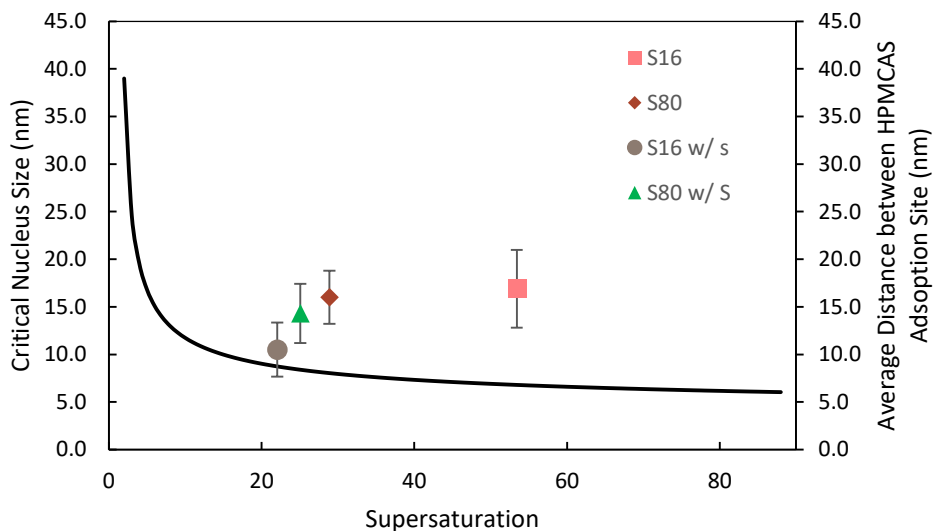


Figure 2-14. Plot of critical nucleus size as a function of supersaturation ratio, according to eq. 2, by using the values from Table 2-3. The discrete data points represent the measured average distance between HPMCAS adsorption sites at residual supersaturation ratio at the end of 16 hr dissolution experiments in the presence of different crystal seeds.

An additional crystallization event, namely secondary nucleation, was observed during seed growth in the absence of polymers for some seed types. Comparison of the aspect ratios before and after growth (Figure 2-7) shows that aspect ratio reduced after growth for S16 crystal seeds, and the extent of aspect ratio enhancement for S80 crystal seeds after growth was smaller as compared to S16 w/ s and S80 w/ s. These observations can be explained by the evolution of fine crystals with low aspect ratios due to secondary nucleation. SEM images in Figure 2-15 lend support to this explanation. From the images, many small needle-like crystals were found adhered to the surface of a larger crystal following growth. Via secondary nucleation, more growth sites are created which can further accelerate desupersaturation, as observed for these seeds. For S16 w/ s and S80 w/ s crystals seeds, secondary nucleation also occurred to some extent during growth, but because a sufficient amount of crystal ends were available, crystal growth was more dominant, and an obvious increase in aspect ratios was observed. The impact of HPMCAS on secondary nucleation is difficult to evaluate, because breakage of the dendritic crystals formed during growth also generates fine needle-like crystals, which are difficult to distinguish from crystals produced by secondary nucleation. However, although not widely studied, it has been suggested that the presence of a polymer can suppress this process.⁹³ Assuming that secondary nucleation is

suppressed by the polymer, the concentration-time profile observed during ASD dissolution when seeds are present is then dictated by the ASD dissolution rate and the growth rate of the crystal seeds. From the dissolution curves (Figure 2-11), it is apparent that the amorphous solubility can be achieved, indicating that the dissolution rate is much faster than the crystal growth rate. This seems to be quite a remarkable observation given the high mass fraction (18 wt. %) of seeds that has been added and needs to be further considered.

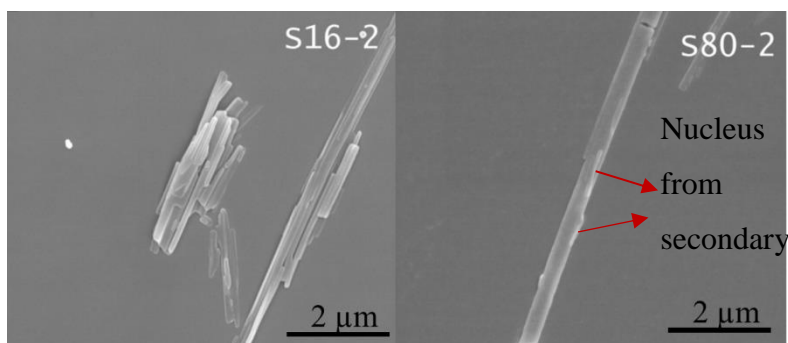


Figure 2-15. SEM images for S16, S80 crystal seeds after growth in the absence of polymers.

The most likely explanation for the quite modest effect of the seeds on the desupersaturation profile is the crystal morphology. For needle-like crystals to evolve, crystal growth of the faces forming the ends of the needles is much faster than the crystal faces forming the sides of the needle. Consequently, per unit mass, needle-shaped seeds with higher aspect ratios have a smaller area for growth relative to needles with a lower aspect ratio, or crystals with more equant shape. This is clearly demonstrated in the current study. The ultra-sonicated seeds (S80 w/ s) are estimated to have a needle end area approximately 7 times larger relative to the equivalent unsonicated seeds (Figure 2-5). This significant increase in the available growth area leads to a faster bulk growth rate both in the absence of polymers (Figure 2-6) and a steeper desupersaturation slope during ASD dissolution where polymer is present (Figure 2-11). Similarly, S16 w/ s seeds have a greater end area per unit mass compared to the unsonicated seeds (S16) and also became narrower. From the size distribution analysis after growth (no polymer), crystals grew wider as well as longer. This growth behavior difference most likely explains why these seeds lead to more rapid and extensive desupersaturation following ASD dissolution (Figure 2-11). Our results clearly demonstrate that for ASD performance, the mass of crystal seeds added is not the relevant parameter to be considered; rather it is the available growth areas and their growth rates.

Thus in considering the likely impact of residual crystals on ASD performance, crystal morphology as well as the effectiveness of the additives in poisoning growth needs to be considered.

We also found that the conditions of seed formation, notably the supersaturation used to generate the seeds, also influences seed properties. Comparing S16 and S80 crystal seeds, both had similar areas for crystal ends per unit mass, as well as crystal size distributions. However, different growth kinetics were observed both in the presence and absence of polymers. Careful examination of SEM and TEM images (Figure 2-16) reveals differences in the interface structure of needle tips. For S16 seeds, the shape of the ends was more pointed and the interface was relatively smooth. In contrast, S80 seeds showed flatter ends which were rougher. The varied morphology of growth surface most likely indicates different growth mechanisms in play for the crystals formed at the different supersaturation levels,⁹⁴ which in turn leads to a different number of active sites available for both polymer adsorption and crystal growth. Schram *et. al.* has reported that crystal seeds prepared in different environments show differences in interface structure as evaluated using atomic force microscopy, which then influenced the subsequent rate of crystal growth.⁸²

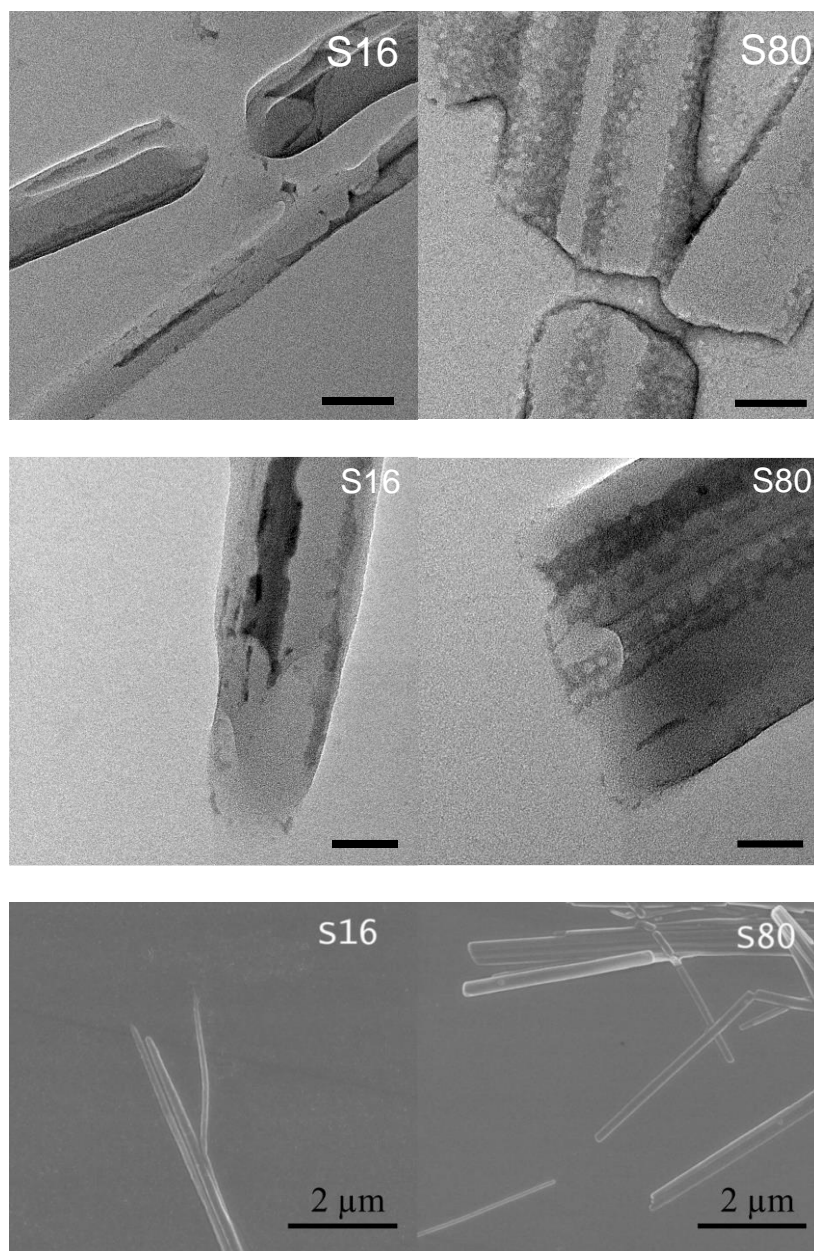


Figure 2-16. SEM images and TEM images of crystal ends for S16 and S80 crystal seeds. The first four pictures are TEM images, while the last two are SEM images.

Generally, in the manufacturing and storage of ASDs, ensuring a completely amorphous drug is considered to be a key element,⁹⁵ although this is not always attainable and hence limits are typically set for the allowable crystallinity. These limits are usually given on a wt. % crystallinity basis and are frequently dictated by the limit of detection of the analytical method used to evaluate residual crystallinity. Clearly this is an arbitrary approach and the percent

crystallinity *per se* is not a predictive indicator of the impact of crystallinity, rather the number of sites available for crystal growth is a more important, albeit difficult, parameter to assess. During the dissolution of paclitaxel/HPMCAS ASDs we can add a high weight fraction of seeds (18 wt. %), and depending on the seed properties, either have virtually no effect, or cause significant desupersaturation. Based on the observations herein, it is likely that high aspect ratio crystals present in an ASD will have a smaller impact per unit weight than more equant residual crystals, all other factors being equal. Clearly this is an area that deserves more investigation in order to ensure appropriate limits on crystal content in amorphous formulations of poorly water soluble drugs.

2.8 Conclusions

The presence of crystal seeds can impair the extent and duration of supersaturation achieved by dissolving amorphous solid dispersions under non-sink conditions. However, the seed impact is highly dependent on seed properties. For paclitaxel amorphous solid dispersions, a high extent and duration of supersaturation was achievable even in the presence of a relatively large weight fraction of crystal seeds for some seed types. In particular, it was noted that high aspect ratio paclitaxel seeds had less impact on desupersaturation rate relative to lower aspect ratio seeds, when an equivalent weight fraction was used. HPMCAS was found to slow crystal growth, where the extent of inhibition was dependent on the critical nucleus size as a function of supersaturation relative to the average distance between HPMCAS adsorption sites. These observations point to the importance of considering seed origin, morphology and interface properties as well as the extent of supersaturation generated during dissolution when evaluating the likely impact of residual crystallinity on the performance of amorphous formulations.

CHAPTER 3. INSIGHTS INTO THE DISSOLUTION BEHAVIOR OF LEDIPASVIR-COPOVIDONE AMORPHOUS SOLID DISPERSIONS: ROLE OF DRUG LOADING AND INTERMOLECULAR INTERACTIONS

INTRODUCTION

A version of this chapter has been previously published in Molecular Pharmaceutics.

DOI:10.1021/acs.molpharmaceut.9b01025

3.1 Abstract

The generation of a colloidal drug-rich phase by dissolving an amorphous solid dispersion (ASD) is thought to have a positive impact on oral absorption and bioavailability. Thus, understanding which formulations generate these species is important. In this study, ledipasvir-copovidone ASDs, with and without surfactants, were prepared and their release performance was examined at different drug loadings. An intrinsic dissolution rate assembly was used, to limit potential surface area variations among formulations, and the release of both polymer and drug were monitored as a function of time. Drug-rich colloids only formed when the drug loading (DL) was at or below 5%; at a DL of 7.5% or above, drug release became negligible. Drug and polymer released congruently at and below 5% DL, and incongruently at higher DLs. Thus, the limit of congruency (LoC) is between 5 and 7.5 % DL. X-ray photoelectron spectroscopy (XPS) of partially dissolved tablet surfaces revealed that a drug-rich layer formed on the surface of the tablet. This was most evident for the higher DL ASDs, and led to amorphous drug-controlled dissolution. Consequently, the surface drug-enriched layer physically hindered polymer from further release. Evidence is provided that the extent of drug-polymer interactions as a function of DL play a central role in dictating the observed release behavior. Some surfactants were found to promote the formation of drug-rich colloids at considerably higher DLs, providing a formulation strategy to increase the LoC.

Keywords: amorphous solid dispersions; drug loading; dissolution; drug-polymer interaction

3.2 Introduction

In recent years, the percentage of developmental and approved drugs possessing low aqueous solubility has increased, whereby it has been estimated that up to 90% can be considered to be poorly soluble.² One formulation strategy increasingly being applied for the oral delivery of poorly soluble drug is amorphous solid dispersion (ASD), where the drug is dispersed in a polymer matrix to form a molecular level mixture. Dissolving an amorphous drug or an ASD formulation can create supersaturation and significantly increase the free drug concentration as compared to the formulations containing crystalline drug,^{3, 71, 73} leading to enhanced oral absorption and improved bioavailability.^{96, 97}

Dissolution of a solid is typically described by coupling the Whitney–Noyes equation with the Nernst–Brunner diffusion layer model to yield the following equation:

$$\frac{dM}{dt} = \frac{DA}{h}(C_s - C) \quad 3-1$$

where dM/dt is the dissolution rate (mass dissolved per unit time), D is the diffusion coefficient of the solute, A is the solid surface area, h is the thickness of the diffusion layer, C_s is the solubility of the dissolving solid form in the dissolution medium, and C is the concentration of solute in the bulk dissolution medium. According to this equation, when the free drug concentration reaches the solubility of the amorphous drug, the term in the parenthesis goes to zero. Therefore, the maximum free drug concentration that can be achieved by dissolving an amorphous drug is the amorphous solubility. One of the benefits of reaching the amorphous solubility in solution is that the membrane transport rate is maximized.⁶² Moreover, equation 1 predicts that the dissolution rate is controlled by the amorphous solubility assuming that the diffusion coefficient, solid surface area, and thickness of the diffusion layer are fixed.

Recent research has shown that dissolution of an amorphous solid dispersion can lead to concentrations that surpass the amorphous solubility, thus equation 1 cannot be applied to ASDs with very rapid drug release.^{83, 98} When this occurs, the system undergoes liquid-liquid phase separation⁷ or glass-liquid phase separation²⁴ (depending on the glass transition temperature of the separated phase) resulting in the formation of a water-saturated drug-rich phase dispersed in the continuous aqueous phase. The drug-rich phase, if in small- or nano-sized colloidal species, can serve as an effective reservoir, enabling a sustained maximum flux during membrane transport.

This was shown *in vitro* using a diffusion cell.⁸ A recent *in vitro* study that coupled dissolution and absorption showed that drug absorption can be further enhanced by increasing the number of drug-rich colloidal species.⁹⁹ Some *in vivo* studies also suggest that the drug-rich colloidal species are beneficial for drug absorption.^{9, 63} Therefore, an emerging opinion is that the optimal outcome from ASD dissolution is to exceed the amorphous solubility with the formation a drug-rich phase in nano-sized colloidal species. However, this desired scenario cannot be attained when dissolution is controlled by the amorphous drug, since the maximum concentration that can be achieved is the drug amorphous solubility, after which the dissolution rate approaches zero. Formation of drug-rich colloids is feasible only when the dissolution is controlled by the polymer.^{10, 11}

Thus, understanding ASD release mechanisms is essential for designing a formulation with optimal release performance. Some mechanistic studies on polyphase mixtures have been carried out by Higuchi *et al.*,^{60, 61} leading to the proposition that the dissolution rate of each component is related to the composition and interactions between solute and solvent, as well as any phase segregation at the dissolution front with the formation of a barrier layer that controls dissolution. However, the interface composition has not been widely studied for ASDs. A recent study by Indulkar *et al.* revealed that when the drug loading (DL) of ritonavir-copovidone (PVPVA) ASDs increased beyond 25 wt. %, drug release switched from being polymer-controlled to drug-controlled, leading to a dramatic decline in the rate and extent of drug release.¹⁰ Similar observations were made for ASDs containing PVPVA and either cilnidipine or nilvadipine.¹¹ However, for these systems, the DL where the release performance became impaired was lower than for ritonavir, 15 and 10 wt. % respectively. The DL boundary where the release rate drastically drops has been termed the limit of congruency (LoC). At low DLs, drug and polymer release at the same rate, similar to that of pure polymer, while above the LoC, drug release is typically slower than polymer release. The LoC appears to be highly variable for PVPVA-based dispersions and it is currently unclear which drug physicochemical properties and/or drug-polymer interactions impact this threshold value. PVPVA dispersions are important as many commercial ASD formulations contain this polymer.¹⁰⁰ Higher drug loading ASDs with poor drug release have also been observed for hypromellose phthalate (HPMCP) ASDs.¹⁰¹

In this study, ledipasvir-PVPVA ASDs were used as the model system. Ledipasvir, which is used to treat hepatitis C infections in combination with other drugs, is formulated as an amorphous solid dispersion in the commercial product. It is a high molecular weight (889 g/mol), lipophilic

compound with a log P of 6.8 and also has a very high glass transition temperature of 160 °C.¹⁰² These properties, together with a complex molecular structure containing a variety of functional groups, provide an important contrast to the low T_g compounds studied previously. Using surface normalized dissolution, drug and polymer release from ASDs was measured as a function of DL. The impact of adding small amounts of select surfactants was also investigated. The structure and composition of the dissolving tablet surface was examined using fluorescence microscopy, micro computed tomography and X-ray photoelectron spectroscopy, while nuclear magnetic resonance spectroscopy was employed to investigate the drug-polymer interactions.

3.3 Materials

Ledipasvir (Figure 3-1a) was purchased from Gojira Fine Chemicals (Bedford Heights, OH, USA), PVPVA 64 (Figure 3-1b), polyvinylpyrrolidone (PVP), and polyvinyl acetate (PVA) were obtained from Ashland Inc. (Covington, KY, USA). Ethanol 200 proof anhydrous, poloxamer 407, sodium dodecyl sulfate and Span[®] 85 were purchased from Sigma-Aldrich (St. Louis, MO, USA). Phosphate buffer (50 mM, pH 6.8) was prepared by dissolving sodium phosphate dibasic and sodium phosphate monobasic monohydrate in water. Both sodium phosphate dibasic and sodium phosphate monobasic monohydrate were purchased from Macron Chemicals (Philipsburg, NJ, USA). Vitamin E TPGS and Tween 80[®] (polysorbate 80) were from BASF (Ludwigshafen, Germany) and Croda (Snaith, UK) respectively. The deuterated solvents for nuclear magnetic resonance (NMR) spectroscopy were toluene and dimethyl sulfoxide (DMSO), containing 0.03 % (v/v) tetramethylsilane (TMS), obtained from Sigma-Aldrich (St. Louis, MO, USA) and Cambridge Isotope Laboratories (Tewksbury, UK) respectively. For the NMR titration study, 1-vinyl-2-pyrrolidinone (VP), purchased from Sigma-Aldrich (St. Louis, MO, USA), was employed.

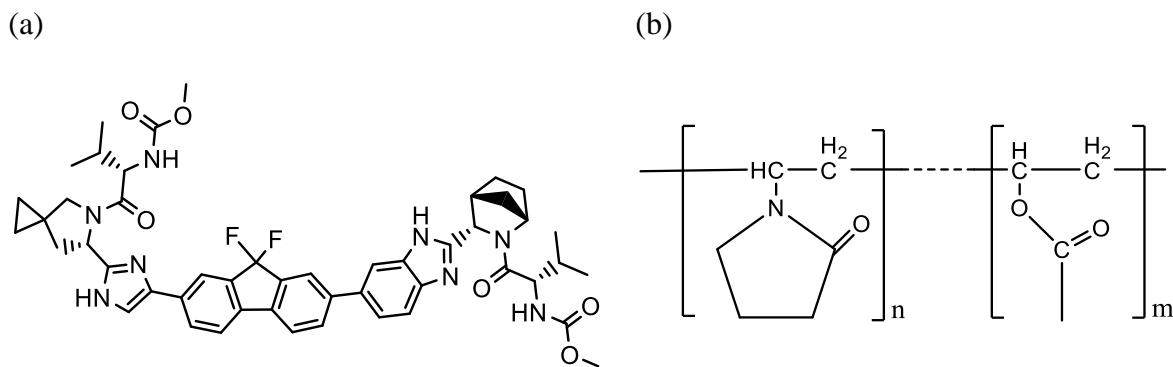


Figure 3-1. Chemical Structures of Ledipasvir (a) and PVPVA with VP/VA mass ratio of 60/40 (b).

3.4 Methods

3.4.1 Preparation of Amorphous Solid Dispersions (ASDs) of Ledipasvir.

The composition of binary amorphous solid dispersions of drug and polymer is typically expressed in weight percent. However, to compare and contrast the effects of a third component on dissolution performance it was important to keep the drug-to-polymer ratio in the ternary formulations the same as in the binary formulations. For this reason, the composition of the ternary formulations is expressed in parts by weight instead of weight percent. All ternary formulations contained 100 parts of drug and polymer and 5 parts of surfactant. For example, the ternary equivalent of a binary formulation with a DL of 20% is 20 parts drug, 80 parts polymer, and 5 parts surfactant. Amorphous solid dispersions of ledipasvir and PVPVA at DLs of 2, 5, 7.5, 10, 20 and 50 wt. % were prepared by solvent evaporation from ethanol using a rotatory evaporator. The pure amorphous ledipasvir was also attained by this method. A total amount of 10 g ledipasvir and PVPVA was dissolved in 200 mL ethanol, and the solvent was removed by a rotary evaporator (Büchi, New Castle, DE) using a water bath set at a temperature of 60 °C. For ASDs containing surfactant, an additional 500 mg of surfactant was added to the pre-mixed ethanol solution containing ledipasvir and PVPVA, and ethanol was evaporated using a rotary evaporator. The ASDs were then placed in a vacuum oven with the temperature set at 40 °C for 24 h to remove residual solvent. The ASD powders were sieved and the 150-250 μm sieve fraction was collected, to achieve a narrower and consistent particle size distribution prior to dissolution.

3.4.2 Determination of Glass Transition Temperature of Amorphous Solid Dispersions by Differential Scanning Calorimetry (DSC).

The neat amorphous ledipasvir, PVPVA, and ASD powders prepared by solvent evaporation were loaded into standard aluminum pans. The pan lids had a pin-hole to allow escape of volatile components. The glass transition temperatures were analyzed by a Q2000 differential scanning calorimeter with a refrigerated cooling accessory (TA Instrument, New Castle, DE). The sample was equilibrated at 1 °C and then heated from 1 °C to 180 °C at 10 °C/min and then cooled back down to 1 °C at 10 °C/min. The heating and cooling cycle was repeated 3 times and the last cycle was used for analysis. The temperature accuracy of the Q2000 was validated by running a 10 °C/min heating ramp on a sample of indium. During the experiment, a nitrogen flow of 50 mL/min was maintained to create a dry environment.

3.4.3 Dissolution of Amorphous Solid Dispersions using Rotating Disk Apparatus.

Surface area normalized dissolution was carried out using an intrinsic dissolution rate measurement assembly (Agilent, Santa Clara, CA). The sieved ASD powder, 100 mg, was compressed at a pressure of 1500 psi with a hydraulic press (Carver Inc, Wabash, IN) in a circular intrinsic die of diameter 8 mm, and the compression pressure was held for 60 s. The die was then attached to a rotating paddle. For neat polymer release, 250 mg PVPVA was used. All the dissolution experiments were performed in 100 mL pH 6.8 50 mM phosphate buffer at 37 °C with a stirring rate of 100 rpm.

3.4.4 Concentration Analysis of Ledipasvir and PVPVA.

For the release studies, at each sampling time point, 3 mL dissolution medium was withdrawn for both ledipasvir and PVPVA concentration analysis, and replaced with 3 mL of neat dissolution medium to maintain the volume at 100 mL. The time points taken were 10, 20, 30, 40, 50, 60 and 90 min. For ledipasvir, 0.4 mL of sample was diluted by addition of 0.6 mL ethanol to ensure all the drug-rich colloids were dissolved, and the drug concentration was analyzed using a high performance liquid chromatography (HPLC) system (1260 Infinity, Agilent, Santa Clara, CA). For the HPLC method, a mobile phase of 60% acetonitrile and 40% water (v/v) at a flow rate of 0.8 mL/min with an injection volume of 20 µL and an ultraviolet (UV) detection wavelength of

205 nm were used. The separation column used was an Ascentis Express C18 (Sigma-Aldrich, St. Louis, MO) with dimensions of 10 cm x 3.0 mm, 2.7 μ m particle size. The remaining 2.6 mL of sample was filtered through a 0.2 μ m nylon syringe filter (Pall Corporation, Port Washington, NY), and the last 0.8 mL of solution was collected and diluted with 0.2 mL methanol for subsequent analysis of PVPVA concentration. The instrument used was an OMNISEC chromatographic system (Malvern Panalytical, Worcestershire, UK), with a mobile phase of 20% methanol and 80% pH 7.4 phosphate buffer solution at a flow rate of 0.75 mL/min with an injection volume of 100 μ L, and PVPVA was detected by a UV detector at a wavelength of 205 nm. The column for PVPVA quantification was an A2500 (Malvern Panalytical, Worcestershire, UK), aqueous GPC/SEC column 300 x 8 mm.

3.4.5 Tablet Morphology Study by Micro Computed Tomography (Micro CT).

Tablet morphology before and after intrinsic dissolution was examined by a high resolution SkyScan-1272 micro CT via X-ray transmission from Bruker (Billerica, MA). The X-ray source was operated at a voltage of 60 kV and a current of 166 μ A. The tablets were placed on the rotating stage, and the total sample rotation was set as 360° with an interval of 0.1°. The spatial resolution was 8 μ m/pixel. The acquisition time for each tablet was about 7 hr. The tablet after dissolution was dried in a vacuum oven overnight to remove all the residue moisture prior to examination, and no phase transformation was expected during acquisition. The reconstruction was carried out by NRecon software (Bruker, Billerica, MA), and the 3-dimensional model rendering and viewing were performed using CT-volume software (Bruker, Billerica, MA).

3.4.6 Amorphous-Amorphous Phase Separation Study by Fluorescence Microscope.

Environment-sensitive fluorescent probes have been used to study phase separation behavior for hydrated, solid ASDs.^{103, 104} In the current study, Nile red, a hydrophobic probe, was used as the “sensor” to detect the hydrophobicity change in the environment following exposure of ASD films to water vapor. Upon formation of a drug-rich phase, the probe will incorporate into the more hydrophobic phase, which is a drug-enriched domain. Ledipasvir-PVPVA ASD films with 5, 10 and 50% DL were prepared by spin coating (KW-4A spin coater, Chemat Technology Inc., Northridge, CA) 200 μ L ethanol solution, containing ledipasvir and PVPVA at the desired

ratio and a trace amount of Nile red. The substrates used were quartz slides of 1 in. x 1 in. x 1 mm dimension (Ted Pella Inc., Redding, CA). The ethanol stock solutions had a total solid concentration of 100 mg/mL while the Nile red concentration was 100 µg/mL. Fluorescence imaging of ASD films was performed before and after exposure to 100% RH at 37°C for 3 days. The instrument used was an Olympus BX-51 Optical Microscope (Olympus Corporation, Tokyo, Japan) with green (520 nm-550 nm) excitation.

3.4.7 X-ray Photoelectron Spectroscopy (XPS).

The compacts before and after dissolution (for 10 min) were ejected manually from the die, and the chemical composition of the tablet surface was probed using XPS. The XPS spectra from the tablets were acquired using a Kratos Axis Ultra DLD Imaging spectrometer (Kratos Analytical, Manchester, UK) with monochromic Al K α radiation (1486.6 eV) at a constant pass energy (PE) of 20 and 160 eV for high-resolution and survey spectra, respectively. To avoid non-homogeneous electric charge of non-conducting samples and to achieve better resolution, a built-in commercial Kratos charge neutralizer was used. For each sample, at least three acquisitions at different spots were collected.

The XPS data were analyzed using CasaXPS software. The charge correction was done by setting the main C 1s component (typically the C-H/C-C component) to a binding energy of 284.8 eV for each measurement. The curve-fitting was performed after a Tougaard background subtraction using model peaks obtained from the pure compounds. The atomic percentages on the tablet surface were calculated using Scofield relative sensitivity factor and taking into account an attenuation length of photoelectrons. The atomic percentages were converted to weight percentage based on the chemical formula of the compounds.

3.4.8 Nuclear Magnetic Resonance Spectroscopy (NMR).

^1H NMR, ^{19}F NMR and ^{13}C NMR were performed using a Bruker DRX 500 MHz spectrometer (Billerica, MA, USA). To confirm the ledipasvir as-received was comparable to literature reports,^{105, 106} ^1H NMR, ^{19}F NMR and ^{13}C NMR spectra were recorded in deuterated DMSO. The rest of the NMR studies were measured in a non-polar solvent, toluene, in order to study intermolecular interactions. The ^{19}F NMR spectra were collected at ledipasvir concentrations

of 0.5, 2, and 4 mg/mL. ^{19}F NMR and ^1H NMR spectra of ledipasvir were collected in the presence of PVP and polyvinyl acetate (PVA) in order to gain insight into which functional group of PVPVA interacted with ledipasvir. A 2 mg/mL stock solution of ledipasvir in deuterated toluene was divided evenly into eight portions for the NMR titration study: A variable amount of 1-vinyl-2-pyrrolidinone (VP), from 2 to 80 mg/mL, was added to each aliquot. Ledipasvir ^{19}F NMR and ^1H NMR spectra were collected for each sample. ^{19}F NMR spectra were also collected at temperatures of 278 K, 298 K and 318 K. All other NMR experiments were performed at 298 K.

3.4.9 Dynamic Light Scattering (DLS).

The particle size of the drug-rich colloidal species generated during ASD dissolution was measured using DLS. A 3 mL aliquot of solution was withdrawn from the dissolution medium at different time points and analyzed by a Nano-Zetasizer (Nano-ZS) from Malvern Instruments (Westborough, MA) equipped with dispersion technology software (DTS). The backscattered light at an angle of 173° was obtained. The cuvette used was a 12 mm square polystyrene disposable cuvette. For all the measurements reported, the polydispersity index (PDI) was less than 0.3, so that the intensity size distributions generated were considered as a monodisperse.

3.5 Results

3.5.1 Glass Transition Temperature (T_g)

The dry glass transition temperatures of amorphous ledipasvir and PVPVA are 161°C and 108°C respectively. From the DSC thermograms all ASDs, with DLs ranging from 2 to 50 wt. %, showed a single glass transition temperature with no melting events, suggesting that the amorphous drug is homogeneously dispersed in the polymer. The measured midpoints of the glass transition temperatures for all ADSs are summarized in Table 3-1.

Table 3-1. Midpoint glass transition temperature for all the ASDs. Mean values \pm standard deviation are shown where n=3.

| Drug Loading | Glass Transition Temperature ($^{\circ}$ C) |
|--------------|--|
| 0% | 107.5 \pm 0.1 |
| 2% | 107.1 \pm 2.4 |
| 5% | 106.7 \pm 0.8 |
| 7.5% | 110.8 \pm 2.0 |
| 10% | 109.2 \pm 0.4 |
| 20% | 119.8 \pm 2.8 |
| 50% | 135.5 \pm 1.2 |
| 100% | 160.9 \pm 0.8 |

3.5.2 Release profiles of Ledipasvir-PVPVA ASDs

The release profiles of ledipasvir-PVPVA ASDs at different DLs, neat amorphous drug, and neat PVPVA are summarized in Figure 3-2. For neat amorphous drug dissolution, no ledipasvir was detected in solution within two hours. The HPLC detection limit for the method used was about 0.2 μ g/mL. For ledipasvir PVPVA ASDs with 2% and 5% DL, the drug releases quickly exceeded the amorphous solubility (which is < 1 μ g/mL), and the formation of a drug-rich phase was visually observed as the dissolution medium became cloudy. The percent release rate for the individual components of the ASD, i.e. ledipasvir and PVPVA, was comparable at each time point, reaching 100% after 60 min, and the drug release rate was similar to the dissolution rate of neat PVPVA. This suggests that the release of drug from the ASD was polymer-controlled. However, when the DL increased to 7.5% and above, no detectable drug release and only minimal polymer release was achieved. Thus LoC was determined to be 5% DL. Moreover, the tablets fractured at around 60 min post exposure to the dissolution medium.

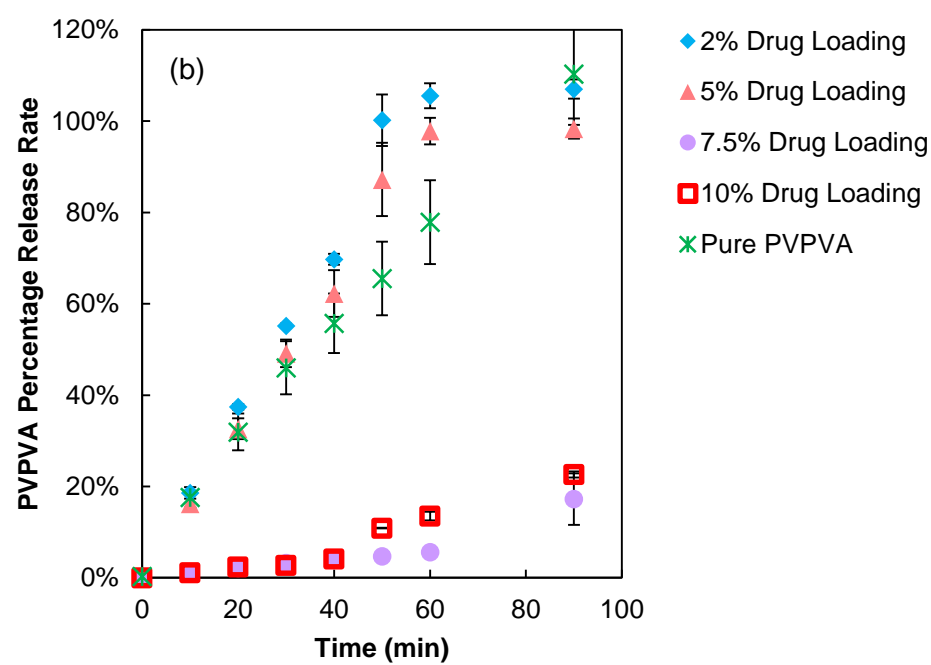
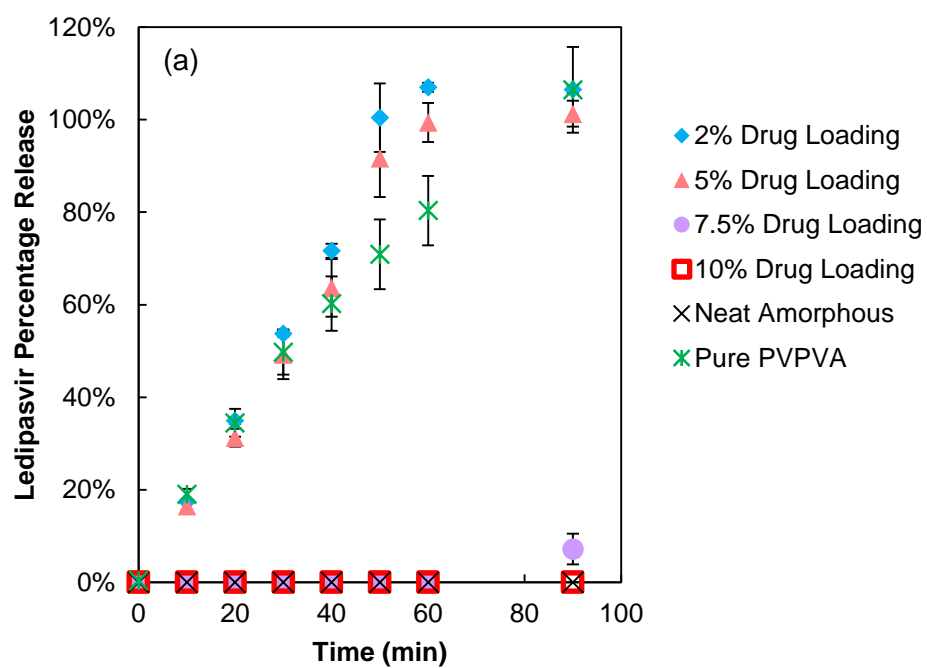


Figure 3-2. Release profiles of (a) ledipasvir and (b) PVPVA from ledipasvir-PVPVA amorphous solid dispersions with different DLs.

3.5.3 Release Profiles of Ledipasvir-PVPVA ASDs containing Surfactant.

In order to study the impact of surfactants on the release behavior of ledipasvir-PVPVA amorphous solid dispersions, five different commonly used surfactants, varying in hydrophilic-lipophilic balance (HLB), were incorporated into the ASDs.

Out of the five, Span[®] 85, Tween 80 and vit E TPGS, did not improve the DL limit for polymer-controlled release, i.e. LoC. The release profiles for 7.5% DL ASDs containing these three surfactants are shown in Figure A.1; these were similar to the profile shown in Figure 3-2 for the 7.5% DL ASD. However, the more hydrophilic surfactants, poloxamer 407 and SDS, improved the LoC to 7.5% DL and 30% DL, respectively (Figure 3-3). Drug and polymer released congruently for both ASDs at a DL of 7.5%, however, the release rate was slower for the ASD containing poloxamer 407, reaching 100% drug and polymer release in about 110 min (Figure 3-3b). For ASDs containing 5 wt.% SDS, LoC was 30%, but slightly slower release rate was observed at this DL (Figure 3-3c). As the DL increased to 40%, a very limited amount of drug or polymer was released from the formulation.

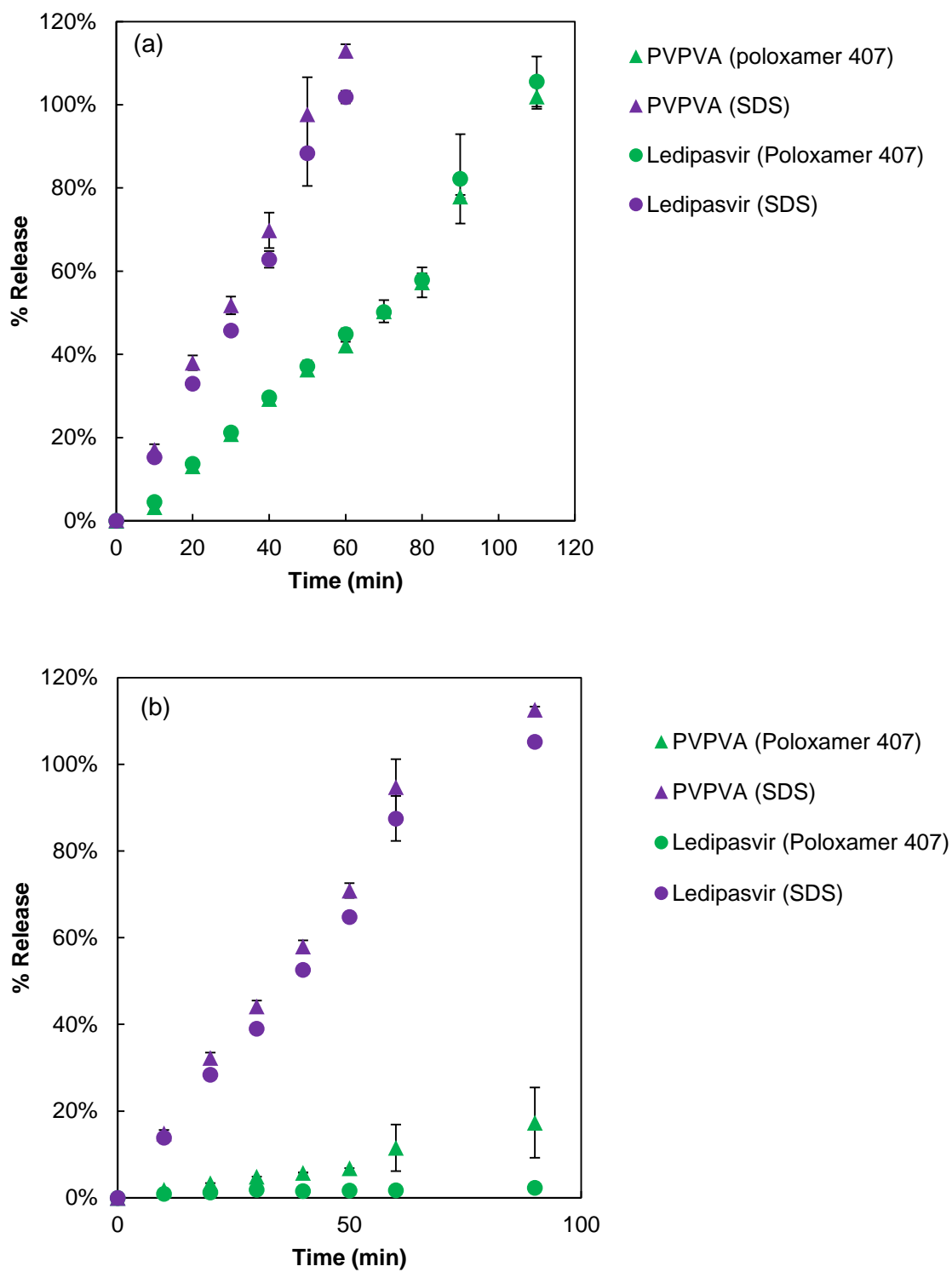
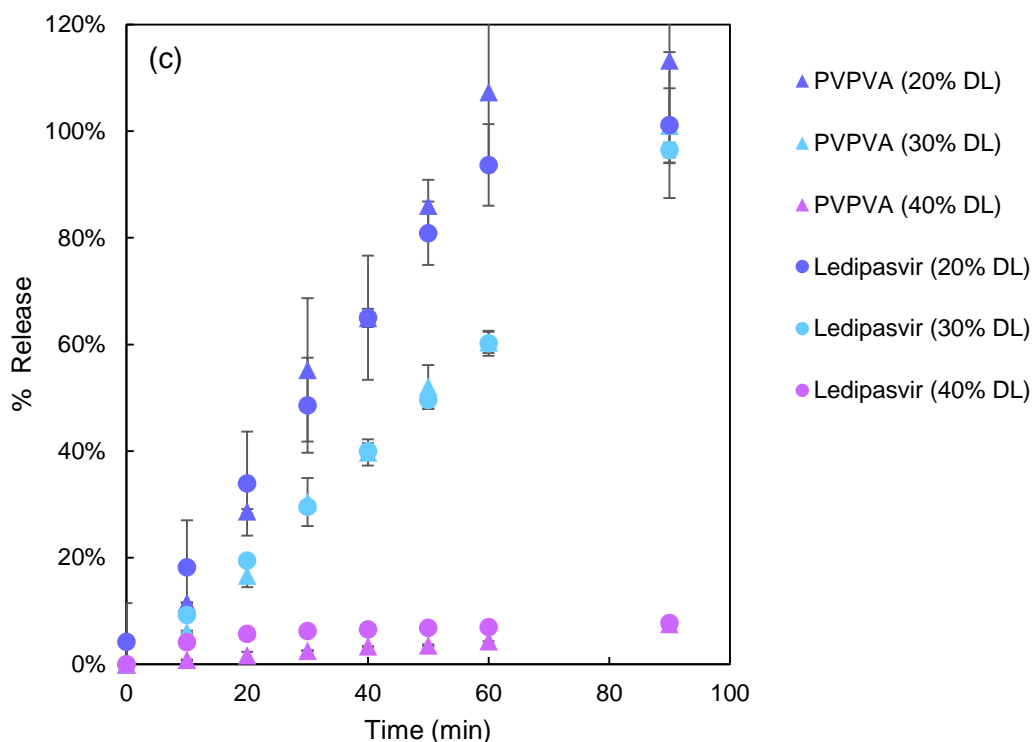


Figure 3-3. Release profiles of (a) 7.5% DL, (b) 10% DL ASDs containing 5 wt% Poloxamer 407 and SDS, (c) ASDs containing 5 wt% SDS with DL of 20, 30, and 40%.

Figure 3.3 continued



3.5.4 Particle Size of the Drug-rich Colloids Formed during Dissolution.

The particle size of colloidal species formed during drug release was monitored for three formulations: 5% ledipasvir-PVPVA, 5% ledipasvir-PVPVA with 5% poloxamer 407 (dissolution profile is shown in Figure A.2), and 7.5% ledipasvir-PVPVA with 5% SDS. All ASDs achieved 100% release, and the dissolution was polymer-controlled. The average particle diameter as a function of time is plotted in Figure 3-4. The particles were relatively stable over the 60 min dissolution period, and no evidence of agglomeration was observed. The dissolution rates of both polymer and ledipasvir were comparable among these ASDs, but the size of the drug-rich colloids varied among formulations. In the presence of SDS and poloxamer 407, the particle sizes were approximately 60 and 120 nm, respectively. This is considerably smaller than the 250 nm particles generated in the absence of surfactant.

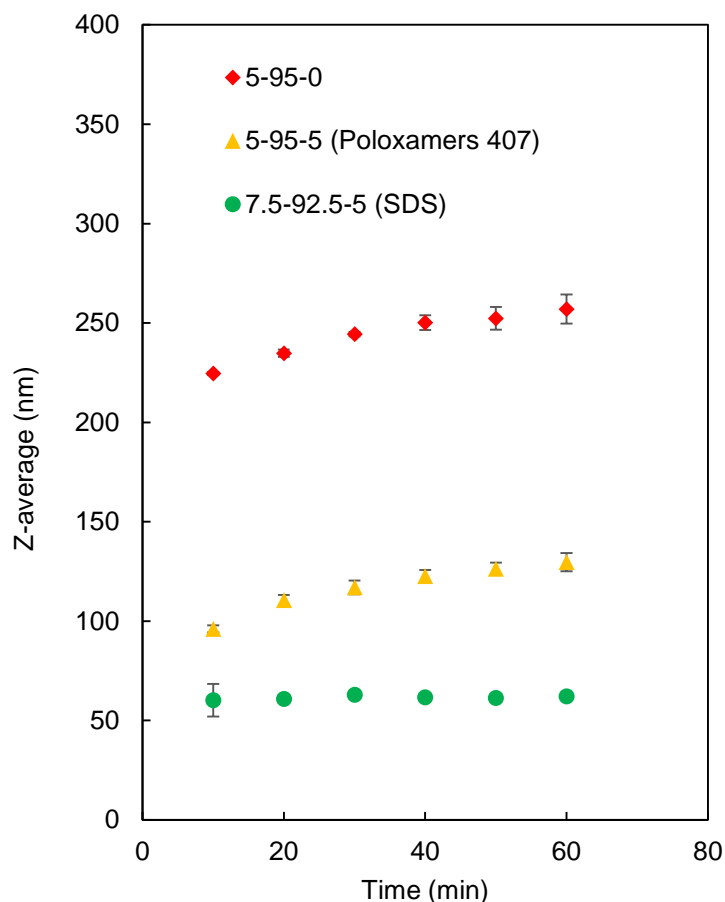


Figure 3-4. Z-average particle diameter for the drug-rich particles generated during ASD dissolution. The x-axis represents the sampling time from the dissolution vessel.

3.5.5 X-ray Micro-computed Tomography Images.

X-ray micro CT was utilized to visualize the morphology evolution of ASD tablets before and after partial dissolution, with images shown in Figure 3-5. For the 5% DL tablet (Figure 3-5b), the tablet thickness decreased after 10 min of dissolution, indicating polymer and drug released from the tablet, consistent with the release rates shown in Figure 3-2. However, for the 10% DL tablet (Figure 3-5c), the thickness did not change significantly over the same time period. Close evaluation of Figure 3-5c, suggests that there is a top layer discriminated from the bulk (as indicated by the double-headed arrow), consistent with hydration of this layer. After 30 min (Figure 3-5d), bulging of the tablet occurred, indicating further hydration. Further, some porosity can be seen in the tablet.

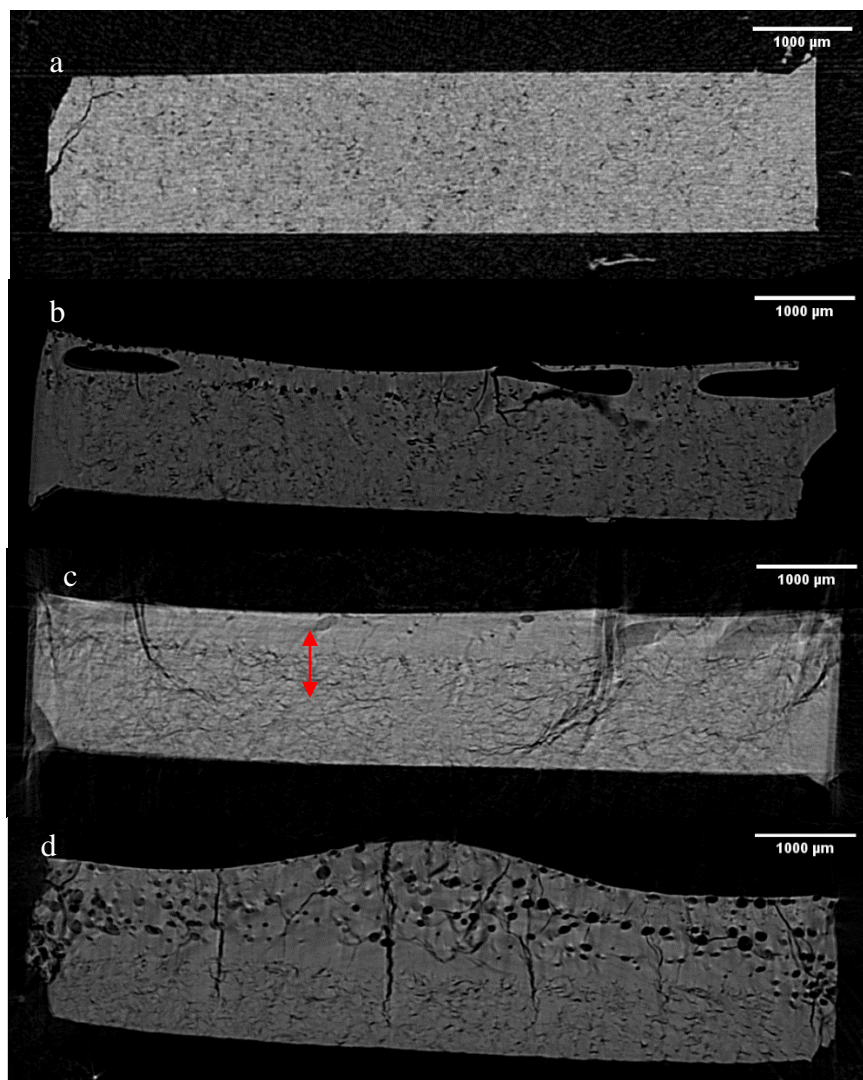


Figure 3-5. X-ray micro-computed tomography cross-section images for (a) tablet before dissolution (b) 5% DL tablet after dissolution for 10 min (c) 10% DL tablet after dissolution for 10 min (d) 10% DL tablet after dissolution for 30 min. The images represent the cross-sectional area at the center of the tablets and were obtained after 2D reconstruction.

3.5.6 Fluorescence Microscopy

For fluorescence microscopy imaging, Nile red was used as a fluorescence probe. Its excitation and emission maximum are around 552 nm and 636 nm respectively, so that the domains containing Nile red show red emission with green excitation. The fluorescence intensity is higher when the dye is in a hydrophobic environment.^{107, 108} Nile red will be predominately found in the drug-rich domains if formed, and hence these domains are expected to have greater fluorescence intensity compared to polymer-rich regions. The ASD films showed smooth and homogenous

fluorescence intensity before exposure to humidity. A representative image is shown in Figure 3-6a. This confirms that there is no phase separation between ledipasvir and PVPVA in the unexposed ASD material at the resolution of the fluorescence microscope. The fluorescence images (Figure 3-6b) of moisture-exposed ASDs showed mostly homogeneous fluorescence intensity for the 5% DL ASD film, suggesting minimal, or no phase separation. The 10% DL ASD film (Figure 3-6c) showed small domains that differ in fluorescence intensity, suggesting some phase separation. The 50% DL film (Figure 3-6d) showed large domains that differ in fluorescence intensity, suggesting more extensive phase separation.

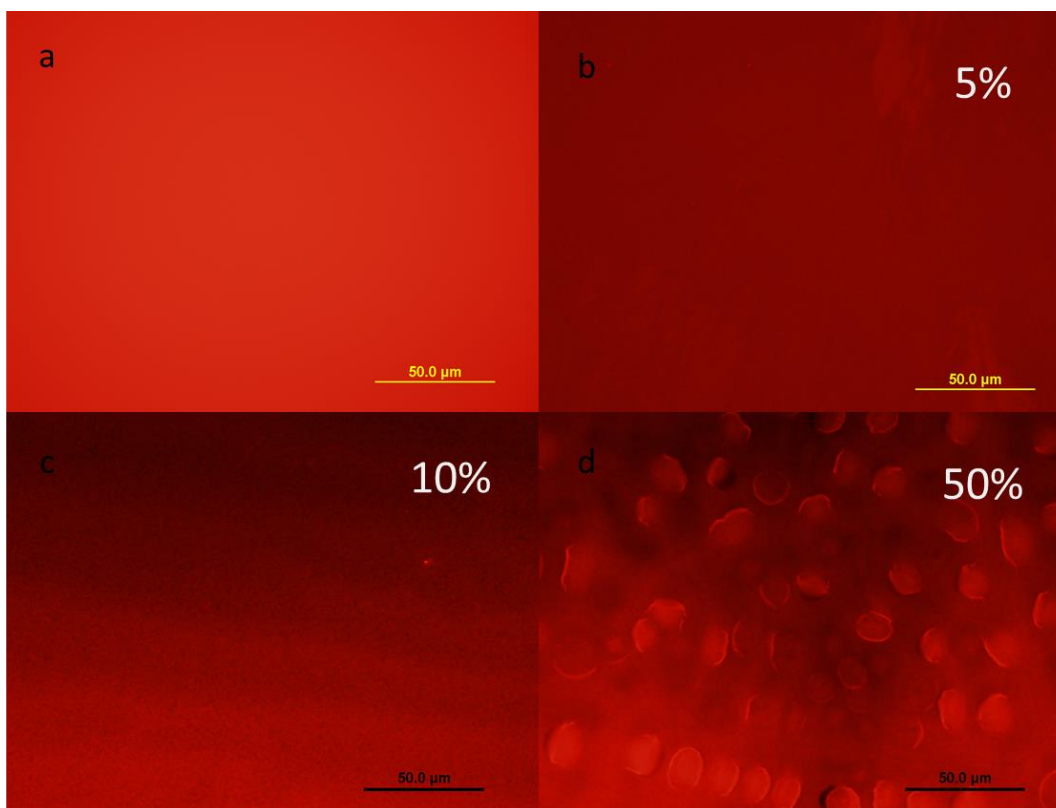


Figure 3-6. Representative fluorescence microscope images of ledipasvir-PVPVA ASDs: (a) before exposure to moisture (50% DL), (b) 5% DL after exposure to moisture, (c) 10% DL after exposure to moisture and (d) 50% DL after exposure to moisture. Samples were exposed to 100% RH, 37 °C for 3 days.

3.5.7 X-ray photoelectron spectroscopy (XPS)

The surface chemical composition of tablet surfaces before and after dissolution for different DL ledipasvir-PVPVA ASDs was also characterized by XPS. Since nitrogen atoms have a different chemical environment in PVPVA as compared to in ledipasvir (Figure A.2), the N 1s

peaks were chosen for peak fitting to calculate the weight ratio between drug and polymer. For the curve fitting of ASD spectra, the N 1s XPS spectra of pure ledipasvir and PVPVA were used to model the data (Figure A.2). From curve fitting, the atomic ratio between ledipasvir and PVPVA (based on the nitrogen atoms) was attained for the ASDs, and, using the chemical structures, this was converted to a weight composition. The weight compositions on the tablet surface are shown in Figure 3-7 for the 20% and 50% DL before and after dissolution for 10 min. According to the XPS data, for the tablet before dissolution, the ledipasvir weight percentage was close to the theoretical value, indicating no major enrichment of either drug or polymer in the near-surface region. The XPS analysis on the tablet surface after dissolution revealed that the surface became drug-enriched. The weight percentage of ledipasvir for the 20%, and 50% DL ASDs increased from 17% and 40% to 54% and 61%, respectively. For DLs below 20%, it was difficult to differentiate drug from polymer based on N1s curve fitting due to the low amount of drug present.

The fluorine (F) 1s XPS peak was also analyzed. Ledipasvir contains two fluorine atoms, while no fluorine is present in the polymer. In the F 1s spectrum of pure amorphous ledipasvir, only one peak with a binding energy of 687.1 ± 0.1 eV was observed. However, when the ledipasvir molecules were dispersed in PVPVA, a new fluorine peak with a binding energy of 684.0 ± 0.2 eV emerged. Example spectra are shown in Figure A.3. This significant negative 3 eV binding energy shift indicates that a portion of the fluorine atoms experienced different interactions in the presence of the polymer, whereby the fluorine atom has become more electron-rich. From fluorine XPS peak curve fitting, the percentage of fluorine with a lower binding energy was 77%, 73%, 42% and 18% for ledipasvir ASDs with DLs of 5%, 10%, 20% and 50% respectively, as shown in Figure 3-8. Thus, as the DL in the ASD increased, the percentage of F 1s that has a lower binding energy, decreased dramatically. This suggests that as the DL increases, the ledipasvir molecules in the dispersion are in closer proximity with one another, while at low DLs, they are more isolated from other ledipasvir molecules.

The intensity of the F 1s peak with a lower binding energy decreased significantly after dissolution for initial DLs of 10%, 20% and 50%, dropping from 77%, 73% and 42% to 9%, 3% and 2% respectively, as shown in Figure 3-9. This dramatic decrease suggests that ledipasvir is no longer in close contact with the polymer, and hence has separated from PVPVA in the presence of water, and is now in a more drug-rich environment. For the 5% DL, the F signal on tablet surface after dissolution was insufficient to quantify.

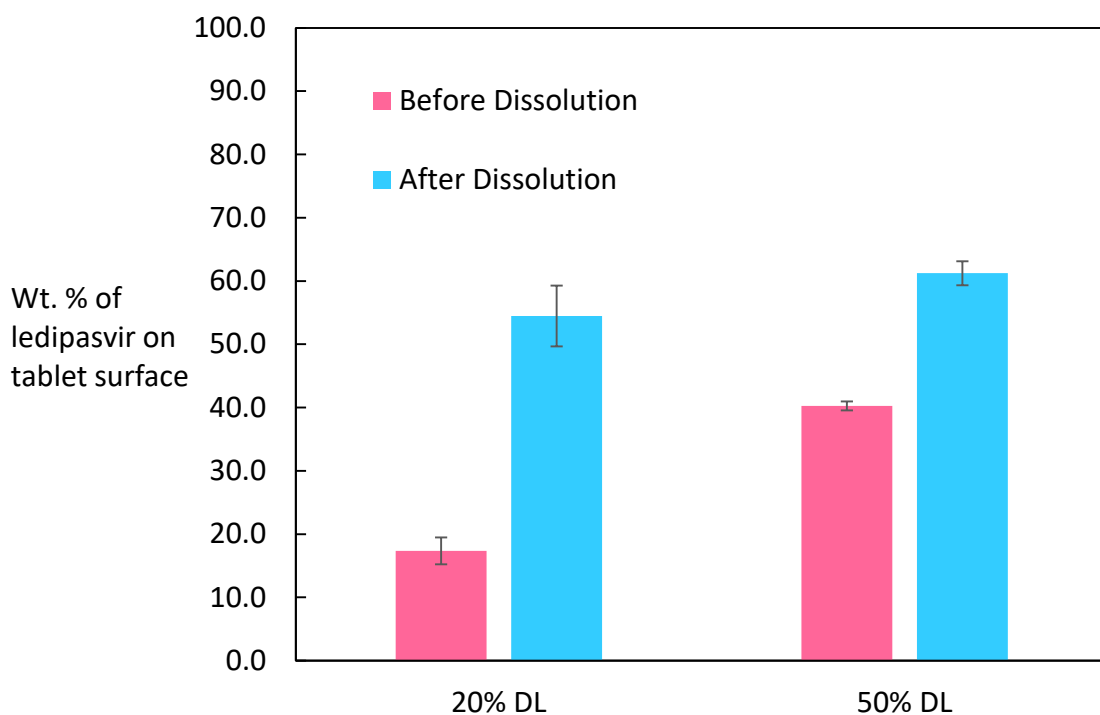


Figure 3-7. Tablet surface composition before and after dissolution for tablets with initial DLs of 20% and 50%. The weight percentage of drug on the near surface increases following dissolution for 10 min.

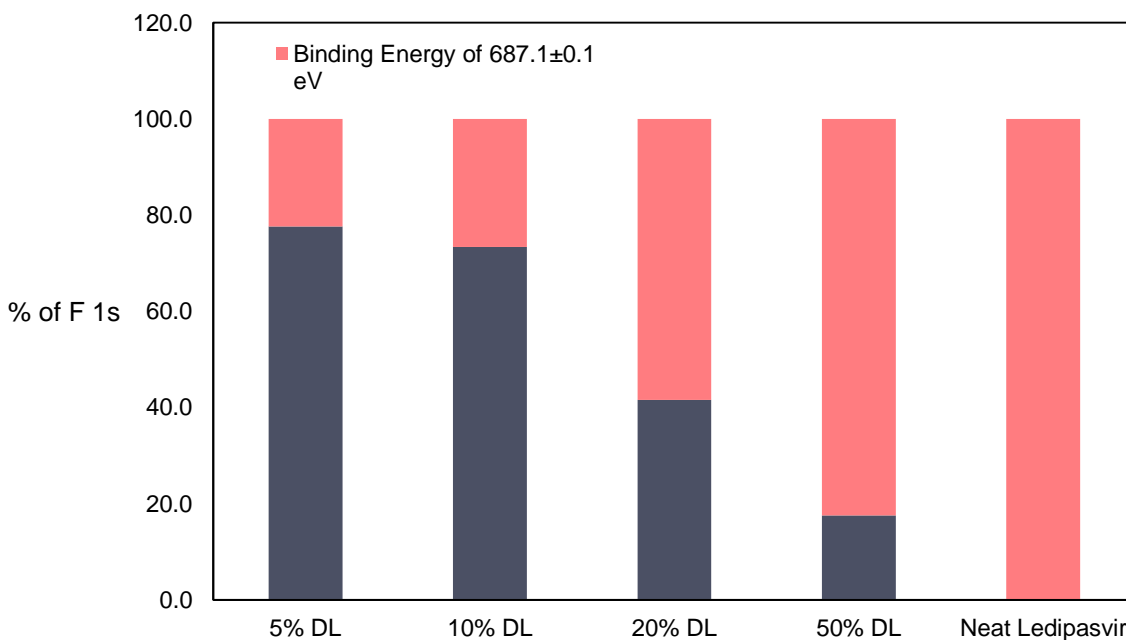


Figure 3-8. Percentage of F 1s peaks with high and low binding energies as a function of DL in the ASD. It is apparent that the low binding energy F1s peak predominates at low DLs, while the high binding energy F1s peak is dominant at high DLs.

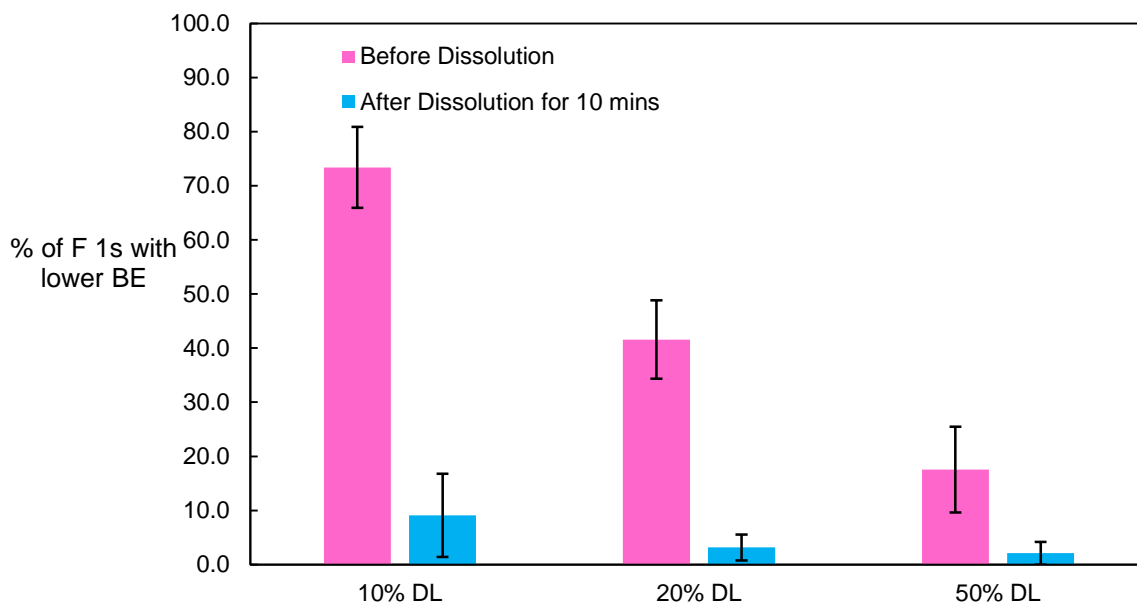


Figure 3-9. Percentage of F 1s with a lower binding energy (BE) of 684.0 ± 0.2 eV for ASDs with DLs of 10%, 20% and 50%, before and after dissolution for 10 min.

3.5.8 Nuclear Magnetic Resonance (NMR) Spectroscopy

The ^1H NMR (Figure A.4(a)), ^{19}F NMR (Figure 10) and ^{13}C NMR (Figure A.4(b)) for ledipasvir in deuterated DMSO were collected to verify the compound identity. In ^{19}F -NMR, the peaks labeled with stars are results of the geminal coupling of the two ^{19}F atoms with different chemical shifts. The NMR spectra for the as-received ledipasvir are comparable to those in literature,^{105, 106} and likely contain trace amount of impurities, as discussed previously.¹⁰⁹ Based on the ledipasvir chemical structure, the carbon with the two fluorine atoms attached is prochiral. In DMSO, a more polar solvent, the fluorine spectrum showed one main peak, presumably due to greater freedom of sigma bond rotation on the two sides of the ledipasvir molecule. However, more than one peak was observed when the solvent was changed to toluene, a less polar solvent (Figure 3-10). In toluene, we reasoned that ledipasvir may have some intermolecular or intramolecular interactions, restricting free chemical bond rotation. As a result, the two ^{19}F atoms experience different chemical environments. ^{19}F NMR spectra at different ledipasvir concentrations confirmed that F peak splitting is due to intermolecular interactions. The concentration effect would be insignificant if interactions were intramolecular. When the drug concentration was

increased from 0.5 to 4 mg/mL (Figure 3-11) the chemical shift difference between the two F atoms became larger. This is because at higher ledipasvir concentrations the probability of forming drug-drug interactions is greater, so a higher fraction of the fluorine atoms are in different chemical environments. ^{19}F NMR spectra were also collected at different temperatures for a sample with a ledipasvir concentration of 2 mg/mL (Figure A.5). With increasing temperature, the chemical shift difference between the two F atoms decreased, due to an increase in chemical bond rotation.

The next set of experiments was designed to study drug-polymer interactions. For these studies, it was important to use a solvent with minimal hydrogen bonding ability, hence toluene was selected. Interestingly, with the addition of only 2 mg/mL PVPVA to the ledipasvir toluene solution, the chemical shift difference between F peaks reduced, while addition of PVA had no impact (Figure 3-12). Thus, PVPVA potentially can break the ledipasvir-ledipasvir interaction, whereby the lack of impact of PVA suggests that the vinylpyrrolidone (VP) group rather than the vinyl acetate moiety may be responsible for the disruption of ledipasvir-ledipasvir interactions. ^{19}F -NMR could not be measured in the presence of PVP due to its minimum solubility in toluene. To further confirm that the VP group disrupts drug-drug interaction, variable amounts of the low molecular weight analog of PVP, 1-vinyl-2-pyrrolidinone (VP), were added to the ledipasvir toluene solution, and the resultant ^{19}F NMR spectra are shown in Figure 3-13. The trends observed are similar to those observed in the presence of PVPVA, with the F peaks merging towards each other. This suggests that VP can disrupt interactions between ledipasvir molecules. From the drug molecular structure, F potentially can form hydrogen bonds with the amine group (NH) of a second ledipasvir molecule, accounting for the changes in the NMR spectrum observed at higher concentrations. When the amine group forms hydrogen bonds, the proton has a much higher chemical shift, as observed in the ledipasvir ^1H -NMR (Figure 3-14). The four peaks with chemical shift greater than 10 ppm represent the four NH groups in the molecule. From the ledipasvir molecular structure, the two NH groups from each imidazole can form intramolecular hydrogen bonds with the carbonyl group to form a seven-member ring (shown in Figure 3-15a). In contrast, the other two NH groups potentially can form intermolecular hydrogen bonding with the fluorine atom (Figure 3-15b). The intramolecular hydrogen bonding is relatively more stable and stronger compared to intermolecular hydrogen bonding, resulting in two proton peaks with larger peak area and higher chemical shift. Moreover, addition of VP did not have significant impact on these intramolecularly hydrogen bonded protons. However, the VP group can disrupt inter-molecular

hydrogen bonding by either forming a hydrogen bond with NH or through a halogen bond or dipolar interaction with F. The formation of a hydrogen bond is more likely in this scenario, as indicated by the greater chemical shift and peak area for NH proton peaks in the presence of VP.

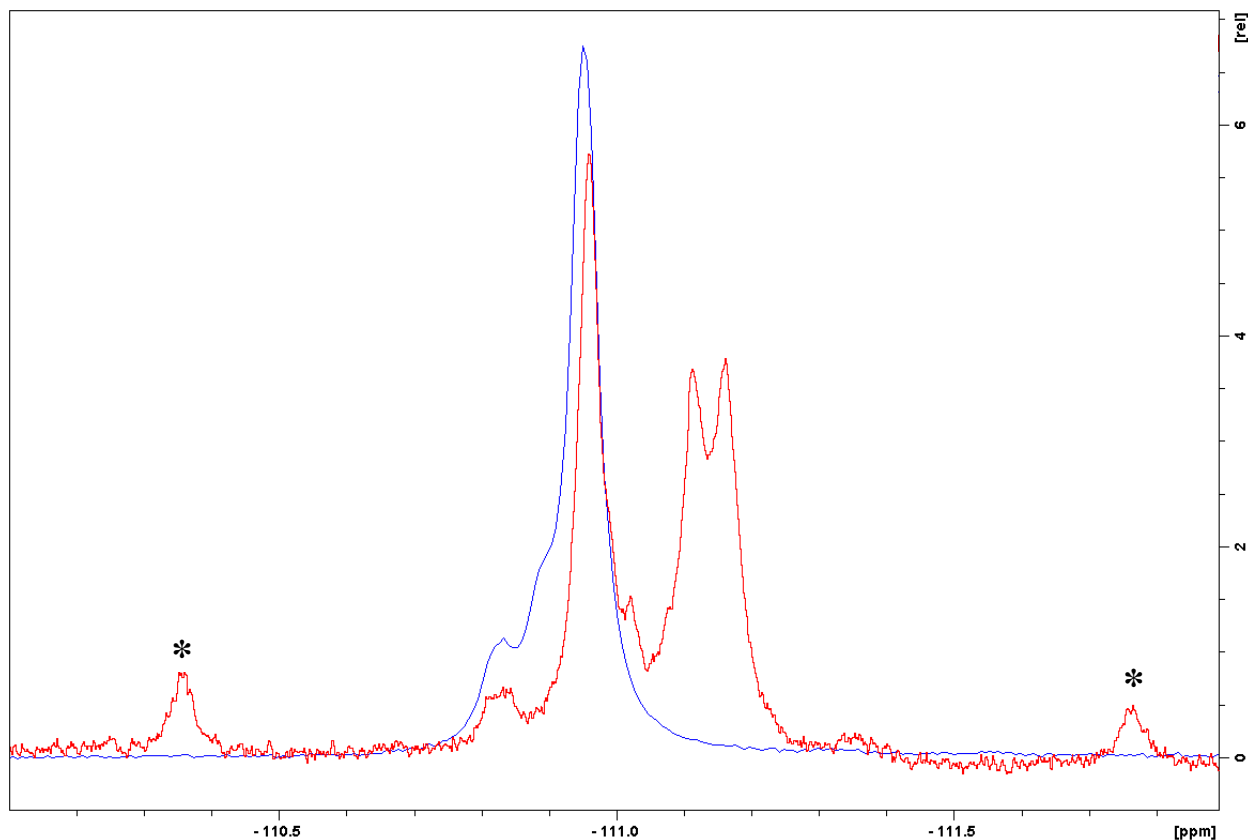


Figure 3-10. ^{19}F -NMR spectra of ledipasvir in deuterated-DMSO (blue line) and deuterated-toluene (red line). The peaks labeled with asterisks are results of the geminal coupling of the two ^{19}F atoms with different chemical shifts.

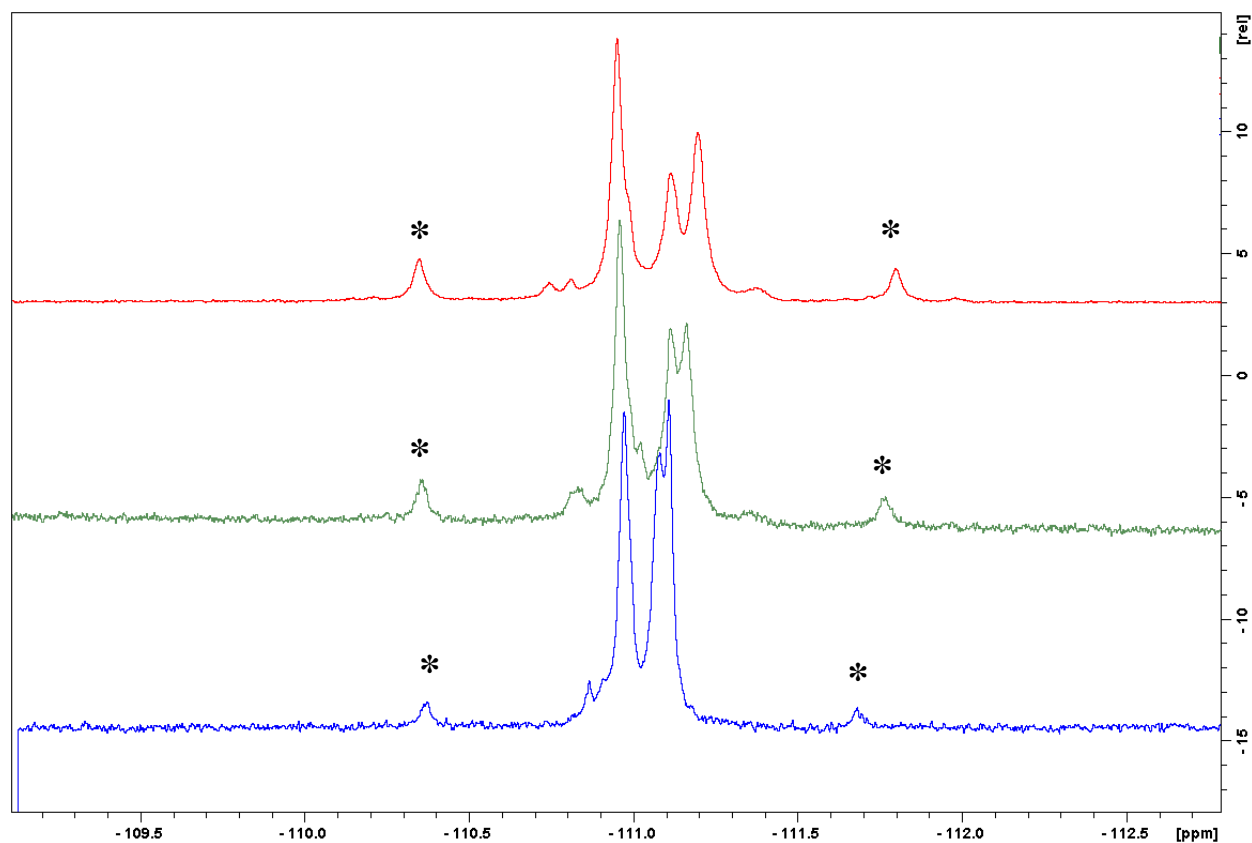


Figure 3-11. ^{19}F -NMR spectra of ledipasvir toluene solutions with concentrations of 0.5 mg/mL (blue line), 2 mg/mL (green line) and 4 mg/mL (red line). The peaks labeled with asterisks are results of the geminal coupling of the two ^{19}F atoms with different chemical shifts.

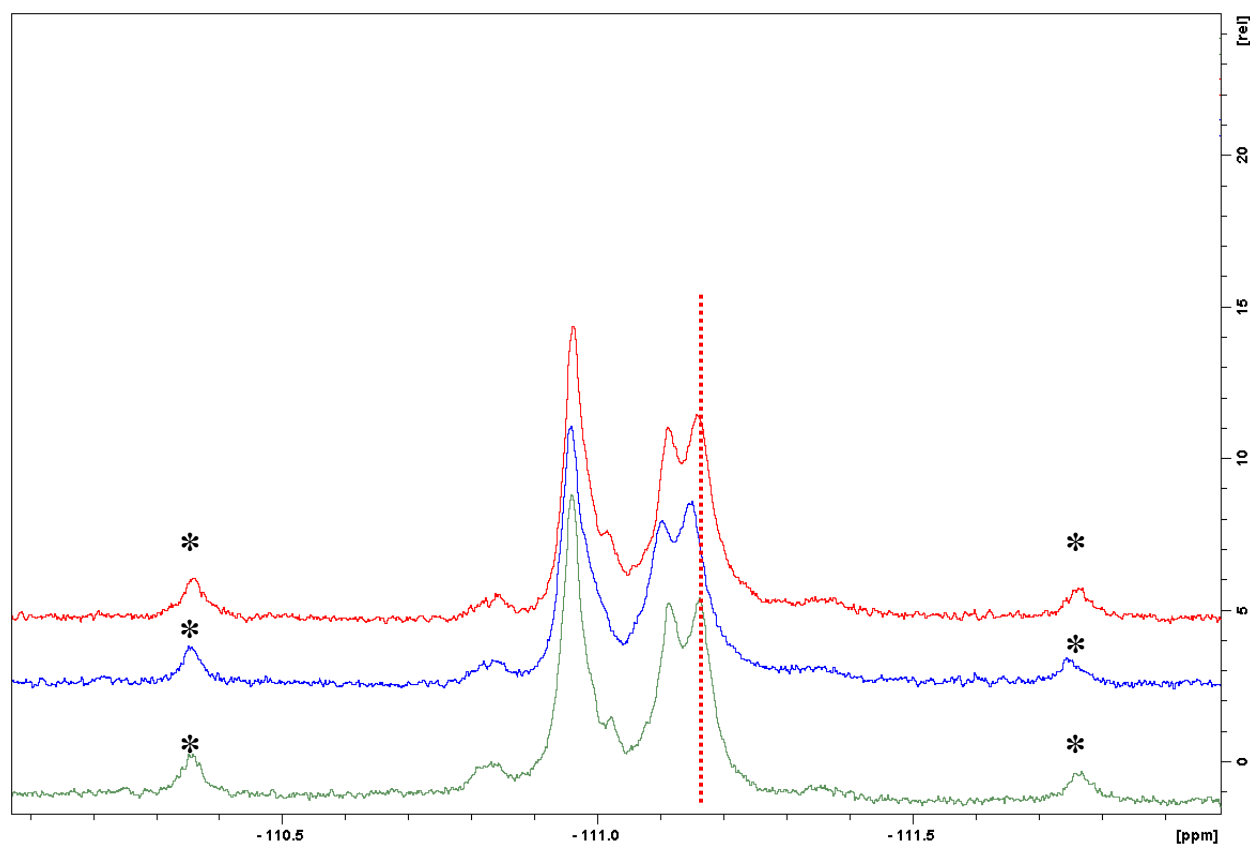


Figure 3-12. ^{19}F -NMR spectra of ledipasvir (green line), in the presence of 2 mg/mL PVPVA (blue line), and in the presence of 2 mg/mL PVA (red line). The concentration of ledipasvir is 2 mg/mL and the solvent is toluene. The peaks labeled with asterisks are results of the geminal coupling of the two ^{19}F atoms with different chemical shifts.

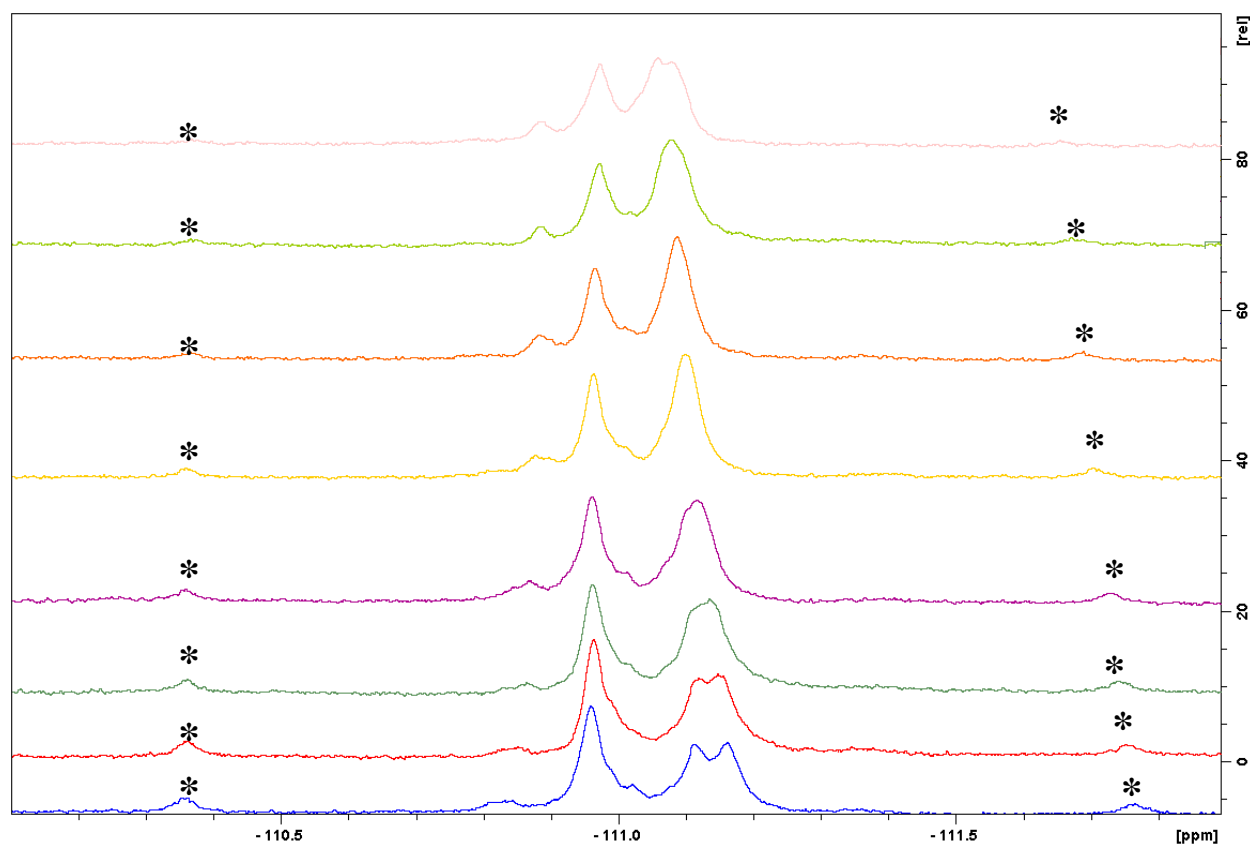


Figure 3-13. ^{19}F -NMR spectra of ledipasvir in the presence of varying amounts of 1-vinyl-2-pyrrolidinone. From bottom to top, the concentration of 1-vinyl-2-pyrrolidinone is 0, 2, 4, 8, 16, 32, 64 and 80 mg/mL respectively. The peaks labeled with asterisks are a result of the geminal coupling of the two ^{19}F atoms with different chemical shifts.

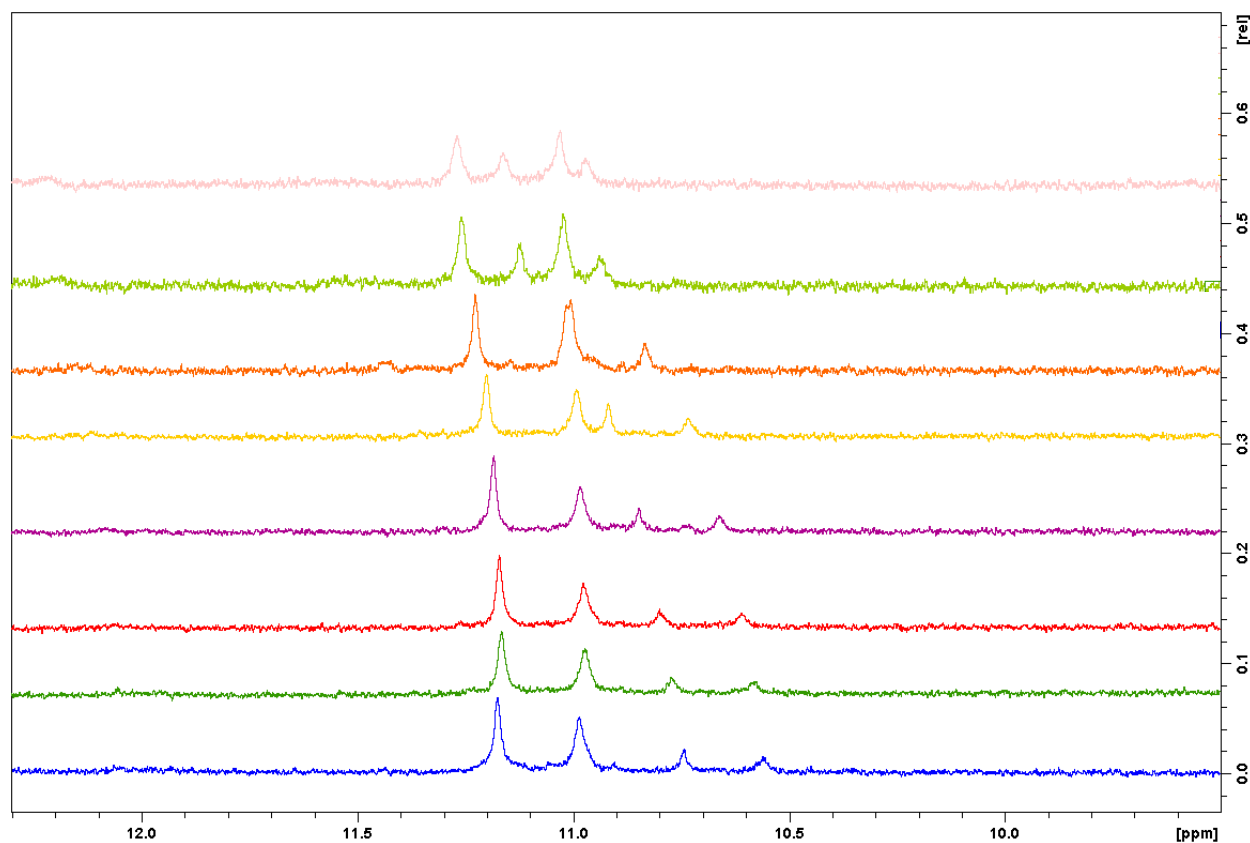
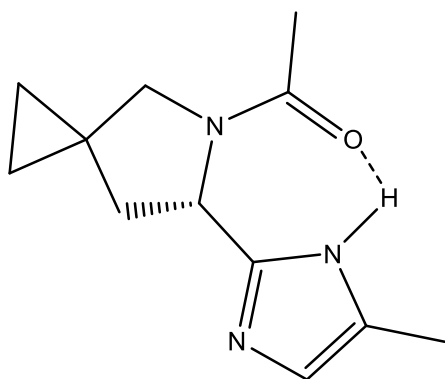


Figure 3-14. ¹H-NMR spectra of NH groups in ledipasvir in the presence of varying amounts of 1-vinyl-2-pyrrolidinone. From bottom to top, the concentration of 1-vinyl-2-pyrrolidinone is 0, 2, 4, 8, 16, 32, 64 and 80 mg/mL respectively.

(a)



(b)

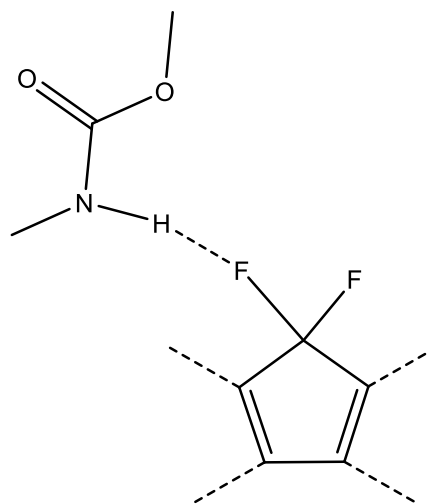


Figure 3-15. Schematic showing (a) intra-molecular hydrogen bonding and (b) inter-molecular hydrogen bonding.

3.6 Discussion

Amorphous solid dispersions have become a popular formulation strategy for orally delivering drugs with poor aqueous solubility. ASDs have many advantages including faster dissolution and improved absorption (in the absence of crystallization) with concomitant implications for *in vivo* performance.^{21, 88, 89} Recent *in vitro*⁸ and *in vivo*^{9, 63} studies show that the formation of a drug-rich colloidal phase during dissolution can be beneficial for drug absorption. This suggests that the generation and maintenance of a supersaturated solution should not be the only desired goal when assessing the dissolution of ASDs. The optimal release profile may be one where the drug concentration exceeds the amorphous solubility with the formation of drug-rich colloidal species, which can serve as an effective reservoir during drug absorption. This can be achieved when the dissolution of the ASD is polymer-controlled, since hydrophilic polymers used for ASD formulations have much higher aqueous solubility compared to the drug. Notably, when dissolution changes from polymer-controlled to drug-controlled, not only is there an absence of colloidal species, but also a drastically decreased drug release rate.^{10, 11}

In the current study, the model compound ledipasvir has a very low amorphous solubility ($\ll 1 \mu\text{g/mL}$) and no crystalline forms have been reported. Given the very low amorphous solubility, simply using the amorphous form of the drug is not sufficient to yield a reasonable dissolution rate, with no detectable drug released after 2 hours (Figure 3-2a). This highlights the essential role played by the polymer in the ASD formulation in promoting drug release from the formulation. The release profiles of the binary systems with low DLs ($\leq 5\%$) clearly demonstrate the role of the polymer in determining the drug release rate, whereby the relative release rates of PVPVA and ledipasvir are the same, and similar to the dissolution rate of pure PVPVA (Figure 3-2). This behavior is defined as congruent release (i.e. both components release at the same rate), and the critical DL where congruent release is retained has been defined as the limit of congruency (LoC).¹⁰ Given the need to produce dosage forms of a reasonable size, it is beneficial to obtain a high LoC for an ASD formulation.

However, for ledipasvir ASDs the LoC is very low. For these systems, increasing the DL by a small increment from 5 to 7.5% resulted in a change in the release mechanism whereby release became incongruent with no detectable drug release and only minimal PVPVA release. The XPS chemical composition analysis of the compact surface revealed that the surface was enriched with ledipasvir (Figure 3-7). This drug-rich layer led to drug-controlled dissolution, which, in the case

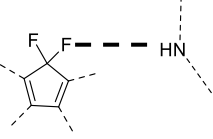
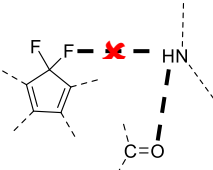
of pure amorphous ledipasvir, is so slow as to be undetectable. From micro-CT images, it appears that this drug-rich layer acts as a physical barrier to prevent further release of components, including the highly water-soluble PVPVA, leading to swelling (Figure 3-5d). Fluorescence microscope images of ASD films also lend support to the contention that water induces ledipasvir to phase separate from the polymer, leading to drug-rich regions (Figure 3-6). It has been reported that ASDs can undergo amorphous-amorphous phase separation upon exposure to high relative humidity.⁴⁵ When the thermodynamics are favorable, phase separation can occur immediately after contact with water.¹⁰³ However, the phase separation tendency and kinetics vary as a function of DL. Purohit *et al.* observed that ritonavir-PVP ASD at a 50% DL phase separated immediately after the sample was immersed into the dissolution medium, whereas at 10% DL there was no evidence of phase separation.¹⁰⁴ In the current study, 10% and 50% DL ASD films showed more discernable phase separation compared to the 5% DL ASD (Figure 3-5). Thus, at low DL, the rate of dissolution may be much faster than the rate of phase separation, resulting in congruent release, or phase separation may not be thermodynamically favorable. In contrast, faster amorphous-amorphous phase separation kinetics at higher DLs can result in the formation of a drug-rich barrier at the dissolution front. Following phase separation, polymer-rich domains at the tablet boundary layer can dissolve while drug molecules are left behind forming a drug-rich layer. Once the tablet surface is covered with a drug-rich phase, polymer in the interior of the compact cannot release. This scenario provides a reasonable explanation for why the dissolution of ASDs with 7.5 and 10% DLs resulted in no drug and only a small amount of PVPVA release (Figure 3-2).

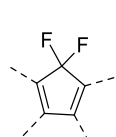
The drug-rich layer on the tablet surface appears to evolve rapidly given that the polymer release rate is retarded within the first 10 min of dissolution for higher DL ASDs. For example, the 20% DL ASD showed only 2% polymer released after 10 minutes (Figure A.7). XPS results revealed that the drug composition on tablet surface increased from 20% to 54% in this 10 min period (Figure 3-7).

Ledipasvir is a hydrophobic drug with Log P of 3.8.¹¹⁰ Hydrophobic drug molecules have limited affinity for water, and therefore, when large amounts of water interact with the ASD as during the dissolution process, will tend to self-associate, leading to phase separation. Water-induced phase separation has been reported for numerous hydrophobic compounds.^{11, 45, 103} The tendency of a given system to undergo water-induced phase separation is thought to depend on the balance of interactions between the three components, namely drug, polymer and water.^{14, 45} It is

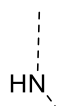
therefore of interest to consider the interactions present in amorphous ledipasvir, and ledipasvir-PVPVA ASDs in the context of the observed release profiles as a function of DL. Ledipasvir appears to form cohesive intermolecular hydrogen bonding interactions between the secondary amine groups and fluorine; fluorine is known to participate in hydrogen bonding interactions as an acceptor.¹¹¹ The ¹⁹F NMR spectra at different ledipasvir concentrations lend the support to this conjecture, where the chemical shift difference between two fluorine increased at higher concentrations (Figure 3-11), consistent with the formation of intermolecular drug-drug interactions. By adding VP, this chemical shift difference decreased, suggesting VP can break this drug-drug interaction. The functional group in VP responsible for this effect is the carbonyl group (C=O). The carbonyl group can form hydrogen bonds with the amine groups in ledipasvir, disrupting intermolecular hydrogen bonding between ledipasvir molecules. Evidence for interactions between VP carbonyl groups and ledipasvir amine groups is provided by proton NMR spectra (Figure 3-14) where it can be noted that two of the NH protons become more deshielded with increasing amounts of the VP monomer, indicating hydrogen bond formation between these two functional groups. This is also consistent with the F1s XPS analysis (Figure 3-8) which indicates that a portion of the fluorine atoms in ledipasvir exist in a more electron-rich environment, when dispersed in PVPVA; this effect is not seen in neat amorphous ledipasvir. In pure ledipasvir, F is the hydrogen bond acceptor, where it shares electrons with a proton in the amine group. When this drug-drug hydrogen bonding is disrupted by the carbonyl group in VP, fluorine gains electrons, explaining the observed shift in binding energy. XPS data therefore provides evidence of drug-PVPVA interaction. Evidence that supports drug-drug hydrogen bonding and VP-drug hydrogen bonding is summarized in Table 3-2.

Table 3-2. Summary of evidence for drug-drug hydrogen bonding and VP-drug hydrogen bonding.

| | ^1H NMR | ^{19}F NMR chemical shift difference between two F | XPS |
|---|---|---|--|
|  | Shifts downfield when ledipasvir concentration increases; shifts upfield when temperature increases | Increases when ledipasvir concentration increases | F 1s shows a higher binding energy |
|  | Shifts downfield when VP concentration increase | Decreases when VP concentration increases | F 1s shows an additional lower binding energy peak |



represents partial structure of ledipasvir,



represents amide group in ledipasvir,



represents VP carbonyl.

From the XPS data, the total number of F atoms at the lower binding energy was calculated from the relative percentage at each DL, and is plotted in Figure 3-16. The number reached a plateau for DLs exceeding 10%. In NMR experiments, different drug:monomer ratios were achieved by addition of varying amounts of VP. This ratio was converted to an equivalent drug weight percentage (an example calculation is shown in the SI). The chemical shift difference between two F atoms was an indicator of the extent of polymer disruption of the drug-drug hydrogen bonding. When the chemical shift difference is plotted as a function of DL (Figure 3-16), it shows that the polymer effectively disrupts drug-drug interaction only when the DL is below 7%. Both NMR and XPS results suggest that interactions between ledipasvir and PVPVA saturate at a fairly low DL (<10%), and drug-drug interactions then predominate. The low extent of drug-PVPVA interactions, combined with the greater extent of drug-drug interactions may contribute to the observed development of surface drug enrichment, which occurred for DLs $\geq 10\%$. It is of interest that the ledipasvir-PVPVA interaction saturation boundary, as determined from XPS and NMR measurements, was close to the DL limit where the release switched from polymer-

controlled to drug-controlled (Figure 3-16). While this may be coincidental, relationships between drug-polymer interactions as a function of DL, and release properties clearly deserve further investigation. Due to the structural complexity of the ledipasvir molecule, it is difficult to further study these interactions. However, it is reasonable to speculate that competition between drug-drug interaction and drug-polymer interaction, in particular in the presence of water may be a key factor influencing the dissolution performance of ASDs. Study of additional drug-PVPVA ASDs is needed to gain greater insight into these relationships.

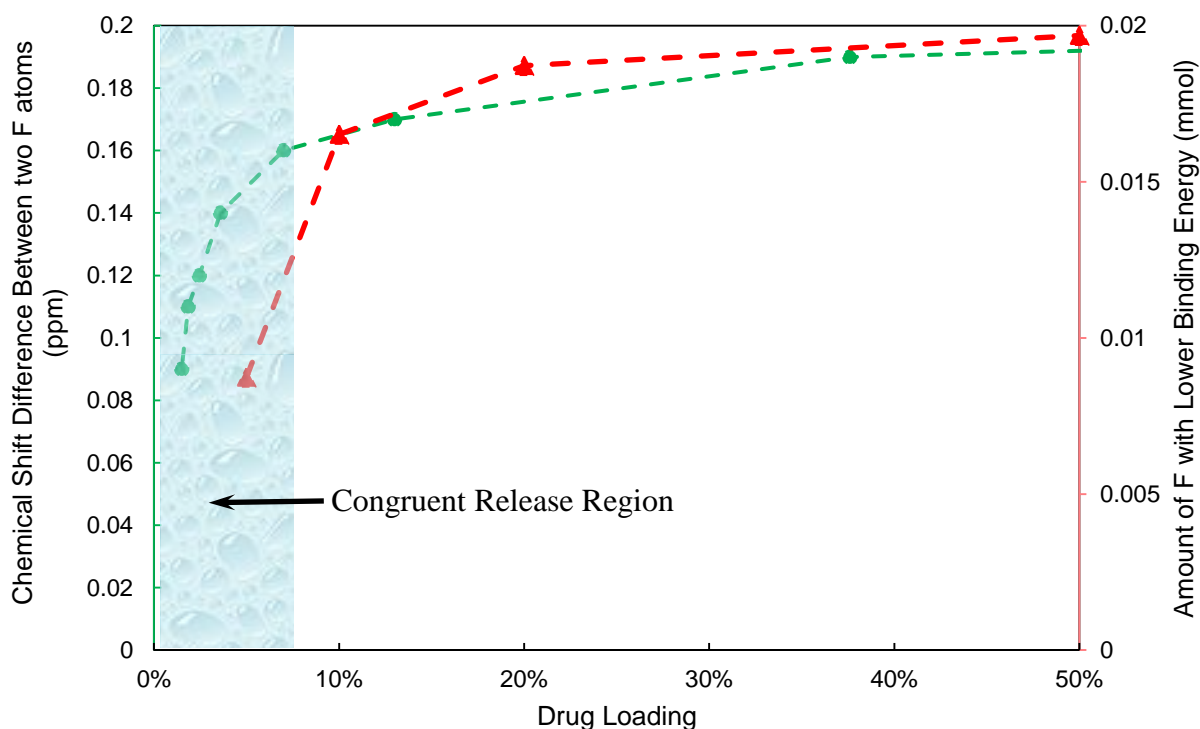


Figure 3-16. The chemical shift difference between fluorine atoms (primary y axis, ^{19}F NMR data, •) and number of fluorine atoms with a lower binding energy (secondary y axis, XPS data, ▲) as a function of DL. The shaded blue area delineates congruent release.

Interestingly, other ASDs formulated with PVPVA have shown higher LoCs than observed herein.^{10, 11} For example, the LoC of ritonavir-PVPVA ASDs was reported as 25% DL, with diminished release above this DL.^{10, 61} However, for ledipasvir-PVPVA ASDs, congruent release was only observed when the DL was 5% while DLs $\geq 7.5\%$ showed no detectable release (Figure 3-2). Ritonavir has a log P of 4.3, which is slightly higher than for ledipasvir.¹¹² Thus, LoC does not appear to depend on compound hydrophobicity or molecular weight (MW) given that ritonavir

and ledipasvir are both high log P and high MW. One interesting difference, however, is the T_g of the compounds. Ritonavir (T_g of 50 °C, wet T_g of around 0 °C) is a supercooled liquid under the conditions of the release experiments, whereas ledipasvir is a glass (T_g of 160 °C).¹¹³ Clearly further investigation is needed to elucidate how the various compound properties and drug-polymer interactions impact drug release from copovidone-based ASDs.

Surfactant is commonly added to ASD formulation to improve the dissolution performance. For example, the commercial ASD products Kaletra® by AbbVie and Kalydeco® by Vertex Pharmaceuticals contain Span® 20 and SDS, respectively. In the current study, among the five different surfactants, which varied in HLB, only poloxamer 407 and SDS were found to improve the LoC. These were the more hydrophilic surfactants. The amount of surfactant added to the ASD is such that, after complete release, the concentration released into the dissolution medium is below their critical micelle concentrations (CMC) according to the reported CMC values in buffer.^{114, 115} Thus, the solubilization effect by the surfactant in bulk solution is negligible. In addition, the drug and polymer in ASDs containing SDS had similar release rates as pure PVPVA, suggesting SDS did not increase the LoC by impacting the polymer release rate. The 7.5% DL ASDs with poloxamer 407 showed slower dissolution than pure PVPVA even though the ledipasvir and PVPVA were released congruently (Figure 3-3a). Interestingly, similar behavior was seen for 30% DL ASDs containing SDS (Figure 3-3c). If the release behavior of ASDs depends on the interplay between the kinetics of release versus amorphous-amorphous phase separation, then it is possible that SDS and poloxamer 407 reduced the rate or tendency of the systems to undergo phase separation, with SDS being much more effective than poloxamer 407. By adding only an additional 5 wt. % SDS, the congruency boundary is increased from ~5% to ~30% DL (Figure 3-3c). The mechanism for this impact of SDS certainly needs more investigation. In addition to their impact on the LoC, drug-rich colloids formed upon drug release had a greater specific surface area in the presence of a surfactant, due to their smaller size (Figure 3-15). This can potentially lead to improved oral absorption, due to a faster drug replenishment rate by this nanodroplet reservoir.¹¹⁶ This is definitely another factor that needs to be considered when designing and differentiating various ASD formulations, especially when their release profiles *in vitro* are comparable.

3.7 Conclusions

When drug release is controlled by polymer dissolution, ASDs are able to form drug-rich colloidal species in solution. However, this phenomenon is highly dependent on the DL. For ledipasvir-PVPVA ASDs, drug-rich colloids can only be attained for very low DLs, 5% DL or less. For these systems drug and polymer releases congruently, at the same rate as neat polymer. Higher DL ASDs show drug enrichment at the tablet surface, upon exposure to dissolution medium, which subsequently acts as a barrier to both drug and polymer release. It appears that the release performance may depend on the relative kinetics between dissolution and amorphous-amorphous phase separation. Drug-polymer interactions at different DLs may play a role in influencing the release behavior. Incorporating certain surfactants enables higher LoCs to be achieved. By incorporating surfactant in the ASDs, the LoCs are increased from 5% to 7.5% and 30% with the addition of poloxamer 407 and SDS, respectively. This study highlights that factors dictating the release rate of drugs from amorphous solid dispersions are not currently well understood.

CHAPTER 4. EVIDENCE FOR HALOGEN BONDING IN SOLUBILITY-ENHANCING DRUG-POLYMER DELIVERY SYSTEMS

4.1 Abstract

Carbon-bound halogen atoms (iodine, bromine, chlorine and occasionally fluorine) are known to act as electron acceptors and form interactions with different species capable of acting as an electron donor. This interaction is termed as halogen bonding, and has been suggested to share some similarities with hydrogen bonding. While hydrogen bonding has been highly studied as an important intermolecular interaction occurring between drugs and additives in pharmaceutical dosage forms, halogen bonding has not been investigated in this context. However, about 20-25% of all drug molecules contain at least one fluorine atom, 14.5% contain chlorine, 1.5% contain bromine and 1.2% contain iodine. Using X-ray photoelectron spectroscopy (XPS), nuclear magnetic resonance (NMR) spectroscopy, and infrared (IR) spectroscopy, this study investigated and demonstrated that the halogen-bearing drugs lacking hydrogen bond donors appear to form a halogen bonding interaction with the carbonyl group of a polymer, when prepared as an amorphous blend. Halogen bonding thus may be a common, but neglected intermolecular interaction in drug-polymer amorphous blends, and potentially important for the properties and performance of these drug delivery systems which are used to enhance drug solubility. This is the first time that the occurrence of halogen bonding has been observed in drug-polymer formulations.

Keywords Amorphous solid dispersions, halogen bonding, X-ray photoelectron spectroscopy, nuclear magnetic resonance, infrared spectroscopy

4.2 Introduction

Drugs are rarely delivered to the body in pure form, instead, highly engineered dosage forms are necessary in order for the drug to reach its intended site of action. Of the many challenges in drug delivery, poor aqueous solubility of modern drug candidates is one of the most prevalent issues.^{1, 117} Miscible blends of a lipophilic drug with a hydrophilic polymer, termed amorphous solid dispersions (ASDs), is one of the most popular formulation strategies for oral delivery of poorly soluble drugs. It is widely recognized that using an ASD formulation can greatly improve

drug bioavailability relative to the crystalline form.^{9, 97} The intermolecular interactions between drug and polymer are considered critical to ASD formulation performance.^{13, 66, 67, 118} One of the most frequently studied intermolecular interactions in ASDs is hydrogen bonding. Several studies have suggested that hydrogen bonding helps delay drug crystallization in solid state,^{12, 15, 45} maintain the supersaturation generated by dissolving an ASD,¹¹⁹ and potentially can improve the dissolution performance.⁶⁷ In contrast, halogen bonding, another noncovalent interaction, has received virtually no attention for these drug formulations.

Halogen bonding (XB) is the attractive interaction between the electrophilic region of halogen (F, Cl, Br, I) substituents and Lewis bases. Even though halogen atoms have the capability to donate a lone pair of electrons, the electrophilic region on the halogen atoms, termed the σ hole, and located *trans* to its σ bond, can attract electron-rich sites, such as oxygen, nitrogen, and halogen atoms.¹⁶ Considering the fact that both halogen bond donors and acceptors are electronegative, the existence of halogen bonding is somewhat counterintuitive. According to a survey of ligand-protein interactions from Protein Data Bank, the most common element acting as electron donor in halogen bonds is the carbonyl oxygen, followed by nitrogen.^{120, 121} Although it has been only 50 years since halogen bonding was first well demonstrated by Hasselt in 1960s,¹²² this interaction has been explored and exploited in many fields including crystal engineering,^{17, 123} material science,¹²⁴ protein-ligand interactions,^{125, 126} and catalysis.^{127, 128} In general, the strength of the halogen bonding depends on the size of the σ -hole, following the trend of $I > Br > Cl > F$. However, the strength can be tuned by changing the chemical environment of the halogens, e.g. by adding electron donating or withdrawing groups in the vicinity of halogen-bonded carbons. Among the halogens, F is the least prone to be involved in halogen bonding, only forming halogen bonds when fluorine atoms are linked to strong electron-withdrawing groups.¹²⁹ Halogen bonds tend to be directional, and the ideal contact angle between σ -hole and halogen bond acceptor is close to 180° .¹³⁰ For optimized systems, the strength of the halogen bond can be comparable to a hydrogen bond.¹⁶ In a study of protein-ligand complexes, the interaction energies for halogen bond were estimated to be from -1.97 to -5.4 kcal/mol, where the stronger halogen bonds have comparable interaction energies as a typical hydrogen bond.¹³¹ For example, the interaction energy of the hydrogen bond between hydroxyl in methanol and carbonyl in acetone is about -5.3 kcal/mol.¹³² It has been shown in several crystal engineering studies that when both intermolecular interactions are available, hydrogen bonding is favored over halogen bonding, but that both interactions can

co-exist.^{17, 133} Another interesting characteristic of halogen bonding is that it tends to be less sensitive to and persists in polar environment.^{130, 134}

The most frequently used experimental technique for studying halogen bonding is X-ray crystallography, which enables measurement of the interatomic distance between halogen donor and acceptor.¹³⁵ However, this technique can only be applied to crystalline materials. Other techniques, such as solid and solution state nuclear magnetic resonance,^{134, 136} infrared spectroscopy,¹³⁷ Raman spectroscopy,¹³⁸ and X-ray photoemission spectroscopy¹²⁴ have been employed to characterize halogen bonding. Density functional theory (DFT) calculation is often used to confirm experimental observations of halogen bonding.¹³⁹

Investigations into halogen bonding are gaining traction, and the occurrence of such interactions in drug formulations is of considerable relevance given that more than 30% of the drug molecules in development contain halogens, and halogen bonds have been observed in a variety of biomolecular systems.¹²⁰ Medicinal chemists have taken advantage of halogen bonding in the design of new therapeutics.^{125, 140} However, the implications of halogen bond formation in drug formulation has been ignored. Of particular interest in this context, are interactions between halogen-bearing drugs dispersed in polymers. Polymers are widely used in drug formulations, and play a pivotal role in the formation of ASDs, a solubility enhancing platform for low aqueous solubility drugs.^{141, 142} While several types of intermolecular drug-polymer interactions have been described previously including hydrogen bonding and ionic interactions,^{12, 64, 68, 69} halogen bonds in these systems have not been reported to date.

In the current study, we chose four model compounds that contain Cl, Br or I, but lack hydrogen bond donors (shown in Figure 4-1), where clotrimazole and loratadine are marketed drugs. Brotrimazole is a derivative of clotrimazole obtained by replacing Cl with Br. Compound 3,3-bis(3,5-diiodo-4-methoxyphenyl)isobenzofuran-1(3H)-one (Me-DIBF) is a methylated derivative of a protein inhibitor.¹⁴³ The polymers investigated (Figure 4-1) were copovidone (PVPVA), which is present in many important commercial ASD formulations,¹⁴² and the somewhat simpler, but closely related polymer, povidone (PVP). To demonstrate and investigate halogen bonding between model compounds and polymers, X-ray photoemission spectroscopy was used to monitor changes in the electronic environment of relevant atoms. Solution nuclear magnetic resonance was used to measure the binding strength between donor and acceptor. Lastly,

infrared spectroscopy was used to provide confirmation of the acceptor group. For the first time, the presence of drug-polymer halogen bonding is demonstrated in amorphous formulations.

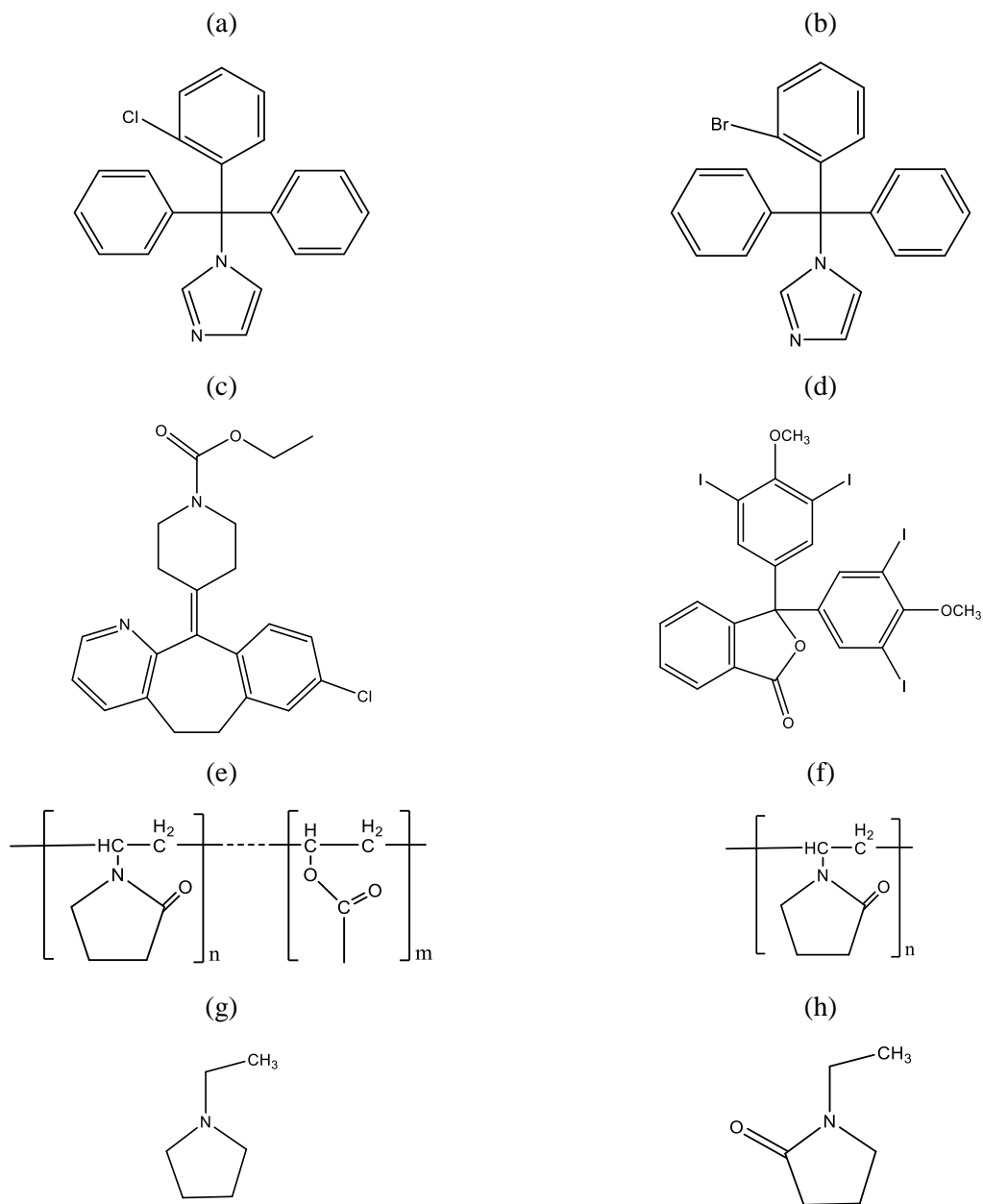


Figure 4-1. Molecular structure of (a) clotrimazole, (b) brotrimazole, (c) loratadine, (d) 3,3-bis(3,5-diiodo-4-methoxyphenyl)isobenzofuran-1(3H)-one (Me-DIBF), (e) PVPVA, (f) PVP, (g) 1-ethylpyrrolidine, and (h) 1-ethyl-2-pyrrolidone.

4.3 Experimental Section

Compound 1-((2-bromophenyl)diphenylmethyl)-1H-imidazole (Brotrimazole) and 3,3-bis(3,5-diiodo-4-methoxyphenyl)isobenzofuran-1(3H)-one (Me-DIBF) were synthesized in house. The synthesis details and final product characterization are provided in supporting information. Single crystal structure of brotrimazole was attained by X-ray crystallography. The single crystals were grown from a solution of dichloromethane and ethyl acetate using hexane vapor diffusion. Two crystals were selected for data collection and analyzed to ensure reproducibility of results. The structure determination and refinement details are shown in the supporting information.

All ASDs were prepared by solvent evaporation using a rotatory evaporator. XPS, NMR, and IR were used to characterize halogen bonding in ASDs. XPS data were obtained by a Kratos Axis Ultra DLD spectrometer using monochromic Al K α radiation (1486.6 eV). The spectra was collect at constant pass energy (PE) at 20 and 160 eV for high-resolution and survey spectra, respectively. A commercial build-in Kratos charge neutralizer was used to avoid non-homogeneous electric charge of non-conducting powder and to achieve better resolution. For NMR titration experiments, a deuterated cyclohexane or toluene stock solution with the host compound (concentration of 14.5 mM) was divided into eight NMR tubes (0.6 mL each). A variable amount of 1-ethyl-2-pyrrolidone (EP) as guest was added to each tube to provide a range of halogen bonding acceptor concentrations. The chemical shift of the host molecule was monitored and the titration curves were fit to a 1:1 binding model, which is a hyperbolic function, using OriginPro 2019 (Originlab Corporation, Northampton, MA) to determine the binding constant. Lastly, the IR spectra for all the ASDs were collected using a Bruker Vertex 70 FTIR spectrometer. More experimental details are in the supporting information.

4.4 Results

4.4.1 X-ray Photoelectron Spectroscopy (XPS)

The chemical composition of all the neat model compounds and ASDs was characterized by XPS. The binding energy of the Cl 2p electrons in clotrimazole and loratadine, the Br 3d electrons in brotrimazole, and the I 3d electrons in Me-DIBF were measured respectively. The 2p and 3d core-level spectra are characterized by a spin-orbit splitting, and therefore show two components. The ratios between the two components are 2:1 and 3:2 for p and d orbitals,

respectively. The spin-orbit splitting for Cl 2p, Br 3d, and I 3d are 1.6, 1.0 and 11.5 eV respectively. The Cl 2p spectrum of pure clotrimazole is one pair of peaks at 200.4 ± 0.1 (Cl 2p_{3/2}) and 202.0 ± 0.1 eV (Cl 2p_{1/2}) as shown in Figure 4-2a. However, when the clotrimazole molecules were dispersed into PVPVA, two new pairs of Cl peaks at 198.1 ± 0.2 (Cl 2p_{3/2}), 199.8 ± 0.2 (Cl 2p_{1/2}) and 196.7 ± 0.4 (Cl 2p_{3/2}), 198.3 ± 0.1 eV (Cl 2p_{1/2}) emerged (Figure 4-2a). Similar results were obtained for clotrimazole and PVP (Figure 4-2b). The Cl 2p peaks for loratadine showed a similar pattern, where two extra pairs of Cl 2p peaks with lower binding energy emerged in ASDs (Figure 4-2d). The Br 3d spectrum from neat brotrimazole also showed an extra pair of photoelectron peaks with lower binding energy, corresponding to a 25% atomic ratio. The probable explanation is crystal disorder (see Figure B.3). The crystal structure refinement revealed that 18% of time the imidazole switched positions with one of the phenyl rings, which resulted in Br interacting with a phenyl ring instead of imidazole. In general, the phenyl ring is a better electron donating group. Therefore, the portion of Br atoms with a lower binding energy are likely a result of Br interacting with a phenyl ring instead of imidazole. In contrast, in the ASD matrix, Br 3d peaks occurring at lower binding energies of 67.1 ± 0.1 , 68.1 ± 0.1 eV were dominant (Figure 4-2c). In Figure 4-2e, the neat Me-DIBF compound showed only one pair of I 3d photoemission peaks with binding energy of 620.7 ± 0.1 (I 3d_{5/2}), 632.2 ± 0.1 eV (I 3d_{1/2}) eV, while an extra pair of peaks at 618.1 ± 0.1 , 629.6 ± 0.1 eV, were observed in the ASDs. Binding energies for all systems are summarized in Table 4-1. For each of these model compounds, which contained different halogen atoms, the halogen atom showed additional lower binding energy peaks in the XPS spectrum when the compounds were molecularly mixed with PVPVA or PVP. A binding energy shift to a lower energy is an indication that the atom has become more electron-rich. Thus, in the ASD matrix, the halogen atoms likely received electrons from carbonyl groups present in PVPVA or PVP.

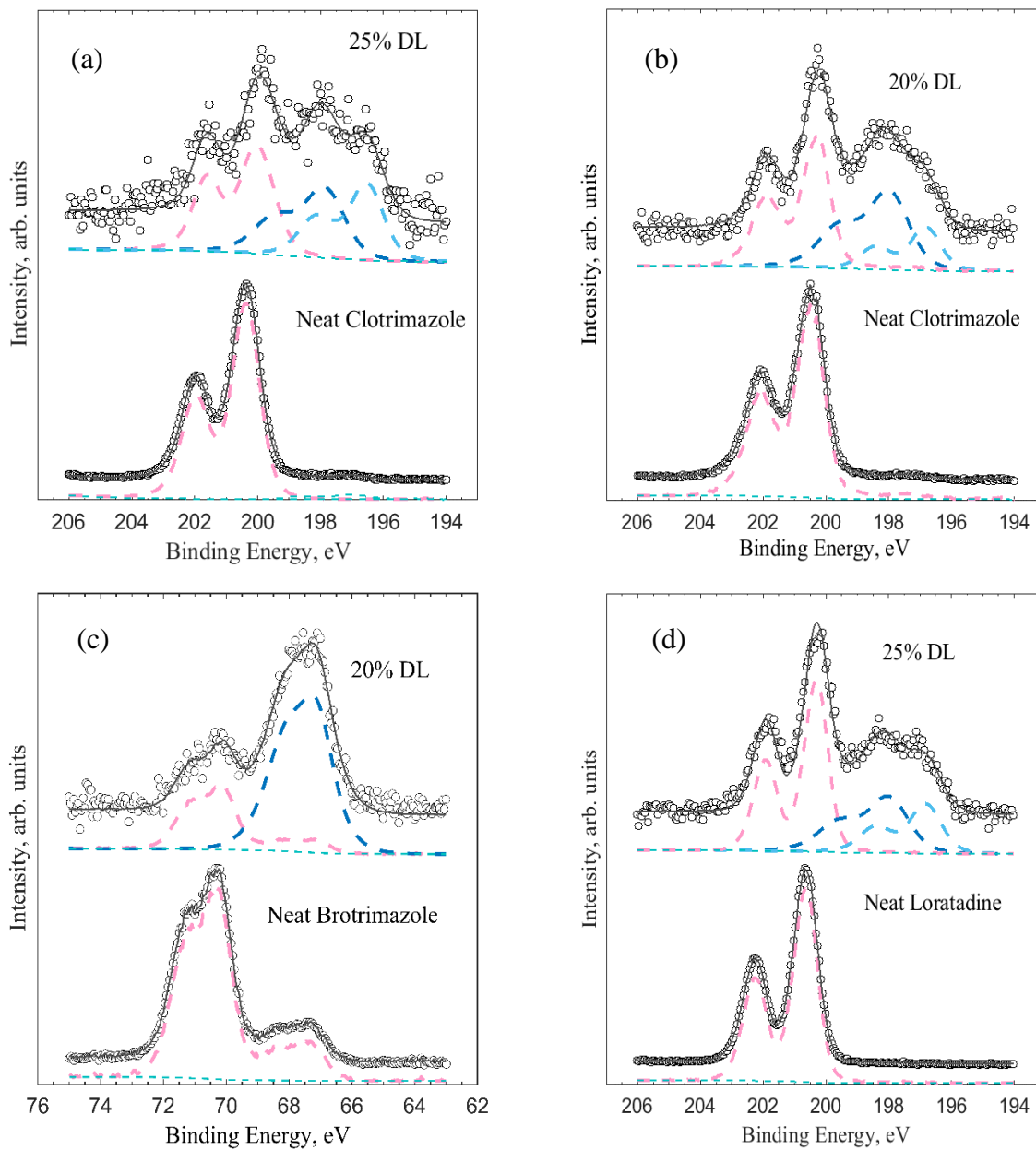


Figure 4-2. Representative halogen X-ray photoemission spectrum for (a) clotrimazole/PVPVA ASDs, (b) clotrimazole/PVP K29-32 ASDs, (c) brotramolze/PVPVA ASDs, (d) loratadine/PVPVA ASDs, and (e) Me-DIBF/PVPVA ASDs. The X-ray photoemission spectrum of neat model compound were also shown as comparison.

Figure 4-2 Continued

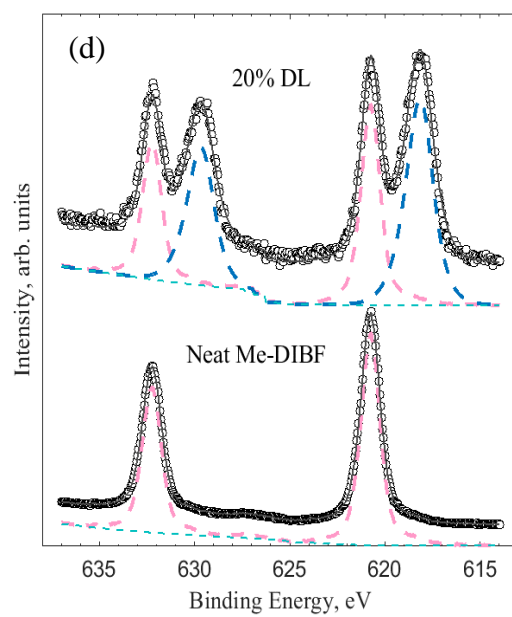


Table 4-1. Binding energy for neat materials and for peaks shifted to the lower binding energies when it is dispersed in PVPVA.

| | Neat Compound (eV) | Low Binding Energy Peaks when Dispersed in Polymer (eV) |
|---------------------------|------------------------------------|--|
| Clotrimazole (PVPVA) | 200.4 ± 0.1 , 202.0 ± 0.1 | 198.1 ± 0.2 , 199.8 ± 0.2 196.7 ± 0.4 , 198.3 ± 0.4 |
| Clotrimazole (PVP K29-32) | 200.4 ± 0.1 , 202.0 ± 0.1 | 197.9 ± 0.1 , 199.5 ± 0.1 196.8 ± 0.1 , 198.4 ± 0.1 |
| Brotrimazole | 70.3 ± 0.1 , 71.2 ± 0.1 | 67.1 ± 0.1 , 68.1 ± 0.1 |
| Loratadine | 200.6 ± 0.04 , 202.2 ± 0.1 | 198.0 ± 0.1 , 199.6 ± 0.1 196.8 ± 0.0 , 198.4 ± 0.0 |
| Me-DIBF | 620.7 ± 0.1 , 632.2 ± 0.1 | 618.1 ± 0.1 , 629.6 ± 0.1 |

By deconvoluting the XPS spectra, the percentage of halogen atoms showing low binding energy peaks was calculated for different drug loadings, with results summarized in Figure 4-3 and numerical values of the percentage of the lower binding energy peaks given in Table B.2. It is rationalized that at low drug loading, the drug molecules are further apart, and hence a majority have a higher tendency to interact with polymer. In contrast, at high drug loading, the drug molecules are in closer proximity to each other, and a majority have a greater likelihood of self-interactions. The trend among all ASDs is that the percentage of halogen atoms possessing a lower binding energy decreased as the drug load increased. This supports the idea that PVPVA is donating electrons to the halogens.

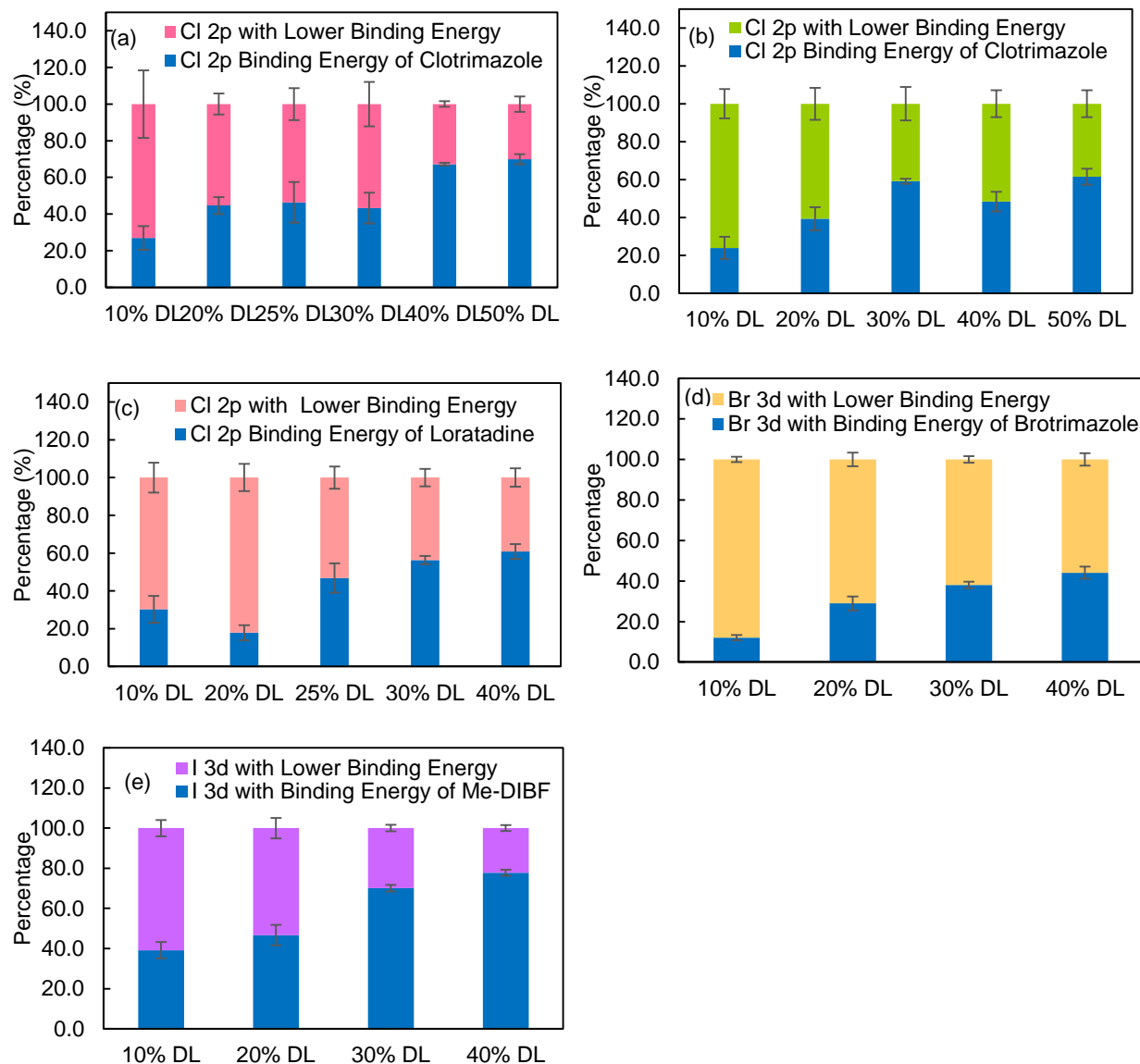


Figure 4-3. The percentage of halogen atoms with high (as found in the neat compound) and low binding energies (new peaks seen in the ASD) as a function of drug loading (DL) in the ASD for ASD system (a) clotrimazole/PVPVA, (b) clotrimazole/PVP K29-32 (c) Loratadine/PVPVA, (d) brotrimazole/PVPVA, (e) Me-DIBF/PVPVA.

4.4.2 Nuclear Magnetic Resonance Spectroscopy (NMR)

Halogen bonding interactions between components were examined, quantitatively, in solution by NMR spectroscopy by measuring the binding constant between the components. The titration experiments entailed addition of 1-ethyl-2-pyrrolidone (EP), a structural analogue of the repeat unit in the polymers, to a solution of the model compound dissolved in deuterated

cyclohexane. Cyclohexane was chosen as solvent to avoid any potential halogen bonding between π electrons and halogen atoms. For clotrimazole, the ^1H NMR spectra showed that the chemical shift of the proton at the para position relative to the chlorine atom changed as a function of EP concentration, as presented in Figure 4-6S (a). The ^{13}C NMR chemical shift for the carbon atom covalently bonded to the chlorine showed a similar change with addition of EP, as shown in Figure 4-6S (b). The change of chemical shift from the ^1H and ^{13}C spectra during EP titration is depicted in Figure 4-4. The binding constant (K_F) values for the halogen bonding interaction between clotrimazole and EP are reported in Table 4-2 for each nucleus. Similar K_F values were obtained for the halogen bonding interaction from the ^1H and ^{13}C NMR titration experiments. Analogous experiments were conducted for brotrimazole and loratadine, and the binding constants are summarized in Table 4-2. As a negative control, solution ^1H NMR of clotrimazole, brotrimazole, and loratadine in the presence of 1-ethylpyrrolidine (no carbonyl group) showed only minor proton shifts (as shown in SI). All the NMR spectra and chemical shift change titration curves are provided in the supporting information. Binding constants were also measured in deuterated toluene (Table B.3). It has been reported that π electrons can be halogen bond donors.¹⁴⁴ In toluene, the binding constants were much smaller compared to those in cyclohexane. This is consistent with, competition between π electrons in toluene and carbonyl groups in EP for the halogen groups. NMR titration experiments were not performed for Me-DIBF due to the complex potential stoichiometry between halogen bond donor and acceptor.

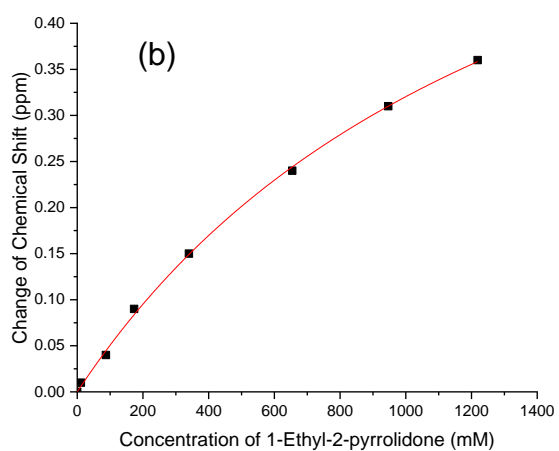
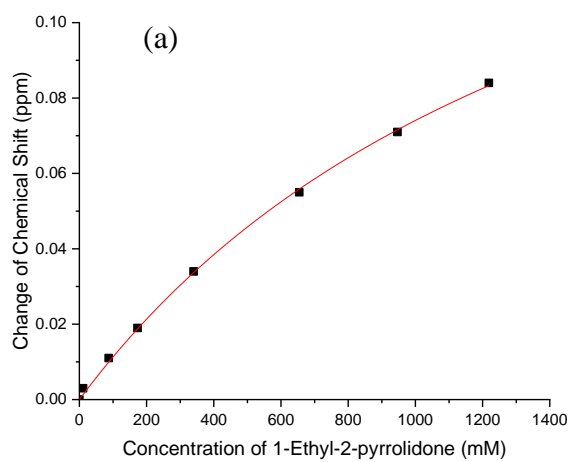


Figure 4-4. (a) ^1H NMR chemical shift change of clotrimazole as a function of the concentration of 1-ethyl-2-pyrrolidone; (b) ^{13}C NMR chemical shift change of clotrimazole as a function of the concentration of 1-ethyl-2-pyrrolidone.

Table 4-2. K_F values for halogen bonding between model compounds and 1-ethyl-2-pyrrolidone from the ^1H and ^{13}C NMR titration experiments at 25 °C in cyclohexane.

| | K_F based on ^1H NMR (M^{-1}) | K_F based on ^{13}C NMR (M^{-1}) |
|--------------|---|--|
| Clotrimazole | 0.63 ± 0.05 | 0.97 ± 0.04 |
| Loratadine | 0.65 ± 0.05 | 1.11 ± 0.07 |
| Brotrimazole | 0.56 ± 0.06 | 0.81 ± 0.04 |

4.4.3 Infrared (IR) Spectroscopy of ASDs

IR spectra of PVPVA in the carbonyl region were examined in the absence and presence of molecularly dispersed drug. For pure PVPVA, the peak for the vinylpyrrolidone (VP) carbonyl was around 1684 cm^{-1} , while the position of the vinyl acetate (VA) carbonyl was at 1736 cm^{-1} . The IR spectra for clotrimazole-PVPVA and brotrimazole/PVPVA ASD system, shown in Figure 4-5a and 4-5b respectively, illustrate that the peak maximum corresponding to the carbonyl group in VP shifted slightly to lower wavenumbers, from 1684 cm^{-1} to 1682 cm^{-1} , as the drug loading was increased from 10% to 90%, while the carbonyl group in VA did not change. This 2 cm^{-1} shift suggests that the carbonyl group in VP is responsible for the halogen bonding interaction between the model compounds and PVPVA. For Me-DIBF, a similar trend was observed with a larger downshift of 6 cm^{-1} , suggesting the halogen bonding interaction is stronger in Me-DIBF ASDs.

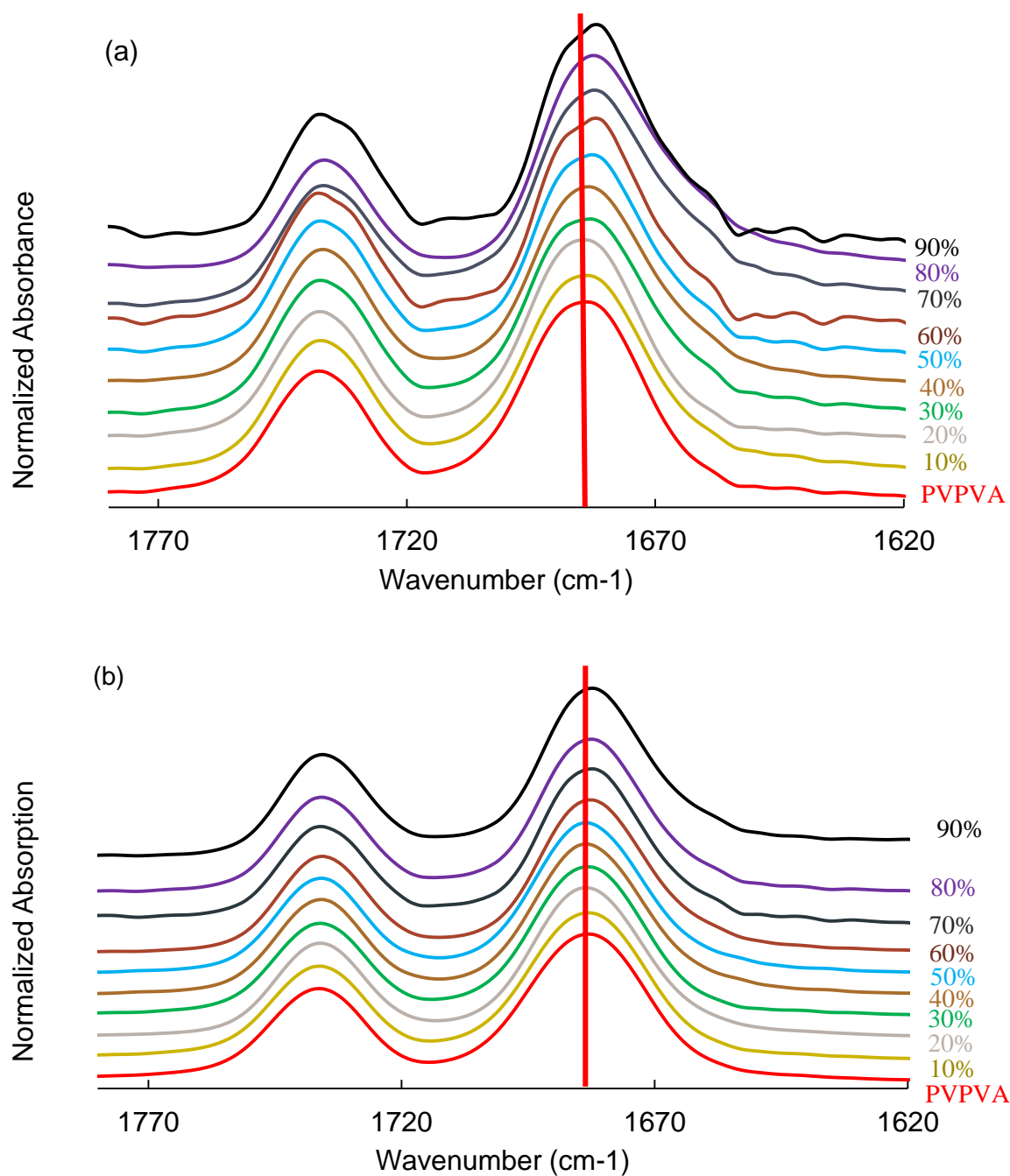
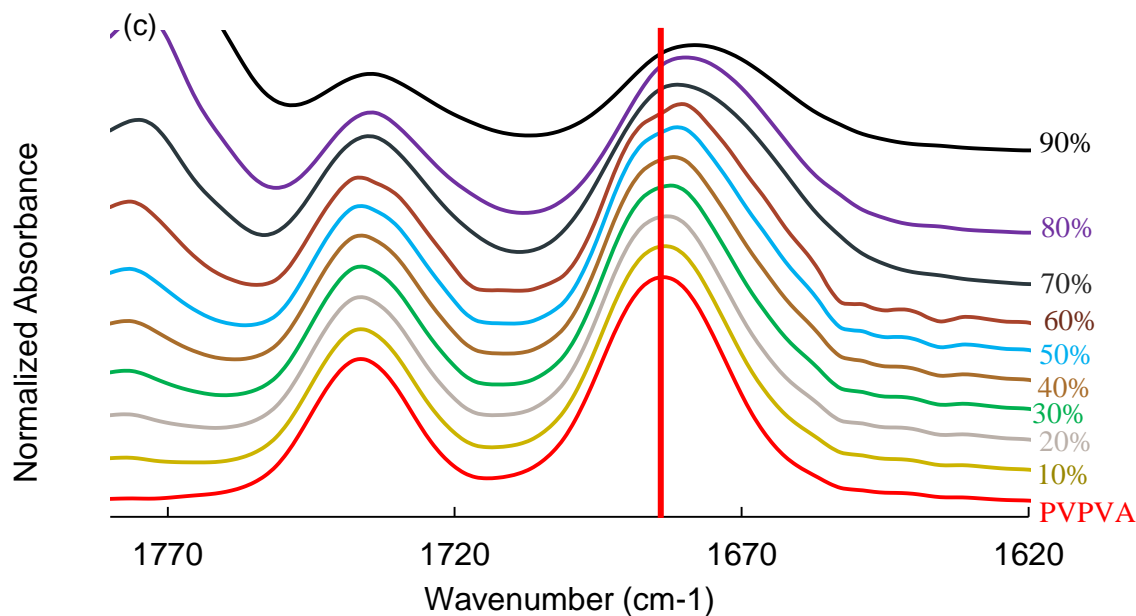


Figure 4-5.(Following page) Infrared spectra of the carbonyl group region of pure PVPVA and (a) clotrimazole-PVPVA ASDs, (b) brotrazole-PVPVA ASDs, and (c) Me-DIBF-PVPVA ASDs.

Figure 4-5 continued



4.5 Discussion

Halogen bonding is emerging as an important intermolecular interaction in various areas of science. In the area of drug research, most studies have focused on X-bonding between halogen bearing drugs and proteins, and its role in improving ligand-receptor interactions. As knowledge in this area increases and utilization of halogen groups as a means to enhance drug efficacy becomes more prominent, it becomes increasingly important to understand the relevance of this interaction for other aspects of drug research such as pharmaceutical formulation development. Molecular recognition is of particular importance to the solid state, playing a critical role in both local and long range ordering of materials. In the context of pharmaceutical systems, non-covalent interactions impact properties such as solubility, solid state form landscape, and phase transformations.

Herein, using a variety of orthogonal analytical techniques, we found compelling evidences of X-bonding between drug or drug-like molecules containing Cl, Br, or I but lacking hydrogen bond donors, and the polymer, PVPVA and PVP. XPS appears to be of particular utility for studying changes in the halogen environment, being one of the few techniques that allow a direct probe of the halogen moiety. Further, the photoelectron spectrum is sensitive to intermolecular

interactions. For example, ionic and hydrogen bond interactions are well known to lead to binding energy shifts in the photoelectron spectrum.^{145, 146} Thus, we note that the binding energies of Cl 2p, Br 3d, and I 3d peaks decreased when the model compounds were molecularly dispersed in PVPVA. The lowering of the binding energy indicates that these halogen atoms gain electron density when the polymer is present. This trend is consistent with halogen bonding, where the σ -hole on the halogen atom is known to attract electrons. Moreover, the 2-4 eV binding energy shift observed is significant and comparable to the binding energy shift produced by hydrogen bonding.¹⁴⁶ This lends support that the shift is due to a specific intermolecular interaction. Shifts to a lower binding energy, albeit to a lesser extent, have been reported for systems containing halogen bonds between I and nitrogen,^{147, 148} providing further support to our interpretation. Oxygen in carbonyl is known to be one of the most common halogen bond acceptors, in particular for protein-ligand interactions.¹²⁰ Further, it is well-known that the carbonyl group of the vinyl pyrrolidone group in PVP and PVPVA is a good hydrogen bond acceptor.⁶⁴ Therefore, it is unsurprising that this group acts as the halogen bond acceptor. The IR spectroscopy results confirm that the vinyl pyrrolidone group is preferred relative to the vinyl acetate group (Figure 4-5). Further support for the supposition that this oxygen group donates electrons to the halogen atom is provided by examination of the O1s peak of PVP in the presence and absence of clotrimazole. For all other systems, XPS spectra contain signal from multiple oxygen atoms, however, for the PVP-clotrimazole system the O1s peak arises solely from the vinylpyrrolidone carbonyl. In the dispersion, the O1s binding energy shifts to a higher value by 0.2 eV relative to neat PVP (Figure B.4), suggesting a reduction in electron density consistent with the formation of a halogen bond. The minimal change in the ¹H NMR spectrum of clotrimazole, brotrimazole and loratadine in the presence of 1-ethylpyrrolidine (which lacks a carbonyl group) relative to the large shifts seen in the presence of the carbonyl containing analogue 1-ethyl-2-pyrrolidone, further supports the role of the VP oxygen as the halogen bond acceptor. Halogen bonding with a carbonyl group has also been seen not only in protein-ligand binding,^{149, 150} but also between two small molecules.^{127, 128} In summary, based on the evidence presented herein, we propose that halogen bonding can occur between the polymer carbonyl and Cl, Br, or I in ASDs, with a greater extent of halogen bonding occurring when the drug loading is low, and thus drug-drug intermolecular interactions are less probable.

Halogen bonds share many similarities with the more commonly encountered hydrogen bonds in terms of physical properties. They are both directional interactions between an electron-deficient moiety and a high electron density region. The binding energy for hydrogen bonding is 0.2 to 40 kcal/mol, while for halogen bonding it is 1.2 to 43 kcal/mol.^{151, 152} Therefore, in theory the interaction strengths between halogen and hydrogen bonds can be comparable. The halogen bonds between the compounds studied herein and PVPVA appear to be similar to weak hydrogen bonding interactions. The binding constants between clotrimazole, brotrimazole, and loratadine with EP (Table 4-2) are between 0.6-1.1 M⁻¹, which are of a similar magnitude to the 0.7 M⁻¹ binding constant corresponding to weak hydrogen bonds, where fluorine is the hydrogen bond acceptor.¹¹¹ The IR carbonyl absorption peak only shifted 2-6 cm⁻¹ when halogen bonded to the model compounds in the ASDs. In contrast, red shifts as large as 20-30 cm⁻¹ have been observed when PVP forms hydrogen bonds with drugs in ASDs.^{45, 153, 154} In general, the strength of halogen bonds is expected to follow the trend I > Br > Cl. However, the binding strengths between Br and Cl were comparable based on the binding constant measured from the NMR titration and the wavenumber shift in the IR absorption of the carbonyl group for clotrimazole and brotrimazole. Thus, replacing Cl with Br did not significantly change the halogen bonding intensity for the drug molecules studied. This observation can perhaps be rationalized based on analysis of cohesive interactions in the crystals. In brotrimazole, there is intermolecular interaction between Br and either the phenyl group or imidazole, however, this interaction was not observed in the clotrimazole crystal. Thus, the tendency for brotrimazole to self-interact may be greater compared to clotrimazole, and this interaction can compete with the brotrimazole-PVPVA intermolecular interaction. The formation of halogen bonds with phenyl groups is further suggested by the smaller binding constants between model compounds and EP in toluene (Tablet B.3), where the π electrons of the solvent molecules can compete with carbonyl groups of EP as halogen bond donors. For Me-DIBF/PVPVA ASDs, the carbonyl moiety showed larger IR shift, suggesting stronger halogen bonding. Although an I atom is a strong halogen bond donor, few drug molecules contain I due to its toxicity.

A comparison of the extent of interaction between the various compounds and the polymer carbonyl is shown in Figure 4-6. Here, the ratio of free-to-halogen bonded VP carbonyls is compared as a function of the amount of compound added. At lower drug loading, there is an excess of carbonyl groups available for halogen bonding and the drug-polymer interaction is

undersaturated. As the drug load increases, a maximum of about 1 halogen bonded carbonyl per 8 free carbonyls is observed, with no further decreases when additional amounts of drug are present. This saturation may be due, at least in part, to steric constraints. Interestingly, the drug-polymer interaction saturates at approximately the same ratio of free carbonyls to halogen bonded carbonyls (y axis in Figure 6) for all systems with increases in drug load, which further suggests possible steric constraints. Halogen bonding extent did not increase when Cl was replaced with Br, as corroborated by NMR titration results (Table 4-2). The iodine containing compound, Me-DIBF, contains four iodine groups per molecule, and multiple halogen bonds can be formed for each molecule, likely leading to the observed rapid saturation.

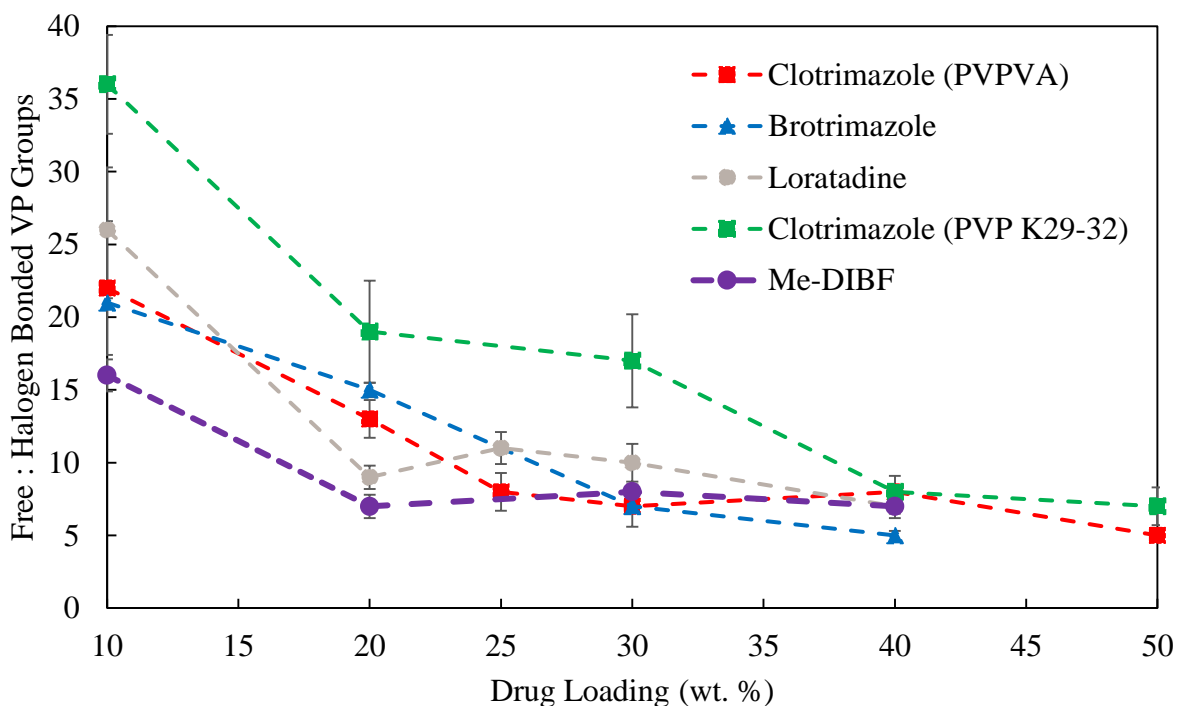


Figure 4-6. Molar ratio of free:halogen bonded vinyl-2-pyrrolidinone moieties as a function of drug loading. Dotted lines are drawn as a guide to the eye. The number of VP carbonyl groups acting as halogen bond acceptors is considered equal to the number of halogen atoms participating in halogen bonding (Fig. 3).

4.6 Conclusions

The halogen-containing molecules studied, namely clotrimazole, loratadine, brotrimazole, and Me-DIBF, were found to form halogen bonds with the carbonyl group of the vinylpyrrolidone moiety in copovidone-based amorphous dispersions. This is the first time that the occurrence of halogen bonding has been reported in drug-polymer blends. Orthogonal spectroscopic techniques, specifically IR, NMR and XPS spectroscopy, showed shifts in peaks consistent with transfer of electrons from the polymer oxygen to halogen atoms in drugs. Based on IR spectroscopic data, iodine appeared to form a stronger interaction than either Cl or Br, which appeared similar in strength. The results from this study serve to highlight the occurrence of this common, but long-neglected intermolecular interactions in drug-polymer formulations. With the increasing utilization of halogen atoms in drug discovery to tailor pharmacological performance, the potential impact of halogen bonding on formulation performance warrants further investigation and exploration.

CHAPTER 5. THE IMPACT OF DRUG-POLYMER INTERMOLECULAR INTERACTIONS ON DISSOLUTION PERFORMANCE OF AMORPHOUS SOLID DISPERSIONS

5.1 Abstract

For poorly soluble drugs formulated as amorphous solid dispersions (ASDs), fast and complete release with generation of nano size drug-rich colloidal particles is beneficial for optimizing drug absorption. However, this ideal dissolution profile can only be achieved when drug releases at the same percent rate as PVPVA, also known as congruent release, where polymer controls the dissolution process. This phenomenon only occurs under certain drug loading (DL). The maximal DL at which congruent release occurs is defined as the limit of congruency (LoC). LoC varies depending on ASD formulation, however, a greater LoC is desirable. Thus, the purpose of this study is to investigate the relationship between functional groups in four model compound and their release performance from amorphous solid dispersions. The release rates were investigated by surface area normalized dissolution. The compounds shared a common scaffold with different functional groups, which can form hydrogen bonds, halogen bonds, or hydrophobic interactions with polymer. ASDs of compounds able to form hydrogen bonds with polymer had lower LoCs, while compounds that were only able to form halogen bonds or hydrophobic interactions with polymer achieved higher LoCs. Furthermore, the compound able to form halogen bonds, but not hydrogen bonds, showed an increase in LoC when PVPVA was replaced by PVP, due to the higher number of halogen bond acceptors in PVP. While the compound interacting with polymer through hydrophobic interactions had a worse dissolution behavior with PVP than with PVPVA, possibly because PVP is more hydrophilic. The types of intermolecular interactions were also confirmed by X-ray photoelectron spectroscopy and infrared spectroscopy. The study highlights the impact of drug-polymer interactions on ASD dissolution performance, providing insights into developing formulations with higher LoCs based on the chemical structures of drug and polymer.

5.2 Introduction

Due to an increasing number of new molecular entities with poor aqueous solubility, amorphous solid dispersions (ASDs) have emerged as one of the preferred formulation strategies to improve drug absorption and bioavailability. Ideally, an ASD is a molecular level mixture of amorphous drug and polymer. ASDs typically demonstrate improved drug dissolution rates due to the amorphous form of the drug. For some drug-polymer systems, the drug release rate is controlled by the polymer. In this instance, the free drug concentration released into solution can surpass the amorphous solubility. In this context, the amorphous solubility is the maximum free drug concentration that can be achieved through the dissolution of neat, water saturated amorphous compound in the absence of crystallization.^{10, 11} When the free drug concentration surpasses the amorphous solubility, a drug-rich phase is generated in the form of initially colloidal species. There is emerging evidence that these species can further improve drug bioavailability relative to formulations which do not generate these colloidal species.^{9, 63, 116} While the underlying mechanisms of any in vivo effects are still under investigation, it has been suggested that these nano-sized drug-rich species can serve as a reservoir, maintaining the drug supersaturation at the maximal level by replenishing drug molecules removed from solution due to absorption.⁸ However, this drug-rich phase forms only when drug release is polymer-controlled, which in turn only occurs when the drug loading (DL) is below a threshold value.^{10, 11} At low DLs, drug and polymer release occurs congruently, at a rate similar to the neat polymer release rate, which can be several orders of magnitude higher than the release rate of the neat amorphous compound.¹⁰ However, at high DLs, release becomes drug-controlled, resulting in slow and incomplete drug release without the formation of nano-sized drug-rich colloidal species. The DL region where this transition in release behavior occurs can be very narrow, whereby the decline in release performance is dramatic. The DL where the change in release behavior is observed has been termed the limit of congruency (LoC). Considering that ASDs with a higher drug loading are often required for high dose drugs to reduce the overall patient pill burden, a high LoC is desirable. However, the LoC has been found to be specific for a given drug and polymer system. For copovidone ASDs, LoC values ranging from 5-25% DL have been reported, with little understanding of how drug properties contribute to this pattern of behavior.

Polymer chemistry and properties are also critical to ASD performance, with drug-polymer intermolecular interactions considered key determinants. For example, hydrogen bonding was shown to be important for drug-polymer miscibility, thus enhancing the processability of polyvinylpyrrolidone (PVP)-based hot melt extrusion formulations.⁶⁶ Hydrogen bonding can also improve the physical stability of ASDs by reducing drug crystallization kinetics in the ASD matrix.^{13, 45, 65, 67} Ionic interactions also delay drug crystallization in the ASD matrix by reducing molecular mobility.⁶⁹ Hydrophobic interactions between drug and polymer that persist in an aqueous environment were demonstrated to be important for supersaturation maintenance following ASD dissolution.^{53, 70} In a recent study, the existence of halogen bonding between drug molecules containing halogen atoms and vinylpyrrolidone (VP) carbonyl (C=O) moieties in copovidone (PVPVA) based ASDs was observed. However, to date there has been little research conducted to study the impact of drug-polymer interactions, if any on the LoC of ASDs. Given the emerging importance of this parameter, this represents a knowledge gap for ASD formulation.

The goal of this study was to elucidate the relationship between compound-polymer intermolecular interactions and release performance from copovidone based ASDs. Copovidone was selected as the polymer of interest due to its widespread use in commercial ASD formulations.^{100, 155} Four compounds sharing a common scaffold, but with different functional groups were studied. Key functionalities expected to participate in specific interactions were iodine and phenolic hydroxyl groups. As shown in Figure 5-1(a-c), one compound contains both hydroxyls and iodine atoms, one contains only hydroxyls, and the third compound contains iodine only. The OH groups can participate in hydrogen bonds with the copovidone carbonyl groups, while the I atom can potentially form a halogen bond with the same polymer acceptor groups. Carbonyl groups are known to be good hydrogen bond and halogen bond acceptors.^{64, 126} Finally, compound d lacks either a hydrogen bond donor or a halogen bond donor, and can interact with the polymer primarily dispersive interactions. PVPVA-based ASDs with these four model compounds were prepared at different DLs, and their release performance was studied using surface normalized dissolution. Intermolecular interactions in the solid state were characterized by infrared (IR) spectroscopy and X-ray photoelectron spectroscopy (XPS). Drug-rich colloidal species, formed in solution during release tests, were studied by dynamic light scattering (DLS) and nano-tracking analysis (NTA). For some ASDs, PVPVA was substituted with povidone (PVP), a more hydrophilic polymer with more vinyl pyrrolidone (VP) carbonyl moieties available.

5.3 Materials

3',3'',5',5''-Tetraiodophenolphthalein (TIPP), phenolphthalein (PHPH), iodomethane, trifluoroacetic acid (TFA) and potassium carbonate were all purchased from Sigma-Aldrich (St. Louis, MO, USA). Structures of TIPP and PHPH are shown in Figure 5-1a and 1b respectively. Compound 3,3-bis(3,5-diiodo-4-methoxyphenyl)isobenzofuran-1(3H)-one (Me-TIPP) (Figure 5-1c) and 3,3-bis(4-methoxyphenyl)isobenzofuran-1(3H)-one (Me-PHPH) (Figure 5-1d) were synthesized in house, and their synthesis details and final product characterization are provided in the supporting information. Copovidone (PVPVA 64) and povidone K29-32 (PVP), Figure 5-1, were obtained from Ashland Inc. (Covington, KY, USA). Ethanol 200 proof anhydrous, acetonitrile (CH₃CN), methanol (MeOH), dimethyl sulfoxide (DMSO), tetrahydrofuran (THF), sodium phosphate monobasic monohydrate, and sodium phosphate dibasic anhydrous were all purchased from Fisher Scientific (Hampton, NH, USA).

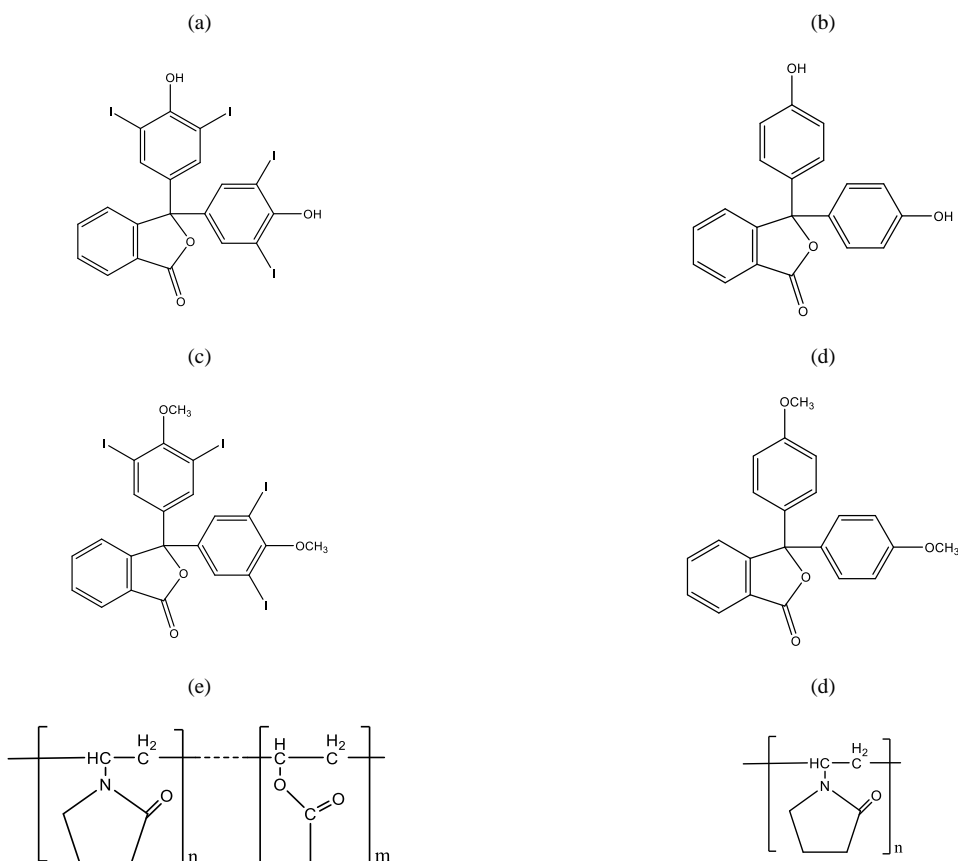


Figure 5-1. Chemical structures of (a) 3',3'',5',5''-Tetraiodophenolphthalein (TIPP), (b) Phenolphthalein (PHPH), (c) 3,3-bis(3,5-diiodo-4-methoxyphenyl)isobenzofuran-1(3H)-one (Me-TIPP), (d) 3,3-bis(4-methoxyphenyl)isobenzofuran-1(3H)-one (Me-PHPH), (e) PVPVA with VP/VA mass ratio of 60/40, and (f) PVP.

5.4 Methods

5.4.1 Determination of Amorphous Solubility

Triplicate measurements were performed at 37 °C using the solvent shift technique to determine the amorphous solubility.^{3, 24} Briefly, a stock solution was injected at a continuous rate into a buffer solution while monitoring the sample for loss of transmitted light due to scattering at a non-absorbing wavelength of 360 nm using a UV-Vis spectrophotometer with an in-situ probe. The UV-Vis spectrophotometer was a SI Photonics (Tuscon, Arizona) CCD Array with a 10 mm path length in-situ probe. Stock solutions of PHPH (20 mg/mL) and MePPH (0.3 mg/ml) were prepared with ethanol, while stock solutions of TIPP (1.5 µg/ml) and MeTIPP (1.5 µg/mL) were prepared with THF or acetone, respectively. The amorphous solubility was measured in 50 mM pH 6.8 phosphate buffer containing 1 mg/ml PVPVA for all compounds except TIPP. TIPP amorphous solubility was measured in 50 mM pH 2.5 phosphate buffer containing 1 mg/ml PVPVA. Solution pH values were selected to ensure that all compounds would be unionized form during the experiments. The measurements were performed using a Pump 11 Elite syringe pump (Harvard Apparatus, Holliston, MA) with a 2.5 ml Hamilton Gastight 1000 Series glass syringe (Hamilton Company, Reno, NV), where the stock solutions were injected at a continuous rate into a 20 ml vial containing 15 ml of the appropriate buffer under constant stirring with stirring rate of 300 rpm.

TIPP and Me-TIPP showed a non-zero relationship between loss of transmitted light and compound concentration from the very beginning of the measurement, indicating that the amorphous solubility was very low and could not be determined precisely with the UV probe due to the immediate formation of scattering species. This result was confirmed with the NanoSight LM10, a nano tracking analysis (NTA) instrument from Malvern Instruments (Worcestershire, United Kingdom). The NTA instrument was equipped with a green laser (75 mW, 532 nm) as the light source and a 20x magnification microscope objective. In this experiment, the two compounds were each dissolved in acetone to prepare solutions using the solvent shift methods. Aliquots of stock solution were added to 15 ml of the appropriate buffer solution at 25 °C under constant stirring. After each aliquot, the solution was analyzed for the presence or absence of nanospecies. One 30 second video was collected for each measurement with a camera sensitivity level of 13. The videos were processed using a threshold value of 5. The results showed that nano particles form at concentrations less than 0.01 µg/ml.

5.4.2 Differential Scanning Calorimetry (DSC)

The glass transition temperatures (T_g) for all the model compounds were measured by DSC using a Q2500 calorimeter with a refrigerated cooling system from TA Instruments (New Castle, DE). TIPP is a fast crystallizer, therefore the T_g was measured using a 90% TIPP 10% PVPVA ASD. The rest of the compounds were converted to their amorphous form, except for MePPHP which was already liquid at room temperature, prior to loading into standard aluminum DSC pans. The experimental procedure to attain amorphous compounds and ASDs is described in Section 3.3. Aluminum pans were sealed with lids that were punctured with a pin to allow for evaporation of any residual solvents. The samples were equilibrated to a temperature significantly below T_g (<50 °C), and then were heated to a temperature at least 30 °C above T_g and cooled to a temperature at least 30 °C below T_g for at least four cycles. The heating and cooling ramps were at 10 °C/min. All the DSC runs were conducted under nitrogen with a nitrogen flow of 50 mL/min to create a dry environment. The temperature accuracy of the Q2000 was validated by running a 10 °C/min heating ramp on a sample of indium. The last heating cycle was used for analysis and the T_g was obtained based on the midpoint.

5.4.3 Preparation of Amorphous Solid Dispersions (ASDs)

All the ASDs, amorphous Me-TIPP, and amorphous PHPH were prepared using a solvent evaporation method. THF was used as solvent for preparing TIPP and Me-TIPP ASDs, while ethanol was used for PHPH and Me-PPHP. Model compound and polymer were fully dissolved in the solvent prior to solvent evaporation. A rotatory evaporator (Brinkman Instruments, Westbury, NY) was used to rapidly remove solvent. The temperature of the water bath for solvent evaporation was 40 °C for THF and 60 °C for ethanol. The ASDs were stored in under vacuum for 24 h to remove residual organic solvent.

5.4.4 Dissolution of Amorphous Solid Dispersions

5.4.4.1 Dissolution using Rotating Disk Apparatus

All the release experiments were conducted using an intrinsic dissolution rate measurement assembly (Agilent, Santa Clara, CA) to normalize the surface area. About 100 mg ASD powder was compressed at a pressure of 1500 psi with a hydraulic press (Carver Inc., Wabash, IN) in a

circular intrinsic die with a diameter of 8 mm. The compression pressure was held for 60 s. The die was then attached to a paddle which was rotated at 100 rpm. For TIPP, studies were carried out at pH 2.5 to suppress ionization, while the other three model compounds were assessed at pH 6.8. All experiments were performed at 37 °C.

5.4.4.2 Concentration Analysis of Model Compounds and Polymer

To study the release behavior of both model compound and polymer, 3 mL dissolution medium was withdrawn at 10, 20, 30, 40, 50, 60, and 90 min post exposure of the compact to the dissolution medium. The total volume of dissolution medium was maintained at 100 mL by replenishing with 3 mL blank dissolution medium at each time point. For TIPP and Me-TIPP, 0.8 mL of withdrawn sample was diluted by addition of 0.2 mL DMSO to prevent precipitation during analysis. For PHPH and Me-PHPH, 0.5 mL of sample was diluted by 0.5 mL ethanol prior to concentration analysis. High performance liquid chromatography (HPLC) was performed using a 1260 Infinity system (Agilent, Santa Clara, CA) to analyze the model compound concentration. The HPLC methods used for the four model compounds are summarized in Table 1. The separation column was an Ascentis Express C18 (Sigma-Aldrich, St. Louis, MO) with dimensions of 10 cm x 3.0 mm with 2.7 µm particle size. The remainder of the 3 mL sample was filtered through a 0.2 µm nylon syringe filter (Pall Corporation, Port Washington, NY). The final 0.8 mL portion of the filtered sample was diluted with 0.2 mL methanol prior to polymer concentration analysis. Polymer concentration was analyzed by HPLC using a size-exclusion column A2500 aqueous GPC/SEC column 300 x 8 mm (MalvernPanalytical, Worcestershire, UK), and the HPLC method is listed in Table 5-1.

Table 5-1. Summary of HPLC methods for model compounds and polymer.

| Model Compound | Injection volume (μL) | Flow rate (mL/min) | Mobile Phase | Detection wavelength (nm) |
|------------------------|------------------------------------|--------------------|---|---------------------------|
| TIPP | 2 | 0.6 | 70% CH_3CN 30% 0.1% (v/v) TFA H_2O | 210 |
| Me-TIPP | 2 | 0.6 | 90% CH_3CN 10% H_2O | 210 |
| PHPH | 2 | 0.6 | 50% CH_3CN 50% 0.1% (v/v) TFA H_2O | 210 |
| Me-PHPH | 2 | 0.6 | 70% CH_3CN 30% H_2O | 210 |
| PVPVA or PVP K29-32 | 50 | 0.5 | 80% pH 7.4 buffer 20% MeOH | 205 |

5.4.5 Characterization of Drug-rich Phase Generated during Release Testing

5.4.5.1 Nanoparticle Tracking Analysis (NTA)

The presence of nanodroplets was confirmed using a NanoSight LM10, a nano tracking analysis (NTA) instrument from Malvern Instruments (Worcestershire, United Kingdom), equipped with a green laser (75 mW, 532 nm) light source and a 20x magnification microscope objective. Samples of 1 ml were taken after 30 min of dissolution and an image of the particles observed under the NTA was captured.

5.4.5.2 Dynamic Light Scattering (DLS)

The size of the drug-rich colloidal species generated during dissolution of the ASDs at a drug loading just below the LoC was measured using a Nano-Zetasizer (Nano-ZS) from Malvern Instrument (Westborough, MA). A 5 mL sample was withdrawn from the dissolution medium after 30 mins and size was analyzed by DLS. The backscattered light was at an angle of 173° . The cuvette used was a 12 mm square polystyrene disposable cuvette. All the experiments were performed in triplicate. The polydispersity index (PDI) was less than 0.3 for all the measurements, therefore the intensity size distribution generated were considered as a monodisperse.

5.4.6 Infrared Spectroscopy

Thin films of the neat PVPVA and the ASDs at different drug loading were prepared by spin-coating for collection of transmission IR spectra. The polymer or compound-polymer mixture was pre-dissolved in an organic solvent with solid content of 50 mg/mL. THF was used to dissolve TIPP and Me-TIPP ASD mixtures, while ethanol was used for PHPH and Me-PHPH ASD mixtures. The general procedure for spin coating was as follows: 100 μ L solution was deposited onto a thallium bromoiodide (KRS-5) window (Harrick Scientific Corporation, Ossining, NY), and the substrate was spun for 15 s at 50 rpm followed by 50 s at 2500 rpm using a spin coater (Chemat Technology Inc., Northridge, CA). The spin coating process was conducted in a humidity-controlled glove box to prevent moisture-induced phase separation during sample preparation. The IR spectra were collected in transmission mode using a Bruker Vertex 70 FTIR spectrometer (Billerica, MA). The average spectrum was based on 128 scans for each sample and a resolution of 4 cm^{-1} . The data were analyzed using OPUS software (version 7.2, Bruker, Billerica, MA).

5.4.7 X-ray Photoelectron Spectroscopy (XPS)

For TIPP/PVPVA ASDs, the chemical composition on the compact surface was examined by XPS, and compared to that of Me-TIPP, which has been reported in a previous study. The sample preparation and the experimental procedures were the same as it was described in Section 3.4.7.

5.5 Results

5.5.1 Physicochemical Properties of Four Model Compounds

Table 5-2 summarizes various physicochemical properties of the four model compounds studied. Three of the compounds have quite high T_g values, while Me-PHPH has a much lower value. The value for TIPP contains 10% polymer, and hence the pure compound value is likely to be slightly lower, given that the T_g of PVPVA is 104°C.¹⁵⁶ Using the Fox equation, the value of the neat compound is estimated to be 84°C. The hydrophobicity of the compounds varies based on the calculated log P values, where the iodo containing compounds are predicted to be more hydrophobic. This is consistent with the low amorphous solubility values observed for these

compounds. The presence of iodine atoms also leads to a considerably elevated MW, relative to the other compounds.

Table 5-2. Physicochemical properties for model compounds. Midpoint T_g and amorphous solubility are presented as mean values \pm standard deviation, where n = 3.

| | MW (g/mol) | Log P | T _g (°C) | Amorphous Solubility (μg/ml) |
|---------|------------|-------------------|-------------------------------------|------------------------------|
| TIPP | 821.91 | 6.39 ^a | 86.1 \pm 1.9 (with 10 wt.% PVPVA) | <0.01 |
| Me-TIPP | 849.97 | 7.6 ^a | 122.7 \pm 7.7 | <0.01 |
| PHPH | 318.3 | 2.63 ^a | 99.0 \pm 3.5 | 27.5 \pm 0.9 |
| Me-PHPH | 346.38 | 3.93 ^a | 25.2 \pm 0.6 | 4.40 \pm 0.04 |

^aPredicted using ACD Lab prediction tool

5.5.2 Release Profiles of ASDs

5.5.2.1 Release Profiles of TIPP, Me-TIPP, PHPH, and Me-PHPH PVPVA ASDs

The release profiles of model compound/PVPVA ASDs with drug loadings spanning the LoC (i.e. highest drug loading where polymer and drug release at the same normalized rate) are presented in Figure 5-2. The polymer alone showed 100% release after 60 minutes (data not shown). At low DLs, both compound and polymer released simultaneously, and showed a similar release rate to neat polymer. Upon increasing the DL, polymer and compound release diverged, where polymer was released faster than compound, and both components showed a slower release rate than the neat polymer whereby release was incomplete at the end of the experimental monitoring period. The highest DL where compound and polymer release simultaneously to give > 80% compound release was taken as the LoC. The LoC values were determined to be 10, 30, 5, and 40% DL for TIPP, Me-TIPP, PHPH, and Me-PHPH ASDs, respectively. For ASDs where DL was at or below the LoC, the concentration exceeded the amorphous solubility value at short dissolution times. The dissolution medium became turbid, which is a visual indication of the formation of the drug-rich phase. Me-TIPP and Me-PHPH PVPVA ASDs at a 40% DL showed 100% PVPVA release, but only 70% Me-TIPP and 80% Me-PHPH release with a visible portion of the compound remaining undissolved in the holder. In some cases, no model compound was released and even PVPVA release was drastically delayed. For example, TIPP/PVPVA ASDs at drug loading of 15% and Me-TIPP/PVPVA ASDs at drug loading of 50%, no detectable model compound release and only minimal PVPVA release was observed. For PHPH/PVPVA at 10%

drug loading and Me-PHPH/PVPVA at 50% drug loading, some extent of dissolution for both model compound and PVPVA were detected, but the rates were slower. Compared the dissolution behavior among different model compound ASDs, it appears that small modification on chemical structure results in drastic change for ASD dissolution behavior.

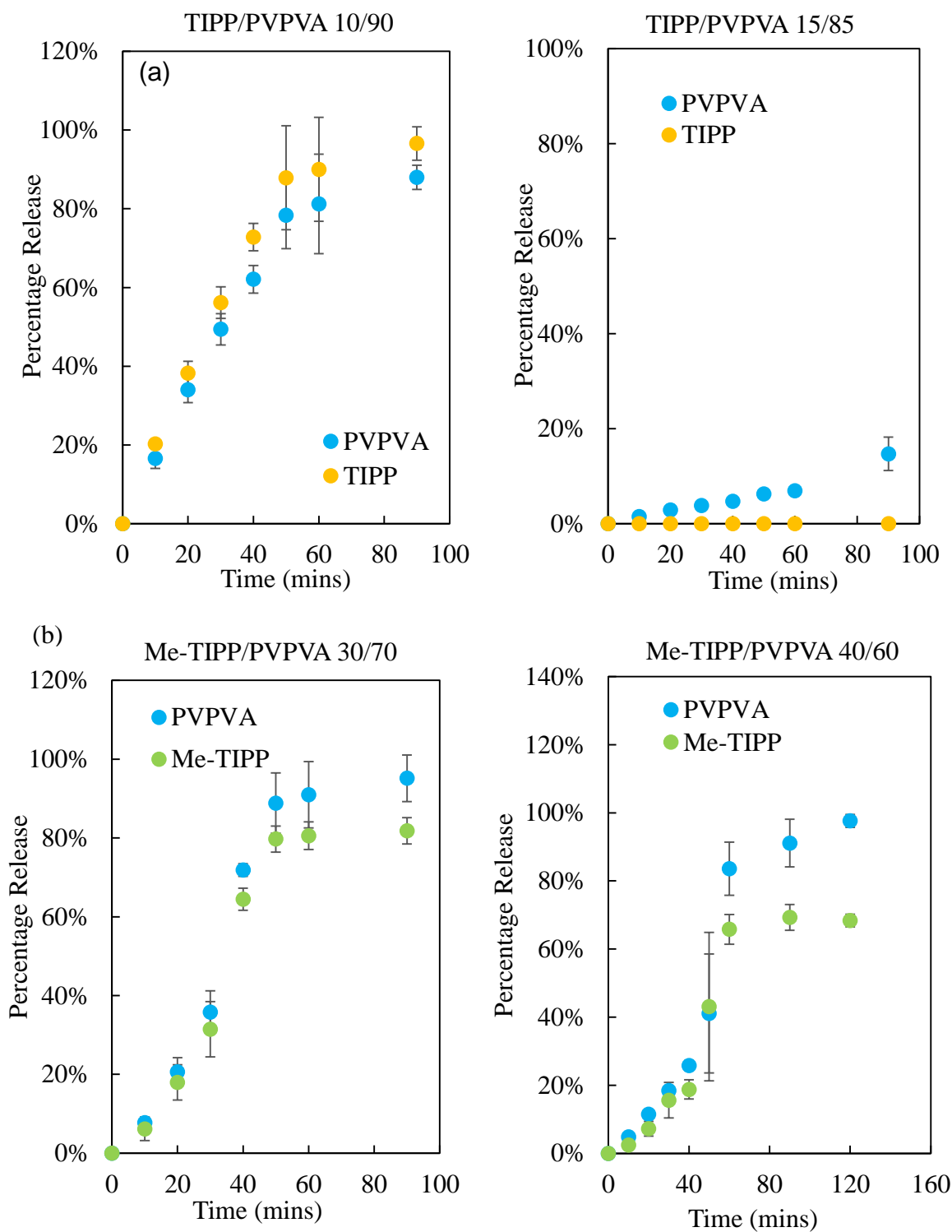


Figure 5-2. Release profiles of (a) TIPP/PVPVA ASDs with drug loading of 10 and 15%, (b) Me-TIPP/PVPVA ASDs with drug loading of 30, 40, and 50%, (c) PHPH/PVPVA ASDs with drug loading of 5 and 10%, and (d) Me-PHPH/PVPVA ASDs with drug loading of 30, 40, and 50%.

Figure 5-2 continued

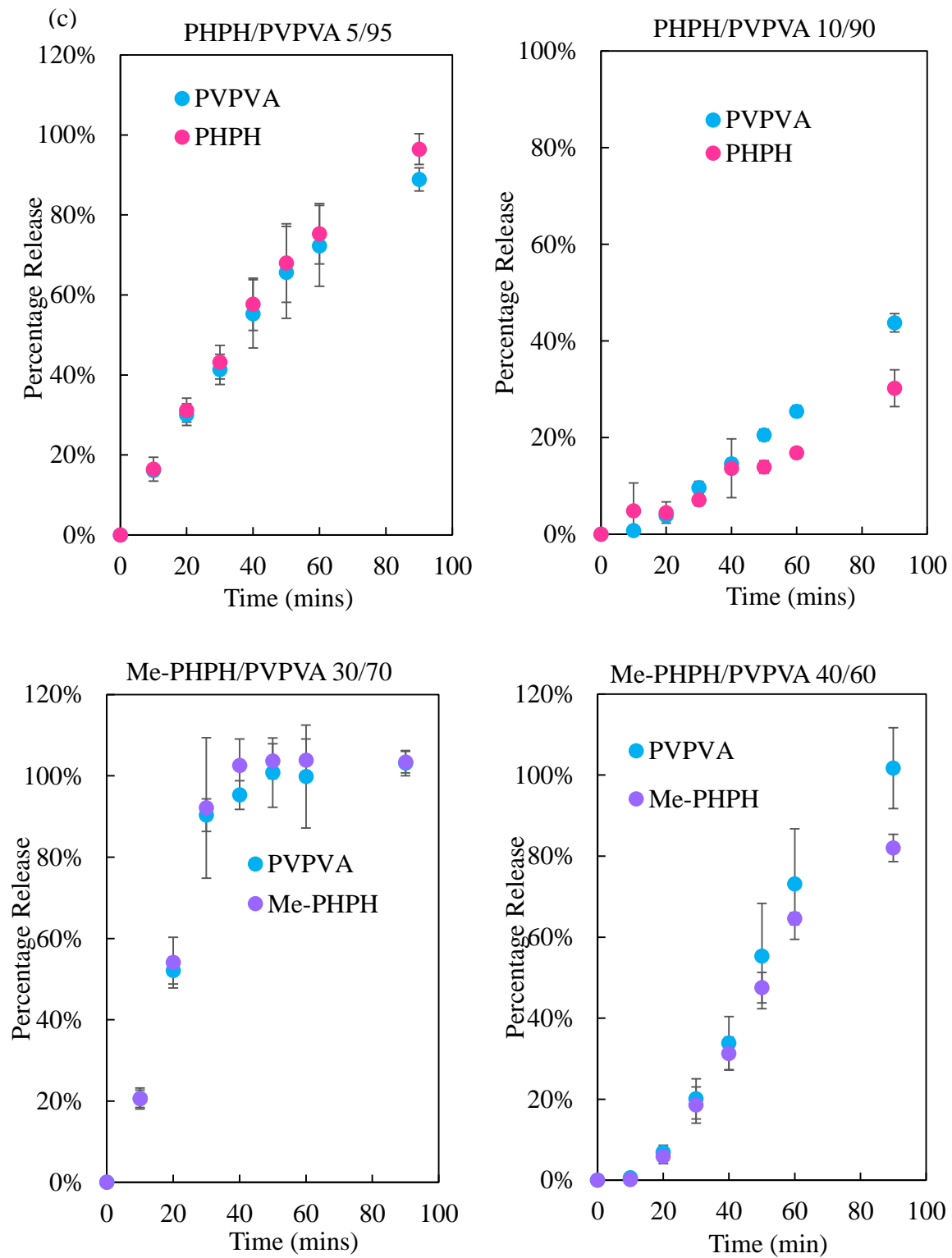
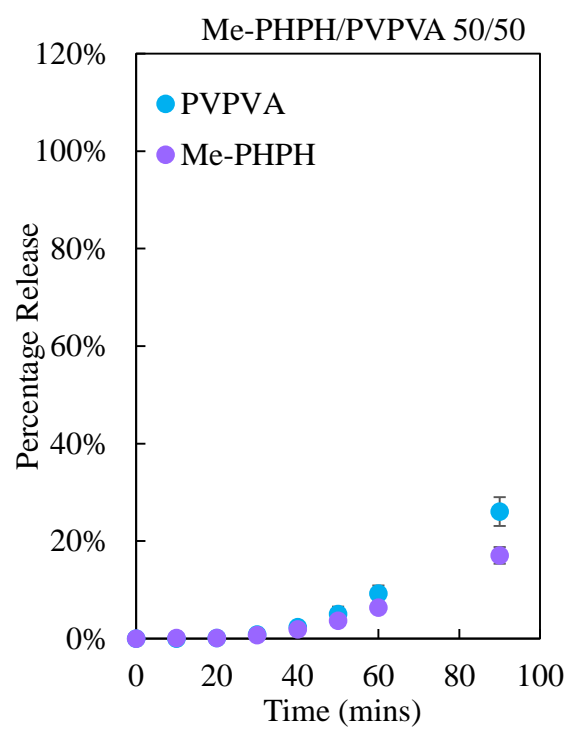


Figure 5-2 continued



5.5.2.2 Release Profiles of Me-TIPP and Me-PHPH PVP K29-32 ASDs

Release profiles from ASDs prepared with PVP K29-32 instead of PVPVA were evaluated for Me-TIPP and Me-PHPH are shown in Figure 5-3. In the case of Me-TIPP/PVP K29-32 ASDs the 40% DL formulation showed complete release of model compound and PVP in about 50 min, with a congruent release profile, while the 50% DL formulation showed a slower congruent release rate with 75% release in 90 minutes. Thus, the release of Me-TIPP was better for the PVP K29/32 ASDs than for the PVPVA ASDs for comparable DLs. In comparison, substituting PVPVA with PVP K29-32 somewhat impaired the dissolution of 40 and 50% DL Me-PHPH ASDs, where 40 and 0% of the model compound released in 90 min, respectively, for the PVP based ASDs versus 80 and 20% for the corresponding PVPVA-based ASDs.

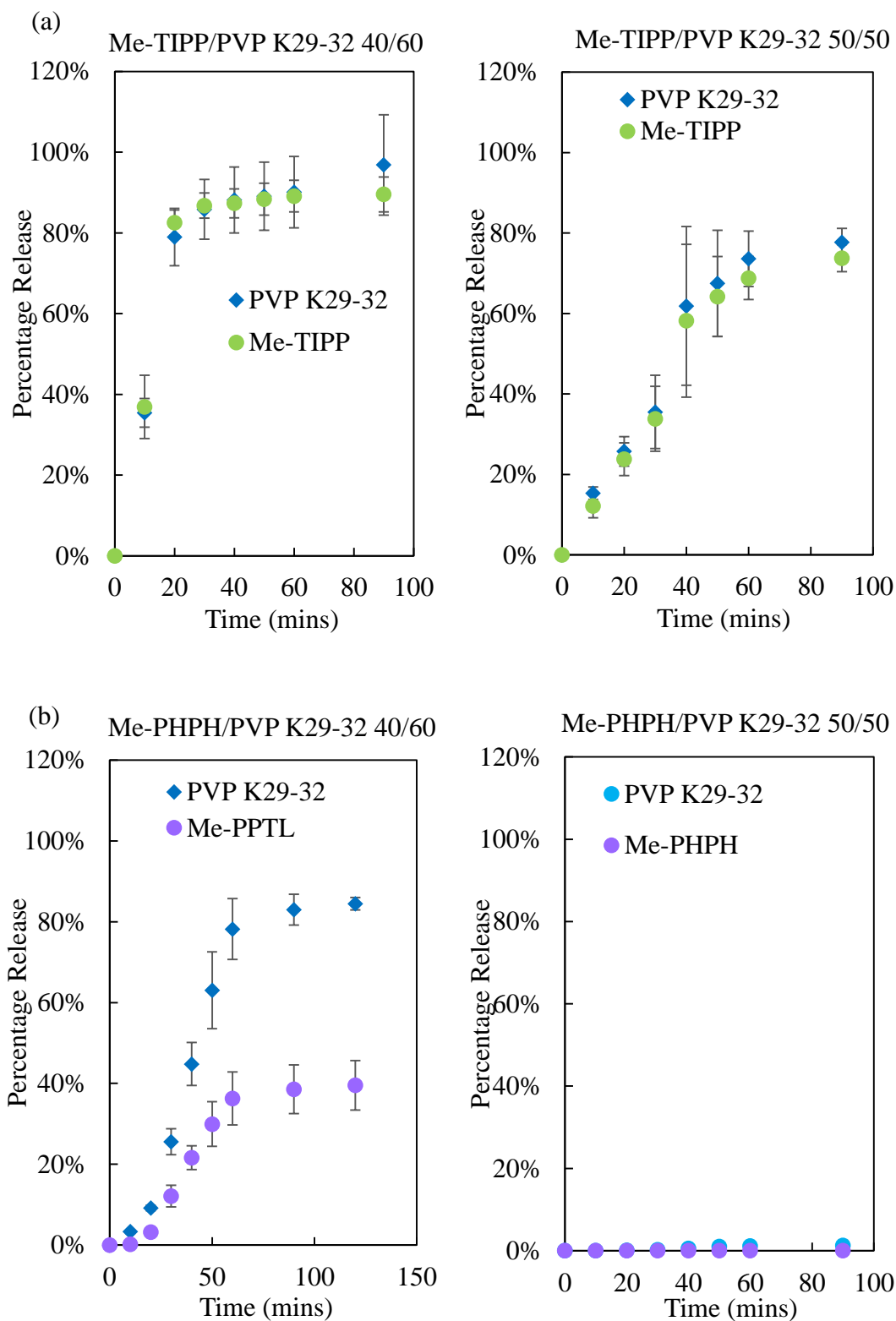


Figure 5-3. Release profiles with drug loading of 40 and 50% for (a) Me-TIPP/PVP K29-32 ASDs (b) Me-PHPH/PVP K29-32 ASDs.

5.5.3 Characterization of Drug-rich Colloidal Species Generated upon Dissolution

The dissolution medium for ASDs with a DL at or below LoC was visibly turbid during release testing, which indicates the formation of drug-rich colloidal species. These colloidal species were examined by DLS and their presence was confirmed with NTA. The particle size measurements by DLS are summarized in Table 5-3, while the representative NTA images are shown in Figure 5-4.

Table 5-3. Particle size for drug-rich colloidal species generated during ASD dissolution. Mean values \pm standard deviation are shown where n=3.

| | Size of drug-rich colloidal species (nm) |
|-------------------------|--|
| TIPP/PVPVA at 10% DL | 179 \pm 8 |
| Me-TIPP/PVPVA at 30% DL | 193 \pm 5 |
| PHPH/PVPVA at 5% DL | 348 \pm 16 |
| Me-PHPH/PVPVA at 30% DL | 364 \pm 5 |

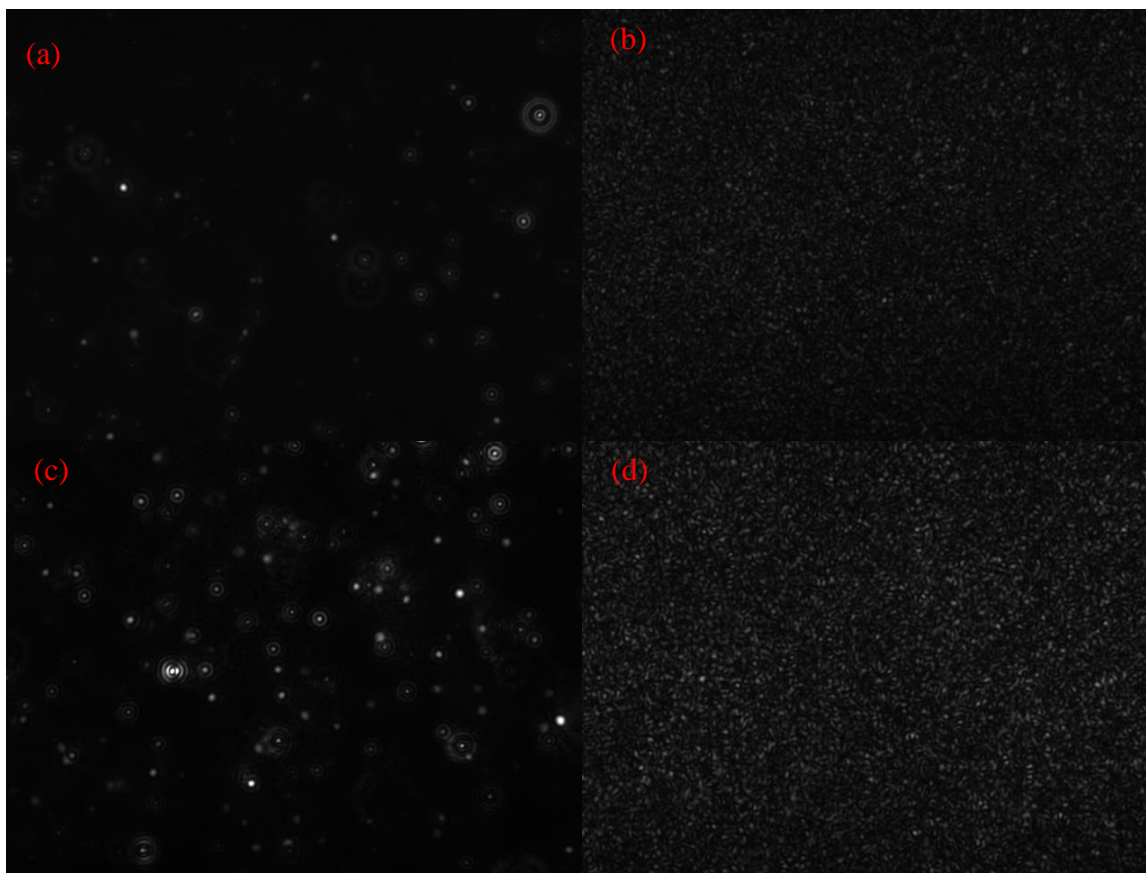


Figure 5-4. NTA scattering images of dissolution medium obtained after dissolution of (a) TIPP, (b) Me-TIPP, (c) PHPH, and (d) Me-PHPH PVPVA ASDs at drug loading of 10, 30, 5, and 30%. The bright spots indicate the presence of drug-rich colloidal species.

5.5.4 Solid State Characterization of ASDs

5.5.4.1 IR

Figure 5-5 shows the IR spectra of the PVPVA and model compound carbonyl groups in ASD films. For neat, dry PVPVA, the peak for the vinylpyrrolidone (VP) carbonyl was observed at around 1684 cm^{-1} , while the peak for the vinyl acetate (VA) carbonyl was located at 1736 cm^{-1} . Both peaks are labeled by a solid red line in Figure 5. The IR spectra of TIPP/PVPVA ASDs (Figure 5-5a) showed a gradual shift of the VP carbonyl to lower wavenumbers as the drug loading increased, accompanied by a broadening of the peak. The maximum observed shift was 30 cm^{-1} at 90% DL. Similarly, Me-TIPP ASDs showed a small shift in the VP carbonyl to a lower wavenumber, however, the maximum shift was only 7 cm^{-1} (Figure 5-5b). PHPH ASDs showed a new peak evolving at around 1654 cm^{-1} (Figure 5-5c) while the original VP carbonyl peak decreased in intensity with an increase in DL. The maximum shift of 30 cm^{-1} is similar in

magnitude to that observed for the TIPP ASDs, however, the peak shape is narrower. Lastly, Me-PPH ASDs showed minimal shift in the VP carbonyl moiety with increasing DL (Figure 5-5d), which is consistent with the lack of either hydroxyl or iodo groups. The VA carbonyl group did not change significantly for any of the ASDs, indicating that the VP carbonyl is responsible for the intermolecular interactions between the model compounds and PVPVA.

In the chemical structure of these four model compounds, there is a carbonyl group, which can interact with hydroxyl or iodo groups to form compound-compound interactions. The carbonyl groups in the model compounds were labeled with a blue dotted line on the IR spectra showed in Figure 5-5. The carbonyl groups in TIPP (Figure 5-5a) shows two different wavenumbers (1772 cm^{-1} , 1756 cm^{-1}), indicating that a portion of the carbonyls are involved in compound-compound interactions, resulting in a 16 cm^{-1} shift to a lower wavenumber (1756 cm^{-1}). As the drug loading decreases, the intensity of the peak at lower wavenumber reduces because the compound-compound interactions are interrupted by the polymer. When the hydroxyl groups in TIPP are methylated to form Me-TIPP, the carbonyl group has only one population at a wavenumber of 1772 cm^{-1} , shown in Figure 5b. This observation suggests that there are no significant compound-compound interactions among Me-TIPP molecules through this carbonyl group. For PPH (Figure 5c), two populations were observed for the carbonyl moiety in the compound at 1765 and 1736 cm^{-1} , respectively. The peak at 1736 cm^{-1} represents the population of compound-compound hydrogen bonding carbonyls, which increases in intensity at higher DL. This peak overlaps with the VA carbonyl peak. Compared to the free carbonyl groups, the hydrogen bonded carbonyls in PPH have a shift of 29 cm^{-1} . The carbonyl groups in Me-PPH only show one peak at 1765 cm^{-1} (Figure 5c), indicating no significant directional compound-compound interactions.

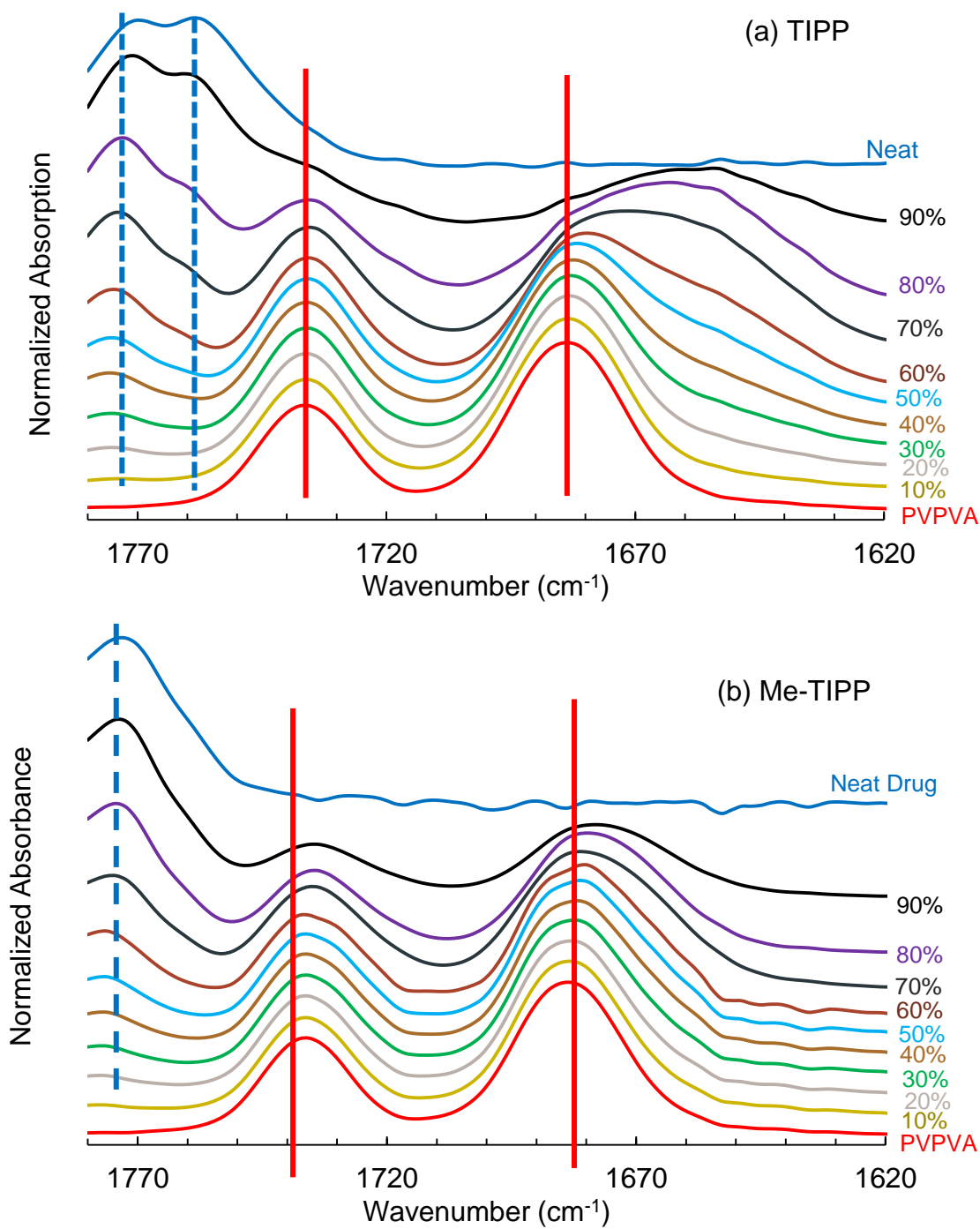
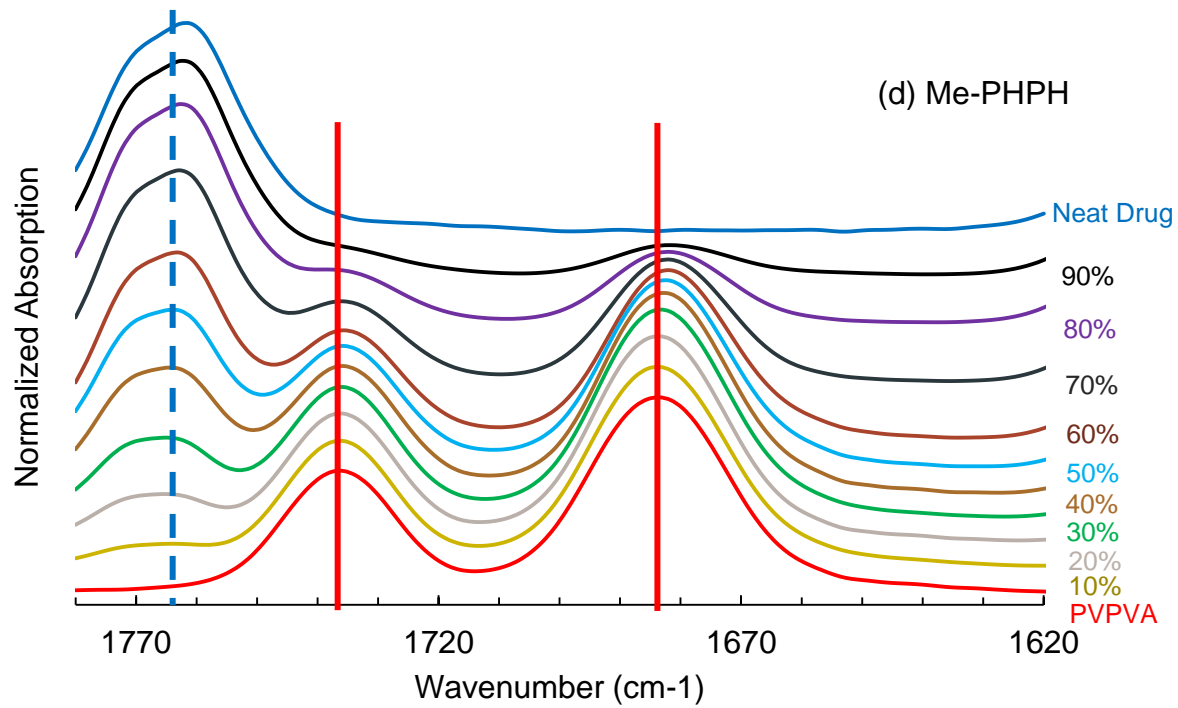
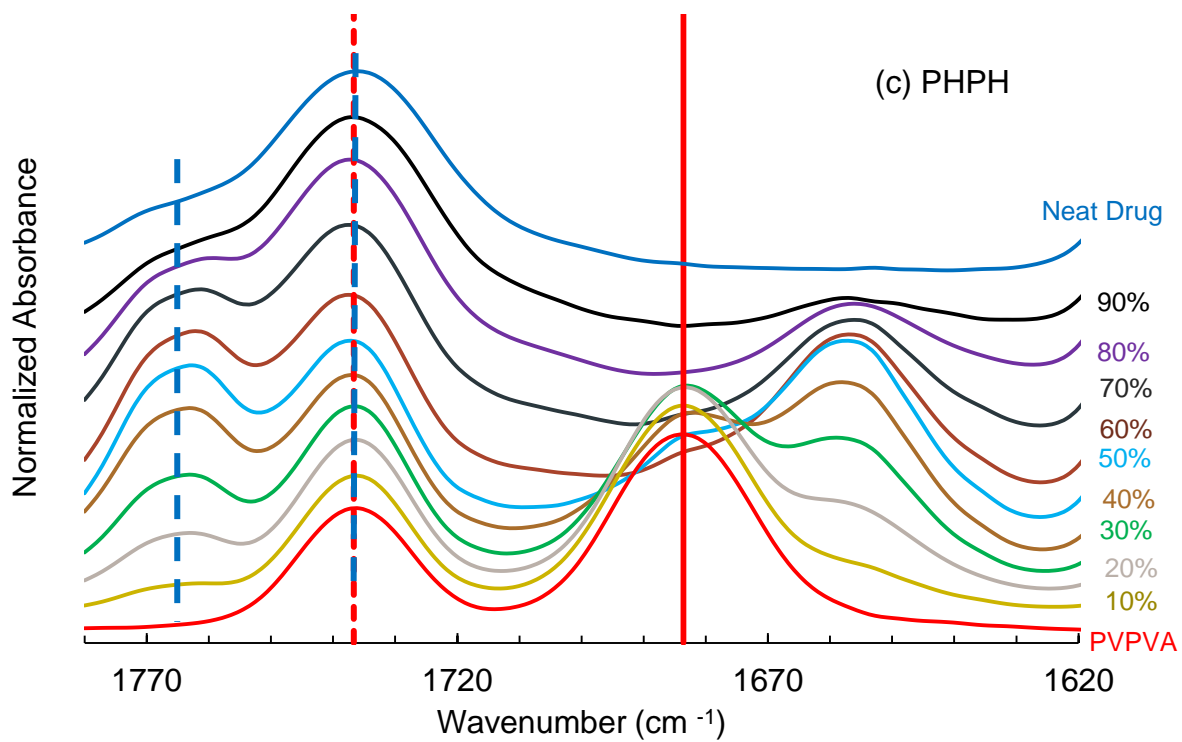


Figure 5-5. IR spectra for (a) TIPP-PVPVA ASDs, (b) Me-TIPP/PVPVA ASDs, (c) PHPH/PVPVA ASDs, and (d) Me-PHPH/PVPVA ASDs with drug loading from 0 to 90%.

Figure 5-5 continued



The chemical composition of the tablet surfaces for TIPP and Me-TIPP PVPVA ASDs with DLs from 10 to 40% were characterized by XPS. The binding energy of I 3d electrons in both neat amorphous model compounds and in ASDs were measured. The I 3d core-level spectra (Figure C.1 and C.2) show two components with a ratio of 3:2 because of spin-orbital splitting. The I 3d photoemission peaks of neat amorphous compounds showed one pair of peaks with binding energies of 620.7 ± 0.01 (I 3d_{5/2}) and 632.2 ± 0.04 eV (I 3d_{3/2}) eV. When Me-TIPP and TIPP were dispersed into PVPVA, a new pair of I 3d photoemission peaks with lower binding energy, located at 618.1 ± 0.05 and 629.6 ± 0.05 eV, were observed, which suggests that a portion of the I atoms have become more electron-rich. The peaks showing a lower binding energy likely result from halogen bonding between I and the carbonyl in vinylpyrrolidone (VP) following dispersion of the compound in the polymer. The atomic percentage of I atoms the lower BE as a function of DLs is summarized in Figure C.3. Based on the atomic percentage of I atoms, the molar amount of I atoms having lower binding energy in a 100 mg ASD tablet can be calculated as a function of DL (Figure 5-6). At 10% drug loading, a similar number of I atoms are involved in halogen bonding for TIPP and Me-TIPP ASDs. However, for DLs of 20% or above, approximately twice as many I atoms are involved in halogen bonding for Me-TIPP ASDs relative to in TIPP ASDs. This observations suggests that there is a competition between halogen and hydrogen bond formation between TIPP and PVPVA. The IR data shows that TIPP and PVPVA do form hydrogen bonding interactions, supporting this supposition.

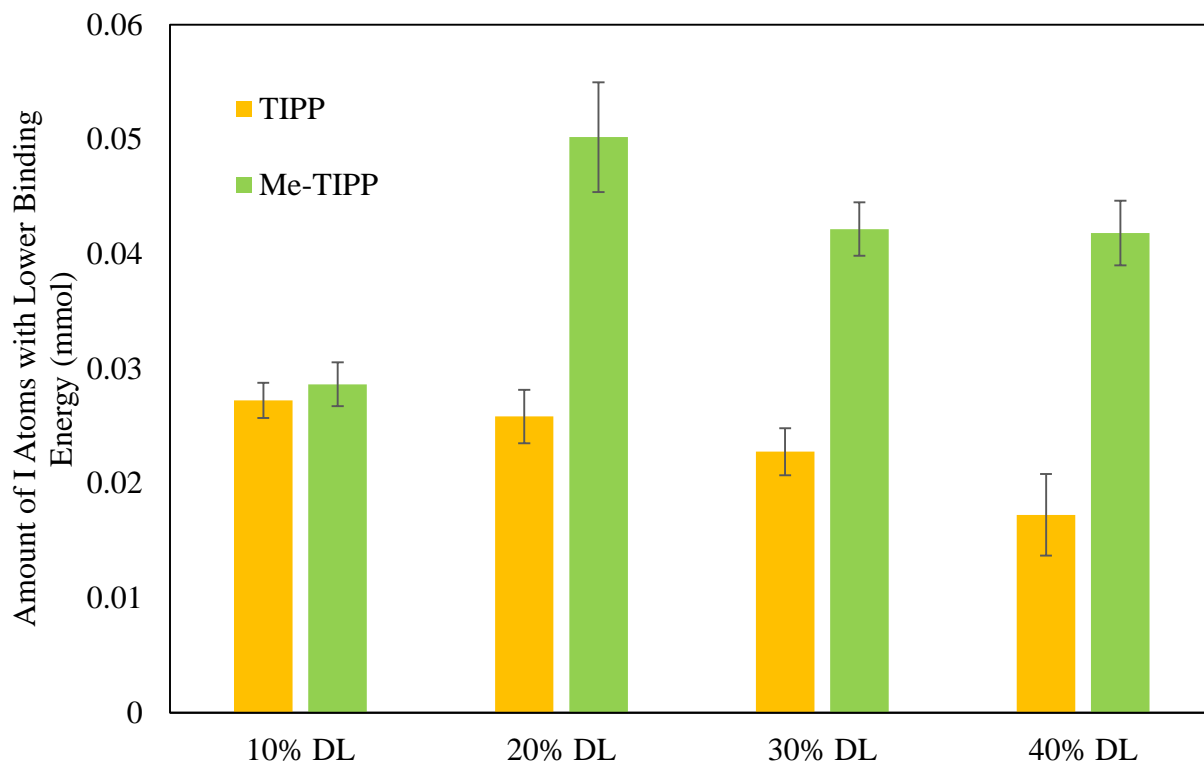


Figure 5-6. Molar amount of I atoms showing lower binding energy in 100 mg PVPVA ASDs for drug loading from 10 to 40 wt.%.

5.6 Discussion

Drug-polymer intermolecular interactions in ASDs and their impact on formulation performance have been studied previously in different contexts. Hydrogen bonding is one of the most frequently studied interactions, and it is considered to play an important role in delaying drug crystallization in the ASD.^{13, 65, 118} In contrast, halogen bonding, a specific interaction considered important in supramolecular chemistry^{157, 158} and for drug potency,¹⁵⁹ has not been considered in terms of its impact on formulation performance. Recently, the existence of drug-polymer halogen bonding interactions in drug-polymer ASD systems has been demonstrated, leading to questions about their role in formulation properties and performance. A halogen bond is an attractive interaction between the electrophilic regions of halogen atoms, termed the sigma hole, and electron-rich moieties, such as oxygen, nitrogen, and other halogen atoms.¹⁶ In general, the I atom is a better halogen bond donor compared to other halogen atoms. Common between both hydrogen and halogen interactions is that their respective partner atoms (i.e. the donor group) must have electron-rich moieties that can donate electrons to form the interactions. Thus, in a system where

both interactions are possible, the occurrence of competition between hydrogen and halogen bonds is probable, although, they can co-exist.^{17, 158} In several crystal engineering studies, it has been shown that hydrogen bonding is generally favored over halogen bonding.¹⁷ However, halogen bonding tends to persist to a greater extent in a more polar environment while hydrogen bonding is less favored.^{130, 134}

The TIPP molecule contains two hydroxyl groups and four iodo groups which can act as hydrogen and halogen bond donors, respectively. Me-TIPP only has the halogen bond-donating iodo groups, while PHPH only has hydrogen bond-donating hydroxyl groups. Lastly Me-PHPH does not have either of these functional groups and therefore can only form non-specific interactions with the polymer. The VP carbonyl group in PVPVA is a good electron donating group and is the acceptor group in the formation of hydrogen^{45, 64} and halogen bonds.^{127, 149, 150} The extensive shift in the VP carbonyl peak (IR spectra, Figure 5-5c) in TIPP and PHPH ASDs confirms the formation of hydrogen bonds between the hydroxyl and carbonyl groups. Similar shifts have been observed previously for other compounds containing hydrogen bond donors.^{12, 45} In contrast, Me-TIPP led to smaller shift in the PVPVA carbonyl peak, suggesting that the halogen bonding interaction is weaker than the hydrogen bond formed with the phenolic group; phenols are known to be good H-bond donors.¹⁶⁰ The supposition that the shift in carbonyl peak is due to halogen bonding is supported by the XPS data, which shows an additional iodine population at a lower binding energy when Me-TIPP is dispersed in a PVPVA matrix. The lower binding energy iodine peaks are also observed for TIPP/PVPVA ASDs, although the molar amount is generally lower than for the Me-TIPP/PVPVA ASDs (Figure 5-6). This suggests that TIPP formed fewer halogen bonds with PVPVA than Me-TIPP (for DLs >10%) most likely due to competition between the hydroxyl and iodo groups with the VP carbonyls in PVPVA. The VP carbonyl shifts in the IR spectra suggest that the two interactions can co-exist, based on the broad peak seen for the TIPP ASDs (Figure 5-5a). This is most readily apparent in the 60% DL TIPP/PVPVA ASD spectrum, where the original VP carbonyl peak shows a small shift (as seen for the halogen bonding interaction in Me-TIPP), while a new peak at around 1650 cm⁻¹ is present, as seen for PHPH. Thus, both hydrogen and halogen bonding appear to be present in TIPP/PVPVA ASDs, but hydrogen bonding seems to be more prevalent, especially at higher DLs. Conversely, it is clear Me-PHPH does not form any directional intermolecular interactions with PVPVA. Thus, there is evidence of halogen bonding only, hydrogen bonding only, both halogen and hydrogen bonding

and no specific interactions in the ASDs prepared with the four different compounds. Given the difference in the release properties of the different ASDs, it is of interest to consider how the compound molecular structure, the resultant physicochemical properties, and compound-polymer interactions may impact the observed release behavior.

In addition to compound-polymer interactions, compound-compound interactions were also observed in the IR spectra. All four model compounds have carbonyl groups, which can potentially form hydrogen and halogen bonds with hydroxyl and iodo groups. TIPP IR spectrum showed two carbonyl peaks compared to Me-TIPP, suggesting the presence of either hydrogen or halogen bonds. However, the XPS spectra of neat TIPP (Figure C.1) and Me-TIPP (Figure C.2) show that all the iodo atoms are in one chemical state, with electron binding energies that are higher compared to the iodo groups that halogen bond to the VP carbonyl in PVPVA. Thus, hydrogen bonding interactions are present in neat TIPP instead of halogen bonding. Compound PHPH, without iodo groups, exhibits strong compound-compound hydrogen bonds, leading to a 29 cm^{-1} downshift of the carbonyl IR peak. This shift is much larger compared to the hydrogen bonding shift observed in TIPP (about 14 cm^{-1}). This suggests that the compound-compound hydrogen bond is stronger in PHPH than TIPP. One explanation is that the iodo groups in TIPP sterically hinder the formation of the hydrogen bond. Interestingly, the compounds with low LoC, PHPH and TIPP, have a higher tendency to form strong compound-compound interactions compared to Me-TIPP and Me-PHPH. One rationale is that the compound-compound interaction potentially can compete with compound-polymer interaction, which reduces the tendency of the ASD to form compound-polymer interactions. In addition, the compound-compound interactions become more dominant at higher DLs.

The four model compounds have different physicochemical properties as a result of the inherent differences in molecular structure (Table X). Me-PHPH, showed a much lower T_g than the other compounds, presumably due to a lack of specific interactions in the neat amorphous material, as well as the lower molecular weight. The iodo-containing compounds, TIPP and Me-TIPP, are more hydrophobic compared to PHPH and Me-PHPH, based on consideration of the calculated log P values, and the greater hydrophobicity most likely explains their very low amorphous solubilities. The iodine-containing compounds also have much higher MWs than the non-iodo counterparts, thus for the dispersions, at any given drug loading, less molecules are present for the former relative to the latter compounds.

The DL where the release performance of the ASD diminishes varies considerably depending on the compound chemistry. A high drug loading, while still maintaining rapid release, is an essential property of an ASD formulation, especially for high dose compounds, in order to minimize the dosage size, since a large dosage form negatively impacts patient compliance. Therefore, understanding the link between molecule physicochemical properties and drug loading limits (LoC), is essential in order to develop the optimum formulation. Properties including Log P, amorphous solubility, T_g , and MW do not show obvious correlations with the LoCs. Interestingly, the compounds that formed strong specific interactions with the polymer, PHPH and TIPP, showed much lower LoC values relative to the compounds that formed weaker specific (halogen bonding, MeTIPP) or non-specific interactions (Me-PHPH). Hydrogen bonding is known to enhance the ASD physical stability,^{13, 45} however, based on our observations, it appears that compound-polymer hydrogen bonding may lead to a reduction in LoC. In contrast, systems with weaker interactions display more robust dissolution behavior at higher DLs.

Further insight into the underlying role of compound-polymer intermolecular interactions is provided by changing the chemistry of the polymer. PVP K29-32 has a similar MW to PVPVA, but contains only the VP monomer, and therefore has a higher concentration of hydrogen bond acceptor groups for a given DL, increasing the potential for halogen bond formation. This increase in the number of polymer acceptor groups increased the LoC from 30% to 40% with substantial release observed even at 50% DL (Figure 5-3a). The same increase in LoC was not observed for Me-PHPH/PVP ASDs. In fact, release performance was degraded by switching to this polymer. This may reflect the greater hydrophilicity of PVP compared to PVPVA and that Me-PHPH interacts with the polymer mostly through non-specific and hydrophobic interactions (in the presence of water). PVPVA can be considered more hydrophobic than PVP, because a substantial fraction of PVPVA is composed of the hydrophobic VA moiety. This result again suggests that halogen bonding, or other weak interactions are beneficial for ASD dissolution.

Polymer-controlled dissolution of ASDs, leads to the formation of colloidal drug species.^{10,}
¹¹ A potential bioavailability advantage is provided by these nano-sized species, which act as drug reservoir, replenished the drug solution concentration when absorption across a membrane occurs.⁸ Moreover, the size of these colloidal species may be important for in vivo performance.¹¹⁶ Interestingly, the size of these drug-rich colloidal species varies by a factor of ~2 among the different model compounds at their respective LoCs (Table 3). The more hydrophobic iodo-

containing compound ASDs yield the smaller colloids. The difference in concentration or molecular interaction cannot explain this observation. Smaller drug-rich colloids can potentially lead to a better oral absorption, due to a faster drug replenishment rate by this reservoir.¹¹⁶ The size of the colloidal species generated may be another important factor to consider when assessing various ASD formulations, and is likely to have some inherent dependence on the parent compound properties, as well as the excipients used in the ASD.

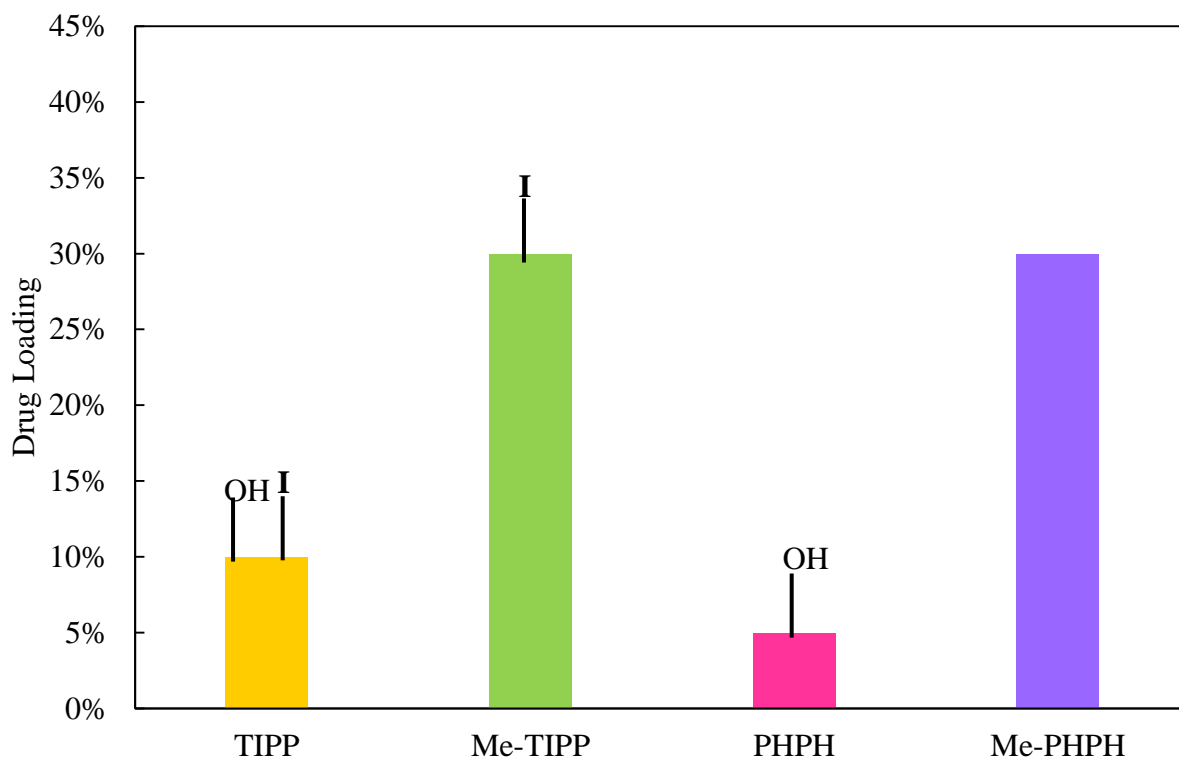


Figure 5-7. LoC for four model compound/PVPVA ASDs, and each column are labeled with types of hydrogen bond (OH) and halogen bond donor (I) for that compound.

5.7 Conclusions

This study investigated the impact of molecular interactions on ASD dissolution performance by studying the release behavior of four model compounds with a common chemical scaffold that was substituted with different functional groups. The optimal dissolution performance of ASDs is characterized by fast and complete release of components where the model compound releases at the same percent rate as the polymer, leading to formation of drug-rich colloidal species after the concentration in solution exceeds amorphous solubility. However, this ideal dissolution behavior can only be achieved at DLs at or below LoC, which was observed to vary among the

ASDs made with these four model compounds. The study suggests that LoC may depend on the specific intermolecular interactions between the model compounds with the polymer. A greater LoC means that ASDs can be formulated at higher DL to reduce patient pill burden without sacrificing dissolution performance. It appears that model compounds that can form hydrogen bonds with PVPVA have a lower LoC, indicating that hydrogen bonding may be detrimental to ASD release performance. On the other hand, halogen bonding and hydrophobic interactions may be beneficial to ASD release performance as compounds possessing only these interactions achieved a higher LoC. The benefit of halogen bonding to ASD dissolution performance was further confirmed by replacing PVPVA with PVP. The increase in halogen accepting groups (VP carbonyls) resulted in an increase in LoC for Me-TIPP/PVP ASDs, likely due to the increase in the number of halogen bonds. Thus, for the first time, a correlation can be made between drug functional groups and ASD release performance, based on the study of a group of closely related model compounds which differ only by small and systematic variations in substituted functional groups. This study highlights that drug-polymer interactions may be a dominate factor dictating how drug and polymer release from ASDs.

APPENDIX A. SUPPORTING INFORMATION FOR CHAPTER 3

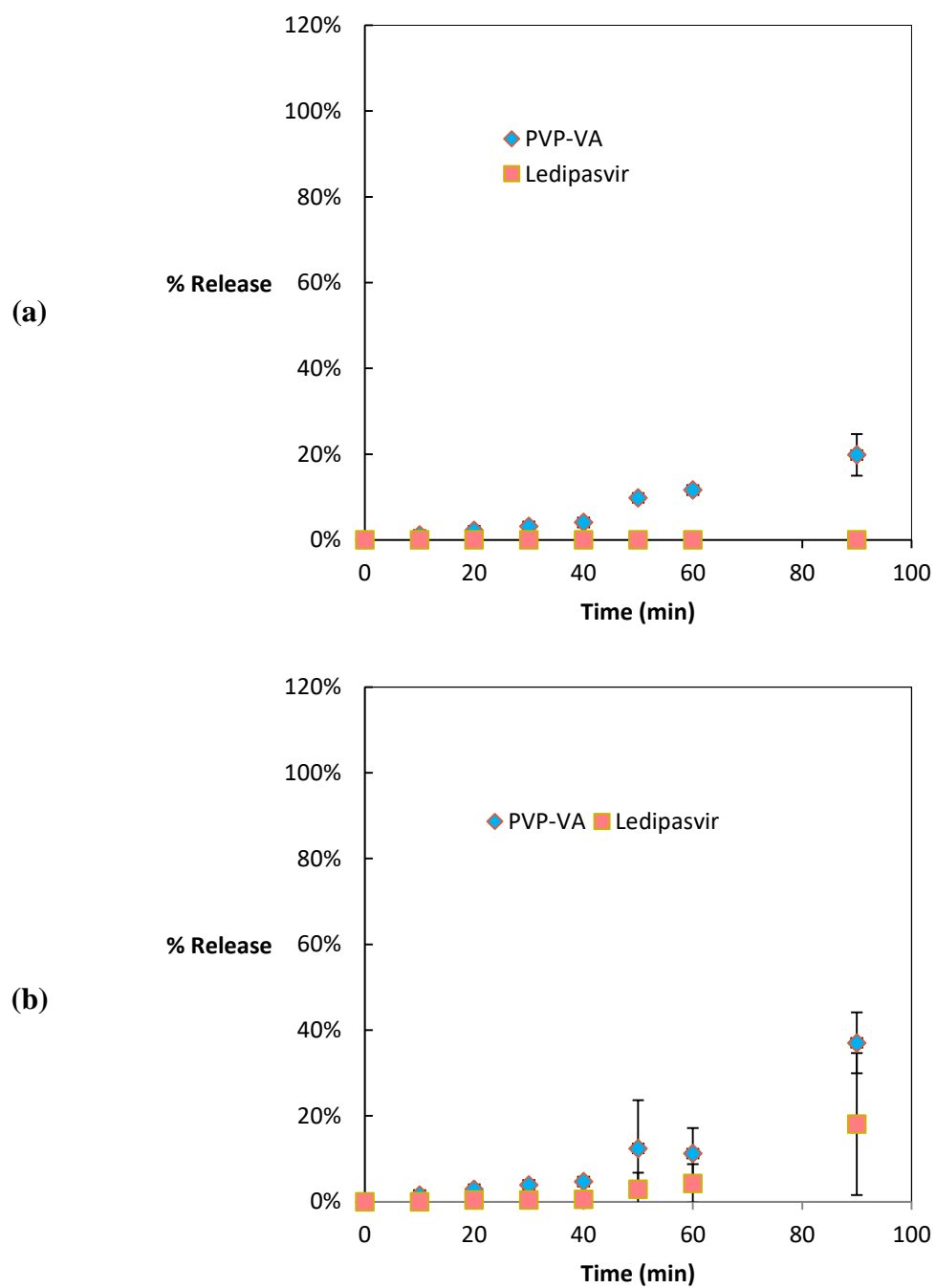
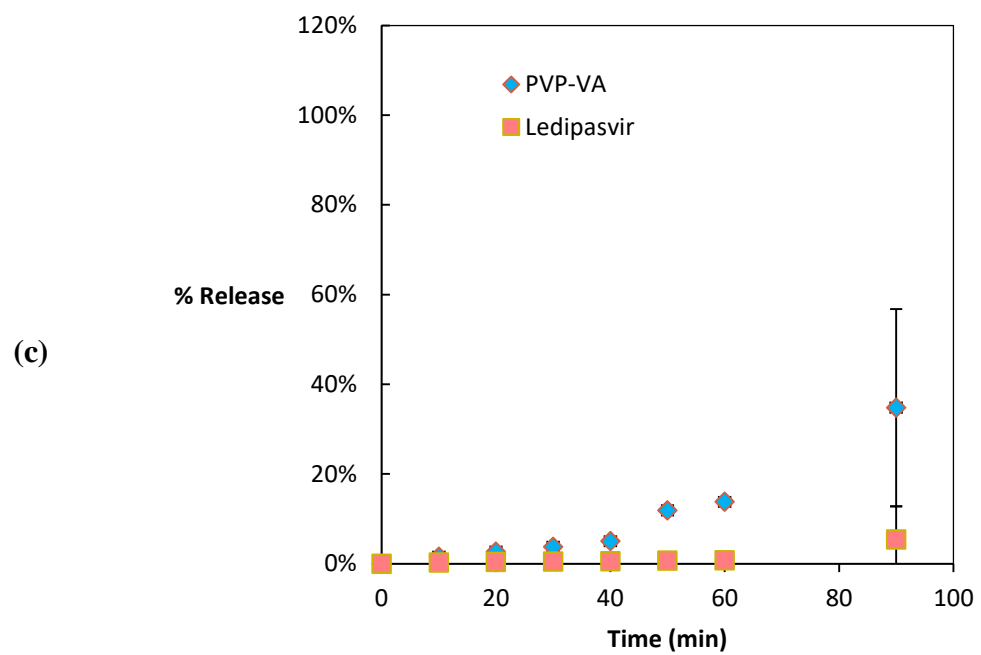


Figure A.1 Release profiles of ASDs containing 5 wt.% (a) Span 85, (b) Tween 80, and (c) Vitamin E TPGS with DL of 7.5%.

Figure A.1 continued



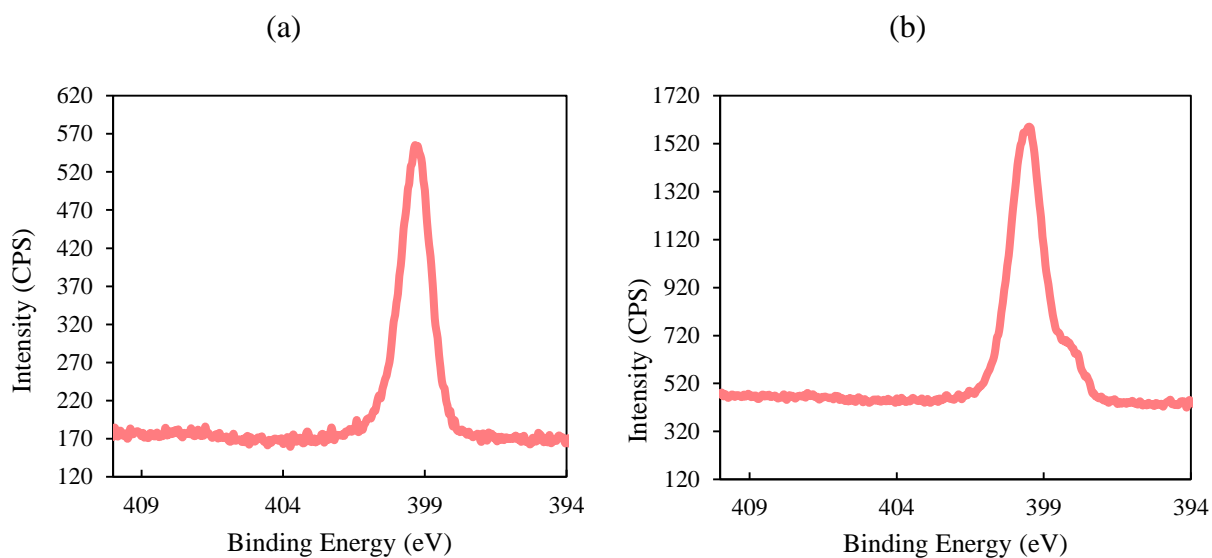


Figure A2. XPS N 1s spectrum for (a) neat PVPVA and (b) neat amorphous ledipasvir.

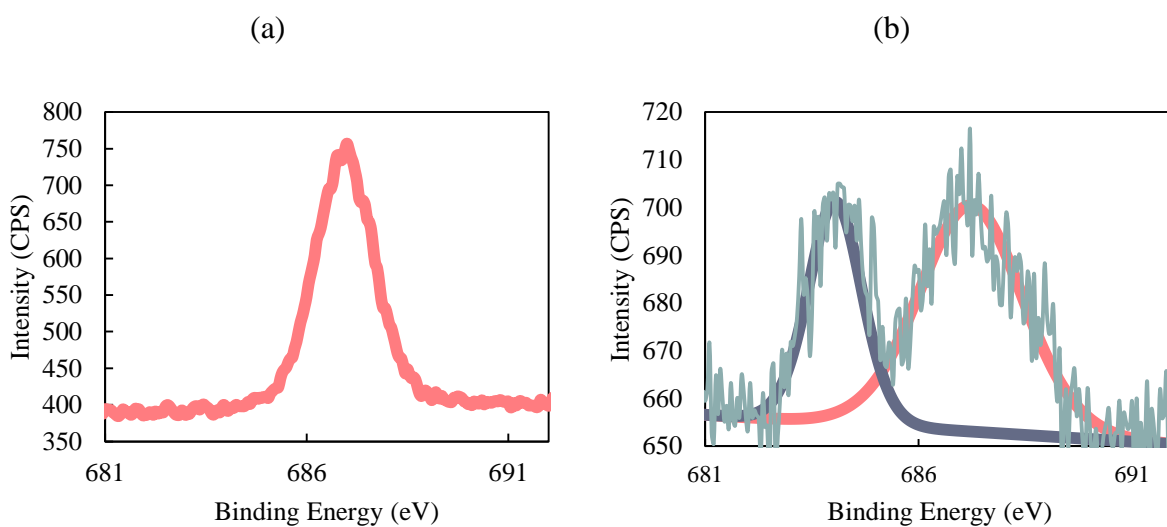


Figure A3. XPS F 1s spectrum for (a) neat amorphous ledipasvir and (b) ledipasvir in ASDs with 20% drug loading.

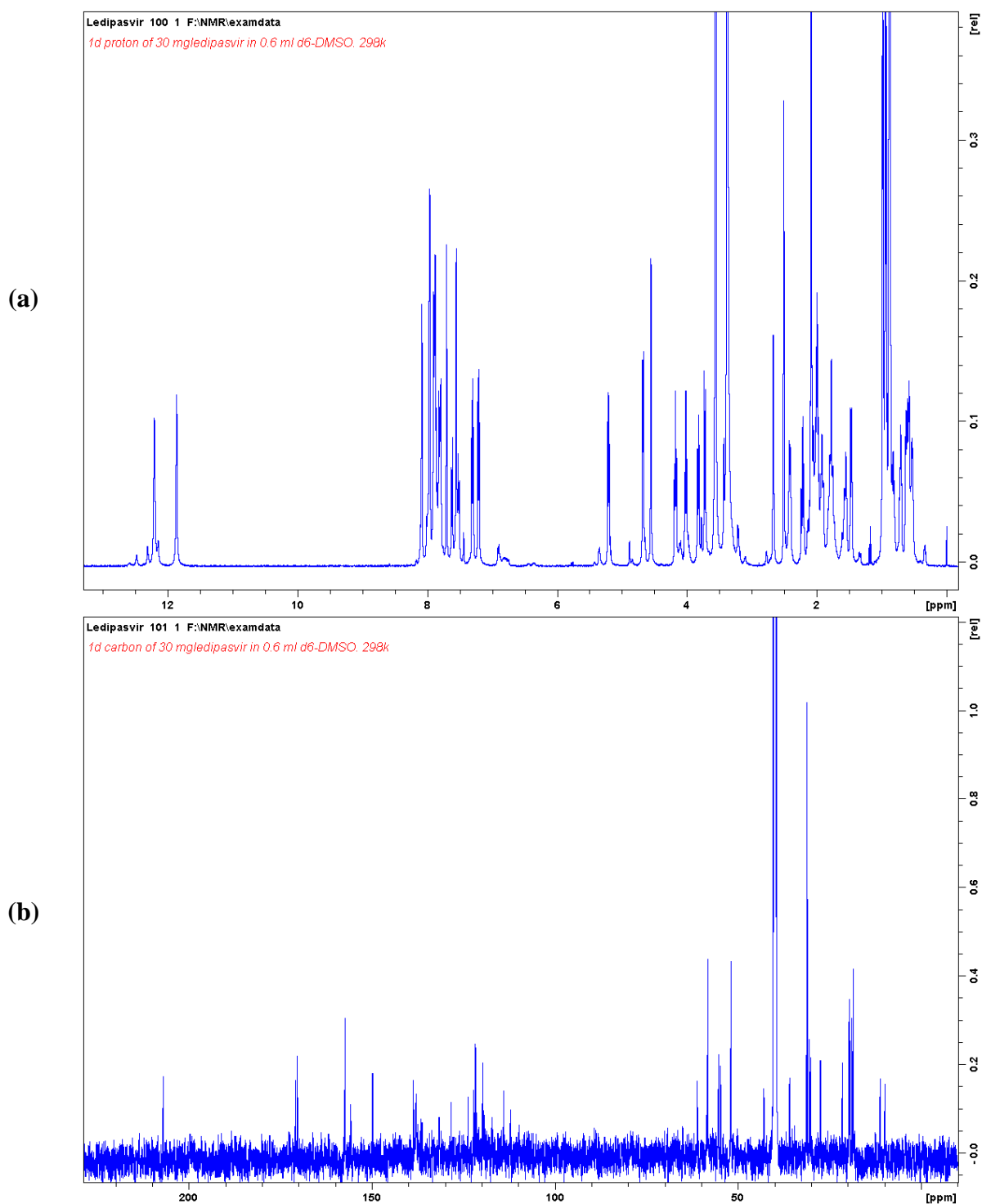


Figure A4. (a) Proton NMR spectrum of ledipasvir (b) ^{13}C NMR spectrum of ledipasvir in deuterated DMSO.

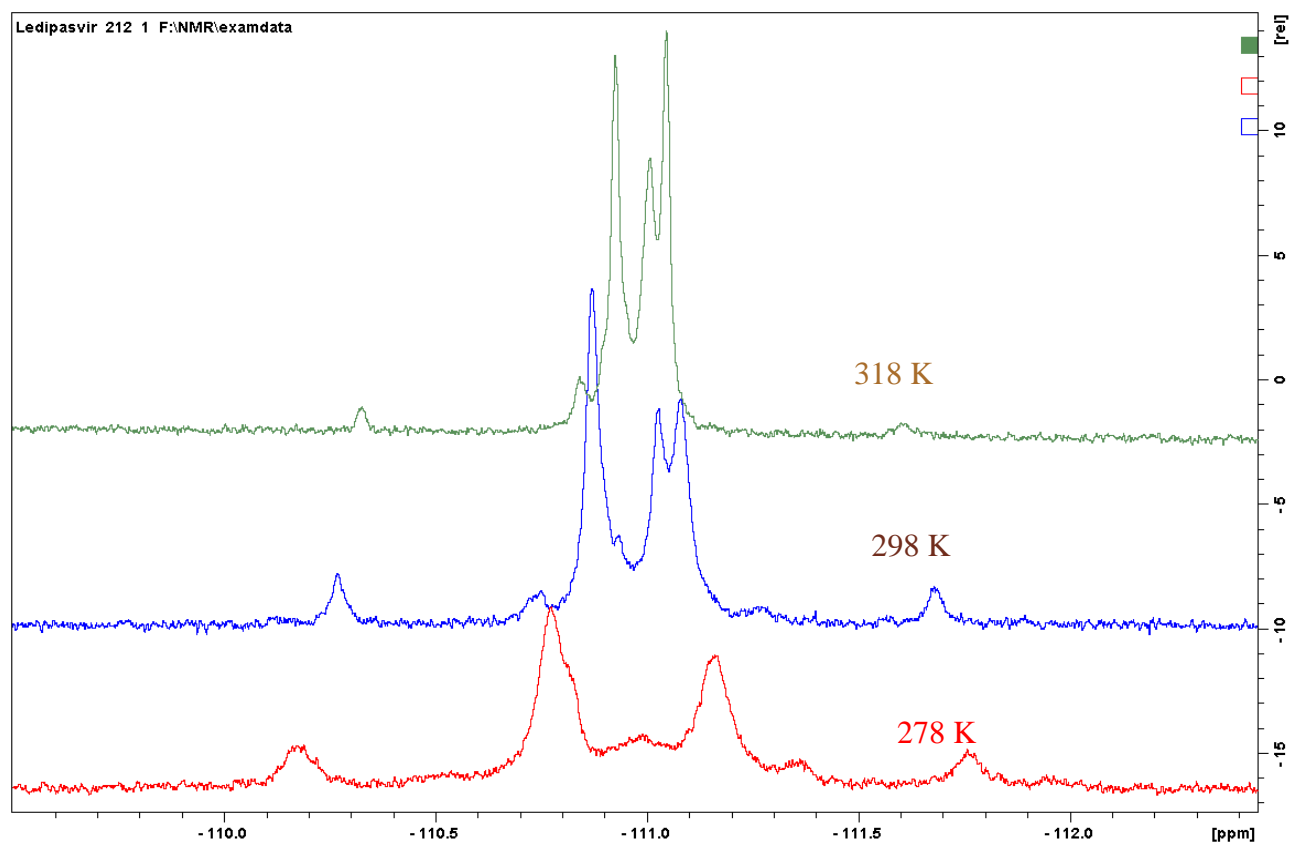


Figure A5. ^{19}F NMR spectra at different temperature with a ledipasvir concentration of 2 mg/mL.

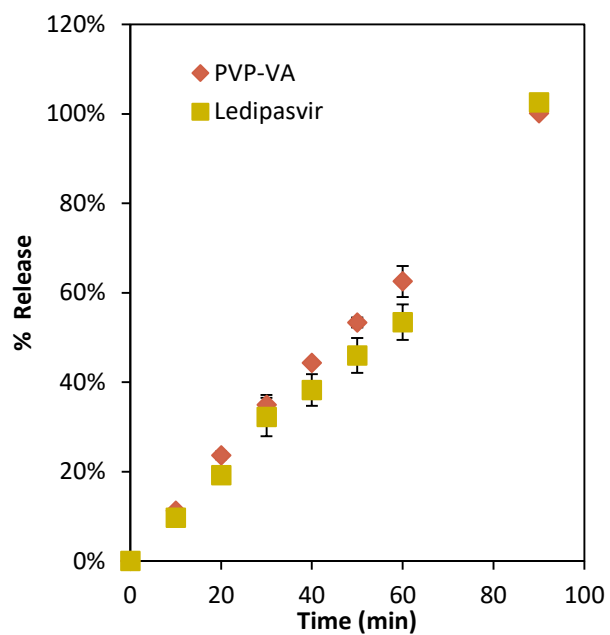


Figure A6. Release profiles for 5% ledipasvir-PVPVA containing 5% poloxamer 407 ASDs.

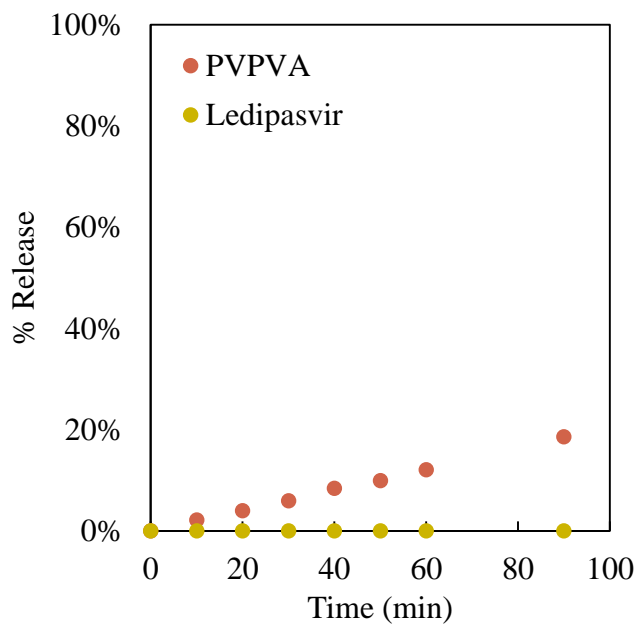


Figure A7. Release profiles for ledipasvir-PVPVA ASDs at 20% DL.

Calculation Example for Figure 3-16

For x axis:

PVPVA 64: 60 wt.% VP, 40 wt.% VA,

MW of VP is 111.14 g/mol, MW of VA is 86.09 g/mol

Thus, the molar ratio between the two, VP and VA, is 5.4 : 4.6, and average MW of the repeat unit is thus 99.62 g/mol

For NMR titration sample that contains 2 mg/mL ledipasvir and 80 mg/mL VP in a 0.6 mL deuterated toluene, the correlated PVPVA mass based on the amount of VP added can be calculated as followed,

$$\frac{80mg}{mL} \times \frac{0.6mL}{114.14 g/mol} \times \frac{10}{5.4} \times 99.62 \frac{g}{mol} = 77 mg PVPVA$$

The drug loading can be calculated,

$$\frac{\frac{2mg}{mL} \times 0.6mL}{\frac{2mg}{mL} \times 0.6mL + 77 mg} = 1.5\%$$

For secondary y axis:

At 10% DL, 73.4% of F atoms showed lower binding energy in XPS in a 100 mg ASD tablet, and each ledipasvir molecule contains two F atoms. Thus, the total molar amount of F with lower binding energy can be calculated,

$$\frac{100 mg \times 10\%}{889 g/mol} \times 2 \times 73.4\% = 0.165 mmol$$

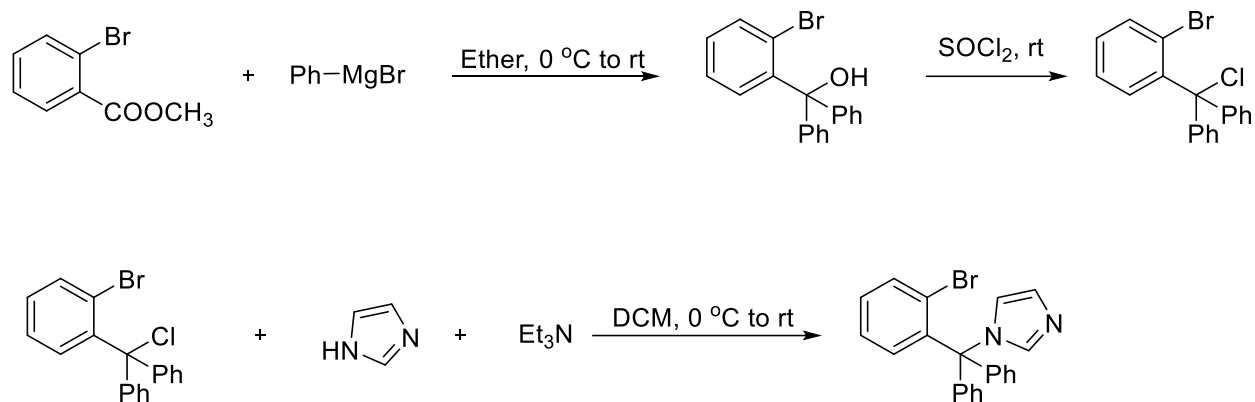
APPENDIX B. SUPPORTING INFORMATION FOR CHAPTER 4

Synthesis of Brotrimazole

(2-bromophenyl)diphenylmethanol The preparation was as described previously¹⁶¹: to a stirred solution of methyl 2-bromobenzoate (2.6 g, 12 mmol, 1.0 equiv) in anhydrous Et₂O (40 mL) at 0 °C under nitrogen was added PhMgBr (8.8 mL, 3.0 M in Et₂O, 2.2 equiv). The reaction mixture was stirred at room temperature overnight. The reaction was quenched by sat. NH₄Cl solution (7 mL). The mixture was extracted by Et₂O, the organic layers were combined and the solvent was removed under vacuum. The residue was purified by silica gel chromatography with hexane as the eluent to afford the product as white solid (3.5 g, 86%).

((2-bromophenyl)chloromethylene)dibenzene (2-bromophenyl)diphenylmethanol (3.4 g, 10.0 mmol, 1.0 equiv) was mixed with SOCl₂ (10 mL, excess) and several drops of DMF was added. The mixture was stirred at room temperature overnight. The stirring was stopped upon the completion of reaction as monitored by ¹H NMR of the crude mixture. Then SOCl₂ was removed under vacuum. To the residue was added DCM (5 mL) and concentrated again and this was repeated for three times to afford ((2-bromophenyl)chloromethylene)dibenzene. This was used directly in the next step without further purification.

1-((2-bromophenyl)diphenylmethyl)-1*H*-imidazole To a precooled solution of 2-bromophenylchloromethylene)dibenzene (10.0 mmol, 1.0 equiv) in anhydrous DMF (20 mL) at 0 °C under argon was added 1*H*-imidazole (1.0 g, 15.0 mmol, 1.5 equiv) and triethylamine (4.2 mL, 30.0 mmol, 3.0 equiv) via a syringe. The reaction mixture was allowed to warm to room temperature and stirred overnight. 50 mL ethyl acetate was added and washed with brine three times, and dried over Na₂SO₄. After filtration and concentration, the crude mixture was purified by column chromatography (silica gel, 50% ethyl acetate in hexanes) to afford the title product (3.0 g, 77.1%).



Scheme B.1. Synthesis of brotrimazole.

^1H NMR (800 MHz, Chloroform-*d*) δ 7.66 (dd, $J = 7.9, 1.5$ Hz, 1H), 7.49 (t, $J = 1.2$ Hz, 1H), 7.36 – 7.32 (m, 6H), 7.30 – 7.28 (m, 1H), 7.24 – 7.21 (m, 5H), 7.07 (d, $J = 1.3$ Hz, 1H), 6.91 (dd, $J = 8.0, 1.7$ Hz, 1H), 6.76 (d, $J = 1.5$ Hz, 1H). ^{13}C NMR (201 MHz, CDCl_3) δ 142.19, 140.36, 139.24, 135.90, 130.93, 130.52, 129.86, 128.46, 128.17, 127.97, 127.56, 125.90, 121.63. HRMS (m/z , APCI): calcd for $\text{C}_{22}\text{H}_{18}\text{BrN}_2(\text{M}+\text{H})^+$: 389.0653. Found: 389.0639.

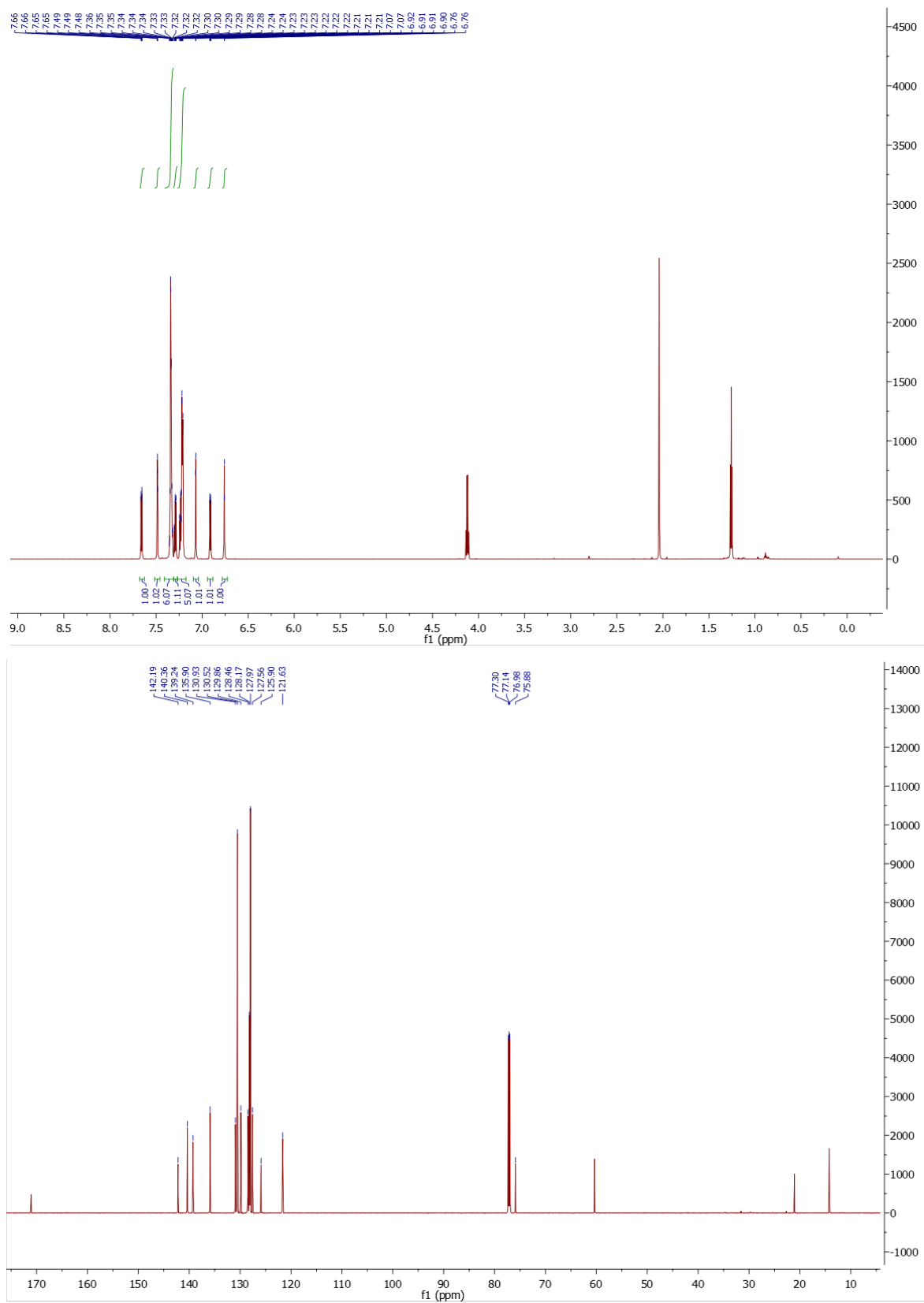


Figure B.1. ¹H NMR and ¹³C NMR for 1-((2-bromophenyl)diphenylmethyl)-1H-imidazole.

Synthesis of 3,3-bis(3,5-diiodo-4-methoxyphenyl)isobenzofuran-1(3H)-one (Me-DIBF)

To a solution of 3,3-bis(4-hydroxy-3,5-diiodophenyl)isobenzofuran-1(3H)-one (6.6 g, 8.0 mmol, 1.0 equiv) in anhydrous DMF (50 mL) at RT under argon was added K_2CO_3 (4.4 g, 32.0 mmol, 4.0 equiv) and MeI (2.5 mL, 40.0 mmol, 5.0 equiv) via a syringe. The reaction mixture was stirred overnight. The mixture was poured into water and filtered to afford the title product as a white solid (6.5g, 95.6%).

^1H NMR (800 MHz, Chloroform-*d*) δ 8.00 – 7.98 (m, 1H), 7.83 – 7.81 (m, 1H), 7.69 – 7.65 (m, 5H), 7.58 – 7.56 (m, 1H), 3.88 (s, 6H). ^{13}C NMR (201 MHz, CDCl_3) δ 168.44, 159.52, 149.85, 139.44, 138.09, 134.97, 130.31, 126.72, 125.09, 123.78, 91.01, 87.36, 60.73. HRMS (*m/z*, ESI): calcd for $\text{C}_{22}\text{H}_{15}\text{I}_2\text{O}_4(\text{M}+\text{H})^+$: 850.7149. Found: 850.7137.

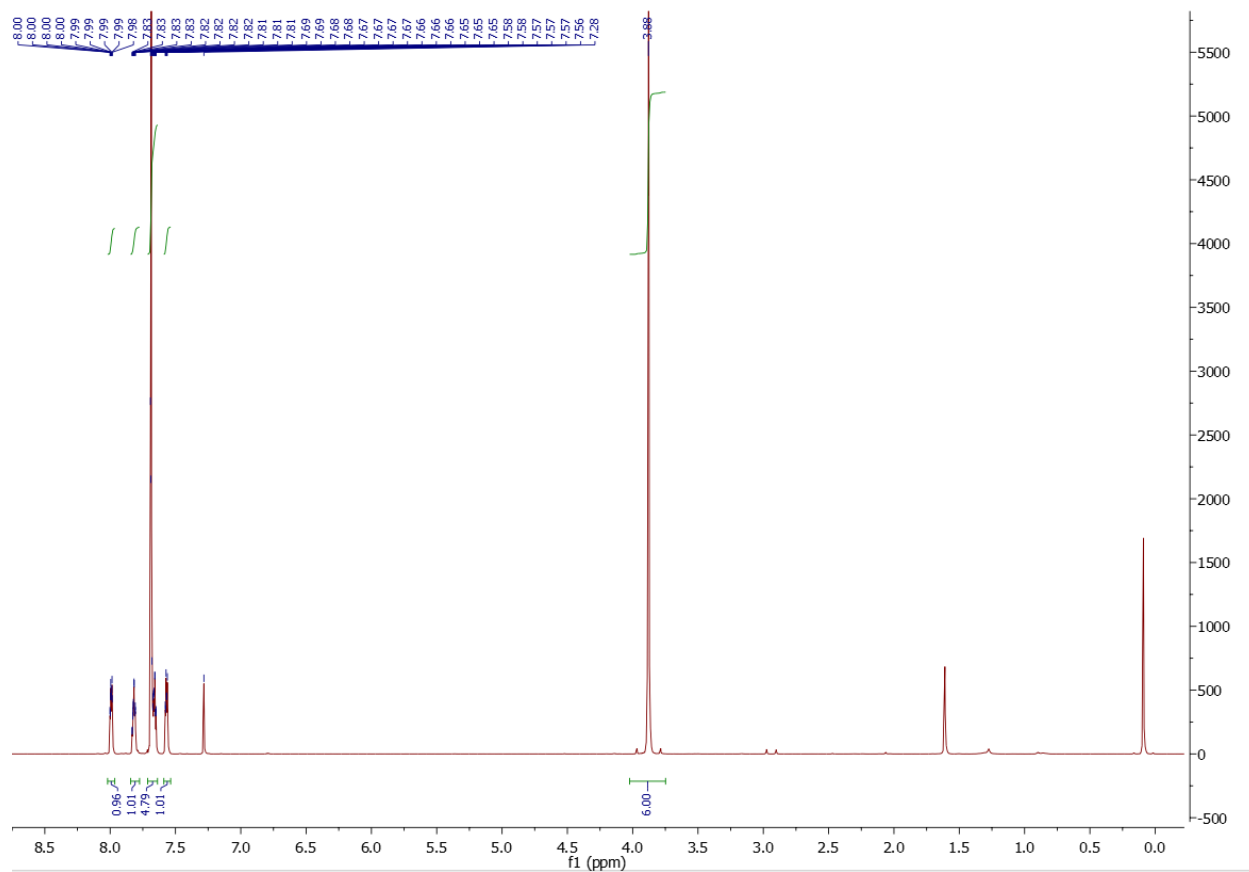
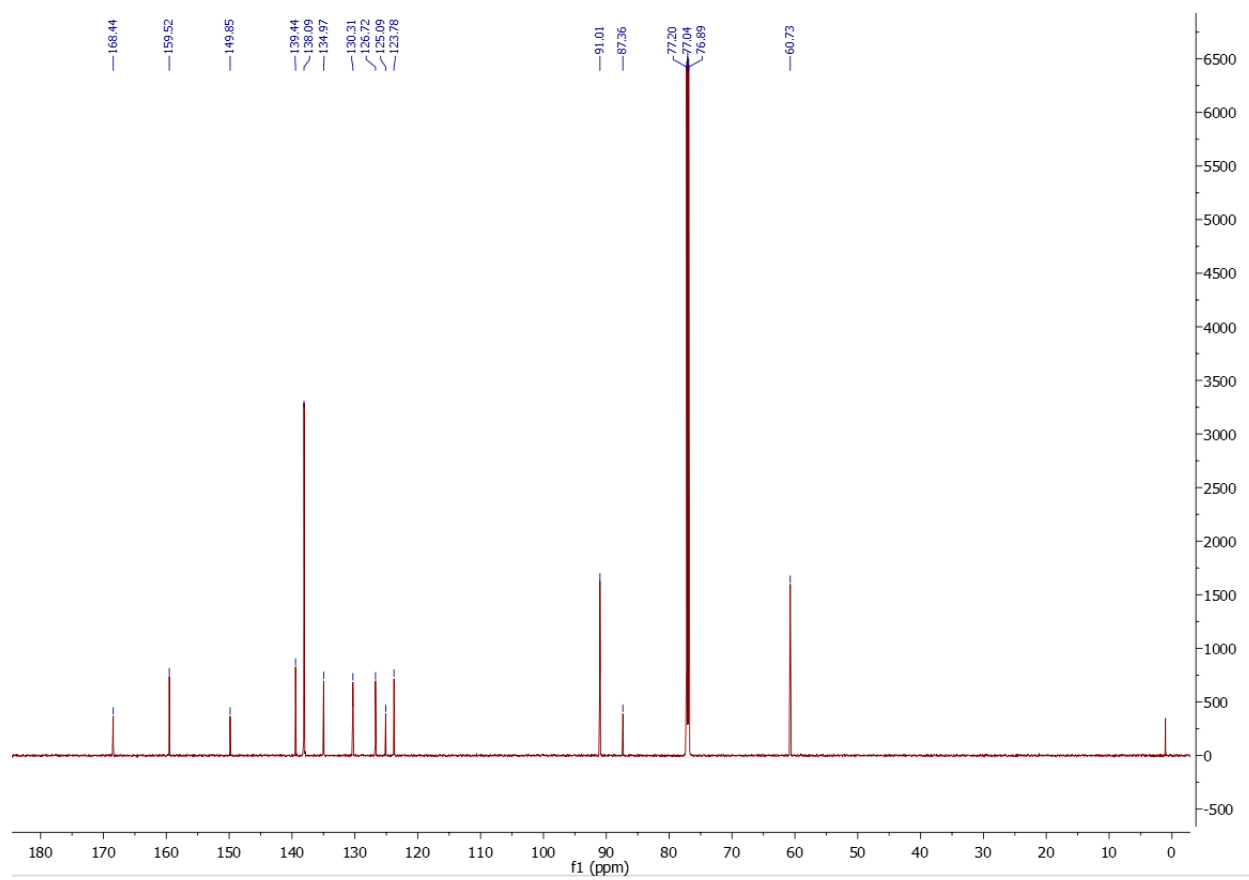


Figure B.2. ^1H NMR and ^{13}C NMR for 3,3-bis(3,5-diiodo-4-methoxyphenyl)isobenzofuran-1(3H)-one.

Figure B.2 continued



..

Single Crystal X-ray

Crystallization and Data Collection

Single crystals were grown from a solution of dichloromethane and ethyl acetate using hexane vapor diffusion. Two crystals were selected for data collection and analyzed to ensure reproducibility of results. The crystals were mounted on a Mitegen micromesh mount using a trace of mineral oil and cooled to 150 K. Data were collected on a Bruker D8 Quest Single Crystal CMOS Diffractometer (Bruker, Billerica, MA) with a sealed tube X-ray source generating Mo-K α radiation ($\lambda = 0.71073 \text{ \AA}$), a curved triumph monochromator with a 10 cm x 10 cm Photon-100 detector and fixed chi angle, and an Oxford Cryostream 800 plus variable temperature device (80-500K). Reflections were collected and processed, and the data was corrected for absorption and scaled by the multi-scan method using the Apex3 software v2018.1-0 (Bruker, Billerica, MA).

Structure Determination and Refinement

The space group was assigned and the structure was solved using XPREP within the SHELXTL suite of programs^{162, 163} by direct methods. Structure refinement was performed in SHELXL version 2018/3^{164, 165} by full matrix least squares on F^2 with all reflections. Hydrogen atoms attached to carbons were geometrically placed in calculated positions and were constrained to ride on their parent atoms, such that the hydrogen-carbon bond distance for the aromatic C-H was 0.95 \AA . $U_{\text{iso}}(\text{H})$ values for the C-H units were set to be a 1.2 multiple of $U_{\text{eq}}(\text{C})$. The imidazole and one of the phenyl groups were refined as disordered. The imidazole was refined in three parts such that two imidazole moieties were placed in similar positions but rotated 180° with one another, while the position of the third imidazole moiety was swapped with the position of one of the phenyl rings. Similarly, the phenyl ring was refined in three parts such that two phenyl moieties were placed in similar positions but slightly off shifted, coinciding with the rotation of the imidazole, while the position of the third phenyl moiety was swapped with the third imidazole moiety. All thermal parameters were restrained to be similar to each other. The bond distance between the central carbon atom and the carbon atom on the disordered phenyl ring was restrained to be similar to the bond distance between the central carbon atom and the carbon atom of one of the non-disordered phenyl rings for all disordered phenyl moieties. Similarly, the bond distance between the central

carbon atom and the nitrogen for the minor moieties was restrained to be similar to that for the major moiety. Lastly, the diffraction intensities were corrected for extinction. Complete crystallographic data, in CIF format, have been deposited with the Cambridge Crystallographic Data Center: CCDC xxxxxx. Additional crystal data, data collection and refinement details can be found in the supporting information. The data can be obtained free of charge from The Cambridge Crystallographic Data Centre via. www.ccdc.cam.ac.uk/datarequest/cif.

Table S1. X-ray crystallography experimental details for brotrimazole

| | |
|--|--|
| Crystal data | |
| Chemical formula | C ₂₂ H ₁₇ BrN ₂ |
| M_r | 389.28 |
| Crystal system, space group | Monoclinic, $P2_1/c$ |
| Temperature (K) | 150 |
| a, b, c (Å) | 11.1106 (6), 11.7583 (6), 13.1793 (7) |
| β (°) | 91.055 (2) |
| V (Å ³) | 1721.48 (16) |
| Z | 4 |
| Radiation type | Mo $K\alpha$ |
| μ (mm ⁻¹) | 2.39 |
| Crystal size (mm) | 0.44 × 0.23 × 0.06 |
| Data collection | |
| Diffractometer | Bruker AXS D8 Quest CMOS diffractometer |
| Absorption correction | Multi-scan SADABS 2016/2: Krause, L., Herbst-Irmer, R., Sheldrick G.M. & Stalke D. (2015). J. Appl. Cryst. 48 3-10. |
| T_{\min}, T_{\max} | 0.600, 0.746 |
| No. of measured, independent and observed [$I > 2\sigma(I)$] reflections | 33666, 5743, 4072 |
| R_{int} | 0.054 |
| $(\sin \theta/\lambda)_{\max}$ (Å ⁻¹) | 0.737 |
| Refinement | |
| $R[F^2 > 2\sigma(F^2)], wR(F^2), S$ | 0.038, 0.092, 1.03 |
| No. of reflections | 5743 |
| No. of parameters | 404 |
| No. of restraints | 864 |
| H-atom treatment | H-atom parameters constrained |
| $\Delta\rho_{\max}, \Delta\rho_{\min}$ (e Å ⁻³) | 0.67, -0.65 |

Computer programs: Apex3 v2018.1-0 (Bruker, 2018), SAINT V8.38A (Bruker, 2016), SHELXS97 (Sheldrick, 2008), SHELXL2018/3 (Sheldrick, 2018), SHELXLE Rev946 (Hübschle *et al.*, 2011).

Single Crystal Structure of Brotrimazole

Structure of brotrimazole were determined at a max resolution of 0.67 Å. As shown in Figure 3S, two phenyl rings are in a conformation of an “open clam”, and the Br atom is in between two “shells”. However, the structure of clotrimazole contains the Cl atom on the opposite side of the two phenyl rings according to the crystal structure in the Cambridge Crystallographic Data Center with ID PUVRIH.¹⁶⁶ Compared to Cl, Br is potentially more structurally hindered as a halogen bond donor. Interestingly, the brotrimazole crystal structure is disordered, where the positions of one of the phenyl rings and imidazole are swapped in 18.3% of the cases, as shown in Figure 3S. This behavior was confirmed in the second crystal analyzed. Despite the conformational differences, the distance between Br and C (shown in the green dotted line in Figure 1) is around 3.4 Å, which is slightly smaller than their sum of Van Der Waals radius, 3.55 Å, indicating intermolecular interaction.

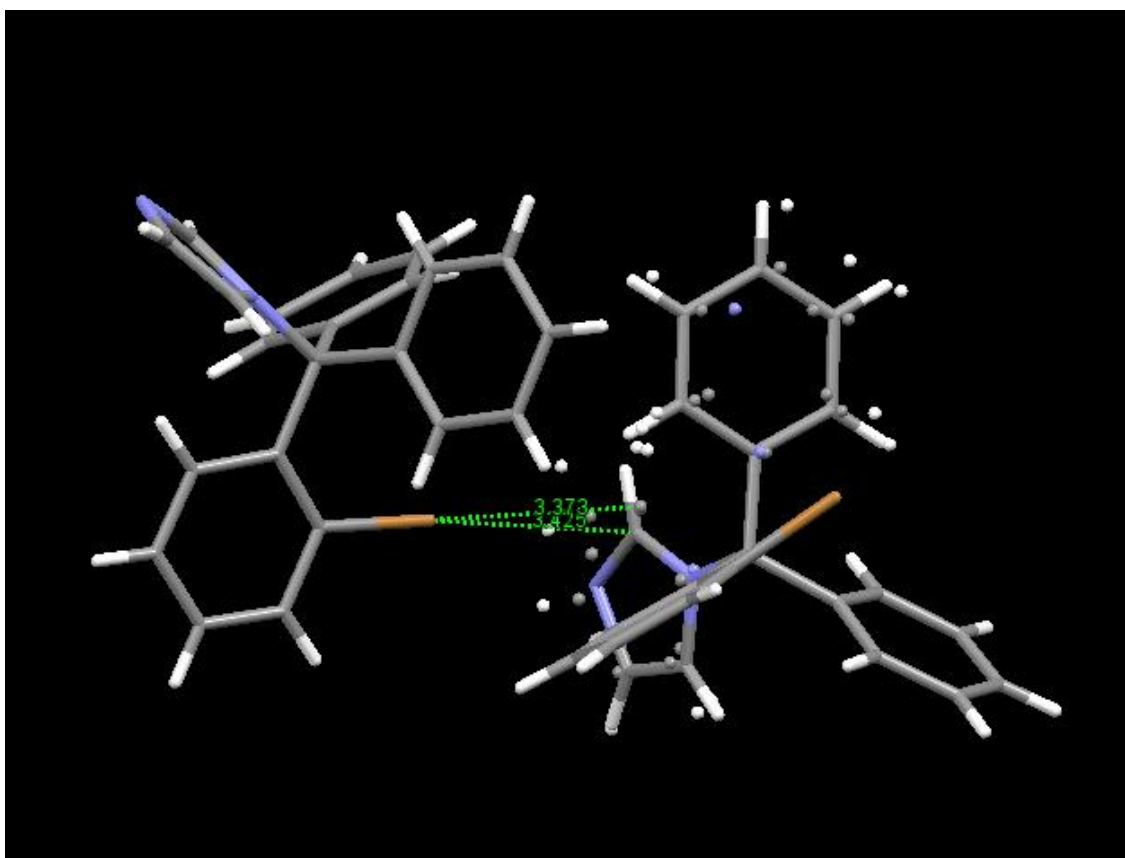


Figure B.3. Single crystal structure of brotrimazole. The interactions are indicated with distance (Å).

Preparation of Amorphous Solid Dispersions (ASDs)

All the amorphous solid dispersions were prepared by solvent evaporation using a rotatory evaporator (Brinkman Instruments, Westbury, NY). The organic solvent used to dissolve both drug and polymer was ethanol, except for Me-IDBF, where tetrahydrofuran was used. The temperature of the water bath was 60 °C and 40 °C for ethanol and tetrahydrofuran, respectively. Subsequently, the ASDs were placed in a vacuum oven for a day to remove residual organic solvent. Clotrimazole-PVPVA, clotrimazole-PVP, and loratadine-PVPVA ASDs were prepared with drug loadings of 10, 20, 25, 30, 40 and 50 wt. %. Brotrimazole-PVPVA and Me-DIBF-PVPVA ASDs were prepared with drug loading of 10, 20, 30 and 40 wt. %.

X-ray Photoelectron Spectroscopy (XPS)

XPS Acquisition and Data Analysis XPS data were obtained by a Kratos Axis Ultra DLD spectrometer using monochromic Al K α radiation (1486.6 eV). The spectra were collected at constant pass energy (PE) at 20 and 160 eV for high-resolution and survey spectra, respectively. A commercial build-in Kratos charge neutralizer was used to avoid non-homogeneous electric charge of non-conducting powder and to achieve better resolution. All the ASD samples for XPS were compressed into tablets prior to examination. 100 mg ASD powder was compressed at 1500 psi with a hydraulic press (Carver Inc, Wabash, IN) in a circular intrinsic die with diameter of 8 mm, and the compression pressure was held for 60s. Then the tablets were ejected manually from the die. The tablets were placed on a stainless steel sample holder bar using a double-sided sticking Cu tape. The XPS spectra were collected at 5 different points for each tablet. The size of analysis spot was 0.5 mm in diameter. XPS data were analyzed with CasaXPS software (www.casaxps.com). Prior to data analysis, the C-C component of the C 1s peak was set to a binding energy (BE) of 284.8 eV to correct for charge at each acquisition spot. Curve-fitting was performed following a Shirley background subtraction using Gaussian/Lorentzian peak shapes. The atomic concentrations of the elements in the near-surface region were estimated after a Shirley background subtraction taking into account the corresponding Scofield atomic sensitivity factors and inelastic mean free path (IMFP) of photoelectrons using standard procedures in the CasaXPS software assuming homogeneous mixture of the elements within the information depths (~10nm).

Table B.2. Total percentage of the lower binding energy halogen atoms in ASDs.

| | Drug (%) | Loading (%) | Percentage of halogen atoms with lower binding energies (%) |
|-------------------------|-------------|----------------|--|
| Clotrimazole/PVPVA | | | |
| | | 10 | 73.0 ± 18.4 |
| | | 20 | 55.3 ± 5.7 |
| | | 25 | 53.6 ± 8.7 |
| | | 30 | 56.7 ± 12.1 |
| | | 40 | 32.8 ± 1.5 |
| | | 50 | 30.1 ± 4.2 |
| Clotrimazole/PVP K29-32 | | | |
| | | 10 | 76.1 ± 7.7 |
| | | 20 | 60.6 ± 8.4 |
| | | 30 | 40.9 ± 8.9 |
| | | 40 | 51.6 ± 7.1 |
| | | 50 | 38.5 ± 7.1 |
| Loratadine/PVPVA | | | |
| | | 10 | 69.7 ± 7.9 |
| | | 20 | 82.1 ± 7.2 |
| | | 25 | 53.2 ± 5.8 |
| | | 30 | 43.7 ± 4.7 |
| | | 40 | 39.1 ± 4.3 |
| Brotrimazole/PVPVA | | | |
| | | 10 | 87.9 ± 1.3 |
| | | 20 | 71.1 ± 3.4 |
| | | 30 | 61.9 ± 1.6 |
| | | 40 | 55.9 ± 3.0 |
| Me-DIBF/PVPVA | | | |
| | | 10 | 60.8 ± 4.1 |
| | | 20 | 53.3 ± 5.1 |
| | | 30 | 29.9 ± 1.6 |
| | | 40 | 22.2 ± 1.5 |

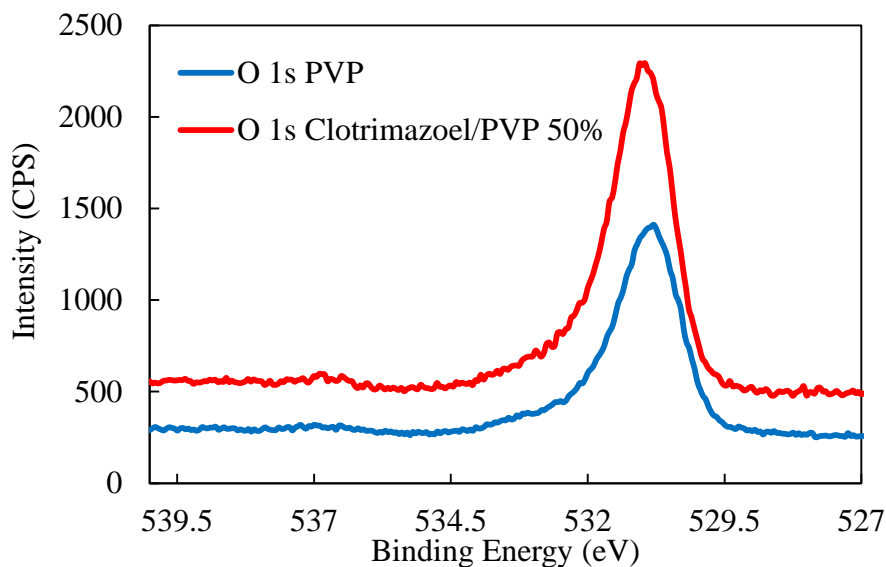


Figure B.4. X-ray photoemission spectrum of the O1s in PVP for pure PVP and clotrimazole/PVP 50/50 wt. %.

Nuclear Magnetic Resonance (NMR) Spectroscopy

^1H and ^{13}C NMR were performed using Bruker Avance-III-800 spectrometer (Billerica, MA) equipped with a QCI cryoprobe. Titration was used to obtain binding constants. Deuterated cyclohexane was chosen as a solvent to ensure sufficient solute solubility and to avoid interference with halogen bonding. Chemical shifts were reported relative to tetramethylsilane (TMS). All the samples were equilibrated at 25 °C for at least 5 min before data collection. To evaluate the weak interaction between drug or its analogy and 1-ethylpyrrolidinone (which is a monomeric analogue of PVP and maintains good solubility in toluene), we monitored model compound chemical shifts by EP titrations. The general procedure for titrations was as follows: a deuterated toluene stock solution with the host compound (concentration of 14.5 mM) was divided into eight NMR tubes (0.6 mL each). A variable amount of 1-ethyl-2-pyrrolidone (EP) as guest was added to each tube to provide a range of halogen bonding acceptor concentrations. The guest concentrations used were 11.0, 87.5, 173.2, 339.9, 654.6, 946.8, 1218.9 mM for each titration sample. The chemical shift of the host molecule was monitored and the titration curves were fit to a 1:1 binding model, which is a hyperbolic function, using OriginPro 2019 (Originlab Corporation, Northampton, MA) to determine the binding constant K_F , which is given by equation 1:

$$K_F = \frac{[AD]}{[A][D]} \quad (1)$$

where [AD] is the concentration of the halogen-bonded complex, while [A] and [D] are the concentrations of the free acceptor and the free donor, respectively.

Using NMR spectroscopic titration to attain binding constants is a widely used approach.^{111, 134, 167,}

¹⁶⁸ Titrations were repeated three times for reproducibility and estimation of errors, one set of representative NMR spectra and the titration curves for each model compound are presented here.

The binding constant was determined by both ¹H NMR and ¹³C NMR. For control experiments, 1-ethylpyrrolidine, which lacks the carbonyl group present in 1-ethylpyrrolidinone, was added to the host solution to examine its impact on the chemical shift.

Titration of Clotrimazole

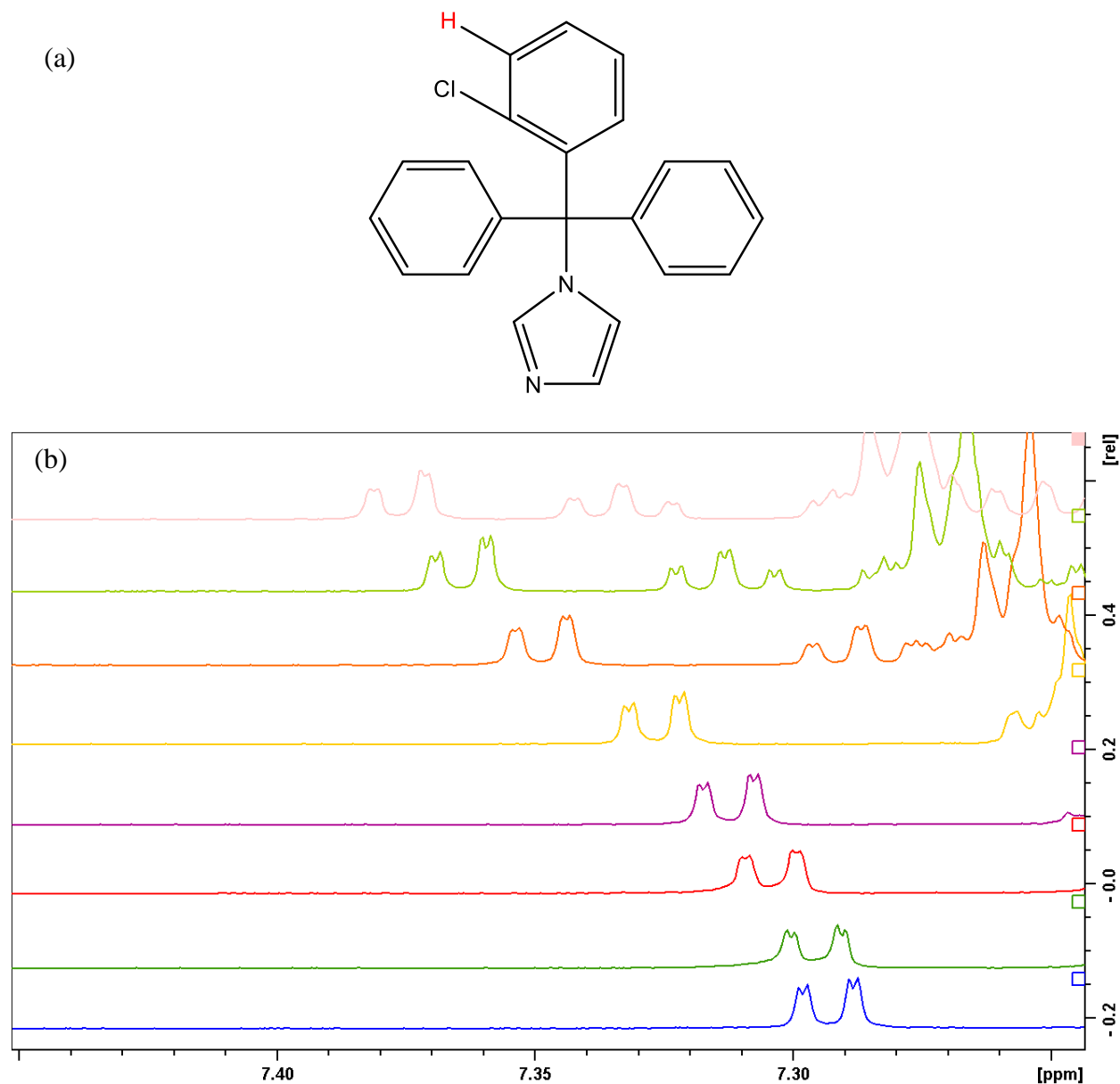
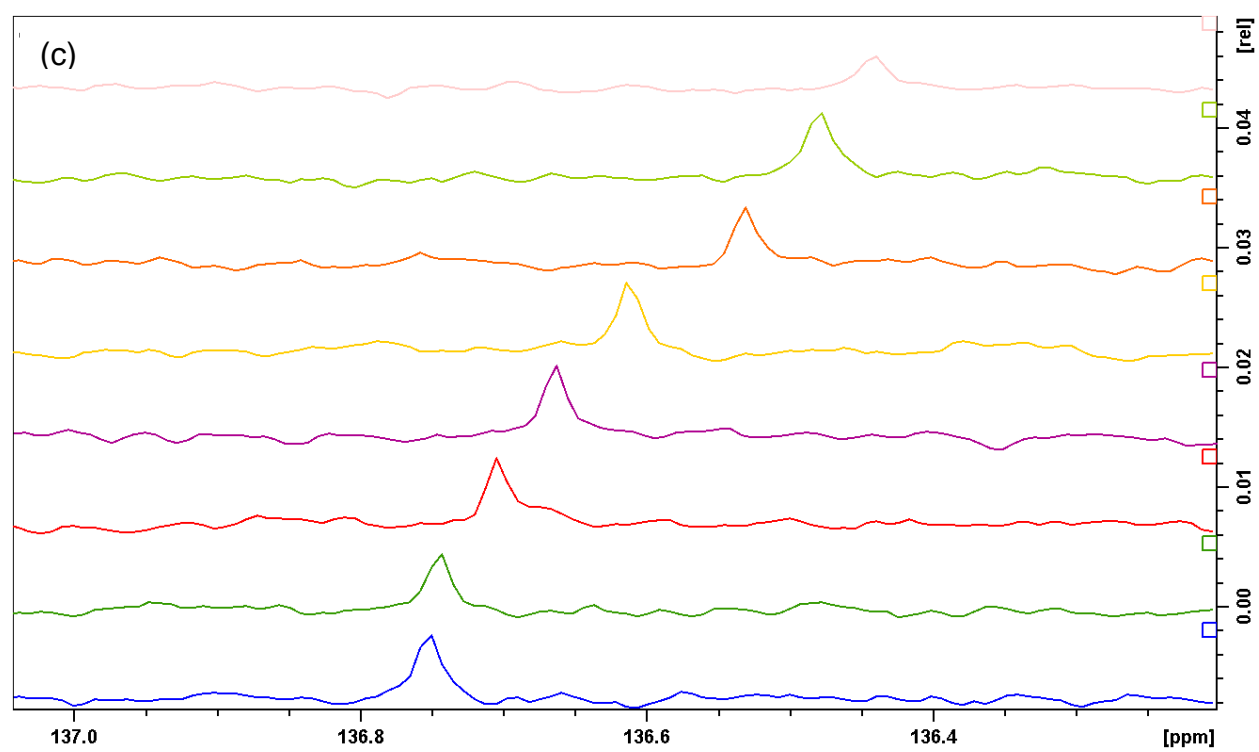


Figure B.5. (a) Chemical structure for clotrimazole. (b) ^1H NMR spectra of the proton on the para position to the chlorine atom in the presence of varying amount of 1-ethyl-2-pyrrolidone.

From bottom to top, the concentration of 1-ethyl-2-pyrrolidone is 0, 11, 87.5, 173.3, 339.9, 654.6, 946.8, 1219 mM. The peaks labeled with stars belong to the proton used in the titration curve. (c) ^{13}C NMR spectra of the chlorine-bonded carbon in the presence of varying amount of 1-ethyl-2-pyrrolidone. From bottom to top, the concentration of 1-ethyl-2-pyrrolidone is 0, 11, 87.5, 173.3, 339.9, 654.6, 946.8, 1219 mM.

Figure B.5 continued



Titration of brotrimazole

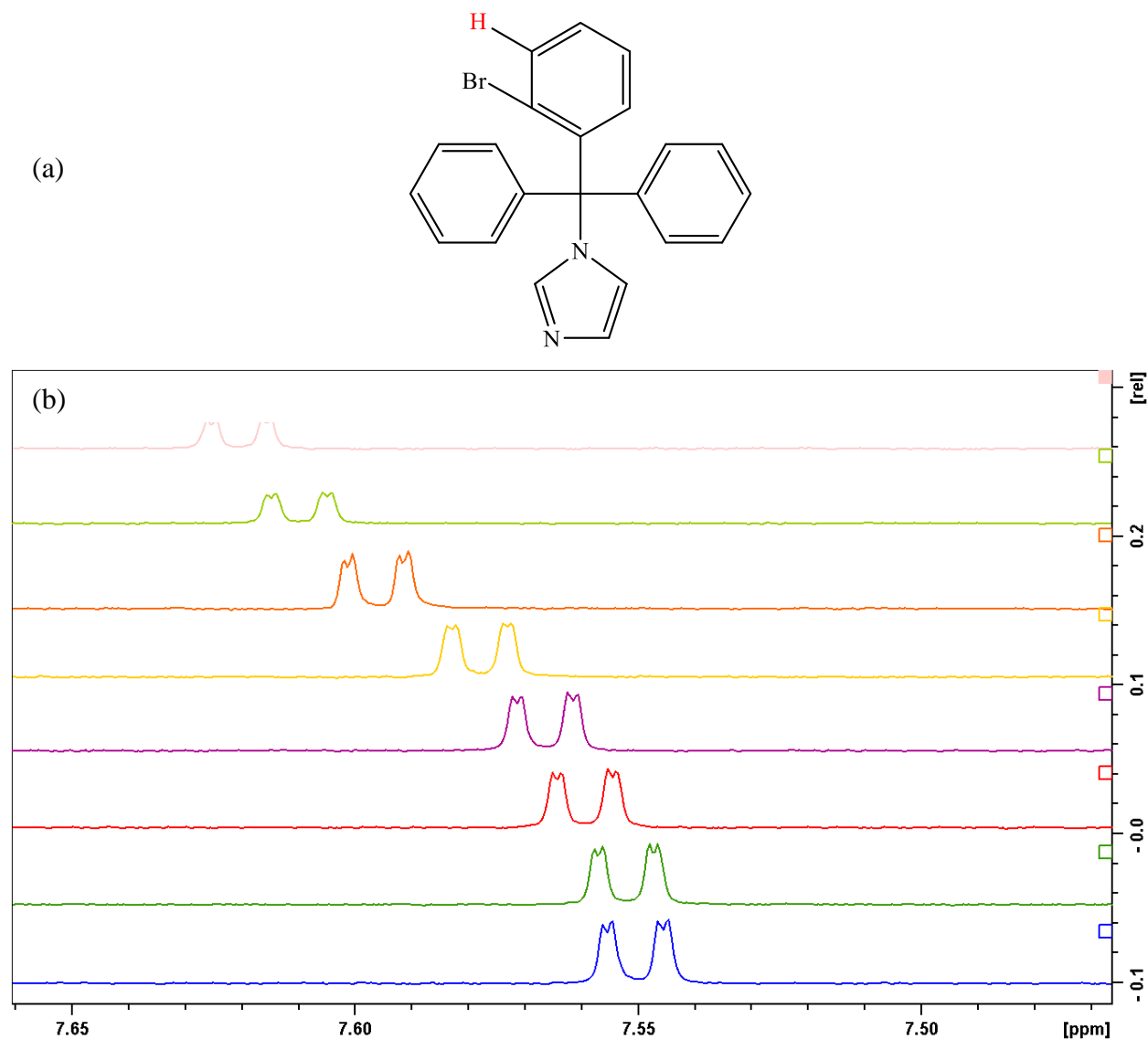
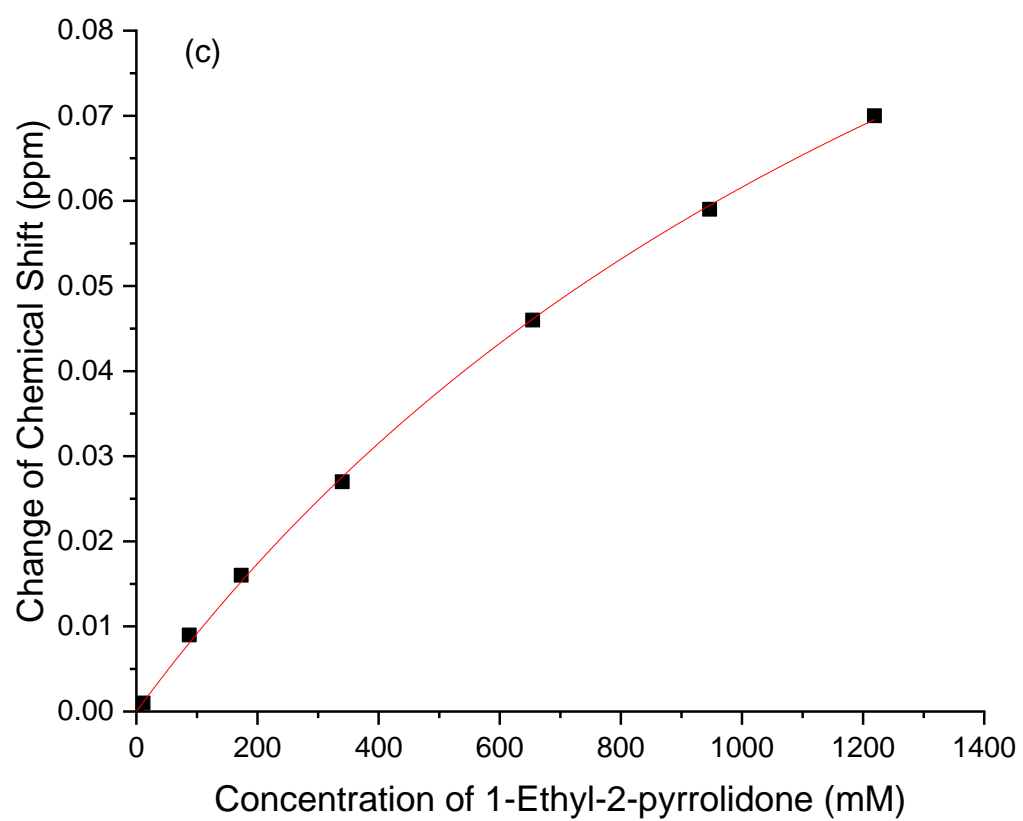


Figure B.6. (a) Chemical structure for brotrimazole. (b) ^1H NMR spectra of the proton on the para position to chlorine atom in the presence of varying amount of 1-ethyl-2-pyrrolidone, from bottom to top the concentration of 1-ethyl-2-pyrrolidone is 0, 11, 87.5, 173.3, 339.9, 654.6, 946.8, 1219 mM respectively. The peaks labeled with stars are the proton peak used for titration curve. (c) Plot of ^1H NMR chemical shift change as a function of the concentration of 1-ethyl-2-pyrrolidone.

Figure B.6 continued



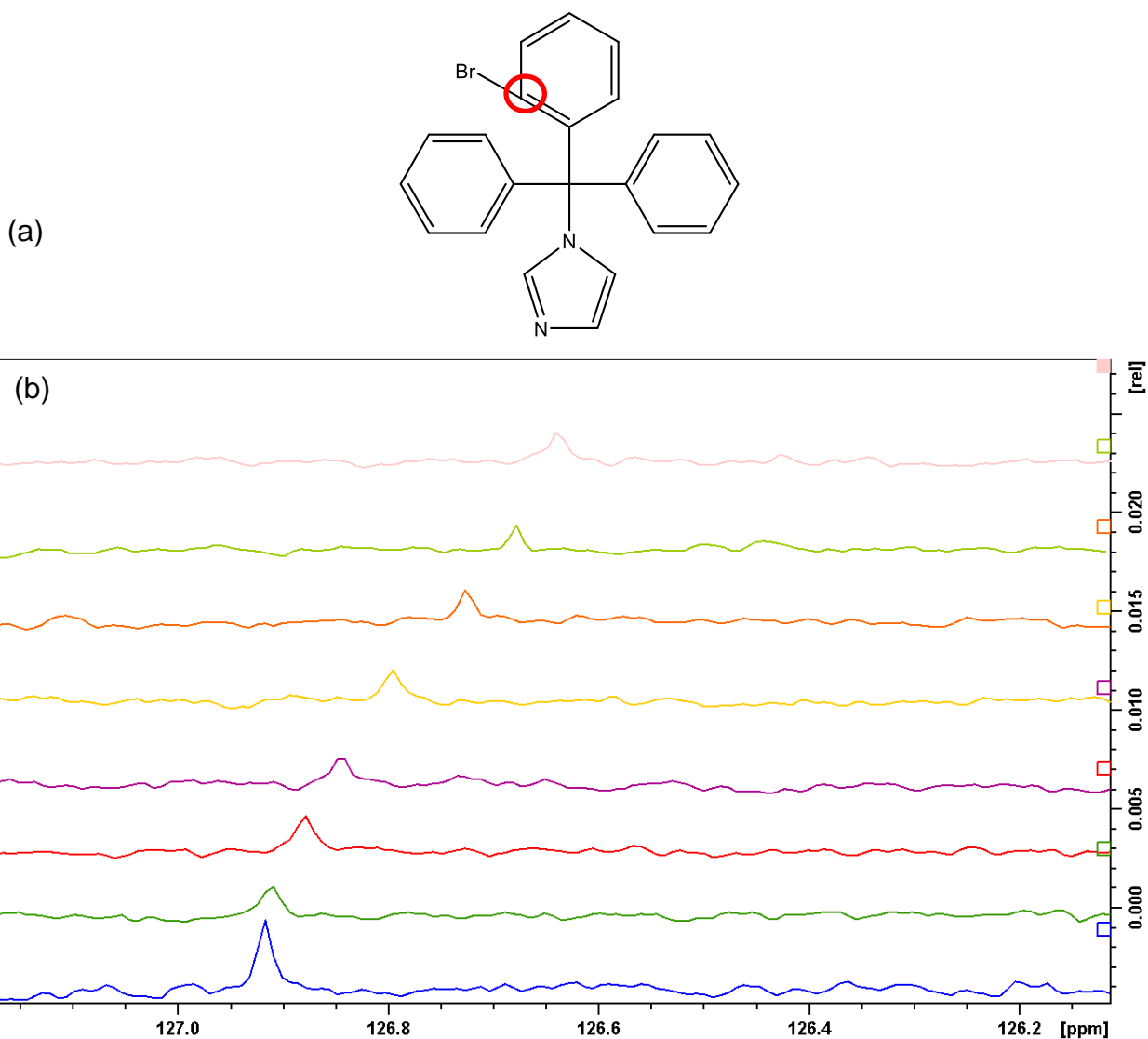
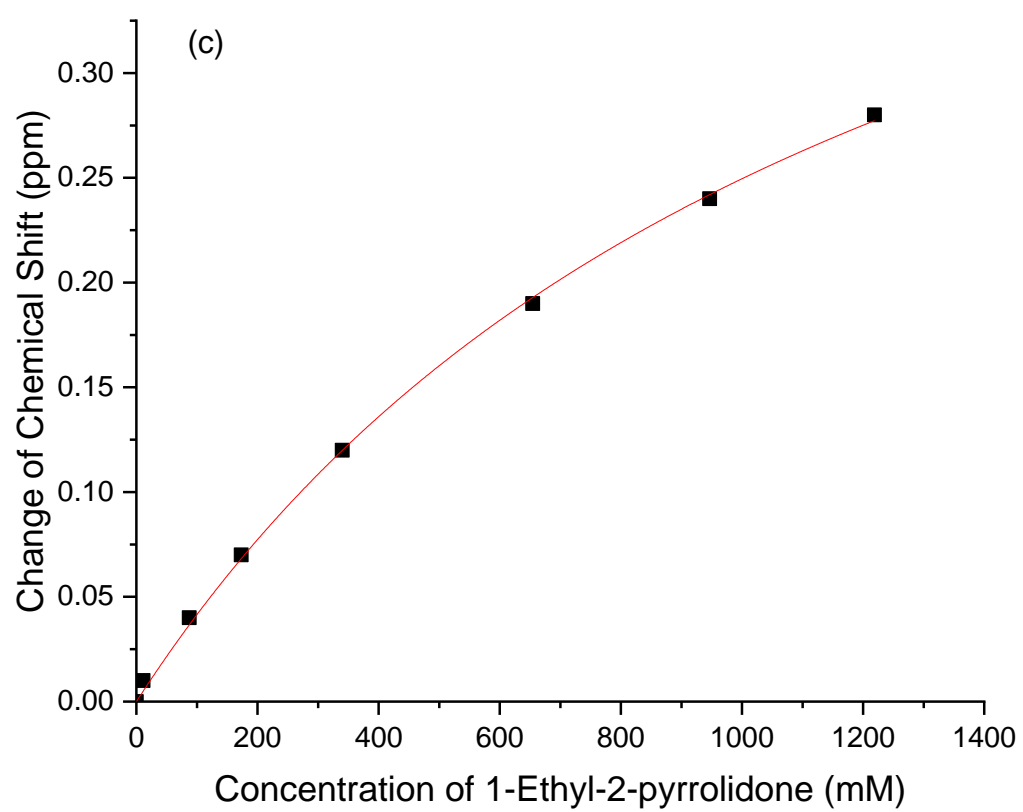


Figure B.7. (a) Chemical structure of brotrazole. (b) ^{13}C NMR spectra of carbon atom highlighted in the presence of varying amount of 1-ethyl-2-pyrrolidone, from bottom to top the concentration of 1-ethyl-2-pyrrolidone is 0, 11, 87.5, 173.3, 339.9, 654.6, 946.8, 1219 mM respectively. (c) Plot of ^{13}C NMR chemical shift change as a function of the concentration of 1-ethyl-2-pyrrolidone.

Figure B.7 continued



Titration of loratadine

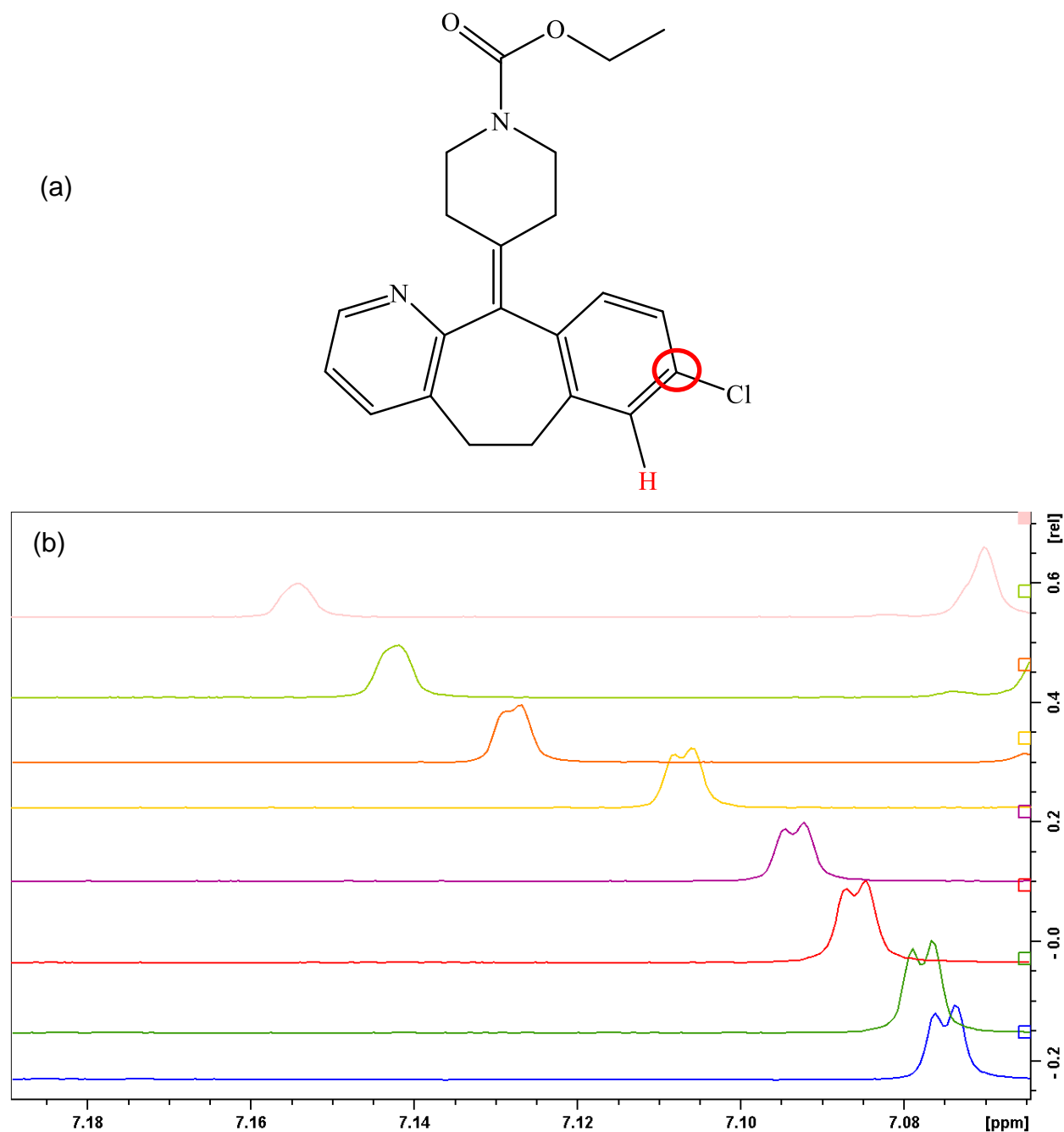
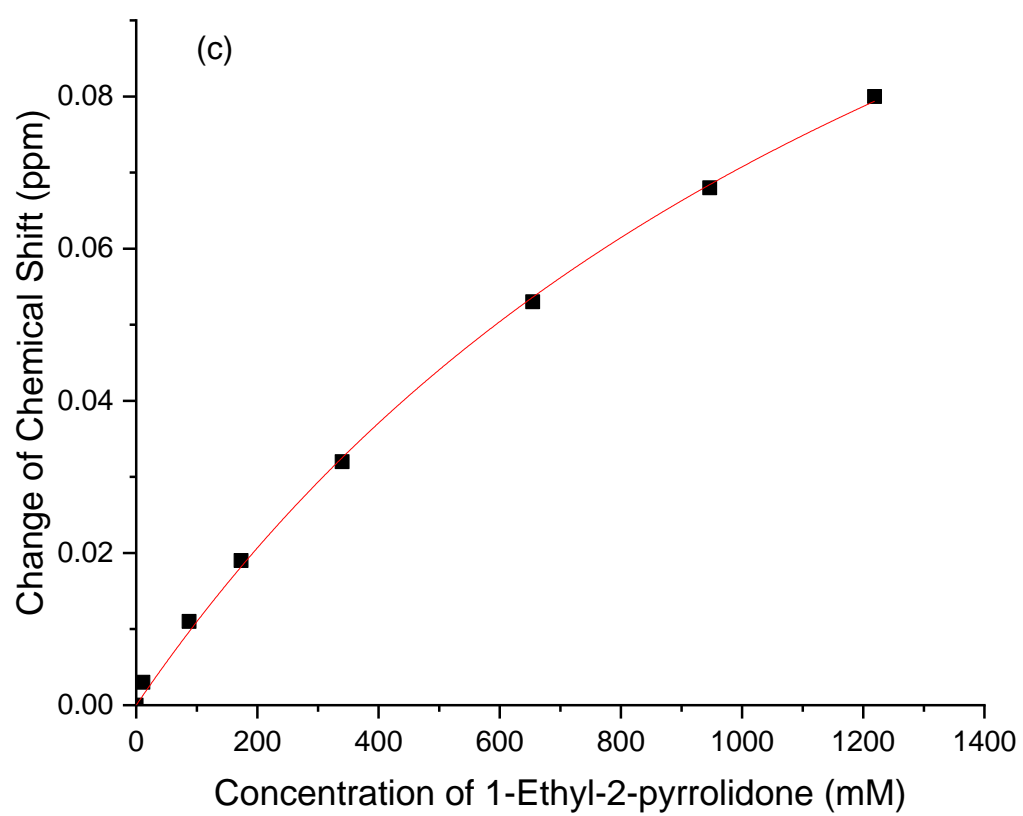


Figure B.8. (a) Chemical structure of loratadine. (b) ^1H NMR spectra of the proton highlighted in the presence of varying amount of 1-ethyl-2-pyrrolidone, from bottom to top the concentration of 1-ethyl-2-pyrrolidone is 0, 11, 87.5, 173.3, 339.9, 654.6, 946.8, 1219 mM respectively. The peaks labeled with stars are the proton peak used for titration curve. (c) Plot of ^1H NMR chemical shift change as a function of the concentration of 1-ethyl-2-pyrrolidone.

Figure B.8 continued



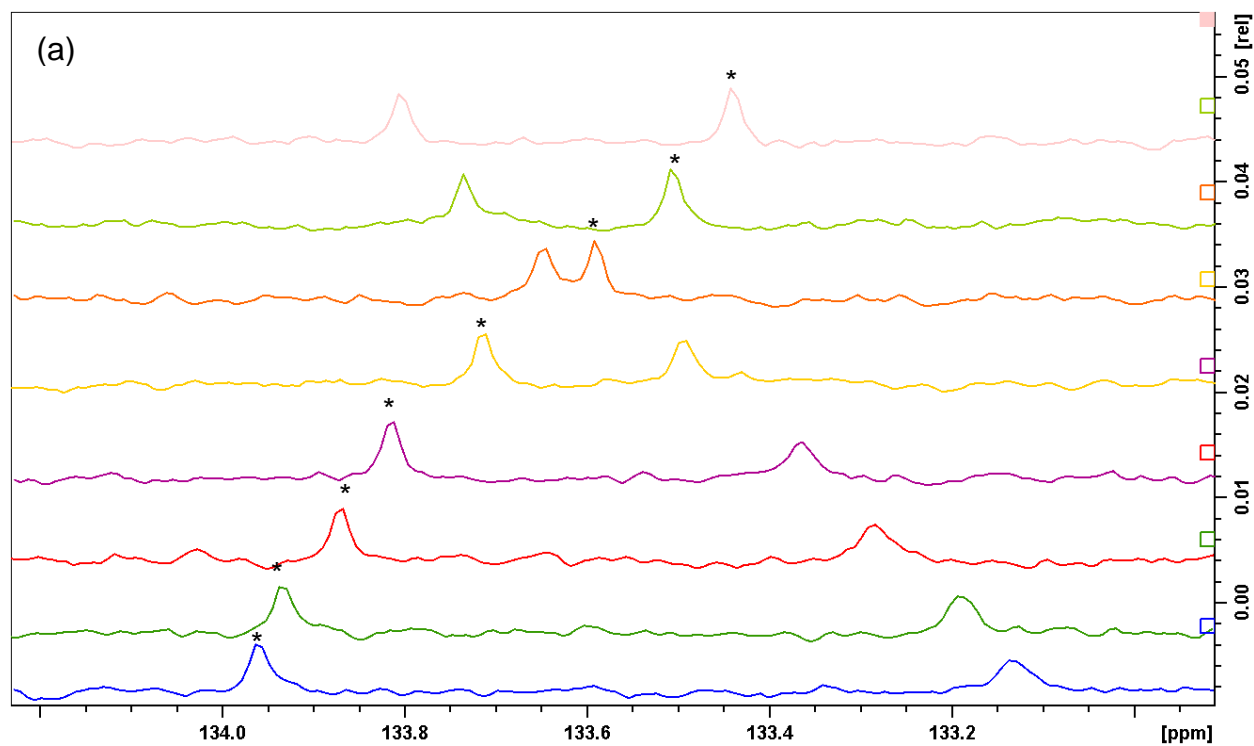
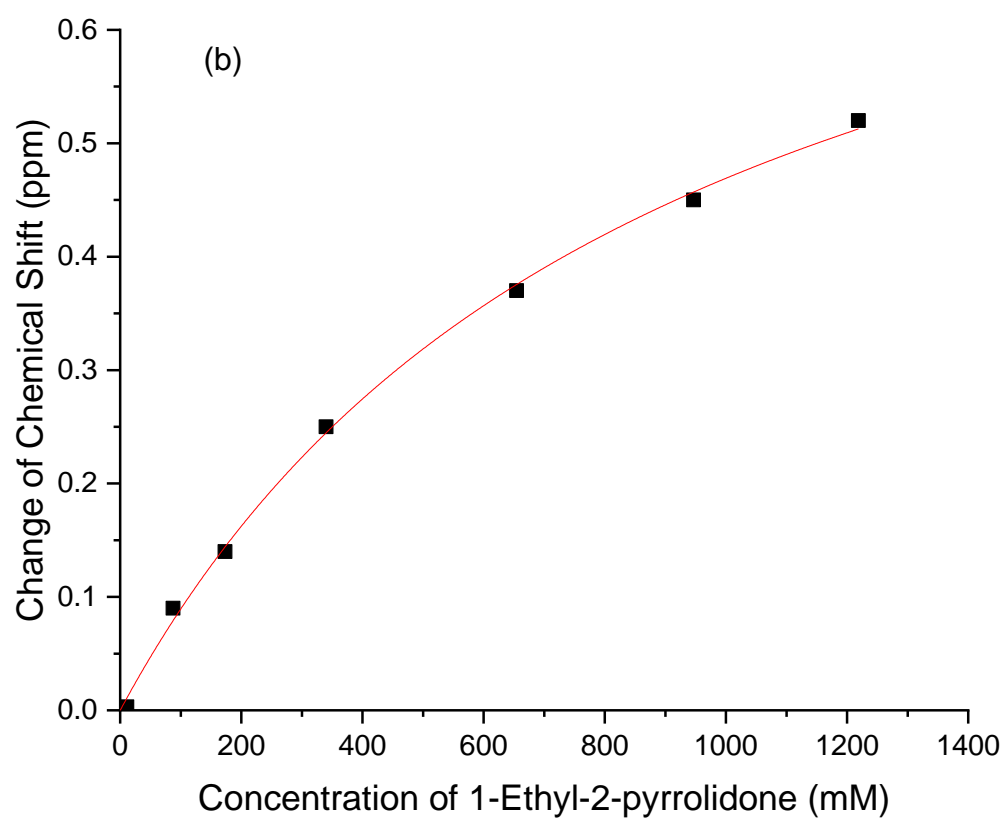


Figure B.9. (a) ^{13}C NMR spectra of carbon atom highlighted in the presence of varying amount of 1-ethyl-2-pyrrolidone, from bottom to top the concentration of 1-ethyl-2-pyrrolidone is 0, 11, 87.5, 173.3, 339.9, 654.6, 946.8, 1219 mM respectively. (b) Plot of ^{13}C NMR chemical shift change as a function of the concentration of 1-ethyl-2-pyrrolidone.

Figure B.9 continued



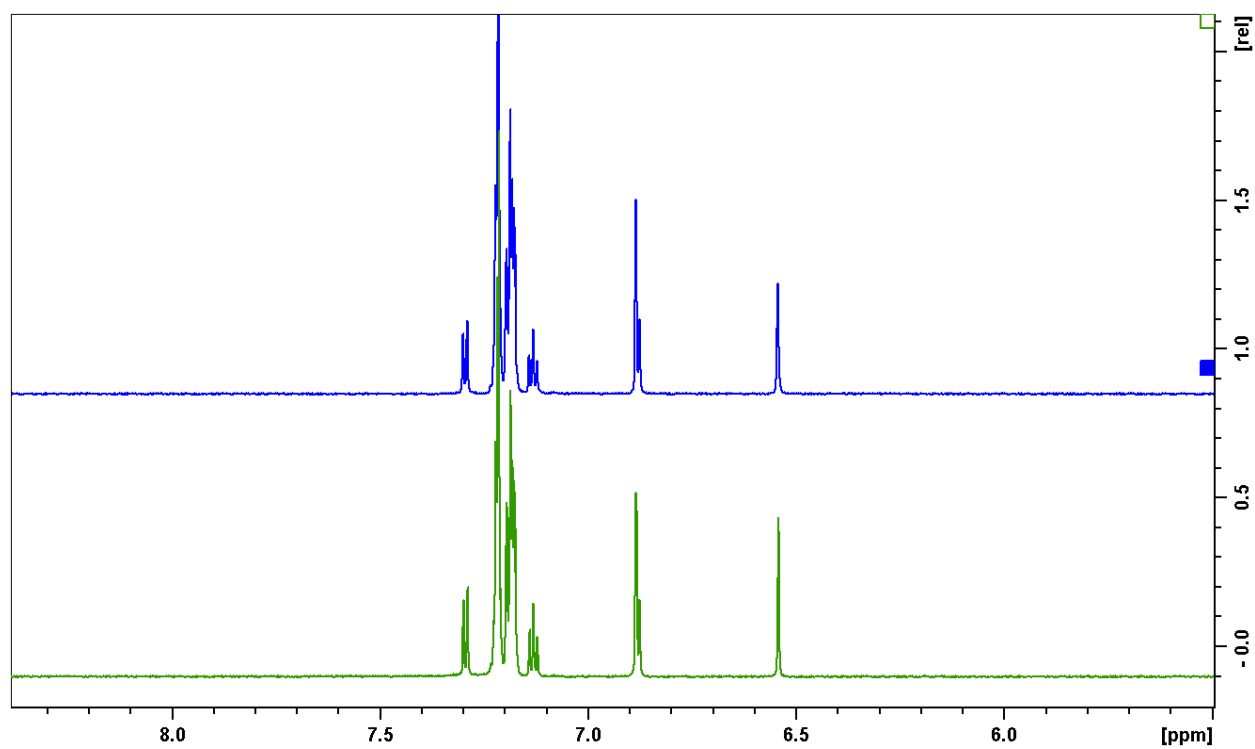


Figure B.10. ^1H NMR for clotrimazole in the presence of 654 mM of 1-ethylpyrrolidine (top spectrum), and 1-ethyl-2-pyrrolidone (bottom spectrum).

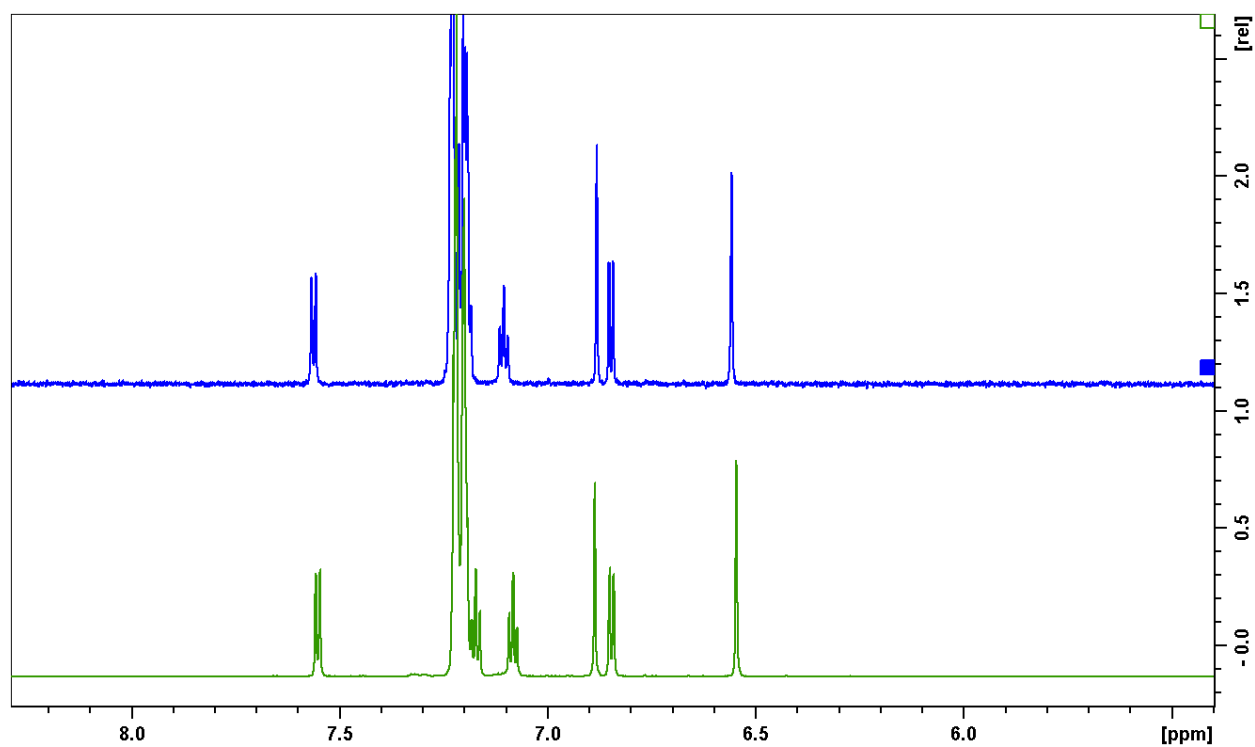


Figure B.11. ^1H NMR for brotriazole in the presence of 654 mM of 1-ethylpyrrolidine (top spectrum), and 1-ethyl-2-pyrrolidone (bottom spectrum).

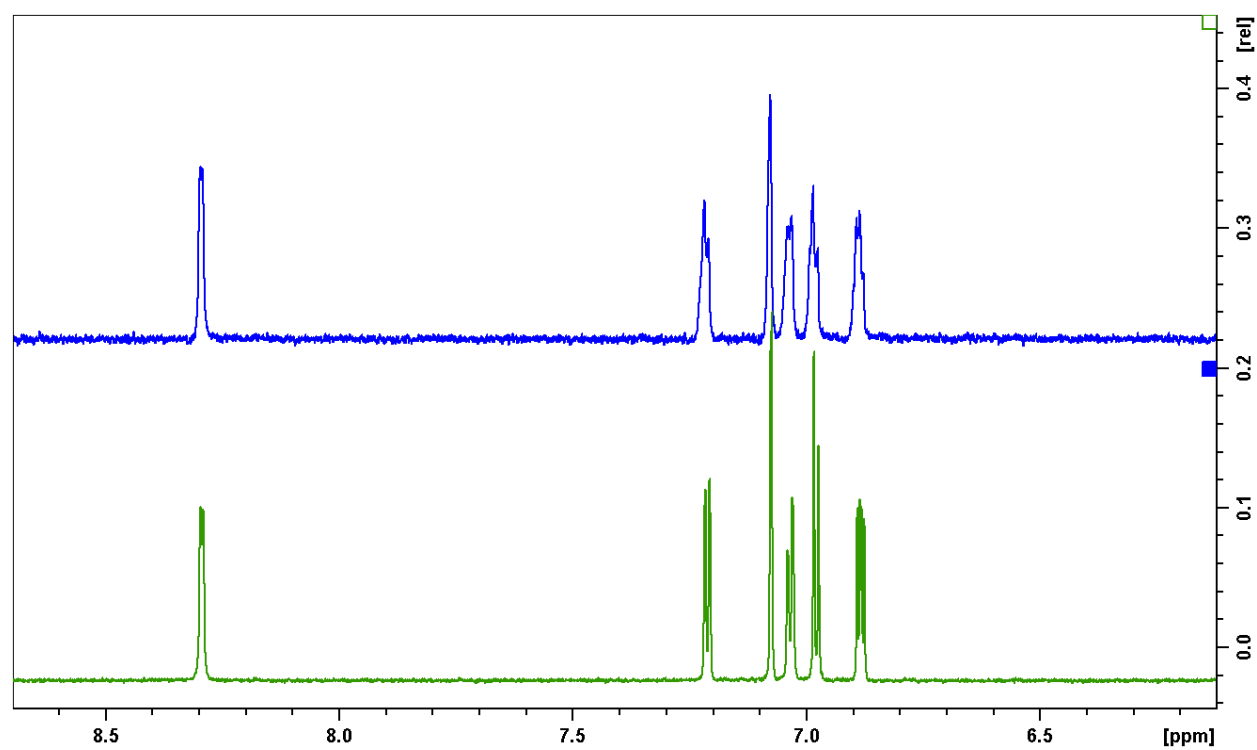


Figure B.12. ^1H NMR for loratadine in the presence of 654 mM of 1-ethylpyrrolidine (top spectrum), and 1-ethyl-2-pyrrolidone (bottom spectrum).

Binding Constants in Toluene

Table B.3. K_F values for halogen bonding between model compounds and 1-ethyl-2-pyrrolidone from the ^1H and ^{13}C NMR titration experiments at 25 °C in toluene.

| | K_F based on ^1H NMR (M^{-1}) | K_F based on ^{13}C NMR (M^{-1}) |
|--------------|---|--|
| Clotrimazole | 0.32 ± 0.09 | 0.35 ± 0.06 |
| Loratadine | 0.35 ± 0.11 | 0.39 ± 0.01 |
| Brotrimazole | 0.30 ± 0.11 | 0.21 ± 0.02 |

Bulk Infrared (IR) Spectroscopy

Thin films of pure PVPVA, clotrimazole-PVPVA mixtures, brotrimazole-PVPVA mixtures, and Me-DIBF-PVPVA mixtures were spin-coated on thallium bromoiodide (KRS-5) windows (Harrick Scientific Corporation, Ossining, NY) using a spin coater (Chemat Technology Inc., Northridge, CA). The general procedure for spin coating was as follows: 50 μL of the PVPVA or drug-PVPVA ethanol solution with solid content of 100 mg/mL was deposited onto the substrate, then it was spun for 15 s at 50 rpm followed by 50 s at 2500 rpm. The IR spectra were collected using a Bruker Vertex 70 FTIR spectrometer (Bruker, Billerica, MA). For each sample, 128 scans were collected for both background and samples at a resolution of 4 cm^{-1} . The data was analyzed utilizing OPUS software (version 7.2, Bruker Billerica, MA). IR spectra for loratadine-PVPVA were not collected due to the overlap of the carbonyl group in loratadine with PVPVA carbonyl group region.

APPENDIX C. SUPPORTING INFORMATION FOR CHAPTER 5

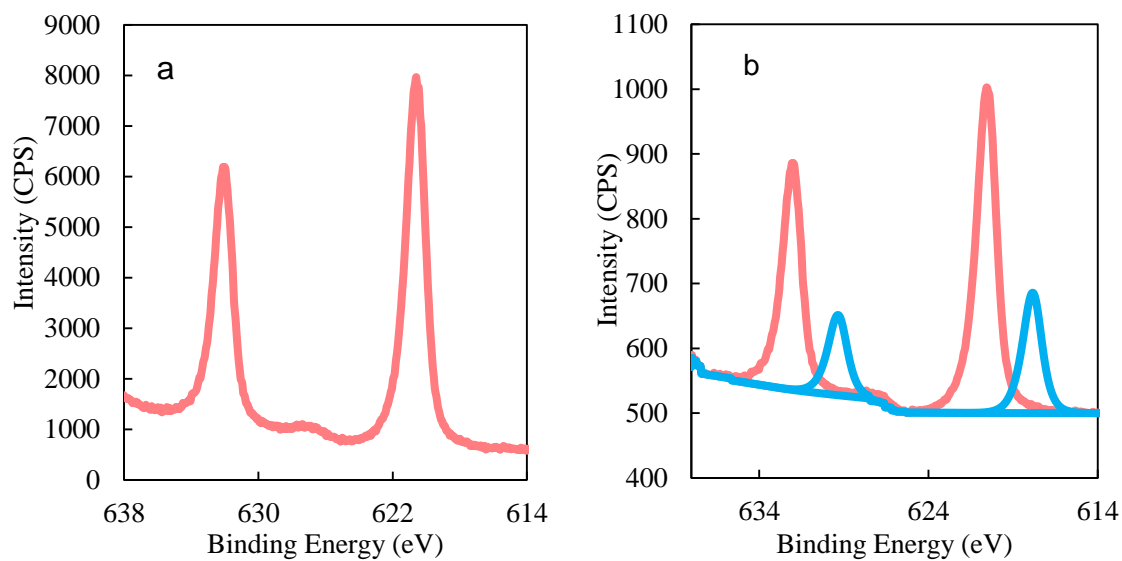


Figure C.2 XPS I 3d spectrum for (a) neat amorphous TIPP and (b) TIPP in ASDs with 20% drug loading.

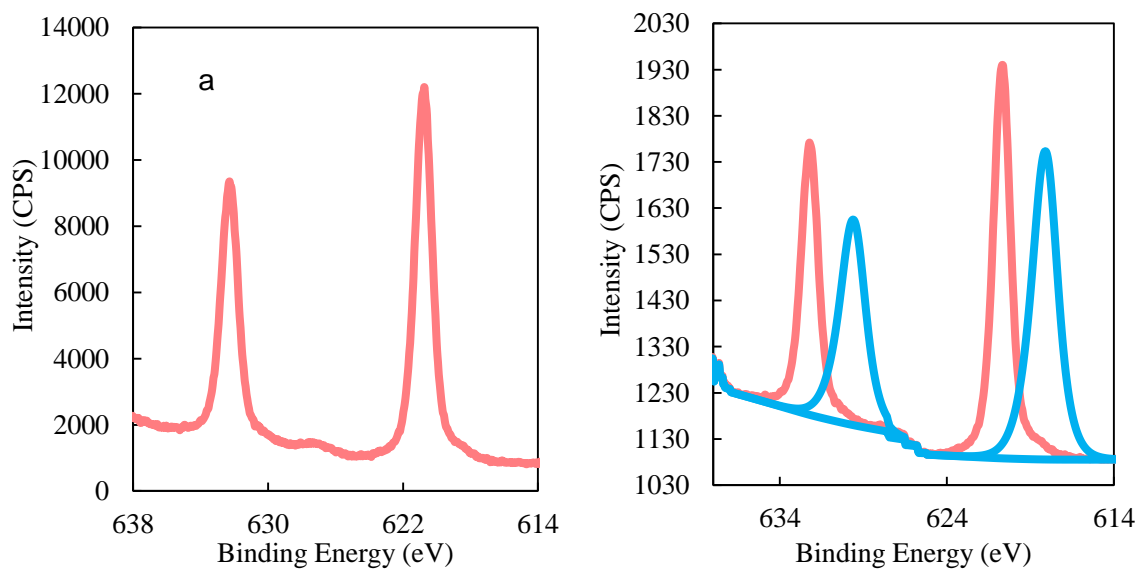


Figure C.2 XPS I 3d spectrum for (a) neat amorphous Me-TIPP and (b) Me-TIPP in ASDs with 20% drug loading.

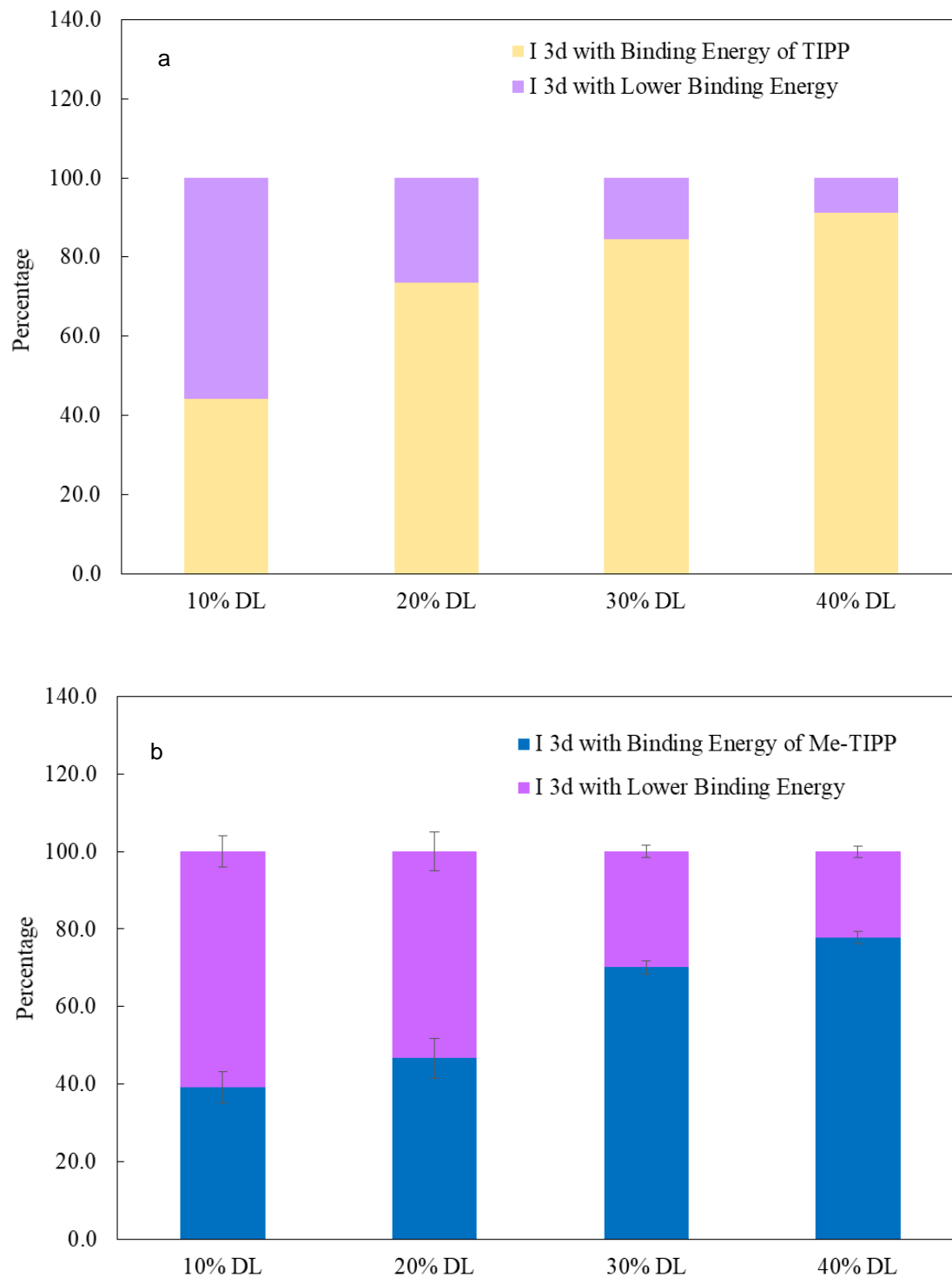


Figure C.3 The percentage of iodo atoms with high (as found in the neat compound) and low binding energies (new peaks seen in the ASD) as a function of drug loading (DL) in the ASD for ASD system (a) TIPPP/PVPVA, (b) Me-TIPPP/PVPVA.

REFERENCES

1. Lipinski, C. A. Drug-like Properties and the Causes of Poor Solubility and Poor Permeability. *Journal of Pharmacological and Toxicological Methods* **2000**, *44*, 235-249.
2. Loftsson, T.; Brewster, M. E. Pharmaceutical Applications of Cyclodextrins: Basic Science and Product Development. *J. Pharm. Pharmacol.* **2010**, *62*, (11), 1607-21.
3. Almeida e Sousa, L.; Reutzel-Edens, S. M.; Stephenson, G. A.; Taylor, L. S. Assessment of the Amorphous "Solubility" of a Group of Diverse Drugs using New Experimental and Theoretical Approaches. *Mol. Pharm.* **2015**, *12*, (2), 484-95.
4. Zha, J. Pharmaceutical compositions for use in the treatment of cystic fibrosis. US 2014/0221424 A1, 2014.
5. Trasi, N. S.; Purohit, H. S.; Taylor, L. S. Evaluation of the Crystallization Tendency of Commercially Available Amorphous Tacrolimus Formulations Exposed to Different Stress Conditions. *Pharm. Res.* **2017**, *34*, (10), 2142–2155.
6. Schmitt, P. D.; Trasi, N. S.; Taylor, L. S.; Simpson, G. J. Finding the Needle in the Haystack: Characterization of Trace Crystallinity in a Commercial Formulation of Paclitaxel Protein-Bound Particles by Raman Spectroscopy Enabled by Second Harmonic Generation Microscopy. *Mol. Pharm.* **2015**, *12*, (7), 2378-2383.
7. Ilevbare, G. A.; Taylor, L. S. Liquid–Liquid Phase Separation in Highly Supersaturated Aqueous Solutions of Poorly Water-Soluble Drugs: Implications for Solubility Enhancing Formulations. *Cryst. Growth Des.* **2013**, *13*, (4), 1497-1509.
8. Indulkar, A. S.; Gao, Y.; Raina, S. A.; Zhang, G. G.; Taylor, L. S. Exploiting the Phenomenon of Liquid-Liquid Phase Separation for Enhanced and Sustained Membrane Transport of a Poorly Water-Soluble Drug. *Mol. Pharm.* **2016**, *13*, (6), 2059-69.
9. Wilson, V.; Lou, X.; Osterling, D. J.; Stolarik, D. F.; Jenkins, G.; Gao, W.; Zhang, G. G. Z.; Taylor, L. S. Relationship between Amorphous Solid Dispersion in vivo Absorption and in vitro Dissolution: Phase Behavior during Dissolution, Speciation, and Membrane Mass Transport. *J. Control. Release* **2018**, *292*, 172-182.
10. Indulkar, A. S.; Lou, X.; Zhang, G. G. Z.; Taylor, L. S. Insights into the Dissolution Mechanism of Ritonavir-Copovidone Amorphous Solid Dispersions: Importance of Congruent Release for Enhanced Performance. *Mol. Pharm.* **2019**, *16*, (3), 1327-1339.
11. Saboo, S.; Mugheirbi, N. A.; Zemlyanov, D. Y.; Kestur, U. S.; Taylor, L. S. Congruent Release of Drug and Polymer: A "Sweet Spot" in the Dissolution of Amorphous Solid Dispersions. *J. Control. Release* **2019**, *298*, 68-82.

12. Taylor, L. S.; Zografi, G. Spectroscopic characterization of interactions between PVP and indomethacin in amorphous molecular dispersions. *Pharm. Res.* **1997**, *14*, (12), 1691-1698.
13. Huang, J.; Wigent, R. J.; Schwartz, J. B. Drug-polymer Interaction and Its Significance on the Physical Stability of Nifedipine Amorphous Dispersion in Microparticles of an Ammonio Methacrylate Copolymer and Ethylcellulose Binary Blend. *J Pharm Sci* **2008**, *97*, (1), 251-62.
14. Rumondor, A. C.; Wikstrom, H.; Van Eerdenbrugh, B.; Taylor, L. S. Understanding the Tendency of Amorphous Solid Dispersions to Undergo Amorphous-amorphous Phase Separation in the Presence of Absorbed Moisture. *AAPS PharmSciTech* **2011**, *12*, (4), 1209-19.
15. Miyazaki, T.; Yoshioka, S.; Aso, Y.; Kojima, S. Ability of polyvinylpyrrolidone and polyacrylic acid to inhibit the crystallization of amorphous acetaminophen. *J. Pharm. Sci.* **2004**, *93*, (11), 2710-2717.
16. Cavallo, G.; Metrangolo, P.; Milani, R.; Pilati, T.; Priimagi, A.; Resnati, G.; Terraneo, G. The Halogen Bond. *Chemical Reviews* **2016**, *116*, (4), 2478-2601.
17. Aakeroy, C. B.; Spartz, C. L.; Dembowski, S.; Dwyre, S.; Desper, J. A Systematic Structural Study of Halogen Bonding versus Hydrogen Bonding within Competitive Supramolecular Systems. *IUCrJ* **2015**, *2*, (Pt 5), 498-510.
18. Gurunath, S.; Pradeep Kumar, S.; Basavaraj, N. K.; Patil, P. A. Amorphous solid dispersion method for improving oral bioavailability of poorly water-soluble drugs. *Journal of Pharmacy Research* **2013**, *6*, (4), 476-480.
19. Ediger, M. D.; Angell, C. A.; Nagel, S. R. Supercooled Liquids and Glasses. *J. Chem. Phys.* **1996**, *100*, (31), 13200-13212.
20. Hoffman, J. D. Thermodynamic Driving Force in Nucleation and Growth Processes. *J. Chem. Phys.* **1958**, *29*, (5), 1192-1193.
21. Hancock, B. C.; Parks, M. What is the True Solubility Advantage for Amorphous Pharmaceuticals? *Pharm. Res.* **2000**, *17*, (4), 397-404.
22. Mullin, J. W., Crystallization. Butterworth-Heinemann: Oxford, 2001.
23. Tung, H.-H.; Paul, E. L.; Midler, M.; McCauley, J. A., *Crystallization of organic compounds: an industrial perspective*. Original ed.; John Wiley & Sons: New Jersey, 2009.
24. Mosquera-Giraldo, L. I.; Taylor, L. S. Glass-Liquid Phase Separation in Highly Supersaturated Aqueous Solutions of Telaprevir. *Mol. Pharm.* **2015**, *12*, (2), 496-503.
25. Mullin, J. W., Nucleation. In *Crystallization (Fourth Edition)*, Butterworth-Heinemann: Oxford, 2001; pp 181-215.

26. Söhnel, O.; Mullin, J. W. Interpretation of crystallization induction periods. *J. Colloid Interface Sci.* **1988**, *123*, (1), 43-50.
27. Qian, R.-Y.; Botsaris, G. D. Nuclei breeding from a chiral crystal seed of NaClO₃. *Chemical Engineering Science* **1998**, *53*, (9), 1745-1756.
28. McBride, J. M.; Carter, R. L. Spontaneous Resolution by Stirred Crystallization. *Angewandte Chemie International Edition in English* **1991**, *30*, (3), 293-295.
29. Reyhani, M. M.; Freij, S.; Parkinson, G. M. In situ atomic force microscopy investigation of the growth of secondary nuclei produced by contact of different growth faces of potash alum crystals under supersaturated solutions. *J. Cryst. Growth* **1999**, *198–199, Part 1*, 258-263.
30. Agrawal, S. G.; Paterson, A. H. J. Secondary Nucleation: Mechanisms and Models. *Chemical Engineering Communications* **2015**, *202*, (5), 698-706.
31. Tai, C. Y.; Tai, C.-D.; Chang, M.-H. Effect of interfacial supersaturation on secondary nucleation. *Journal of the Taiwan Institute of Chemical Engineers* **2009**, *40*, (4), 439-442.
32. Garside, J.; Davey, R. J. INVITED REVIEW SECONDARY CONTACT NUCLEATION: KINETICS, GROWTH AND SCALE-UP. *Chemical Engineering Communications* **1980**, *4*, (4-5), 393-424.
33. Burton, W. K.; Cabrera, N.; Frank, F. C. The Growth of Crystals and the Equilibrium Structure of their Surfaces. *Philos. Trans. R. Soc., A* **1951**, *243*, (866), 299-358.
34. Kossel, W. Zur Theorie des Kristallwachstums. *Nachrichten von der Gesellschaft der Wissenschaften zu Göttingen, Mathematisch-Physikalische Klasse* **1927**, *1927*, 135-143.
35. Markov, I. V., *Crystal growth for beginners: fundamentals of nucleation, crystal growth and epitaxy*. World scientific: 2003.
36. Hartman, P.; Perdok, W. On the relations between structure and morphology of crystals. I. *Acta Crystallographica* **1955**, *8*, (1), 49-52.
37. Mullin, J. W., 6 - Crystal growth. In *Crystallization (Fourth Edition)*, Butterworth-Heinemann: Oxford, 2001; pp 216-288.
38. Kostov, R., Crystals: Growth, Morphology and Perfection. The Canadian Mineralogist: 2005.
39. Noyes, A. A.; Whitney, W. R. THE RATE OF SOLUTION OF SOLID SUBSTANCES IN THEIR OWN SOLUTIONS. *Journal of the American Chemical Society* **1897**, *19*, (12), 930-934.
40. Berthoud, A. L., *Theorie de la formation des faces d'un cristal*. 1912.

41. Valetton, J. I. Wachstum und Auflösung der Kristalle. III. *Zeitschrift für Kristallographie-Crystalline Materials* **1924**, 60, (1-6), 1-38.
42. Broman, E.; Khoo, C.; Taylor, L. S. A comparison of alternative polymer excipients and processing methods for making solid dispersions of a poorly water soluble drug. *Int. J. Pharm.* **2001**, 222, (1), 139-151.
43. Hancock, B. C.; Shamblin, S. L.; Zografi, G. Molecular mobility of amorphous pharmaceutical solids below their glass transition temperatures. *Pharm. Res.* **1995**, 12, (6), 799-806.
44. Flory, P. J., *Principles of polymer chemistry*. Cornell University Press: 1953.
45. Rumondor, A. C. F.; Marsac, P. J.; Stanford, L. A.; Taylor, L. S. Phase Behavior of Poly(vinylpyrrolidone) Containing Amorphous Solid Dispersions in the Presence of Moisture. *Mol. Pharm.* **2009**, 6, (5), 1492-1505.
46. Ilevbare, G. A.; Liu, H.; Edgar, K. J.; Taylor, L. S. Maintaining Supersaturation in Aqueous Drug Solutions: Impact of Different Polymers on Induction Times. *Cryst. Growth Des.* **2013**, 13, (2), 740-751.
47. Trasi, N. S.; Abbou Oucherif, K.; Litster, J. D.; Taylor, L. S. Evaluating the influence of polymers on nucleation and growth in supersaturated solutions of acetaminophen. *CrystEngComm* **2015**, 17, (6), 1242-1248.
48. Lindfors, L.; Forssén, S.; Westergren, J.; Olsson, U. Nucleation and crystal growth in supersaturated solutions of a model drug. *J. Colloid Interface Sci.* **2008**, 325, (2), 404-413.
49. Anwar, J.; Boateng, P. K.; Tamaki, R.; Odedra, S. Mode of Action and Design Rules for Additives That Modulate Crystal Nucleation. *Angewandte Chemie International Edition* **2009**, 48, (9), 1596-1600.
50. Tai, C. Y.; Wu, J.-F.; Rousseau, R. W. Interfacial supersaturation, secondary nucleation, and crystal growth. *J. Cryst. Growth* **1992**, 116, (3-4), 294-306.
51. Shirai, Y.; Nakanishi, K.; Matsuno, R.; Kamikubo, T. Effects of Polymers on Secondary Nucleation of Ice Crystals. *Journal of Food Science* **1985**, 50, (2), 401-406.
52. Ilevbare, G. A.; Liu, H.; Edgar, K. J.; Taylor, L. S. Understanding Polymer Properties Important for Crystal Growth Inhibition · Impact of Chemically Diverse Polymers on Solution Crystal Growth of Ritonavir. *Cryst. Growth Des.* **2012**, 12, (6), 3133-3143.
53. Ilevbare, G. A.; Liu, H.; Edgar, K. J.; Taylor, L. S. Impact of polymers on crystal growth rate of structurally diverse compounds from aqueous solution. *Mol Pharm* **2013**, 10, (6), 2381-93.
54. Fleer, G.; Stuart, M. C.; Scheutjens, J.; Cosgrove, T.; Vincent, B., *Polymers at interfaces*. Springer Science & Business Media: 1993.

55. Roiter, Y.; Minko, S. AFM single molecule experiments at the solid– liquid interface: In situ conformation of adsorbed flexible polyelectrolyte chains. *Journal of the American Chemical Society* **2005**, *127*, (45), 15688-15689.
56. Schram, C. J.; Beaudoin, S. P.; Taylor, L. S. Impact of polymer conformation on the crystal growth inhibition of a poorly water-soluble drug in aqueous solution. *Langmuir* **2015**, *31*, (1), 171.
57. Kubota, N.; Mullin, J. W. A kinetic model for crystal growth from aqueous solution in the presence of impurity. *J. Cryst. Growth* **1995**, *152*, (3), 203-208.
58. Kubota, N. Effect of Impurities on the Growth Kinetics of Crystals. *Cryst. Res. Technol.* **2001**, *36*, (8-10), 749-769.
59. Macheras, P., *Modeling in Biopharmaceutics, Pharmacokinetics and Pharmacodynamics Homogeneous and Heterogeneous Approaches*. 2nd ed.. ed.; Cham : Springer International Publishing : Imprint: Springer: 2016.
60. Higuchi, W. I.; Mir, N. A.; Desai, S. J. Dissolution Rates of Polyphase Mixtures. *J. Pharm. Sci.* **1965**, *54*, (10), 1405-1410.
61. Simonelli, A.; Mehta, S.; Higuchi, W. Dissolution Rates of High Energy Polyvinylpyrrolidone (PVP)-Sulfathiazole Coprecipitates. *J. Pharm. Sci.* **1969**, *58*, (5), 538-549.
62. Raina, S. A.; Zhang, G. G. Z.; Alonzo, D. E.; Wu, J.; Zhu, D.; Catron, N. D.; Gao, Y.; Taylor, L. S. Enhancements and Limits in Drug Membrane Transport using Supersaturated Solutions of Poorly Water Soluble Drugs. *J. Pharm. Sci.* **2014**, *103*, (9), 2736-2748.
63. Stewart, A. M.; Grass, M. E.; Brodeur, T. J.; Goodwin, A. K.; Morgen, M. M.; Friesen, D. T.; Vodak, D. T. Impact of Drug-Rich Colloids of Itraconazole and HPMCAS on Membrane Flux in Vitro and Oral Bioavailability in Rats. *Mol Pharm* **2017**, *14*, (7), 2437-2449.
64. Yuan, X.; Xiang, T. X.; Anderson, B. D.; Munson, E. J. Hydrogen Bonding Interactions in Amorphous Indomethacin and Its Amorphous Solid Dispersions with Poly(vinylpyrrolidone) and Poly(vinylpyrrolidone-co-vinyl acetate) Studied Using (13)C Solid-State NMR. *Mol Pharm* **2015**, *12*, (12), 4518-28.
65. Xiang, T. X.; Anderson, B. D. Effects of Molecular Interactions on Miscibility and Mobility of Ibuprofen in Amorphous Solid Dispersions With Various Polymers. *J Pharm Sci* **2019**, *108*, (1), 178-186.
66. Chan, S. Y.; Qi, S.; Craig, D. Q. An Investigation into the Influence of Drug-polymer Interactions on the Miscibility, Processability and Structure of Polyvinylpyrrolidone-based Hot Melt Extrusion Formulations. *Int J Pharm* **2015**, *496*, (1), 95-106.

67. Chen, Y.; Chen, H.; Wang, S.; Liu, C.; Qian, F. A Single Hydrogen to Fluorine Substitution Reverses the Trend of Surface Composition Enrichment of Sorafenib Amorphous Solid Dispersion upon Moisture Exposure. *Pharm Res* **2019**, *36*, (7), 105.
68. Lu, X.; Huang, C.; Lowinger, M. B.; Yang, F.; Xu, W.; Brown, C. D.; Hesk, D.; Koynov, A.; Schenck, L.; Su, Y. Molecular Interactions in Posaconazole Amorphous Solid Dispersions from Two-Dimensional Solid-State NMR Spectroscopy. *Mol. Pharm.* **2019**.
69. Mistry, P.; Mohapatra, S.; Gopinath, T.; Vogt, F. G.; Suryanarayanan, R. Role of the strength of drug–polymer interactions on the molecular mobility and crystallization inhibition in ketoconazole solid dispersions. *Mol. Pharm.* **2015**, *12*, (9), 3339-3350.
70. Chen, Y.; Pui, Y.; Chen, H.; Wang, S.; Serno, P.; Tonniss, W.; Chen, L.; Qian, F. Polymer-Mediated Drug Supersaturation Controlled by Drug-Polymer Interactions Persisting in an Aqueous Environment. *Mol Pharm* **2019**, *16*, (1), 205-213.
71. Williams, H. D.; Trevaskis, N. L.; Charman, S. A.; Shanker, R. M.; Charman, W. N.; Pouton, C. W.; Porter, C. J. H. Strategies to Address Low Drug Solubility in Discovery and Development. *Pharmacol. Rev.* **2013**, *65*, (1), 315-499.
72. Di, L.; Artursson, P.; Avdeef, A.; Ecker, G. F.; Faller, B.; Fischer, H.; Houston, J. B.; Kansy, M.; Kerns, E. H.; Krämer, S. D.; Lennernäs, H.; Sugano, K. Evidence-based approach to assess passive diffusion and carrier-mediated drug transport. *Drug Discov. Today* **2012**, *17*, (15), 905-912.
73. Vasconcelos, T.; Sarmiento, B.; Costa, P. Solid Dispersions as Strategy to Improve Oral Bioavailability of Poor Water Soluble Drugs. *Drug Discov. Today* **2007**, *12*, (23), 1068-75.
74. Hancock, B. C.; Zografi, G. Characteristics and Significance of the Amorphous State in Pharmaceutical Systems. *J. Pharm. Sci.* **86**, (1), 1-12.
75. Wegiel, L. A.; Mauer, L. J.; Edgar, K. J.; Taylor, L. S. Crystallization of amorphous solid dispersions of resveratrol during preparation and storage-Impact of different polymers. *J. Pharm. Sci.* **2013**, *102*, (1), 171-84.
76. Matsumoto, T.; Zografi, G. Physical Properties of Solid Molecular Dispersions of Indomethacin with Poly(vinylpyrrolidone) and Poly(vinylpyrrolidone-co-vinyl-acetate) in Relation to Indomethacin Crystallization. *Pharm. Res.* **1999**, *16*, (11), 1722-1728.
77. Marsac, P. J.; Rumondor, A. C.; Nivens, D. E.; Kestur, U. S.; Stanciu, L.; Taylor, L. S. Effect of temperature and moisture on the miscibility of amorphous dispersions of felodipine and poly(vinyl pyrrolidone). *J. Pharm. Sci.* **2010**, *99*, (1), 169-85.
78. Toth, S. J.; Schmitt, P. D.; Snyder, G. R.; Trasi, N. S.; Sullivan, S. Z.; George, I. A.; Taylor, L. S.; Simpson, G. J. Ab Initio Prediction of the Diversity of Second Harmonic Generation from Pharmaceutically Relevant Materials. *Cryst. Growth Des.* **2015**, *15*, (2), 581-586.

79. Keraticewanun, S.; Yoshihashi, Y.; Sutanthavibul, N.; Terada, K.; Chatchawalsaisin, J. An Investigation of Nifedipine Miscibility in Solid Dispersions Using Raman Spectroscopy. *Pharm. Res.* **2015**, *32*, (7), 2458-2473.
80. Wanapun, D. K.; Umesh S.; Kissick, David J.; Simpson, Garth J.; Taylor, L. S. Selective detection and quantitation of organic molecule crystallization by second harmonic generation microscopy. *Anal. Chem.* **2010**, *82*, (13), 5425–5432.
81. Alonzo, D. E.; Raina, S.; Zhou, D.; Gao, Y.; Zhang, G. G. Z.; Taylor, L. S. Characterizing the Impact of Hydroxypropylmethyl Cellulose on the Growth and Nucleation Kinetics of Felodipine from Supersaturated Solutions. *Cryst. Growth Des.* **2012**, *12*, (3), 1538-1547.
82. Schram, C. J.; Beaudoin, S. P.; Taylor, L. S. Polymer Inhibition of Crystal Growth by Surface Poisoning. *Cryst. Growth Des.* **2016**, *16*, (4), 2094-2103.
83. Jackson, M. J.; Kestur, U. S.; Hussain, M. A.; Taylor, L. S. Dissolution of Danazol Amorphous Solid Dispersions: Supersaturation and Phase Behavior as a Function of Drug Loading and Polymer Type. *Mol. Pharm.* **2016**, *13*, (1), 223-31.
84. Cabrera, N.; Vermilyea, D., *Growth and Perfection of Crystals*. Wiley: New York, 1958; p 393-410.
85. Goddard, E. D.; Turro, N. J.; Kuo, P. L.; Ananthapadmanabhan, K. P. Fluorescence probes for critical micelle concentration determination. *Langmuir* **1985**, *1*, (3), 352-355.
86. Iswanto, N.; Hardin, M.; White, E. T. The growth rate spread of sugar seed crystals. *Proc. Aust. Soc. Sugar Cane Technol.* **2006**, 28.
87. Macrae, C. F.; Edgington, P. R.; McCabe, P.; Pidcock, E.; Shields, G. P.; Taylor, R.; Towler, M.; van de Streek, J. Mercury: visualization and analysis of crystal structures. *J. Appl. Crystallogr.* **2006**, *39*, (3), 453-457.
88. Taylor, L. S.; Zhang, G. G. Z. Physical Chemistry of Supersaturated Solutions and Implications for Oral Absorption. *Adv. Drug Delivery Rev.* **2016**, *101*, 122-142.
89. Brouwers, J.; Brewster, M. E.; Augustijns, P. Supersaturating Drug Delivery Systems: the Answer to Solubility-limited Oral Bioavailability? *J. Pharm. Sci.* **2009**, *98*, (8), 2549-2572.
90. Wu, S. Calculation of interfacial tension in polymer systems. *J. Polym. Sci., Part C: Polym. Symp.* **1971**, *34*, (1), 19-30.
91. Fukunishi, Y.; Tateishi, T.; Suzuki, M. Octane/Water Interfacial Tension Calculation by Molecular Dynamics Simulation. *J. Colloid Interface Sci.* **1996**, *180*, (1), 188-192.
92. Lu, J.; Ormes, J. D.; Lowinger, M.; Mann, A. K. P.; Xu, W.; Patel, S.; Litster, J. D.; Taylor, L. S. Impact of Bile Salts on Solution Crystal Growth Rate and Residual Supersaturation of an Active Pharmaceutical Ingredient. *Cryst. Growth Des.* **2017**, *17*, (6), 3528-3537.

93. Evans, T. W.; Margolis, G.; Sarofim, A. F. Mechanisms of secondary nucleation in agitated crystallizers. *AIChE J.* **1974**, *20*, (5), 950-958.
94. Sunagawa, I., *Crystals: Growth, Morphology and Perfection*. Original ed.; Cambridge University Press: 2005.
95. Shah, N.; Sandhu, H.; Choi, D. S.; Chokshi, H.; M Alick, A. W., *Amorphous Solid Dispersions: Theory and Practice*. Springer: 2014.
96. Newman, A.; Knipp, G.; Zografi, G. Assessing the performance of amorphous solid dispersions. *J. Pharm. Sci.* **2012**, *101*, (4), 1355-1377.
97. Law, D.; Schmitt, E. A.; Marsh, K. C.; Everitt, E. A.; Wang, W.; Fort, J. J.; Krill, S. L.; Qiu, Y. Ritonavir–PEG 8000 Amorphous Solid Dispersions: In vitro and In vivo Evaluations. *J. Pharm. Sci.* **2004**, *93*, (3), 563-570.
98. Alonzo, D. E.; Gao, Y.; Zhou, D.; Mo, H.; Zhang, G. G. Z.; Taylor, L. S. Dissolution and precipitation behavior of amorphous solid dispersions. *J. Pharm. Sci.* **2011**, *100*, (8), 3316-3331.
99. Hate, S. S.; Reutzel-Edens, S. M.; Taylor, L. S. Insight into Amorphous Solid Dispersion Performance by Coupled Dissolution and Membrane Mass Transfer Measurements. *Mol. Pharm.* **2018**.
100. LaFontaine, J. S.; McGinity, J. W.; Williams, R. O., 3rd. Challenges and Strategies in Thermal Processing of Amorphous Solid Dispersions: A Review. *AAPS PharmSciTech* **2016**, *17*, (1), 43-55.
101. Davis, M. T.; Potter, C. B.; Mohammadpour, M.; Albadarin, A. B.; Walker, G. M. Design of spray dried ternary solid dispersions comprising itraconazole, soluplus and HPMCP: Effect of constituent compositions. *Int. J. Pharm.* **2017**, *519*, (1-2), 365-372.
102. Jetli, R. R.; Singh, A.; Beeravelly, S.; Pathuri, S.; Bandi, N. Polymorphic Form of Ledipasvir. WO 2016/193919 A1, 2016.
103. Purohit, H. S.; Taylor, L. S. Phase Separation Kinetics in Amorphous Solid Dispersions Upon Exposure to Water. *Mol. Pharm.* **2015**, *12*, (5), 1623-1635.
104. Purohit, H. S.; Taylor, L. S. Phase Behavior of Ritonavir Amorphous Solid Dispersions during Hydration and Dissolution. *Pharm. Res.* **2017**, *34*, (12), 2842-2861.
105. Swain, D.; Samanthula, G. Study on the forced degradation behaviour of ledipasvir: Identification of major degradation products using LC-QTOF-MS/MS and NMR. *J. Pharm. Biomed. Anal.* **2017**, *138*, 29-42.

106. Link, J. O.; Taylor, J. G.; Xu, L.; Mitchell, M.; Guo, H.; Liu, H.; Kato, D.; Kirschberg, T.; Sun, J.; Squires, N.; Parrish, J.; Kellar, T.; Yang, Z. Y.; Yang, C.; Matles, M.; Wang, Y.; Wang, K.; Cheng, G.; Tian, Y.; Mogalian, E.; Mondou, E.; Cornpropst, M.; Perry, J.; Desai, M. C. Discovery of Ledipasvir (GS-5885): a Potent, Once-Daily oral NS5A Inhibitor for the Treatment of Hepatitis C Virus Infection. *J. Med. Chem.* **2014**, *57*, (5), 2033-46.
107. Greenspan, P.; Fowler, S. D. Spectrofluorometric Studies of the Lipid Probe, Nile Red. *J. Lipid Res.* **1985**, *26*, (7), 781-789.
108. Sackett, D. L.; Wolff, J. Nile Red as a Polarity-sensitive Fluorescent Probe of Hydrophobic Protein Surfaces. *Anal. Biochem.* **1987**, *167*, (2), 228-234.
109. *Pharmacology/Toxicology NDA Review and Evaluation* 205834; 2014.
110. Hassouna, M. E.-K. M.; Abdelrahman, M. M.; Mohamed, M. A. Assay and dissolution methods development and validation for simultaneous determination of sofosbuvir and ledipasvir by RP-HPLC method in tablet dosage forms. *J Forensic Sci & Criminal Inves* **2017**, *1*, (3), 001-11.
111. Dalvit, C.; Vulpetti, A. Weak Intermolecular Hydrogen Bonds with Fluorine: Detection and Implications for Enzymatic/Chemical Reactions, Chemical Properties, and Ligand/Protein Fluorine NMR Screening. *Chemistry* **2016**, *22*, (22), 7592-601.
112. Colbers, A.; Greupink, R.; Litjens, C.; Burger, D.; Russel, F. G. Physiologically based modelling of darunavir/ritonavir pharmacokinetics during pregnancy. *Clinical pharmacokinetics* **2016**, *55*, (3), 381-396.
113. Sun, Y.; Deac, A.; Zhang, G. G. Assessing Physical Stability of Colloidal Dispersions Using a Turbiscan Optical Analyzer. *Mol. Pharm.* **2019**, *16*, (2), 877-885.
114. Grimaudo, M. A.; Pescina, S.; Padula, C.; Santi, P.; Concheiro, A.; Alvarez-Lorenzo, C.; Nicoli, S. Poloxamer 407/TPGS Mixed Micelles as Promising Carriers for Cyclosporine Ocular Delivery. *Mol. Pharm.* **2018**, *15*, (2), 571-584.
115. Indulkar, A. S.; Mo, H.; Gao, Y.; Raina, S. A.; Zhang, G. G. Z.; Taylor, L. S. Impact of Micellar Surfactant on Supersaturation and Insight into Solubilization Mechanisms in Supersaturated Solutions of Atazanavir. *Pharm. Res.* **2017**, *34*, (6), 1276-1295.
116. Kesisoglou, F.; Wang, M.; Galipeau, K.; Harmon, P.; Okoh, G.; Xu, W. Effect of Amorphous Nanoparticle Size on Bioavailability of Anacetrapib in Dogs. *J. Pharm. Sci.* **2019**.
117. Gardner, C. R.; Walsh, C. T.; Almarsson, Ö. Drugs as materials: valuing physical form in drug discovery. *Nature Reviews Drug Discovery* **2004**, *3*, (11), 926.
118. Frank, D. S.; Matzger, A. J. Probing the Interplay between Amorphous Solid Dispersion Stability and Polymer Functionality. *Mol Pharm* **2018**, *15*, (7), 2714-2720.

119. Yokoi, Y.; Yonemochi, E.; Terada, K. Effects of sugar ester and hydroxypropyl methylcellulose on the physicochemical stability of amorphous cefditoren pivoxil in aqueous suspension. *Int. J. Pharm.* **2005**, *290*, (1), 91-99.
120. Xu, Z.; Yang, Z.; Liu, Y.; Lu, Y.; Chen, K.; Zhu, W. Halogen bond: its role beyond drug-target binding affinity for drug discovery and development. *J Chem Inf Model* **2014**, *54*, (1), 69-78.
121. Shinada, N. K.; de Brevern, A. G.; Schmidtke, P. Halogens in Protein-Ligand Binding Mechanism: A Structural Perspective. *J. Med. Chem.* **2019**.
122. Hassel, O. Structural Aspects of Interatomic Charge-Transfer Bonding. *Science* **1970**, *170*, (3957), 497-502.
123. Zordan, F.; Brammer, L.; Sherwood, P. Supramolecular Chemistry of Halogens: Complementary Features of Inorganic (M–X) and Organic (C–X') Halogens Applied to M–X···X'–C Halogen Bond Formation. *Journal of the American Chemical Society* **2005**, *127*, (16), 5979-5989.
124. Gilles Berger; Jalal Soubhyea; Meyer, F. Halogen Bonding in Polymer Science: From Crystal Engineering to Functional Supramolecular Polymers and Materials. *Polymer Chemistry* **2015**, *6*, 3559-3580.
125. Hardegger, L. A.; Kuhn, B.; Spinnler, B.; Anselm, L.; Ecabert, R.; Stihle, M.; Gsell, B.; Thoma, R.; Diez, J.; Benz, J.; Plancher, J. M.; Hartmann, G.; Banner, D. W.; Haap, W.; Diederich, F. Systematic investigation of halogen bonding in protein-ligand interactions. *Angew Chem Int Ed Engl* **2011**, *50*, (1), 314-8.
126. Sirimulla, S.; Bailey, J. B.; Vegesna, R.; Narayan, M. Halogen Interactions in Protein–Ligand Complexes: Implications of Halogen Bonding for Rational Drug Design. *Journal of Chemical Information and Modeling* **2013**, *53*, (11), 2781-2791.
127. Gliese, J. P.; Jungbauer, S. H.; Huber, S. M. A halogen-bonding-catalyzed Michael addition reaction. *Chem Commun (Camb)* **2017**, *53*, (88), 12052-12055.
128. Jungbauer, S. H.; Walter, S. M.; Schindler, S.; Rout, L.; Kniep, F.; Huber, S. M. Activation of a carbonyl compound by halogen bonding. *Chem Commun (Camb)* **2014**, *50*, (47), 6281-4.
129. Metrangolo, P.; Murray, J. S.; Pilati, T.; Politzer, P.; Resnati, G.; Terraneo, G. Fluorine-Centered Halogen Bonding: A Factor in Recognition Phenomena and Reactivity. *Cryst. Growth Des.* **2011**, *11*, (9), 4238-4246.
130. Wilcken, R.; Zimmermann, M. O.; Lange, A.; Joerger, A. C.; Boeckler, F. M. Principles and applications of halogen bonding in medicinal chemistry and chemical biology. *J Med Chem* **2013**, *56*, (4), 1363-88.

131. Riley, K. E.; Hobza, P. Strength and Character of Halogen Bonds in Protein–Ligand Complexes. *Cryst. Growth Des.* **2011**, *11*, (10), 4272-4278.
132. Lommerse, J. P.; Price, S. L.; Taylor, R. Hydrogen bonding of carbonyl, ether, and ester oxygen atoms with alkanol hydroxyl groups. *Journal of computational chemistry* **1997**, *18*, (6), 757-774.
133. Christer B. Aakeröy; Meg Fasulo; Nate Schultheiss; John Desper; Moore, C. Structural Competition between Hydrogen Bonds and Halogen Bonds. *Journal of American Chemical Society* **2007**, *129*, (45), 13772-13773.
134. Robertson, C. C.; Wright, J. S.; Carrington, E. J.; Perutz, R. N.; Hunter, C. A.; Brammer, L. Hydrogen bonding vs. halogen bonding: the solvent decides. *Chemical Science* **2017**, *8*, (8), 5392-5398.
135. Nemec, V.; Fotović, L.; Friščić, T.; Cinčić, D. A Large Family of Halogen-Bonded Cocrystals Involving Metal–Organic Building Blocks with Open Coordination Sites. *Cryst. Growth Des.* **2017**, *17*, (12), 6169-6173.
136. Xu, Y.; Viger-Gravel, J.; Korobkov, I.; Bryce, D. L. Mechanochemical Production of Halogen-Bonded Solids Featuring P=O⋯I–C Motifs and Characterization via X-ray Diffraction, Solid-State Multinuclear Magnetic Resonance, and Density Functional Theory. *The Journal of Physical Chemistry C* **2015**, *119*, (48), 27104-27117.
137. Laurence, C.; Queignec-Cabanetos, M.; Dziembowska, T.; Queignec, R.; Wojtkowiak, B. 1-Iodoacetylenes. 1. Spectroscopic evidence of their complexes with Lewis bases. A spectroscopic scale of soft basicity. *Journal of the American Chemical Society* **1981**, *103*, (10), 2567-2573.
138. M.T. Messina; P. Metrangolo; W. Navarrini; S. Radice; G. Resnati; Zerbi, G. Infrared and Raman Analyses of the Halogen-bonded Non-covalent Adducts Formed by a,v-diiodoperfluoroalkanes with DABCO and Other Electron Donors. *Journal of Molecular Structure* **2000**, *524*, (87-94).
139. Poleshchuk, O. K.; Branchadell, V.; Brycki, B.; Fateev, A. V.; Legon, A. C. HFI and DFT Study of the Bonding in Complexes of Halogen and Interhalogen Diatomics with Lewis Base. *Journal of Molecular Structure: THEOCHEM* **2006**, *760*, (1), 175-182.
140. Liao, J. J.-L. Molecular recognition of protein kinase binding pockets for design of potent and selective kinase inhibitors. *J. Med. Chem.* **2007**, *50*, (3), 409-424.
141. Karolewicz, B. A review of polymers as multifunctional excipients in drug dosage form technology. *Saudi Pharmaceutical Journal* **2016**, *24*, (5), 525-536.
142. Rumondor, A. C. F.; Dhareashwar, S. S.; Kesisoglou, F. Amorphous Solid Dispersions or Prodrugs: Complementary Strategies to Increase Drug Absorption. *J Pharm Sci* **2016**, *105*, (9), 2498-2508.

143. Shoichet, B. K.; Stroud, R. M.; Santi, D. V.; Kuntz, I. D.; Perry, K. M. Structure-based discovery of inhibitors of thymidylate synthase. *Science* **1993**, 259, (5100), 1445-1450.
144. Politzer, P.; Murray, J. S.; Clark, T. Halogen bonding: an electrostatically-driven highly directional noncovalent interaction. *Physical Chemistry Chemical Physics* **2010**, 12, (28), 7748-7757.
145. Zhou, X.; Goh, S. H.; Lee, S. Y.; Tan, K. L. X-ray Photoelectron Spectroscopic Studies of Interactions between Poly(p-vinylphenol) and Poly(vinylpyridine)s. *Applied Surface Science* **1997**, 119, (1), 60-66.
146. Cecchet, F.; Rudolf, P.; Rapino, S.; Margotti, M.; Paolucci, F.; Baggerman, J.; Brouwer, A. M.; Kay, E. R.; Wong, J. K. Y.; Leigh, D. A. Structural, Electrochemical, and Photophysical Properties of a Molecular Shuttle Attached to an Acid-Terminated Self-Assembled Monolayer. *The Journal of Physical Chemistry B* **2004**, 108, (39), 15192-15199.
147. Wang, F.; Ma, N.; Chen, Q.; Wang, W.; Wang, L. Halogen bonding as a new driving force for layer-by-layer assembly. *Langmuir* **2007**, 23, (19), 9540-2.
148. Xu, J.; Liu, X.; Ng, J. K.-P.; Lin, T.; He, C. Trimeric supramolecular liquid crystals induced by halogen bonds. *Journal of Materials Chemistry* **2006**, 16, (35).
149. Himmel, D. M.; Das, K.; Clark, A. D.; Hughes, S. H.; Benjahad, A.; Oumouch, S.; Guillemont, J.; Coupa, S.; Poncelet, A.; Csoka, I. Crystal structures for HIV-1 Reverse Transcriptase in Complexes with Three Pyridinone Derivatives: a New Class of Non-nucleoside Inhibitors Effective Against a Broad Range of Drug-resistant Strains. *J. Med. Chem.* **2005**, 48, (24), 7582-7591.
150. Riley, K. E.; Murray, J. S.; Politzer, P.; Concha, M. C.; Hobza, P. Br...O Complexes as Probes of Factors Affecting Halogen Bonding: Interactions of Bromobenzenes and Bromopyrimidines with Acetone. *J Chem Theory Comput* **2009**, 5, (1), 155-63.
151. Steiner, T. The Hydrogen Bond in the Solid State. *Angew. Chem. Int. Ed* **2002**, 41, 48-76.
152. Metrangolo, P.; Neukirch, H.; Pilati, T.; Resnati, G. Halogen Bonding based Recognition Processes: a World Parallel to Hydrogen Bonding. *Acc Chem Res* **2005**, 38, (5), 386-95.
153. Wegiel, L. A.; Mauer, L. J.; Edgar, K. J.; Taylor, L. S. Mid-infrared spectroscopy as a polymer selection tool for formulating amorphous solid dispersions. *J Pharm Pharmacol* **2014**, 66, (2), 244-55.
154. Kestur, U. S.; Van Eerdenbrugh, B.; Taylor, L. S. Influence of polymer chemistry on crystal growth inhibition of two chemically diverse organic molecules. *CrystEngComm* **2011**, 13, (22), 6712-6718.
155. Hermans, A.; Kesisoglou, F.; Xu, W.; Dewitt, K.; Marota, M.; Colace, T. Possibilities and Limiting Factors for the Use of Dissolution as a Quality Control Tool to Detect Presence of

- Crystallinity for Amorphous Solid Dispersions: An Experimental and Modeling Investigation. *J Pharm Sci* **2019**, *108*, (9), 3054-3062.
156. Moseson, D. E.; Taylor, L. S. The application of temperature-composition phase diagrams for hot melt extrusion processing of amorphous solid dispersions to prevent residual crystallinity. *Int. J. Pharm.* **2018**, *553*, (1-2), 454-466.
 157. Thordarson, P. Determining association constants from titration experiments in supramolecular chemistry. *Chemical Society Reviews* **2011**, *40*, (3), 1305-1323.
 158. Aakeröy, C. B.; Fasulo, M.; Schultheiss, N.; Desper, J.; Moore, C. Structural Competition between Hydrogen Bonds and Halogen Bonds. *Journal of the American Chemical Society* **2007**, *129*, (45), 13772-13773.
 159. Ibrahim, M. A. Molecular mechanical study of halogen bonding in drug discovery. *Journal of computational chemistry* **2011**, *32*, (12), 2564-2574.
 160. Szatyłowicz, H. Structural aspects of the intermolecular hydrogen bond strength: H-bonded complexes of aniline, phenol and pyridine derivatives. *Journal of Physical Organic Chemistry* **2008**, *21*, (10), 897-914.
 161. Cai, F.; Pu, X.; Qi, X.; Lynch, V.; Radha, A.; Ready, J. M. Chiral Allene-Containing Phosphines in Asymmetric Catalysis. *Journal of the American Chemical Society* **2011**, *133*, (45), 18066-18069.
 162. *SHELXTL suite of programs, Version 6.14, 2000-2003, Bruker Advanced X-ray Solutions, Bruker AXS Inc., Madison, Wisconsin: USA*
 163. Sheldrick, G. M. A short history of SHELX. *Acta Crystallographica Section A: Foundations of Crystallography* **2008**, *64*, (1), 112-122.
 164. Sheldrick, G. M. University of Göttingen, 2018.
 165. Sheldrick, G. M. Crystal structure refinement with SHELXL. *Acta Crystallographica Section C: Structural Chemistry* **2015**, *71*, (1), 3-8.
 166. Song, H.; Shin, H.-S. The Antifungal Drug Clotrimazole. *Acta Crystallographica Section C* **1998**, *54*, (11), 1675-1677.
 167. Gurka, D.; Taft, R. W. Studies of Hygeon-Bonded Complex Formation with p-Fluorophenol. IV. The Fluorine Nuclear Magnetic Resonance Method. *Journal of American Chemical Society* **1969**, *91*, (17), 4794-4801.
 168. Thordarson, P. Determining Association Constants from Titration Experiments in Supramolecular Chemistry. *Chemical Society Reviews* **2011**, *40*, 1305-1323.

VITA

Chailu Que received her Bachelor of Science in Chemistry from Nankai University and Bachelor of Engineering in Chemical Engineering from Tianjin University, Tianjin, China in 2010. After that she joined University of Memphis to achieve her Master in Chemistry in 2014. In the August 2014, Chailu joined the Industrial and Physical Pharmacy at Purdue University, West Lafayette, Indiana.